Missouri S&T Library and Learning Resources

Scholars' Mine

Doctoral Dissertations | Student Theses and Dissertations

Summer 2020

Investigation of wide bandgap semiconductors for room temperature spintronic, and photovoltaic applications

Vishal Saravade

Follow this and additional works at: https://scholarsmine.mst.edu/doctoral_dissertations

Part of the Electrical and Computer Engineering Commons

Department: Electrical and Computer Engineering

Recommended Citation

Saravade, Vishal, "Investigation of wide bandgap semiconductors for room temperature spintronic, and photovoltaic applications" (2020). *Doctoral Dissertations*. 3138.
https://scholarsmine.mst.edu/doctoral_dissertations/3138

This thesis is brought to you by Scholars' Mine, a service of the Missouri S&T Library and Learning Resources. This work is protected by U. S. Copyright Law. Unauthorized use including reproduction for redistribution requires the permission of the copyright holder. For more information, please contact scholarsmine@mst.edu.

INVESTIGATION OF WIDE BANDGAP SEMICONDUCTORS FOR ROOM TEMPERATURE SPINTRONIC, AND PHOTOVOLTAIC APPLICATIONS

by

VISHAL SARAVADE

A DISSERTATION

Presented to the Graduate Faculty of the

MISSOURI UNIVERSITY OF SCIENCE AND TECHNOLOGY

In Partial Fulfillment of the Requirements for the Degree

DOCTOR OF PHILOSOPHY

in

ELECTRICAL ENGINEERING

2020

Approved by:

Ian Ferguson, Advisor
Chuanle Zhou, Co-Advisor
Na Lu
Edward Kinzel
Chang-Soo Kim
Steve E. Watkins
Jie Huang

© 2020

Vishal Saravade

All Rights Reserved

ABSTRACT

Suitability of wide bandgap semiconductors for room temperature (RT) spintronic, and photovoltaic applications is investigated.

Spin properties of metal-organic chemical vapor deposition (MOCVD) – grown gadolinium-doped gallium nitride (GaGdN) are studied and underlying mechanism is identified. GaGdN exhibits Anomalous Hall Effect at room temperature if it contains oxygen or carbon atoms but shows Ordinary Hall Effect in their absence. The mechanism for spin and ferromagnetism in GaGdN is a combination of intrinsic, metallic conduction, and carrier-hopping mechanisms, and is activated by oxygen or carbon centers at interstitial or similar sites. A carrier-related mechanism in MOCVD-grown GaGdN at room temperature makes it a suitable candidate for spintronic applications.

Zinc oxide (ZnO) doped with transition metals such as nickel and manganese and grown by MOCVD is investigated, and bandgap tunability is studied. A bandgap reduction with transition metal doping is seen in ZnO with dilute doping of nickel or manganese. Transition metals could introduce energy states in ZnO that result in a bandgap reduction and could be tuned and controlled by growth conditions and post-growth processing such as annealing, for spintronic and photovoltaic applications.

ACKNOWLEDGMENTS

I would firstly like to express my sincere gratitude to my advisor, Dr. Ian Ferguson, for his guidance, consistent encouragement and support throughout my PhD journey, and efforts into developing me into a better researcher. I am grateful to Dr. Chuanle Zhou for her feedbacks, research discussions, and help in experimental designs and analysis. Many thanks to Dr. Na Lu and Dr. Edward Kinzel for their parts of advising, and for providing motivation. I am thankful to Dr. Steve Watkins, Dr. Chang-Soo Kim, and Dr. Jie Huang for their assessment and constructive criticisms of the research work.

I would like to thank Dr. Amirhossein Ghods, Dr. Zahra Manzoor, Mr. Andrew Woode, Mr. Tao Liu, Ms. Alexis Corda, Mr. Cameron Ferguson, and Mr. Paresh Patel for their help and constructive discussions in the research effort. I deeply appreciate the help and support that I received from current and previous lab members primarily from the POETS Group, and secondarily from SMART Lab and Thermal Radiation Lab.

I am grateful to Columbus Photovoltaic LLC, and National Science Foundation for their financial support to conduct the PhD research work.

I would like to thank my parents, brother, and grandparents for their constant support, patience, and blessings. Finally, thanks to all my friends for their love and support.

TABLE OF CONTENTS

Page

ABSTRACT iii

ACKNOWLEDGMENTS iv

LIST OF ILLUSTRATIONS xi

LIST OF TABLES xx

NOMENCLATURE xxii

SECTION

1. INTRODUCTION 1

1.1. SPINTRONICS 4

1.1.1. Next Generation Spintronic Devices. 6

1.1.2. Next Generation Spintronic Applications. 9

1.1.3. Materials Platform for Spintronics. 13

1.2. PHOTOVOLTAIC 17

1.3. COMPOUND SEMICONDUCTORS 18

1.4. GROWTH OF GALLIUM NITRIDE AND ZINC OXIDE 19

1.5. GALLIUM NITRIDE AND ZINC OXIDE DEVICES AND APPLICATIONS 23

1.5.1. Spintronics. 23

1.5.2. Photovoltaics. 29

1.5.3. Thermoelectrics. 30

1.5.4. Light Emitting Diodes. 32

1.5.5. Neutron Detection. 33

1.5.6. Other Applications. 34

1.6. SPINTRONICS AND COMPOUND SEMICONDUCTORS SUMMARY 36

2. GADOLINIUM-DOPED GALLIUM NITRIDE FOR ROOM TEMPERATURE SPINTRONICS 37

2.1. GADOLINIUM-DOPED GALLIUM NITRIDE 37

2.2. METAL-ORGANIC CHEMICAL VAPOR DEPOSITION GROWTH OF GADOLINIUM-DOPED GALLIUM NITRIDE 45

2.3. STRUCTURAL PROPERTIES OF GADOLINIUM-DOPED GALLIUM NITRIDE 50

2.4. MAGNETIC PROPERTIES OF GADOLINIUM-DOPED GALLIUM NITRIDE 54

2.5. ELECTRICAL CHARACTERIZATION OF GADOLINIUM-DOPED GALLIUM NITRIDE 56

2.6. ANOMALOUS HALL EFFECT CHARACTERIZATION OF GADOLINIUM-DOPED GALLIUM NITRIDE 61

2.6.1. Hall Effect. 61

2.6.2. Anomalous Hall Effect. 62

2.6.3. Anomalous Hall Effect Characterization of GaGdN. 67

2.6.4. Mechanism for Anomalous Hall Effect in GaGdN. 69

2.7. MECHANISM FOR SPIN PROPERTIES OF GADOLINIUM-DOPED GALLIUM NITRIDE 72

3. ROLE OF OXYGEN AND CARBON IN GADOLINIUM-DOPED GALLIUM NITRIDE FOR SPINTRONICS 75

3.1. SPIN-RELATED ELEMENTS IN GaGdN 75

3.2. ION IMPLANTATION OF OXYGEN AND CARBON IN GaGdN 85

3.3. STRUCTURAL STUDY OF OXYGEN AND CARBON-IMPLANTED GADOLINIUM-DOPED GALLIUM NITRIDE 87

3.4. ANOMALOUS HALL EFFECT CHARACTERIZATION OF OXYGEN AND CARBON-IMPLANTED GADOLINIUM-DOPED GALLIUM NITRIDE 91

3.5. EFFECT OF ANNEALING ON OXYGEN AND CARBON-IMPLANTED GADOLINIUM-DOPED GALLIUM NITRIDE 95

3.5.1. Annealing O- and C-implanted GaGdN. 95

3.5.2. Structural Study of Annealed O- and C-implanted GaGdN. 97

3.5.3. Anomalous Hall Effect Characterization of Annealed O- and C-implanted GaGdN. 100

3.6. MECHANISM FOR SPIN-RELATED PROPERTIES OF OXYGEN AND CARBON-IMPLANTED GADOLINIUM-DOPED GALLIUM NITRIDE 102

3.7. MECHANISM FOR SPIN IN GaGdN AT ROOM TEMPERATURE 103

4. MOCVD GROWTH AND CHARACTERIZATION OF TRANSITION-METAL DOPED ZINC OXIDE 105

4.1. ZINC OXIDE FOR BANDGAP TUNABILITY 105

4.2. METAL-ORGANIC CHEMICAL VAPOR DEPOSITION OF ZINC OXIDE 112

4.3. STRUCTURAL AND OPTICAL CHARACTERIZATION OF ZINC OXIDE 117

4.4. METAL-ORGANIC CHEMICAL VAPOR DEPOSITION OF ZINC NICKEL OXIDE – PHASE I : EFFECTS OF NICKEL CONCENTRATION 122

4.5. STRUCTURAL AND OPTICAL PROPERTIES OF ZINC NICKEL OXIDE – PHASE I : EFFECTS OF NICKEL CONCENTRATION 125

4.5.1. Structural Properties. 125

4.5.2. Optical Properties. 129

4.6. METAL-ORGANIC CHEMICAL VAPOR DEPOSITION OF ZINC NICKEL OXIDE – PHASE II : EFFECTS OF GROWTH CONDITIONS.. 133

4.7. STRUCTURAL AND OPTICAL PROPERTIES OF ZINC NICKEL OXIDE – PHASE II: EFFECTS OF GROWTH CONDITIONS 134

4.7.1. Structural Properties. 134

4.7.2. Optical Properties. 137

4.7.3. Effects of Annealing. 140

4.8. METAL-ORGANIC CHEMICAL VAPOR DEPOSITION OF ZINC MANGANESE OXIDE 142

4.9. STRUCTURAL AND OPTICAL PROPERTIES OF ZINC MANGANESE OXIDE..... 144

4.9.1. Structural Properties. 144

4.9.2. Optical Properties. 147

4.9.3. Effects of Annealing. 150

4.10. HALL EFFECT ANALYSIS OF TRANSITION-METAL DOPED ZINC OXIDE 153

4.11. CONCLUSION – TRANSITION METAL DOPED ZINC OXIDE..... 154

5. FIELD-EFFECT SCHOTTKY SOLAR CELLS 156

5.1. SOLAR CELLS 156

5.2. FIELD-EFFECT SCHOTTKY SOLAR CELLS THEORY 159

5.3. FABRICATION OF GALLIUM ARSENIDE FIELD-EFFECT SCHOTTKY SOLAR CELLS 162

5.4. GALLIUM ARSENIDE FIELD-EFFECT SCHOTTKY SOLAR CELLS CHARACTERIZATION AND RESULTS..... 169

5.5. FIELD-EFFECT SCHOTTKY SOLAR CELLS SUMMARY 173

6. EQUIVALENT CIRCUIT MODELING OF INFRARED FREQUENCY SELECTIVE SURFACES 174

6.1. FREQUENCY SELECTIVE SURFACES 174

6.2. HEXAGONAL CLOSE PACKED DISK (HCP) INFRARED FREQUENCY SELECTIVE SURFACE (FSS) 176

6.3. HCP FSS EQUIVALENT CIRCUIT MODEL (ECM) 177

6.4. OPTIMIZED EQUIVALENT CIRCUIT OF INFRARED HCP FSS 178

6.5. GEOMETRY-DEPENDENCE OF THE FSS FREQUENCY RESPONSE .. 181

6.6. MATERIAL-DEPENDENCE OF THE FSS FREQUENCY RESPONSE 184

6.7. PERFECT ABSORBER DESIGN USING ECM 186

6.8. TRANSMISSION LINE BASED MODEL FOR INFRARED FREQUENCY SELECTIVE SURFACES - SUMMARY 189

7. CONCLUSIONS AND FUTURE WORK 190

7.1. CONCLUSIONS 190

7.1.1. Mechanism for RT Spin Functionality in MOCVD-grown GaGdN. ... 190

7.1.2. Bandgap Tunability in MOCVD-grown Transition Metal-doped Zinc Oxide. 194

7.1.3. Development and Analysis of Field-effect Schottky Solar Cells. 197

7.1.4. Development of Equivalent Circuit Model for Infrared Frequency Selective Surfaces. 197

7.2. FUTURE WORK 199

7.2.1. Spin-related Characterization of MOCVD-grown GaGdN. 199

7.2.2. MOCVD-GaGdN Based Spin-LEDs 202

7.2.3. Additional Characterization of GaN and ZnO Materials. 203

7.2.4. Compound Semiconductor Materials for Bandgap Tunability. 204

7.2.5. Development of ICBS Solar Cells in Multijunction Configuration. 205

7.2.6. Investigation of Equivalent Circuit Model for Infrared FSS..... 206

BIBLIOGRAPHY 207

VITA 244

LIST OF ILLUSTRATIONS

Page

Figure 1.1 Progress of electronics, and trend according to Moore's law. 1

Figure 1.2 Simultaneous control of spin and charge functionality of an electron. 4

Figure 1.3 Resistance and magnetization with parallel and anti-parallel spin alignment... 5

Figure 1.4 A magnetic tunnel junction spintronic device with memory and logic functionality. 6

Figure 1.5 Schematic model of a AlSb/GaSb/InAs based spin transistor..... 7

Figure 1.6 Schematic of a spinLED, and applications of a Co_2FeSi-Fe based spinLED for optical communication transfer and corresponding photocurrent in a detector spinLED at temperature of 20K. 8

Figure 1.7 Spintronics for neuromorphic computing – Magnetic tunnel junction as a neuron, and neuromorphic computing-related processes and constituent device base. 10

Figure 1.8 Schematic of FeB/MgO/CoFeB spintronic nano-oscillator and spoken digits recognition rate. 11

Figure 1.9 Memristor units, corresponding crossbar array, and a configuration for applications such as artificial retina. 12

Figure 1.10 MOCVD chamber flow flange, substrate holder, grown ZnO sample, and resulting photoluminescence spectra. 21

Figure 1.11 Room temperature ferromagnetism in p-type GaGdN. 25

Figure 1.12 Magnetization measurement of GaMnN and GaFeN nanostructures grown on AlN on sapphire by MOCVD. 26

Figure 1.13 Magnetic properties of Fe-doped ZnO bulk crystal grown by melt growth technique, and Gd-doped ZnO thin film grown by MOCVD. 28

Figure 1.14 Seebeck coefficient and power factor of various ZnO compositions..... 31

Figure 1.15 Seebeck coefficients of GaN based materials. 32

Figure 2.1 Indirect exchange mechanisms in dilute magnetic semiconductors. 38

Figure 2.2 Computed Curie Temperature of dilute magnetic semiconductors. 39

Figure 2.3 Magnetization response of GaMnN:Si at 5 K and effect of Si-codoping, and transmission spectra of GaMnN and GaMnN at 293 K. 40

Figure 2.4 Energy and configuration coordinate figure of Mn-related transitions in GaMnN. 41

Figure 2.5 Electronic structure density of states of Gd-doped GaN. 42

Figure 2.6 Room temperature ferromagnetism in MBE-grown GaGdN. 43

Figure 2.7 Magnetic characterization of GaN grown by molecular beam epitaxy on silicon substrates and implanted with Gd. 43

Figure 2.8 Effect of annealing on Gd-implanted GaN. 44

Figure 2.9 Schematics of metal-organic chemical vapor deposition process. 46

Figure 2.10 Metal-organic chemical vapor deposition (MOCVD) tool used for the growth of GaGdN 47

Figure 2.11 Chemical formulas of gadolinium precursors – $(TMHD)_3Gd$ and Cp_3Gd. ... 48

Figure 2.12 Summary of GaGdN MOCVD growth process and schematic of the deposited structure[238] 49

Figure 2.13 XRD of MOCVD-grown GaGdN from $(TMHD)_3Gd$ precursor over a wide and short range, and GaGdN from Cp_3Gd precursor over a short range. 50

Figure 2.14 Williamson-Hall plot analysis of MOCVD-grown un-doped GaN, and Gd-doped GaN from $(TMHD)_3Gd$ and Cp_3Gd precursors to determine vertical correlation lengths and strain. 53

Figure 2.15 Williamson-Hall plot analysis of MOCVD-grown un-doped GaN, and Gd-doped GaN from $(TMHD)_3Gd$ and Cp_3Gd precursors to determine horizontal correlation lengths and tilt angles. 54

Figure 2.16 Magnetic properties of MOCVD-grown GaGdN grown from two Gd precursors – $(TMHD)_3Gd$ and Cp_3Gd[230]. 55

Figure 2.17 Room temperature magnetic characterization of GaGdN from $(TMHD)_3Gd$ precursor with Si and Mg co-doping. 56

Figure 2.18 MOCVD-grown GaN and GaGdN Spin-light emitting diodes schematics and characteristics – Current-voltage, and spin polarization. 57

Figure 2.19 Van der Pauw geometry configuration to measure resistivity of MOCVD-grown GaGdN and reference GaN samples. 58

Figure 2.20 Hall Effect measurement schematic with an applied current i and magnetic field H_z and measured voltage V_H. 59

Figure 2.21 Hall Effect measurement configuration..... 60

Figure 2.22 Mobility and carrier density of MOCVD-grown GaGdN and reference GaN. 61

Figure 2.23 Typical Hall Effect response. 62

Figure 2.24 Summary of determination of mechanisms based on relationship between Hall resistivity and sample's net resistivity. 64

Figure 2.25 Summary of Anomalous Hall Effect mechanisms based on the conductivity range of the samples. 66

Figure 2.26 Transverse and longitudinal resistivity of un-doped GaN. 68

Figure 2.27 Transverse and longitudinal resistivity of GaGdN from Cp_3Gd precursor. .. 69

Figure 2.28 Transverse and longitudinal resistivity of MOCVD-grown GaGdN from $(TMHD)_3Gd$ precursor. 70

Figure 2.29 Transverse resistivity of GaGdN from $(TMHD)_3Gd$ source processed to determine the anomalous Hall component. 71

Figure 2.30 Relationship between Anomalous Hall conductivity and longitudinal conductivity for MOCVD-grown GaGdN from $(TMHD)_3Gd$ precursor. 72

Figure 3.1 Summary of magnetic measurement results of MOCVD-grown GaGdN and chemical composition of the two Gd precursors $(TMHD)_3Gd$ and Cp_3Gd that were used..... 76

Figure 3.2 X-ray magnetic circular dichroism (XMCD) at Gd and superconducting quantum interference device (SQUID) measurement of MBE-grown GaGdN on SiC. 77

Figure 3.3 Thermally simulated current spectroscopy profile of MBE-grown GaGdN. .. 78

Figure 3.4 Total density of states in GaGdN and partial density of states related to oxygen interstitial site. 79

Figure 3.5 Total and partial density of states of GaGdN with O interstitial incorporation at octahedral and tetrahedral sites. 80

Figure 3.6 Band structural of oxygen split interstitial sites in GaGdN. 81

Figure 3.7 Projected density of states of 4f and 5d orbitals of Gd, and 2p orbitals of O in GaGdN. 82

Figure 3.8 Configuration of C-doped GaGdN nanostructures with different locations of C and Gd atoms in GaGdN, and related band structure. 83

Figure 3.9 Density of states of C, Gd, and Ga. 84

Figure 3.10 Stopping and range of ions in matter (SRIM) simulation of implantation parameters of O and C in GaGdN. 88

Figure 3.11 Long range 2θ-ω scans of O- and C-implanted GaGdN and comparison with as-grown GaGdN from Cp_3Gd source. 89

Figure 3.12 X-ray diffraction 2θ-ω scans of (002) peaks of O- and C-implanted, and as-grown GaGdN with vertical axes on linear and log scales. 90

Figure 3.13 Hall Effect analysis of as-grown GaGdN from Cp_3Gd source. 92

Figure 3.14 Anomalous Hall Effect in O-implanted GaGdN from Cp_3Gd source. 93

Figure 3.15 Anomalous Hall Effect in C-implanted GaGdN from Cp_3Gd source. 94

Figure 3.16 Annealing time and temperature for O- and C-implanted GaGdN. 96

Figure 3.17 X-ray diffraction 2θ-ω scans of annealed O- and C-implanted GaGdN and their comparison with as-implanted GaGdN and as-grown GaGdN from Cp_3Gd source. 97

Figure 3.18 X-ray diffraction 2θ-ω scans of (002) peaks of annealed O- and C-implanted GaGdN and their comparison with as-implanted GaGdN and as-grown GaGdN from Cp_3Gd source with vertical axes on linear and log scales. 98

Figure 3.19 Anomalous Hall Effect in annealed and as-implanted GaGdN:O. 100

Figure 3.20 Anomalous Hall Effect in annealed and as-implanted GaGdN:C. 101

Figure 4.1 Current-voltage characterization of ZnO/Ag Schottky solar cell at different axes limits..... 106

Figure 4.2 ZnO based tandem solar cell. 107

Figure 4.3 Summary of common thin film deposition techniques. 108

Figure 4.4 Bandgap and transmittance of un-doped and Ni-doped ZnO thin films grown by a DC/RF magnetron sputtering method. 109

Figure 4.5 Absorption spectra of Ni-doped zinc oxide with different nickel content. ... 110

Figure 4.6 A configuration coordinate model of ionization of Mn^{2+} states and related transitions in a hypothetical ionic system. 111

Figure 4.7 Absorption spectra of un-doped, Ni- and Mn-doped ZnO nanopowders by sol-gel technique, and their bandgap determination using Kramers-Kronig method. 111

Figure 4.8 Metal-organic vapor deposition system for growth of un-doped and transition-metal doped zinc oxide. 113

Figure 4.9 Metal-organic vapor deposition system for growth of un-doped and transition-metal doped zinc oxide – Control panel. 114

Figure 4.10 Schematic of metal-organic chemical vapor deposition system for growth of un-doped and transition-metal doped zinc oxide. 115

Figure 4.11 A simplified block diagram (mass flow controllers, sources, reaction chamber) of zinc oxide growth. 116

Figure 4.12 Software control of metal-organic chemical vapor deposition system for growth of un-doped and transition-metal doped zinc oxide. 117

Figure 4.13 X-ray diffraction results of an un-doped ZnO sample..... 119

Figure 4.14 Energy-dispersive X-ray characterization results of un-doped ZnO. 120

Figure 4.15 Effect of precursors' flows on the thickness of un-doped ZnO..... 120

Figure 4.16 Photoluminescence characterization results of un-doped ZnO. 121

Figure 4.17 Effect of precursors' flows on the bandgap of un-doped ZnO. 121

Figure 4.18 Photoluminescence characterization of sapphire, un-doped zinc oxide and nickel oxide..... 122

Figure 4.19 Ni-doped ZnO on silicon samples. 123

Figure 4.20 Ni-doped ZnO on sapphire (Phase I) Samples A-1 to A-4 with an increase in the Ni content. 125

Figure 4.21 Energy-dispersive X-ray spectroscopy results of a Ni-doped ZnO sample on sapphire (Phase I). 126

Figure 4.22 X-ray diffraction results of MOCVD-grown ZnNiO on sapphire (Phase I). 128

Figure 4.23 Photoluminescence diffraction results of MOCVD-grown ZnNiO on sapphire (Phase I). 130

Figure 4.24 Absorbance spectra and Tauc plots of MOCVD-grown ZnNiO on sapphire (Phase I). 132

Figure 4.25 Trend of variation in band gap of MOCVD-grown Ni-doped ZnO on sapphire (Phase I) with Ni content. 133

Figure 4.26 Energy-dispersive X-ray diffraction spectroscopy of Ni-doped ZnO on sapphire samples (Phase II). 135

Figure 4.27 X-ray diffraction results of Ni-doped ZnO on sapphire (Phase II). 136

Figure 4.28 Photoluminescence spectra of ZnNiO on sapphire growth at different growth conditions (Phase II). 138

Figure 4.29 Absorption spectra of ZnNiO on sapphire grown under varying temperature and pressure conditions (Phase II). 139

Figure 4.30 Tauc plots of ZnNiO on sapphire grown under varying temperature and pressure conditions (Phase II). 139

Figure 4.31 Photoluminescence spectra of as-grown and annealed ZnNiO. 140

Figure 4.32 Absorption spectra of as-grown and annealed ZnNiO. 141

Figure 4.33 Tauc plots of as-grown and annealed ZnNiO. 141

Figure 4.34 Pictures of 3 samples – sapphire, un-doped ZnO and ZnMnO. 144

Figure 4.35 X-ray diffraction results of MOCVD-grown ZnMnO. 145

Figure 4.36 Energy dispersive X-ray spectroscopy of MOCVD-growth ZnMnO. 147

Figure 4.37 Photoluminescence spectra of MOCVD-grown ZnMnO. 148

Figure 4.38 Absorption spectra of MOCVD-grown ZnMnO. 148

Figure 4.39 Tauc plots of MOCVD-grown ZnMnO. 149

Figure 4.40 Variation in band gap of MOCVD-grown ZnMnO with Mn source injection in ZnMnO growth at varying growth conditions. 149

Figure 4.41 X-ray diffraction results of as-grown and annealed ZnMnO. 150

Figure 4.42 Photoluminescence spectra of as-grown and annealed ZnMnO. 152

Figure 4.43 Absorption spectra of as-grown and annealed ZnMnO. 152

Figure 4.44 Tauc plots of as-grown and annealed ZnMnO. 153

Figure 4.45 Initial Hall Effect analysis of Ni-doped zinc oxide 154

Figure 5.1 Efficiency of solar cells with different active layer materials[358]. 156

Figure 5.2 Energy gap and lattice constants of selected compound semiconductors[377]. 157

Figure 5.3 Table showing Schottky barrier heights of junctions made of common metals with Si, Ge, and GaAs. 159

Figure 5.4 (a) Band-bending in n-type Schottky junction cell under illumination with carrier collection contact in the space charge region, and (b) Effect of isolated bias layer and external band-bending in ICBS solar cell. 161

Figure 5.5 Schematic of an ICBS solar cell. 162

Figure 5.6 Theoretical modeling of energy band structure of ICBS solar cell 163

Figure 5.7 Geometries of photomasks. 165

Figure 5.8 Illustration of a typical ICBS device fabrication process. 166

Figure 5.9 Working principle of atomic layer deposition with a sequential flow of two precursors and carrier gas. 167

Figure 5.10 Overview of ICBS device structures through the fabrication process. 168

Figure 5.11 ICBS solar cells for electrical characterization 169

Figure 5.12 Current-voltage characterization results of developed ICBS solar cells. 170

Figure 5.13 Device structure and current-voltage characteristics of gate-effect solar cells under the application of external voltage at the gate. 172

Figure 5.14 Effect of applied gate voltages on the short circuit current in field-effect Schottky solar cells. 173

Figure 6.1 Hexagonal close packed array frequency selective surface. 177

Figure 6.2 Equivalent circuit model of hexagonal closed packed array frequency selective surface. 178

Figure 6.3 Comparison of S_{11} magnitude and phase from HFSS simulation and equivalent circuit model. 181

Figure 6.4 Ground inductance L_1 with variation in the disk diameter for different period values with h = 0.3 µm, and different thickness values with p = 3 µm. 182

Figure 6.5 Capacitance C_2 with variation in the disk diameter for different period values with h = 0.3 µm, and different thickness values with p = 3 µm. 183

Figure 6.6 Inductance L_2 with variation in the disk diameter for different period values with h = 0.3 µm, and different thickness values with p = 3 µm. 183

Figure 6.7 Resistance R_2 with variation in the disk diameter for different period values with h = 0.3 µm, and different thickness values with p = 3 µm. 184

Figure 6.8 Capacitance C_2 with variation in dielectric permittivity of the layer between disks and ground 185

Figure 6.9 Conditions for perfection absorption by the hexagonal close packed array frequency selective surface: Diameter determines the resonant wavelength, and thickness and period determine absorptivity. 187

Figure 7.1 Schematic of magnetic circular dichroism measurement process. 200

Figure 7.2 Typical experimental setup for magnetic circular dichroism measurement. . 201

Figure 7.3 Schematic of a MOCVD-grown GaGdN based Spin-LED 202

Figure 7.4 Thermo-emf in Ni-doped ZnO by spray deposition. 203

Figure 7.5 Lowest energy electronic transitions of transition metal doped zinc sulfide as per first principles calculations[441]. 204

Figure 7.6 Absorption Tauc plots of MOCVD-grown ZnFeS with varying Fe content. 205

LIST OF TABLES

Page

Table 2.1 Energy-dispersive X-ray scattering spectroscopy results of GaGdN samples grown by MOCVD 51

Table 2.2 Anomalous Hall Effect mechanisms based on conductivity regimes and relationships between anomalous Hall conductivity and sample's net conductivity. 65

Table 3.1 Literature review of O implantation in GaN based materials. 85

Table 3.2 Summary of X-ray diffraction results of O- and C-implanted GaGdN. 91

Table 3.3 Electrical and Hall Effect characterization results of O- and C-implanted GaGdN from Cp_3Gd source 94

Table 3.4 Summary of X-ray diffraction results of annealed and implanted O- and C-implanted GaGdN and their comparison with as-implanted GaGdN and as-grown GaGdN from Cp_3Gd source. 99

Table 3.5 Summary of electrical and Hall Effect characterization annealed and implanted O- and C-implanted GaGdN and their comparison with as-implanted GaGdN and as-grown GaGdN from Cp_3Gd source. 102

Table 4.1 MOCVD growth / precursors' flow details of un-doped zinc oxide 118

Table 4.2 MOCVD growth parameters of set S of Ni-doped ZnO on silicon. 123

Table 4.3 MOCVD growth details of Ni-doped ZnO on sapphire – Phase I. 124

Table 4.4 Energy dispersive X-ray spectroscopy results of MOCVD-grown ZnNiO on sapphire (Phase I). 127

Table 4.5 X-ray diffraction results of MOCVD-grown ZnNiO on sapphire (Phase I). .. 129

Table 4.6 MOCVD growth details of Ni-doped ZnO on sapphire – Phase II 134

Table 4.7 Energy-dispersive X-ray spectroscopy results of ZnNiO on sapphire (Phase II). 136

Table 4.8 X-ray diffraction results of Ni-doped ZnO on sapphire (Phase II). 137

Table 4.9 MOCVD growth details of ZnMnO on sapphire. 143

Table 4.10 X-ray diffraction results of ZnMnO on sapphire 146

Table 4.11 X-ray diffraction results of as-grown and annealed ZnMnO. 151

Table 6.1 Constants in equivalent circuit model formulas. 180

NOMENCLATURE

Symbol	Description
DMS	Dilute magnetic semiconductors
T_C	Curie Temperature
RT	Room temperature
GaN	Gallium nitride
ZnO	Zinc oxide
MBE	Molecular beam epitaxy
MOCVD	Metal-organic chemical vapor deposition
TMGa	Trimethyl gallium
TMHD	2, 2, 6, 6 – tetramethyl-3, 5 – heptanedionato
Cp	cyclopentadienyl
XRD	X-ray diffraction
EDS	Energy-dispersive X-ray spectroscopy
θ, ω	Incident of diffraction angle (in context of XRD)
$\beta_{2\theta\text{-}\omega\text{–}1}$	Size-related XRD peak broadening
λ	Incident X-ray wavelength
$L_{\|\|}$	Vertical correlation length
$\beta_{2\theta\text{-}\omega\text{–}2}$	Strain-related XRD peak broadening
ε	Strain distribution
$\beta_{\omega\text{-RC}}$	XRD ω rocking curve peak broadening
VSM	Vibrating sample magnetometer

ρ_{4pt}	Longitudinal 4-point resistivity
ρ_{xx}	sample's resistivity
E	Electric field
H_z	Applied magnetic field
q	charge carriers
F	Force on charge carriers
v	Charge carrier velocity
AHE	Anomalous Hall effect
EHE	Extraordinary Hall Effect
ρ_{xy}	Hall resistivity
σ_{AHE}	Anomalous Hall conductivity
σ_{xx}	Longitudinal conductivity
OHE	Ordinary Hall effect
R_o	Ordinary Hall coefficient
ρ_{AHE}	Anomalous Hall component of Hall resistivity
R_{AHE}	Anomalous Hall coefficient
M	Magnetization
XMCD	X-ray magnetic circular dichroism
TSC	Thermally simulated current spectroscopy
O_i	Oxygen interstitials
DOS	Density of states
SRIM	Stopping and range of ions in matter
MFC	Mass flow controllers

DEZn	Diethyl zinc
β	Full width at half maximum
FWHM	Full width at half maximum
α	Absorption coefficient
h	Planck's constant
ν	Speed of light
GaAs	Gallium arsenide
ALD	Atomic layer deposition
V_{OC}	Open circuit voltage
V_{bias}	Externally applied bias voltage
I_{SC}	Short circuit current
FSS	Frequency selective surfaces
ECM	Equivalent circuit method
HCP	Hexagonal Close Packed Array
HFSS	High frequency structure simulator
p	HCP disks periodicity
d	HCP disks' diameter
h	HCP dielectric thickness
ε_r	Relative permittivity of crystalline silicon dielectric in HCP model
R_2	HCP disk resistance
L_2	HCP disk inductance
C_2	HCP disk capacitance
R_1	Ground resistance in HCP model

L_1	Ground inductance in HCP model
Z	Input impedance of HCP FSS structure
Z_{FSS}	Characteristic impedance of FSS layer in HCP model
Z_{in}	Input impedance towards ground in HCP model
k_0	Wave vector
Z_1	Characteristic impedance of the Al substrate in HCP model
MCD	Magnetic circular dichroism
LCP	Left-circularly polarized
RCP	Right-circularly polarized
PL	Photoluminescence
EL	Electroluminescence
EPR	Electron paramagnetic response
MOKE	Magneto-optical Kerr Effect
QW	Quantum wells
EELS	Electron energy loss spectroscopy
SIMS	Secondary ion mass spectroscopy
QW	Quantum wells
LED	Light emitting diode

1. INTRODUCTION

Wide bandgap compound semiconductors are investigated in this work, intended to address challenges in electronics and energy harvesting with focus on spintronics and photovoltaics respectively.

There has been an exponential growth in the microelectronics industry over the last decades with a consistent miniaturization of transistors' size and increase in the speed and on-chip transistors' density with reasonable power consumption, as seen in Figure 1.1[1]. This is based on developments in chip manufacturing and silicon CMOS technology, but the trend will saturate soon especially due to the unintended thermal noise that is dissipated, as the density of transistors on the chips increase and as the corresponding electronics approach their physical limits[2–5].

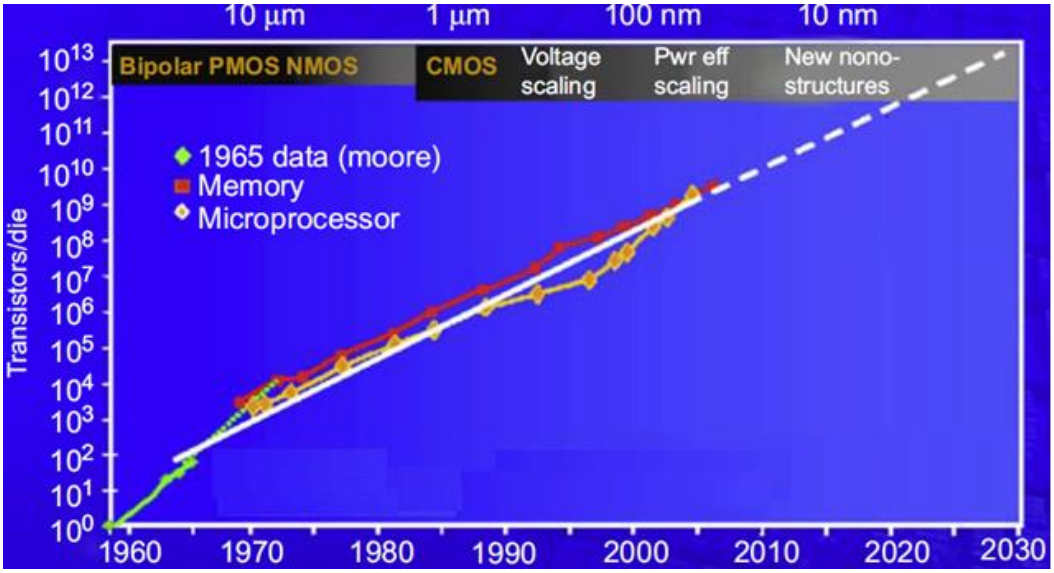

Figure 1.1 Progress of electronics, and trend according to Moore's law[1].

Developing processors for future computing platforms such as quantum information, neuromorphic computing, artificial intelligence, and big data need devices that are scalable with low power requirement and yet high speed. There is a need to implement new processing and computing techniques with more compact size, lower power consumption and enhanced performance.

In energy harvesting, there has been an increasing need to harness renewable energy sources such as solar energy to build a cleaner and greener environment and yet satisfy electrical power requirements[6–9]. However, the efficiency of solar cells is typically limited to ~20% which could be potentially improved by developments in solar cells technology.

Semiconductors have been among the most impactful materials recently and have been used in electronics and photovoltaics industries[10–12]. The need for better electronic and energy harvesting devices has propelled interests in newer semiconductors. Compound semiconductors such as III-V and II-VI materials or similar could be alternatives to conventional semiconductors such as silicon[13–17]. These materials have recently been explored for applications in electronics, energy harvesting, sensing, and bio-medicine.

This document presents a systematic study of compound semiconductors that could be used in future spintronic and photovoltaic technologies.

Section 1 briefly introduces spintronics, photovoltaics, and the compound semiconductors gallium nitride and zinc oxide. Challenges currently faced in the mentioned topics are identified and potential solutions are investigated in the next sections. Materials with spin functionalities at room temperature, and bandgap tunability that could be built into devices are of interest. Sections 2 and 3 explore gadolinium-doped gallium nitride grown by metal-organic chemical vapor deposition which could be an interesting

material for spintronic applications at room temperature, but the underlying causes of the conducive properties observed in the material are not clear. Also, the role of constituent elements in rendering spin properties needs more experimental study. It is essential to understand the mechanism of material properties in order to be able to control, manipulate, and apply them in practical devices and processors. In Sections 2 and 3, experiments targeted towards this understanding are discussed, and the mechanism is identified.

Bandgap tunability is an important property of compound semiconductor such as zinc oxide which makes it applicable for multi-junction solar cells' applications as an active layer. Also, bandgap tunability implies a control over the energy states in zinc oxide with doping. Doping with transition metals could introduce unpaired electrons in zinc oxide thereby widening its applications in spintronics and thermoelectrics. Section 4 discusses bandgap tunability in zinc oxide doped with nickel or manganese and grown by metal organic chemical vapor deposition.

Section 5 reviews and presents experimental efforts towards development of field-effect Schottky solar cells. External bias at the gate isolated from the probing layers in solar cells provides additional band-bending resulting in a better power conversion efficiency. Design and fabrication of gallium arsenide based Isolated Collection and Biasing Solar Cells (ICBS) are discussed. Gate effect in the solar cells is studied.

A transmission line based equivalent circuit model is developed in Section 6 to enable a rapid design of frequency selective surfaces in the infrared region with a physical insight into its functioning through circuit parameters.

Section 7 summarizes the findings and conclusions from this work and provides suggestions for future directions.

1.1. SPINTRONICS

Spintronics is an enabling technology to meet the speed, power, and scalability requirements for the next generation of computing such as quantum information and neuromorphic computing[18–20]. It promises to continue trend of miniaturization of electronic devices with lower power requirement as compared to the current technology[21–27]. The non-volatile nature of spintronic memory could help to tackle the power efficiency related challenges of microelectronics.

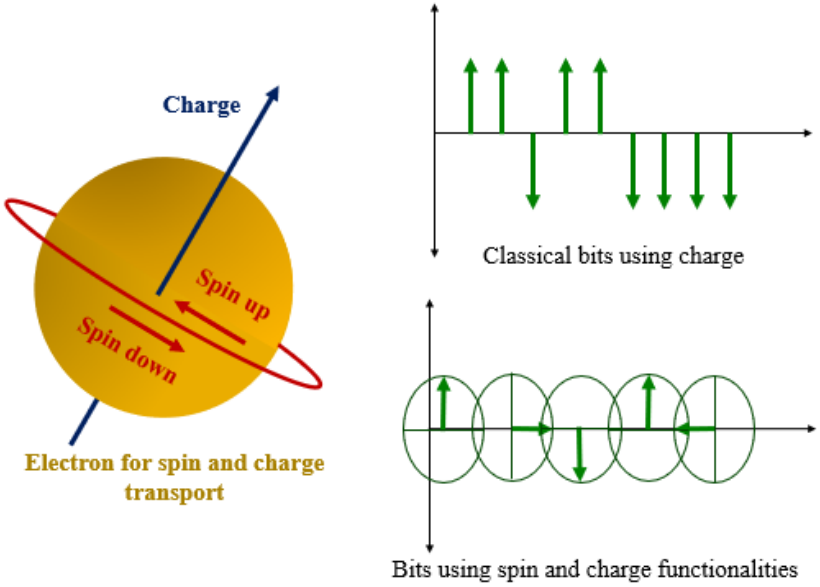

Figure 1.2 Simultaneous control of spin and charge functionality of an electron.

Spins are defined by their polarization as up-spin or down-spin as shown in Figure 1.2 and resulting effect could be a superposition of various quantum states. In a simplified jargon, if the two polarization directions of electrons are considered as variables to store bits (analogous to charged and discharged state of a capacitor), then to maintain electrons in a specific spin polarization, an external power source is not needed. This not only helps in

increasing non-volatile memory capacity but also results in reduced power consumption and miniaturization, as compared to current silicon-based semiconductor devices.

Early work around 1970s spintronics focused on theories and ways to inject and detect the spin. If external magnetic field up to 50 T is applied to layers of Ni and Al, a few Å thick, then voltage across the material can be measured in positive and negative directions as per the applied field[28]. These results can be compared to the measured voltages and related with the magnetic field. Such an experiment can predict the nature of spin in Ni-Al structure. Hanle effect, where the spin is detected with the help of the polarization of wave emitted by electrons-transition within energy bands, was also explored. An impetus to this technology was achieved by the discovery of the Giant Magnetoresistance (GMR) in 1988 by Albert Fert and Peter Grünberg[29]. When two ferromagnetic materials are in placed in a layered structure, then depending whether their spins are aligned in the same or opposite directions, the resistance measured changes as shown in Figure 1.3. One of the ferromagnets is typically kept in in a fixed direction and the other ferromagnet is tuned by external field[30].

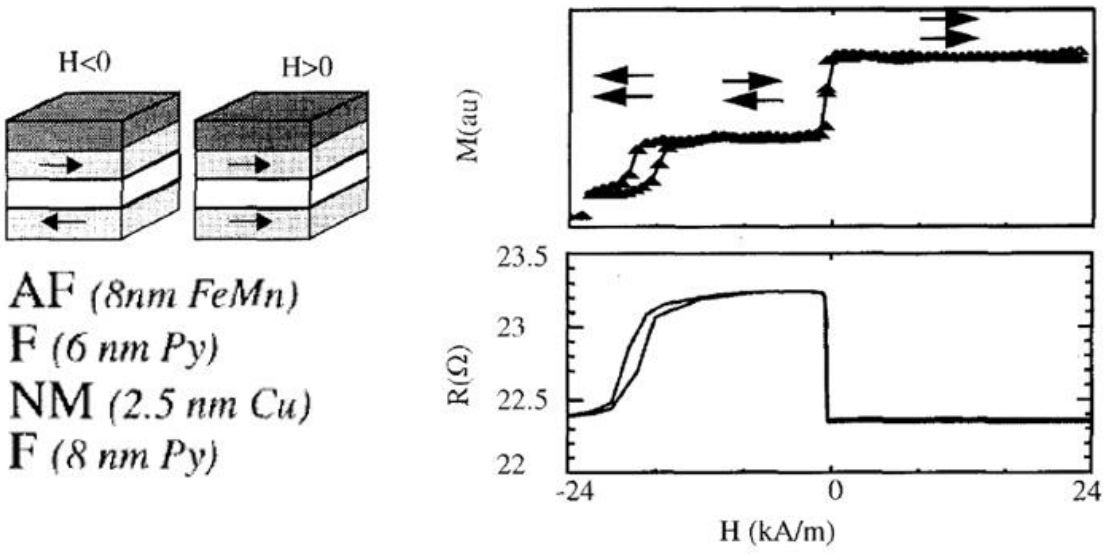

Figure 1.3 Resistance and magnetization with parallel and anti-parallel spin alignment[30].

1.1.1. Next Generation Spintronic Devices. In analogy with electronics devices, the working of spintronics-based devices would be governed by the control and manipulation of quantum states such as spin injection, spin transfer and spin detection.

Figure 1.4 shows a figure of a magnetic tunnel junction or a spintronic device with combined memory and logic functionalities[31,32]. An external current could be used to apply magnetic fields to the free ferromagnetic layer and result in logic 0 and logic 1 based on the orientation of spins between the free layer and ground layer separated by an insulator. When two ferromagnetic materials with same polarization are arranged in a layered structure and separated by a thin non-magnetic film, carriers with same spin tunnel through the intermediate layer. Ways to perform read and write operations with less latency and in an error-prone environment has been a topic of interest recently. Power consumption in such devices could be further reduced by utilizing the heat dissipation in the devices such as the residual heat can set the current that is used to tune the magnetic field[32,33].

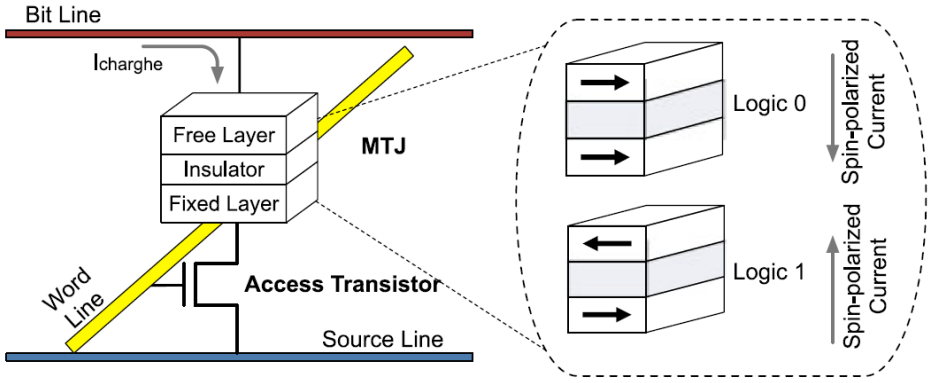

Figure 1.4 A magnetic tunnel junction spintronic device with memory and logic functionality[31].

Errors in memory storage could be reduced by increasing the difference between the resistances in anti-parallel and parallel arrangements. For example, tunneling magnetoresistance of 604% at room temperature and of 1144% at 5K were achieved in Ta/ $Co_{20}Fe_{60}B_{20}$/ MgO/ $Co_{20}Fe_{60}B_{20}$ configuration[34].

Spin transistors are an integral part of spintronics-based devices for their tunability in logic and memory applications[35,36]. The output current would depend on the magnetization configuration of the source and drain. A spin transistor could consist of ferromagnets or half-metallic-ferromagnets acting as source and drain and separated by an oxide[35]. The AlSb/GaSb/InAs spin transistor device model is shown in Figure 1.5[37]. Bulk inversion asymmetry could be utilized, and spin detection could be performed using spin-dependent resonant inter-band tunneling. The gate voltage controls the spin relaxation rates. However, calculations in the spin transistor model were performed at low temperature, which needs to be scaled up to room temperature for practical spin transistors.

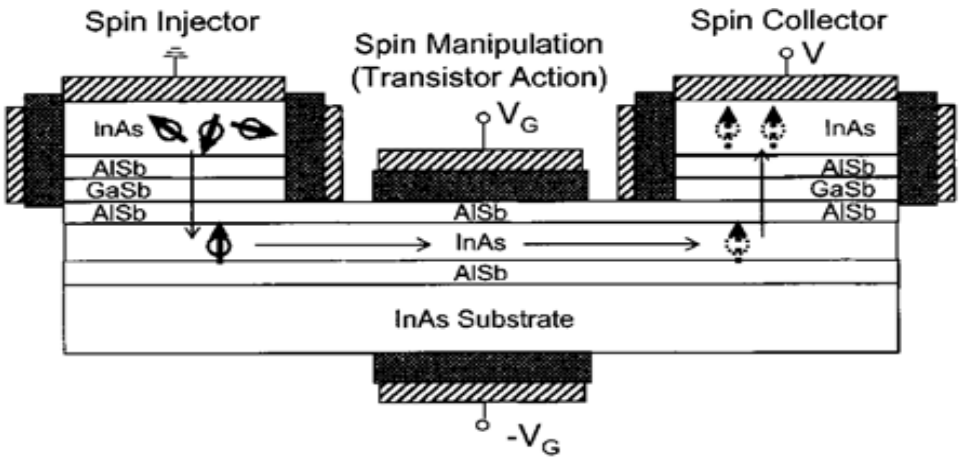

Figure 1.5 Schematic model of a AlSb/GaSb/InAs based spin transistor[37].

Injection, detection and transfer of spin has been a challenge. Light emitting diodes (LEDs) operate on the emission of light corresponding to the movement of electrons from higher energy band to lower energy band in a material[38–41]. If these electrons have an associated spin, then the emitted light will be polarized with respect to the spin of the involved electrons.

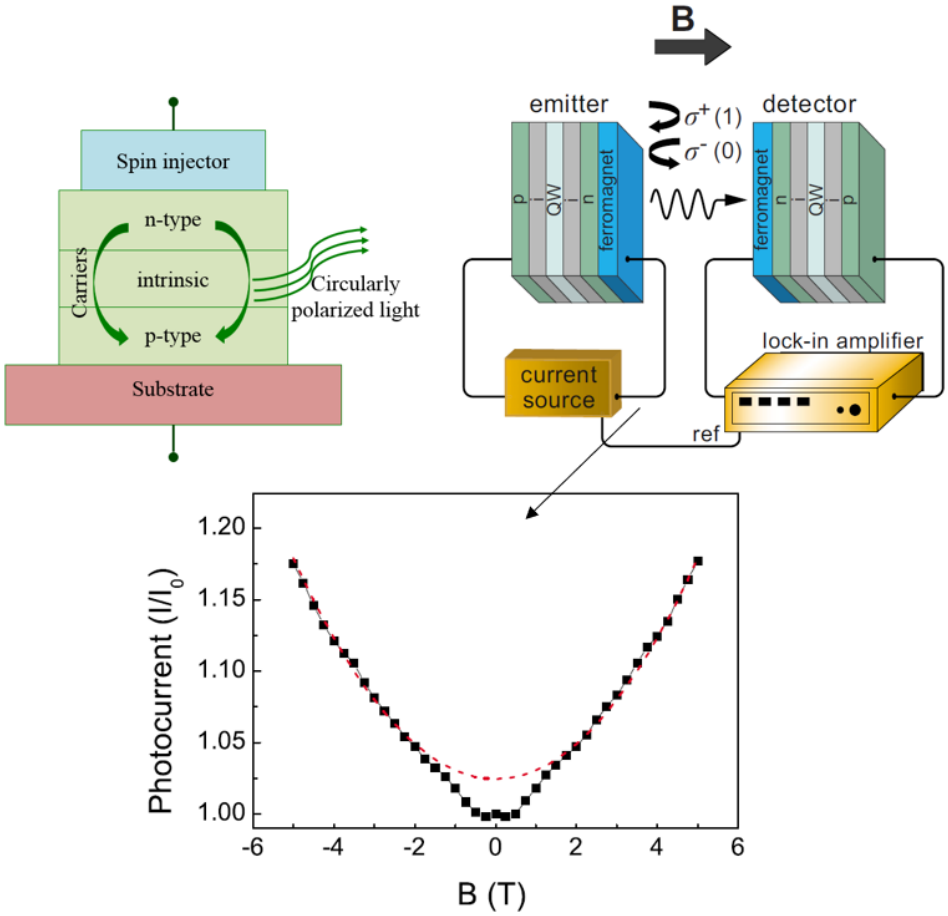

Figure 1.6 Schematic of a spinLED, and applications of a Co_2FeSi-Fe based spinLED for optical communication transfer and corresponding photocurrent in a detector spinLED at temperature of 20K[39].

Ferromagnetic metals have been most widely explored as spin injectors into an LED. Electron-spin polarization up to 32% was achieved in MBE-grown GaAs quantum

well at 4.6 K via a Fe/AlGaAs Schottky contact. Spin polarization of 80% was observed by using GaMnAs as the injector at 4.6 K[40]. Room temperature spin-polarized GaN-based LED using a FeCo/MgO spin injector showed spin polarization of 6% at room temperature[38]. The spin lifetime depends on the dislocation defects which could one of the reasons for a lower circular polarization.

Spin-LEDs have applications in the transfer of information using spin. This has been demonstrated in GaAs/AlGaAs quantum wells with Co_2FeSi and Fe injectors at 20 K and shown in Figure 1.6[39]. Accurate transfer of spin and increasing spin relaxation time is necessary for usage of spin in devices. This spin transfer can be achieved by using spin-LED. The spin of an electron is embedded in the emitted polarized light. Light can be detected by another spin-LED at the receiving end to decipher the spin information that was sent. The photocurrent in the receiver will be a function of the polarization of incident light, and the spin in the transmitter.

1.1.2. Next Generation Spintronic Applications. Spintronics aims at developing electronic device technology based on spin degrees of freedom. Quantum information, neuromorphic computing, artificial intelligence, and Big data require high computing speed and scalable sized device; simultaneous control of spin and charge for logic and memory could pave the way for such applications[42–45].

Neuromorphic computing involves development of processors that mimic biological processes and the human brain. Spintronic devices discussed in the previous Section 1.1.1 could be used as mammalian brain-like elements for complex architecture and data processing. A spin torque in a magnetic tunnel junction and corresponding interfaces could emulate neurons and synapses. Neuromorphic computing consists of

several sub-branches of neural networks, optimization, pattern detection, intelligent decision-making. The process of neuromorphic computing along with various sub-branches and potential device base is summarized in Figure 1.7[46-47].

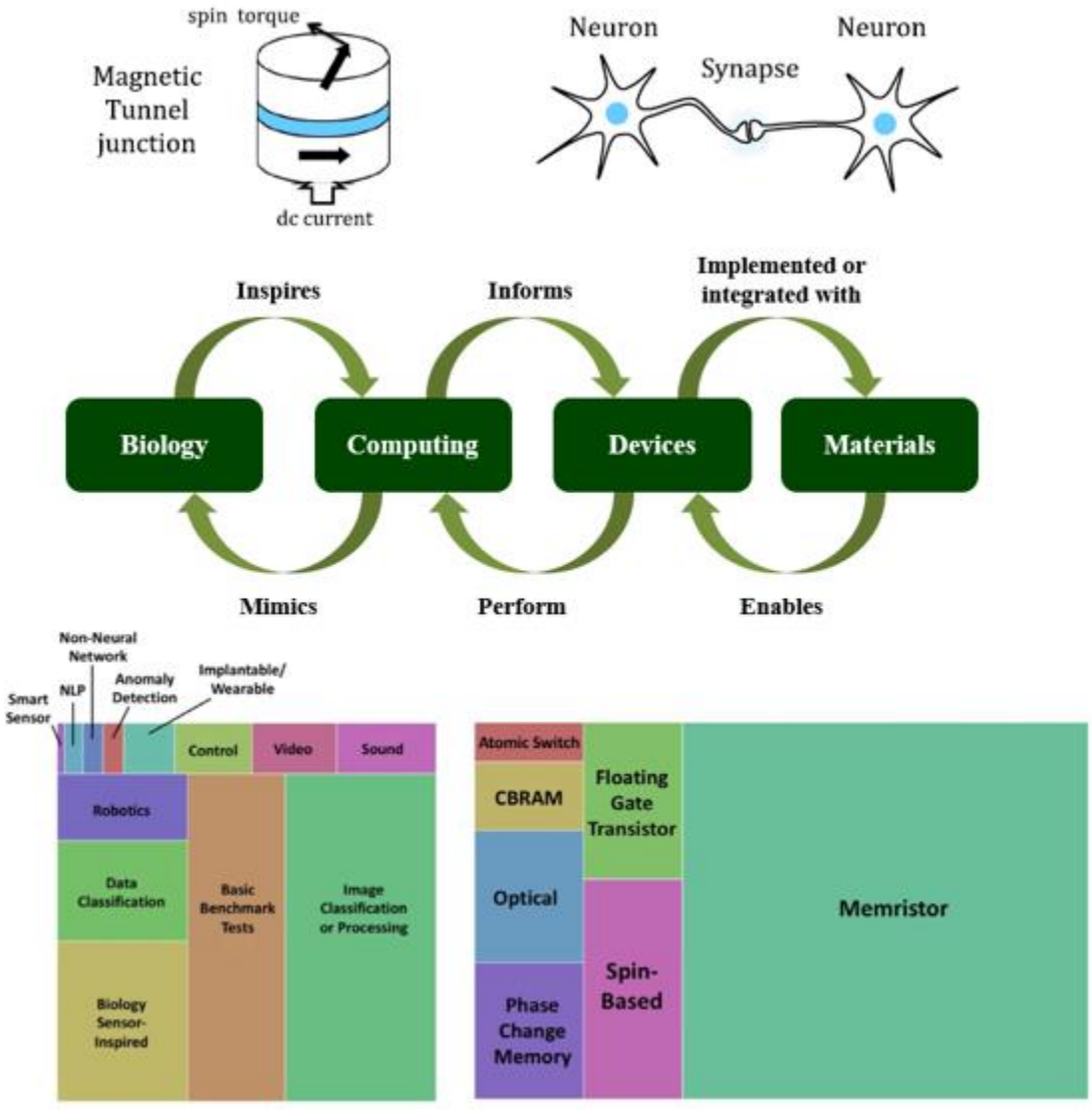

Figure 1.7 Spintronics for neuromorphic computing – Magnetic tunnel junction as a neuron, and neuromorphic computing-related processes and constituent device base[46-47].

Spintronic nano-oscillators could be developed as shown in Figure 1.8[48]. The processor would consist of a magnetic tunnel junction. Spin-polarized current would flow through the device at high frequencies in GHz resulting in generation of magnetic fields or torques. The magnetic field could then be captured as spin signals or converted to charge voltage signals through magnetoresistance, and the processor could be used as a spin-based oscillator. A schematic of a FeB/MgO/CoFeB based nano-oscillator and resulting spoken digits recognition rate are shown in Figure 1.8. Such devices could have applications in sensors, random number generators, and pattern recognition[49,50].

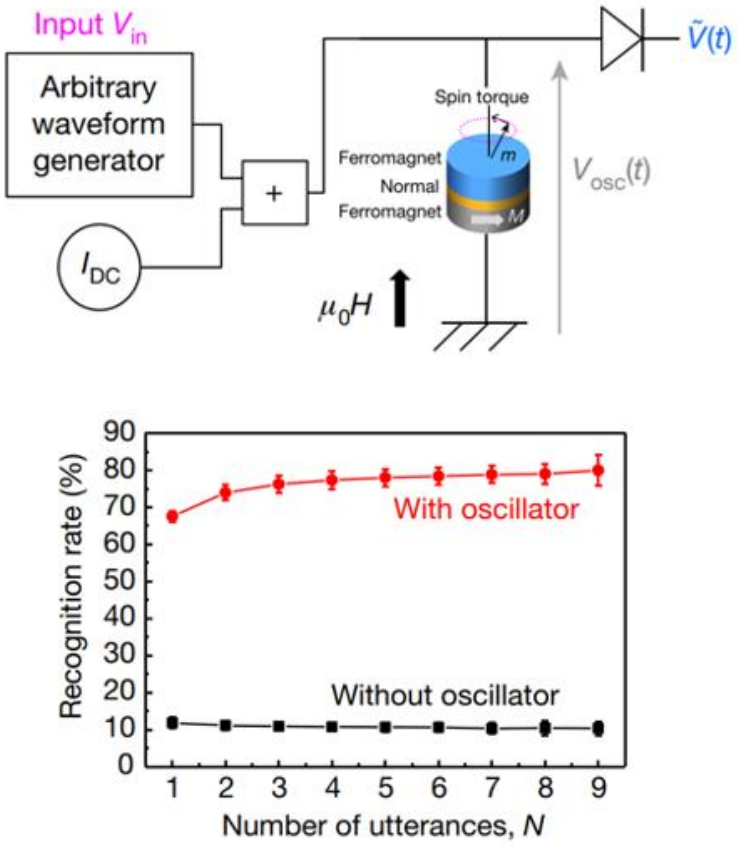

Figure 1.8 Schematic of FeB/MgO/CoFeB spintronic nano-oscillator and spoken digits recognition rate[48].

Memristor devices could be stacked together in a crossbar array to form neural networks for application in artificial intelligence. Each memristor unit could have a tunable resistance and spin as per applied current. When arranged in a crossbar array, memristor units could transfer information as per their logic levels and act as synapses and neurons. Suitable processing could be done and the information could be sent to the suitable neurons to take decisions, as shown in Figure 1.9 considering the case of vehicle traffic monitoring[46,51,52].

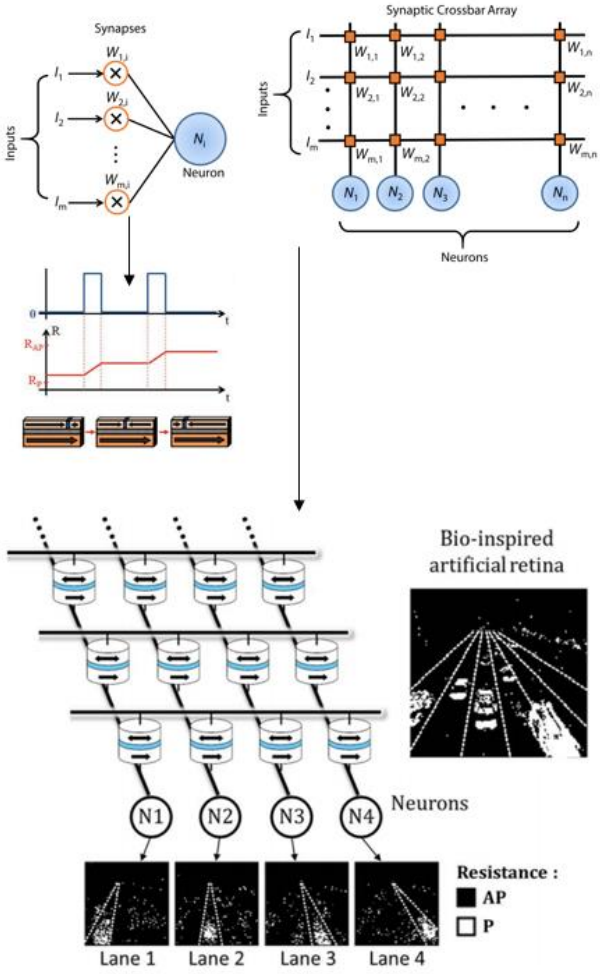

Figure 1.9 Memristor units, corresponding crossbar array, and a configuration for applications such as artificial retina[46,51,52].

1.1.3. Materials Platform for Spintronics. Spin of a material is directly related with its magnetic, electrical, and optical properties.

It is necessary to investigate materials and understand their properties to control and manipulate their spin for spintronic applications. However, most materials show conducive properties for spintronics at cryogenic temperatures, which limits their practical applications. Presence of Johnson-Nyquist-like noise which is minimum at cryogenic temperatures but increases with temperature makes it difficult to control the spin and to implement spintronics at room temperature[53–55]. There is a need to investigate spintronic materials for quantum applications at room temperature (RT) in order to build spintronic devices for practical purposes. Dilute magnetic semiconductors are strong candidates for such applications considering reports of ferromagnetism at room temperature and their compatibility with existing CMOS devices.

One of the requirements towards building spintronics-based electronics is the design of semiconductor, so that ferromagnetism could be tuned at room temperature. For practical spintronic applications, a material with controllable magnetic and semiconducting characteristics at room temperature (RT) is required. Transition metal (TM) or rare earth elements with partially filled d and/or f orbitals are doped in semiconductors with an intent to have ferromagnetic and semiconducting properties in a homogeneous material. DMS such as GaN, ZnO, TiO_2, GaAs, CdTe, InAs and InP are investigated for spintronics[56,57]. DMS based thin films are ferromagnetic; but the mechanism for the ferromagnetism is not clear. The magnetic properties could be due to defects, dopants, carriers, magnetic clusters, spin glass or secondary phases. Control of the spin and understanding of underlying mechanisms for ferromagnetism are still challenging. Theoretical modeling based on Zener

model predicts the Curie temperatures for semiconductors containing 5% Mn and 3.5 x 10^{20} holes per cm^3. GaN and ZnO, if successfully designed and fabricated, have potential for room temperature ferromagnetism. Understanding of the carrier concentration, mobility, crystal structure and defects in DMS and their relationship with the spin is necessary for the realization of spin-based devices such as spin-LEDs, spin-transistors, spin-sensors and so on. Gallium nitride and zinc oxide for spintronic applications are discussed in Section 1.5.

TiO_2 has been investigated for spin-based applications considering its chemical stability and electrical and optical properties. TiO_2 nanorods doped with 5% Mn and synthesized using hydrothermal method showed ferromagnetism that is influenced by the Mn concentration, oxygen vacancies and other defects in the structure[58]. The ferromagnetism is seen to increase with Mn content. It is likely caused by interactions of Mn with defects including oxygen vacancies that are locally present around the Mn ions. V is a TM that has ionic radius close to Ti and an extra electron than Ti. TiO_2 based nanotubes were doped with 5% V and calcinated in air or argon[59]. The magnetization in argon-calcinated $TiVO_2$ was stronger than air-calcinated. A bound magnetic polaron mechanism seems to be the cause for the RT ferromagnetism. Oxygen vacancies are more favored in argon environment than in air which possibly contributed to the ferromagnetism. These oxygen vacancies overlap with the magnetic ions to induce ferromagnetism. Oxygen vacancies induced RT ferromagnetism was also observed in TiO_2 nanotubes synthesized by sol-gel method and doped with 5% Co[60].

RT ferromagnetism was observed in InAs doped with TM with a Curie temperature above RT[61]. The Curie temperature of clusters such as MnAs and MnGa are 318 and 400

K respectively; so the ferromagnetism with a Curie temperature of 350 K seems to be a characteristic of InMnAs quantum dots than that of clusters. The ferromagnetism is likely due to the p-d exchange coupling between the host and Mn or due to possible disorders in the quantum dots. In case of InCrAs quantum dots grown by MBE on GaAs, RT ferromagnetism was observed; the magnetic moment enhanced with an increase of Cr in the quantum dots[62]. Cr was incorporated into an interstitial site as an acceptor while mediating the ferromagnetism.

ZnS nanowires and nanobelts were doped with Mn and Fe and prepared on Au-coated Si substrate using vapor-liquid-solid mechanism[61]. Higher pressure of about 20 Torr resulted in nanobelts while pressure of about 5 Torr resulted in nanowires. As per X-ray diffraction, doping by Mn and Fe did not change the crystal structure of ZnS even though the growth directions of the nanowires and nanobelts were different. ZnS:Mn, ZnS:Fe and ZnS:Fe,Mn showed RT hysteresis.

Self-assembled GaMnAs based quantum dots grown by Stranski-Krantanov growth mode were ferromagnetic at RT with a possible hole-mediated or hopping mechanis[63–65]. InP quantum dots doped with Mn and synthesized by hot colloidal nanochemistry showed superparagmetic response at RT and ferromagnetism at temperatures below 25 K[66]. GaP and AlN nanowires doped with Mn and synthesized by thermal evaporation and chemical vapor deposition respectively also showed ferromagnetism at RT[67,68].

Si nanowires implanted with Mn demonstrated RT ferromagnetic properties[69]. Annealing at 600 ^{0}C increased the magnetization but annealing at 800 ^{0}C made the material diamagnetic. The ferromagnetism is likely due to the long-range ferromagnetic ordering between carriers of the host and the Mn atoms. The increase in magnetization with

annealing at 600 ^{0}C is attributed to the mitigation of crystal damages. At 800 ^{0}C, the Mn atoms originally present in the silicon formed precipitates with oxygen or silicon, escaped to the surface with a sufficient thermal energy acquired from annealing, and made the Mn-implanted Si nanowires diamagnetic. Segregation of magnetic elements to the surface is one of the challenges in using nanostructures. In 2-dimensional nanostructures, the magnetic elements and precipitates have higher chances to remain incorporated or homogeneous with the film even though they segregate and move to the surface. Such problems could be less encountered in epitaxial thin films

Magnetoresistance of 19% was observed in Ni/graphene/Ni spin valve nanostructure with the application of 2000 Oe magnetic field[70]. In the absence of magnetic field, antiferromagnetic coupling was observed between the spins of the two opposite nickel layers. Mechanism for ferromagnetism in these C based materials could be due to defects in the structure[70–74]. Organic materials have shown properties favorable for spintronic application[70,71]. Graphene quantum dots demonstrate carrier confinement[72]. Analysis of anomalous Hall effect in Q-carbon shows side-jump electronic scattering mechanisms and intrinsic mechanisms for the observed RT ferromagnetism[73].

Nitrogen vacancy (N-V) centers in diamond and silicon carbide have been recently studied for spintronic applications[75,76]. Diamond has a high thermal conductivity, is hard, and transparent. Carbon atoms could be deposited on silicon substrates using chemical vapor deposition. N-V centers are single impurities in diamond and are n-type, could carry and retain spin at RT with lesser contributions from spin-orbit interactions, and could emit single photons.

$MoSe_2$, $MoTe_2$, WS_2, CdS, CdTe, GeMn, Ge/Si are other potential candidates for spintronics applications[77–81]. Two dimensional materials in the MXenes family such as Cr_2C, Cr_2CFCl, Cr_2CClBr, Cr_2CHCl, Cr_2CH, Cr_2CFOH, $Hf_2MnC_2O_2$, $Hf_2VC_2O_2$, Ti_2NO_2 and Cr_2NO_2 are also being recently studied for spintronic applications[82–85]. Other materials studied for spintronic applications include silicon carbide, chalcogenides, Heusler compounds, topological materials, and DNA spintronics[84–95].

Several materials show spin properties at low temperature but achieving controllable spin at RT is still a major challenge. Among materials with a potential for RT spin, the mechanisms seem to be defect-based and could be complicated to control. Also, organic materials could have limitations on substrates compatibility for used in device applications. Compound semiconductors epitaxially grown that show interesting semiconducting, magnetic, and optical characteristics need to be explored. GaN and ZnO show RT ferromagnetism, as per theoretical modeling. Also, GaN doped with gadolinium has shown a potential for RT ferromagnetism that might be mediated by carriers in the material. A carrier-mediated mechanism is suitable for spintronics as it offers a direct control over the spin properties, and devices such as spin-transistors, spin-diodes, spinLEDs, memristors could be built.

1.2. PHOTOVOLTAIC

An increasing need for renewable energy sources has recently brought intensive attention to the field of photovoltaics. Development and optimization of devices that could efficiently harness solar energy and convert to electricity are crucial. Silicon solar cells have a power conversion efficiency up to ~25%. Solar cells' efficiency could be improved

by using single-junction materials configurations that result in a higher power conversion efficiency, and by development of multijunction solar cells to achieve a resulting high power conversion ratio. Compound semiconductors could be tuned to have varying bandgaps and be used in tandem structures. Moreover, materials such as zinc oxide could be tuned to act as passivating and anti-reflection layers thereby reducing defects-related carrier traps when used with a ZnO active layer based solar cell. P-type doping of ZnO is challenging due to the presence of n-type native defects. Hence, the configuration of Schottky junction solar cells needs to be updated to achieve a higher efficiency in harnessing solar energy. More introduction on photovoltaics is provided in Section 5.

1.3. COMPOUND SEMICONDUCTORS

Compound semiconductors are introduced in this section with emphasis on gallium nitride and zinc oxide.

Gallium nitride has received research attention especially after the successful development of GaN based LEDs in the 1990s, for various future applications such as spintronics, light emitting diodes, photodetectors, power electronics, neutron detection, and photovoltaics, mainly due to its bandgap of 3.4 eV which could be brought down to 0.7 eV with In doping, high thermal conductivity and stability, high breakdown voltages, chemical stability, and emission properties.

Zinc oxide (ZnO) is a multi-functional material of research interest over the last decades due to the tunability in its characteristics and direct applications in various areas such as energy harvesting, electronics, and bio-medicine[98–104]. A direct and wide band gap, a high exciton binding energy, stability at high temperature and power, earth-abundance,

and environmental-friendly nature has arisen interest in ZnO for photovoltaics, thermoelectrics, spintronics, electronics, sensing, piezoelectrics, and biomedicine[105–111]. ZnO is abundant and non-toxic, which widens its applications in biomedicine.

A high carrier mobility and breakdown voltage in GaN and ZnO as compared to commonly used semiconductors such as silicon and gallium arsenide, make them potential materials for future transistor electronics. These materials are stiff, hard, and show piezoelectric and thermoelectric effect due to a non-centrosymmetric crystal structure[112,113]. ZnO and GaN have a similar wurtzite structure, and hence could be stacked and used for photodetector and similar applications[114–116]. They are immune to high energy incidence, and could be used for space applications and neutron detection[105,117]. GaN and ZnO could be grown as thin films, bulk, as well as nanostructures, and each structure could have its unique morphology[101,118,119]. The resulting properties of also depend on the growth methodologies. A better understanding of GaN and ZnO growth, precursors' roles, defects, and properties is crucial for its utility in future applications.

1.4. GROWTH OF GALLIUM NITRIDE AND ZINC OXIDE

Optimum growth conditions and constituent element sources are required to grow GaN and ZnO with desired structure and properties. Several growth techniques such as metal-organic chemical vapor deposition (MOCVD), molecular beam epitaxy (MBE), atomic layer deposition (ALD), pulsed laser deposition (PLD), hydrothermal method, sol-gel technique, and magnetron sputtering have been used to grow GaN and ZnO, on substrates such as sapphire, silicon carbide, silicon, gallium arsenide, $LiTaO_3$, and glass[98–

[101,103,105,120–122]. Sapphire is the most common substrate due to its lattice match, crystallinity, optical transparency, low cost, and stability at high temperatures and pressure.

MOCVD is an established technology to grow GaN and ZnO at high/low temperatures, and results in a well-controlled and uniform growth with a good crystal quality and growth rate, over a large area, and could be employed at laboratory as well as commercial scale[123–128]. MOCVD involves a controlled vaporization of a metal-organic zinc source, followed by a vapor-pressure chemical reaction with oxygen source under optimum growth conditions (temperature, pressure, substrate rotation) resulting in thin film deposition on the substrate. Figure 1.10 shows a flow flange of a MOCVD system chamber with points where zinc, oxygen, and carrier gas enter the chamber right above the susceptor, substrate holder, grown zinc oxide samples, and resulting photoluminescence response of a ZnO sample.

An optimum heat exchange is maintained between the flow flange and the susceptor to satisfy boundary layer conditions and effectively result in a chemical reaction and material deposition. High purity bulk ZnO can be grown using a pressurized melt growth technique, which involves melting of raw materials, followed by crystallization as the temperature is lowered[129–132]. ZnO powder is heated up to ~1950 ^{o}C in a crucible, and the crucible is steadily moved away resulting in bulk crystallization. The composition of transition metal dopant could be set by the stoichiometric amounts of source powders before starting the growth. Temperature changes and pulling rate of the bulk crystal control the resulting properties, defects, and grain boundaries of ZnO.

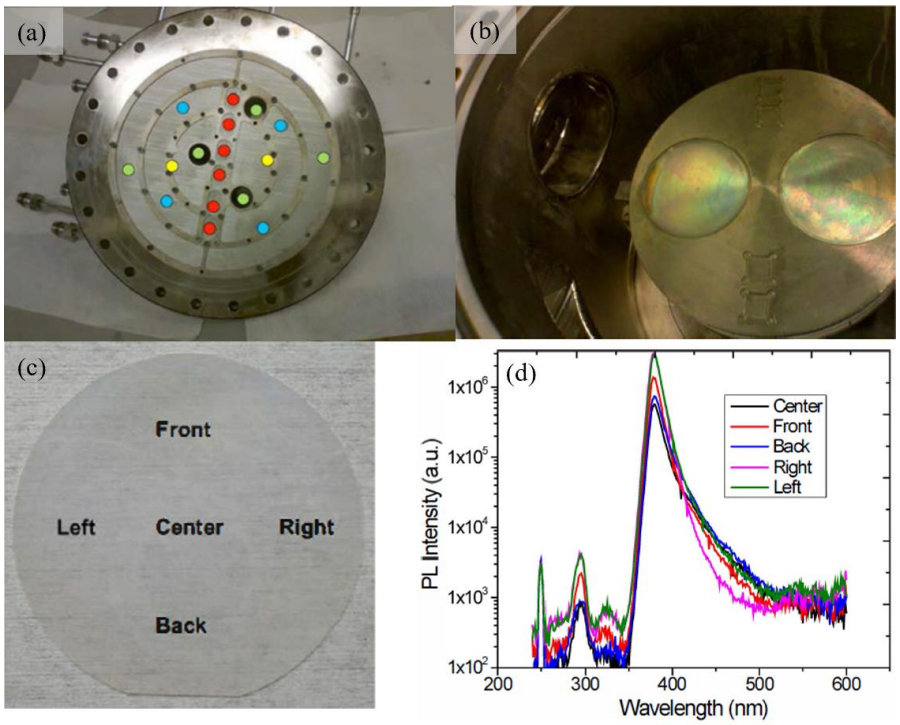

Figure 1.10 MOCVD chamber flow flange, substrate holder, grown ZnO sample, and resulting photoluminescence spectra[123].

Molecular beam epitaxy also results in a uniform growth of GaN and ZnO with a high crystallinity, however the growth rate could be lower than other techniques, and system maintenance cost could be high[133,134]. Magnetron sputtering and PLD are among other commonly used growth methods[126,135]. In magnetron sputtering, an electric field is applied between the target and ions' source. Ions striking the target release atoms which are deposited on a substrate. Magnetron sputtering usually results in defects which makes it difficult to effectively control material properties. In the case of PLD, a laser beam is incident on the target instead of ions. Pure or doped / alloyed GaN and ZnO could be used as targets in this growth method. Sol-gel is another popular technique to grow GaN and ZnO, and involves mixing constituent elements' precursors to form a clear solution, and

then placing the solution on a substrate or dipping the substrate in the solution, at temperatures above ~100 ºC to deposit thin films[136–141].

Zinc oxide could also be grown using ALD that consists of sequential and self-limiting self-reactions at low temperatures (~200 ºC) and results in a conformal and uniform deposition of ZnO films, that are typically a few nanometers thick[142–148]. Incorporation of dopants could be precisely controlled in ALD, but the growth rate is lower than other techniques; the reactor geometry, precursor injection schemes, and purge times could be potentially optimized to achieve higher growth rates[149,150].

GaN and ZnO in stable form have an asymmetric structure. Depending on the overall growth mechanism, sites in ZnO which are oxygen deficient, or zinc deficient, or which do not have Zn and O bonded, are likely. These cause defects and scattering in ZnO[151,152]. Defects in ZnO primarily arise due to vacancies, interstitials, and unintended sites activated. Zinc interstitials, oxygen vacancies, and zinc antisites, are common donor defects, while oxygen interstitials, zinc vacancies, and oxygen antisites are acceptor defects[153–155]. Acceptor-type defects have high energy of formation and result in instability at room temperature (RT), while donor defects are more common and exist at RT in thermodynamically stable states. Common donor-type defects could be conducive for a high n-type carrier density of ZnO but make p-doping of ZnO challenging. On the other hand, p-type doping of GaN has been achieved.

1.5. GALLIUM NITRIDE AND ZINC OXIDE DEVICES AND APPLICATIONS

This section discusses about the applicability of GaN and ZnO in various areas of electronics, energy harvesting, and sensing such as spintronics, photovoltaics, photovoltaics, light /laser emitters, neutron detection, and biomedicine.

1.5.1. Spintronics. GaN and ZnO doped with transition metal could have a Curie temperature above RT and be an interesting material for spintronic applications[56,57,156].

The suitability of GaN as a dilute magnetic semiconductor (DMS) primarily stems from the ability to dope GaN with transition metals (TM) and rare-earth metals (RE) to achieve room temperature ferromagnetism. Combining the magnetic moments of electrons in partially filled d orbital of TM, or d and f orbitals of RE metals, with the semiconducting and optical properties of GaN has raised interest in spintronic applications such magnetic memories, spin polarized LEDs, spin valves and spin-based transistors.

Theoretical analysis based on Zener's ferromagnetism predicted the existence of RT ferromagnetism in GaMnN with 5% Mn and 3.5×10^{20} holes/cm^3. Small lattice constant and presence of nitride anion in GaN, doped with Mn containing a half-filled d orbital result in this ferromagnetism. Local spin density calculations show that magnetic TM-doped DMS forms deep levels in GaN, and that the Curie temperature (Tc) initially increases with an increase in the TM concentration but at high concentrations, the Tc decreases due to the formation of TM clusters[157–159]. These clusters have antiferromagnetic TM-N and ferromagnetic TM-TM coupling. Annealing reduced the magnetization possibly due to the formation of phases that do not contribute to ferromagnetism. Si codoping compensates the Mn acceptors that substitute Ga. Additionally, Si cooping and annealing increase the Fermi level resulting in nitrogen vacancies and trapped donor electrons.

Similar behavior of RT ferromagnetism was also observed in GaFeN with 0.7% Fe doping grown using MOCVD, except that no change is observed with Si codoping[160]. The effect of thickness of Fe films on the Fe/GaN interface roughness and on the resulting ferromagnetic behavior was investigated by growing Fe films using MBE on MOCVD-grown GaN on sapphire[161]. An increase in roughness at the GaN/Fe interface was observed with an increase in the Fe layer thickness up to 10 nm, which resulted in enhanced coercivity and saturation magnetization. GaCrN, is another TM doped DMS grown using radio-frequency plasma-assisted MBE on sapphire substrates that showed RT ferromagnetism[100]. On doping the samples with Si, crystal quality improved and magnetization was reduced. Long-range mediation between Cr, Si and VGa is considered responsible for this behavior. The spin properties of most transition metal doped GaN seem to be mediated by defects and impurity bands introduced by the dopants in GaN.

Elements such as Gd, Er, Eu, Sm and Nd have been doped in GaN with intent to investigate the optical, electrical and magnetic properties[56,162–166]. Gd has been the most explored rare-earth dopant with half-filled f and partially filled d orbitals. GaGdN can be doped with donors or acceptors with a density more than that of Gd to introduce additional spin-polarized carriers. Room temperature ferromagnetism was observed in GaGdN grown using ammonia-assisted MBE on SiC and doped with Gd. As the GaGdN samples were insulating, the observed ferromagnetism was not carrier mediated. The samples contained oxygen, which possibly resulted in p-d hybridization and contributed to the magnetic moment of the sample. In another study, MOCVD-grown GaN was doped with Gd from two sources, ($(TMHD)_3Gd$) that has oxygen in its organic ligand, and (Cp_3Gd) that does not contain oxygen[166]. RT ferromagnetism was observed only in samples with oxygen-

containing Gd source. Magnetization in GaGdN could be enhanced by codoping with Si and Mg co-doping. VSM measurements of p-doped GaGdN are shown in Figure 1.11. Holes seem to be more dominant than electrons in contributing to the ferromagnetism in GaGdN[166,167]. First principle calculations of Mg doped nanowires predict lattice distortions when Mg substitutes Ga. Also, codoping with C is predicted to effect magnetic properties in GaGdN as per Zeners' p-d exchange mechanism[168].

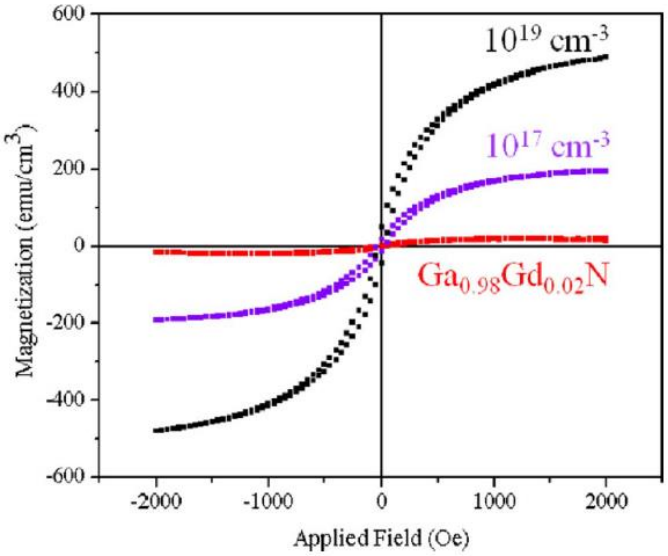

Figure 1.11 Room temperature ferromagnetism in p-type GaGdN[166].

GaN nanostructures doped with 2% Mn or 3% Fe and synthesized using MOCVD and Stranski-Krastonow like growth showed superparamagnetic behavior at RT and ferromagnetism at 5 K as shown in Figure 1.12[169,170]. Precursors used were Trimethyl gallium (TMGa) for Ga, trimethyl aluminium (TMAl) for Al, ammonia (NH_3) for N, Bis-cyclopentadienyl manganese (Cp_2Mn) for Mn and bis-cyclopentadienyl iron (Cp_2Fe) for Fe. The nanostructures were grown on AlN layer on sapphire substrates. GaTMN was

deposited in an optimized two-step process of low temperature (<850 ^{0}C) and low V/III ratios (<30) followed by high temperature (up to 970 ^{0}C) growth in a nitrogen environment. GaMnN and GaFeN showed hysteresis at 5 K and superparamagnetic behavior with reduced coercive field at RT; such a behavior could be due to dopant-related clusters. Similar superparamagnetic-like behavior was observed in GaMnN nanowires with Mn up to 3% and synthesized using vapor-liquid-solid method and a nonmagnetic Au catalyst[171].

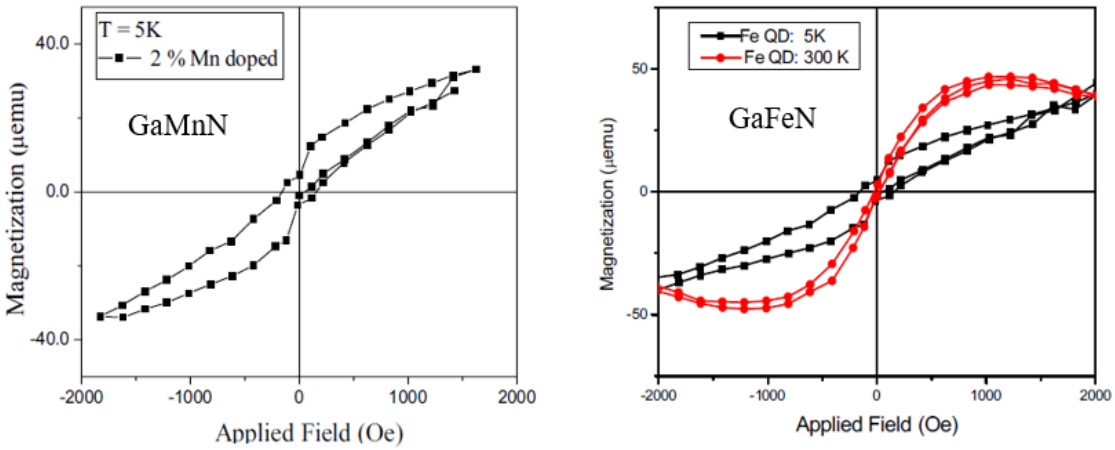

Figure 1.12 Magnetization measurement of GaMnN and GaFeN nanostructures grown on AlN on sapphire by MOCVD[169].

In another study, $Ga_{0.93}Mn_{0.07}N$ nanowires were grown by controlled transport of gallium chloride ($GaCl_3$), manganese chloride ($MnCl_2$) and NH_3 at 800 ^{0}C on sapphire or silicon carbide coated with nickel[172]. RT ferromagnetism was observed. The ferromagnetism seems to be due to secondary paramagnetic phases. GaMnN nanostructures synthesized by carbothermal nitridation and doped with carbon also showed RT ferromagnetism wherein the saturation magnetization enhanced with an increase in the

C source[173]. This could be due to the hybridization of some states of C or of Ga or N vacancies with spin-polarized states of Mn clusters.

GaN nanorods grown on patterned Ti/Si substrate using MBE nanostructures showed an enhancement in ferromagnetism with Si doping and increased nanorods diameter[174]. Si dopants adds more carriers but a complete explanation of introduction of spin in the material is unclear.

Ga vacancies may also contribute to the observed ferromagnetism in GaGdN and GaN[175,176]. Ga vacancies could possibly contribute to ferromagnetism in TM and RE doped GaN, but act as a primary mechanism in unintentionally doped GaN.

GaN-based compounds have been explored for magnetic behavior and have the potential for use in spintronic applications. Although several theories and mechanisms have been proposed to explain ferromagnetism in TM and RE doped GaN and experiments are performed, further work is necessary to understand the origin of magnetism in GaN-based materials.

ZnO in a bulk form doped with Mn, Co, and Fe was grown using a melt growth technique for the study of ferromagnetism in the materials[131,132]. Mn-doped ZnO showed antiferromagnetic behavior, while Co-doped ZnO showed signs of ferromagnetism at RT. However, the origin of this magnetic behavior is not clear and is most likely due to Mn and Co clusters. In the case of ZnCoO, 3d orbitals of Co could overlap with impurity bands in ZnO. Doping ZnO with Mn and Co could also help to tune its dielectric properties and dielectric constant from ~8.5 to over 25[177]. In another study, Fe was doped in bulk ZnO and ferromagnetic hysteresis curve was observed at RT[131]. Ni-doped ZnO thin films grown by MOCVD also exhibited RT ferromagnetism. Rare earth element Gd-doped ZnO thin

films showed ferromagnetism at RT, but ZnGdO bulk material showed a diamagnetic response. Figure 1.13 shows magnetization hysteresis plots of ZnO:Fe bulk crystal grown by melt-growth technique, and MOCVD-grown ZnO:Gd thin films. The ferromagnetic behavior could be due to interaction of the dopant carriers with the host material carriers, or defect/impurity states, or magnetic clusters, or due to dopant-induced defects.

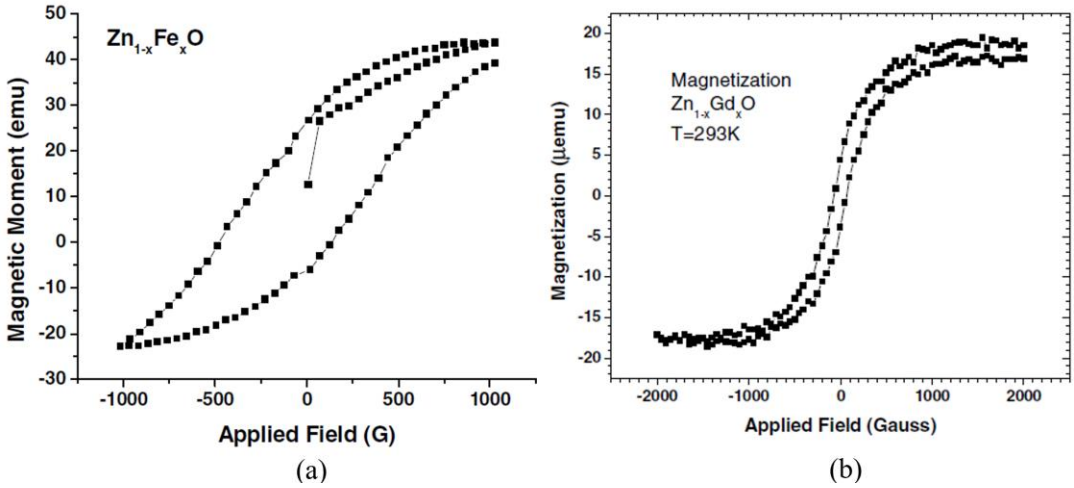

Figure 1.13 Magnetic properties of Fe-doped ZnO bulk crystal grown by melt growth technique, and Gd-doped ZnO thin film grown by MOCVD[132].

Mn-doped ZnO nanostructures were synthesized using chemical vapor deposition[178]. Growth temperature of 600 ^{0}C resulted in nanorods while lower growth temperatures of 500 ^{0}C and 400 ^{0}C resulted in bowls and cages nanostructures respectively. The ZnMnO nanorods showed ferromagnetism at low temperatures but were paramagnetic at RT. On the other hand, the bowls and cages nanostructures showed RT ferromagnetism with a coercivity of 77 Oe and their magnetization at lower temperature was weaker than the ZnMnO nanorods. Stronger magnetization in the nanorods at 5 K could be due to the higher Mn content in nanorods. RT Ferromagnetism only in bowl and cage nanostructures

is probably a result of more uniform distribution of Mn in the nanostructures at low temperature growth.

ZnO nanowires doped with Cu showed RT hysteresis. ZnO nanowires were synthesized by reactive vapor deposition and then implanted with 2% Cu[178–181]. The samples were annealed at 600 ^{0}C in oxygen or argon for 2 hours to reduce the crystal damages by ion implantation. While as-implanted samples were paramagnetic, annealed samples were ferromagnetic at RT with the magnetic properties in oxygen-annealed samples being stronger than argon-annealed ones. Oxygen seems to have a role in the magnetic properties. However, it is not clear if the ferromagnetism stemmed from nanowire related properties or Cu or oxygen.

Ferromagnetic ZnO nanowires doped with 2% Nd showed magnetic anisotropy, that is, the magnetization was higher for in-plane applied magnetic field than for out-of-plane field[182]. This anisotropy likely has roots from the orbital anisotropy of doped Nd ions. The ferromagnetism is mediated by the interaction of the Nd ions with the O ions, but this is not clear. Theoretical calculations also show that C, N or In doping could result in ferromagnetism in ZnO nanowires[183–185].

1.5.2. Photovoltaics. A direct band gap, high carrier diffusivity, carrier concentration / mobility, along with a non-toxic nature, abundancy, and a crystalline structure, enables ZnO to be applicable in various parts of solar cells[102,124,125,128,186–197]. Bandgap engineering and photon absorption are factors that make it a good active layer. ZnO could also be a substrate, passivation layer, carrier blocking layer, or transparent oxide layer. Having multi-functionality in a single material base could reduce interface-related defects in layered and multi-junction solar cell structures. Details about applications of

ZnO in solar cells are discussed in Section 4. Also, GaN alloyed with InN has shown applications in solar cells[100]. Phase separation could result in deterioration of solar cells' performance but could be potentially resolved by tuning growth conditions.

1.5.3. Thermoelectrics. There has been a recent interest in thermoelectric materials, considering the potential of effectively harnessing heat energy that is naturally available, and that is usually wasted as a byproduct[98,105,112,198–201].

Thermoelectric materials are characterized by a thermoelectric figure of merit defined as $ZT=S^2\sigma/(k_e+k_l)$, where T is the temperature, S is the Seebeck coefficient, σ is the electrical conductivity, k_e is the carrier thermal conductivity, and k_l is the lattice thermal conductivity; $S^2\sigma$ is the power factor. A high power factor or ZT, and a large Seebeck coefficient are conducive for energy generation, and sensing applications. Materials with a low thermal conductivity and high electrical conductivity are of interest, in order to maintain a temperature difference and yet have a carrier flow through the material. σ and k_e are inter-dependent as per the Wiedemann-Fran relation, which makes it difficult to achieve a figure of merit greater than unity. Bi_2Te_3, Sb_2Te_3 are commonly explored thermoelectric materials, however, they are expensive, toxic, and not sufficiently stable at high temperatures.

ZnO and GaN have a high temperature stability and have shown potential for thermoelectrics. ZnO could be a good alternative to conventional thermoelectric materials due to its non-toxicity, abundancy, and a high temperature stability.

Codoping with Al and Ga could optimize the thermoelectric properties of ZnO[200,201]. Bulk ZnO has been reported to have a Seebeck coefficient up to 478 μV/K, with a power factor of $0.75\text{x}10^{-4}$ W/mK^2 [200,201]. ZnO doped with Al and Ga have been reported

to have a ZT up to 0.45 (and power factor up to 15 W/mK^2) at 1000 K, however the electrical conductivity was low[200,201]. Figure 1.14 shows Seebeck coefficients and power factors of ZnO materials. High Seebeck coefficients are seen for bulk ZnO and ZnAlO thin films. Bulk ZnAlGaO and ZnAlO have a high power factor. Al or Ga dopant could substitute Zn in ZnO, possibly result in defects centers, and result in an enhanced electrical conductivity, yet maintaining a low thermal conductivity. Figure of merit and Seebeck coefficient of ZnO:Al improved by co-doping with Sm, Fe, and Ni, however, this could result in a low electron mobility[105].

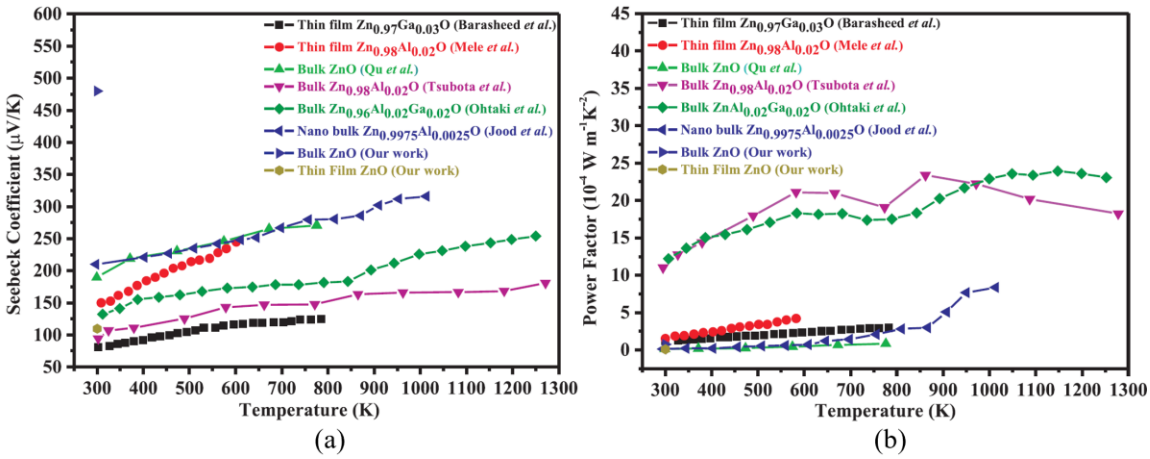

Figure 1.14 Seebeck coefficient and power factor of various ZnO compositions[200]

ZnO nanoparticles could be embedded in cement to utilize the heat energy and temperature differences in concrete structures[112,113]. ZnO and Al-doped ZnO were mixed in cement with a varying ZnO content in one set of cement and varying ZnO:Al in another[113]. The Seebeck coefficient increases, and thermal conductivity decreases with

ZnO or ZnO:Al incorporation in cement paste. ZnO could reduce hydration reactions and result in an improved thermoelectric performance.

Also, a high Seebeck coefficient up to 500 μV/K was observed in GaN based thin films, and ZT up to 0.86 in GaN nanostructures at 300 K. Figure 1.15 shows Seebeck coefficient of GaN based materials[100].

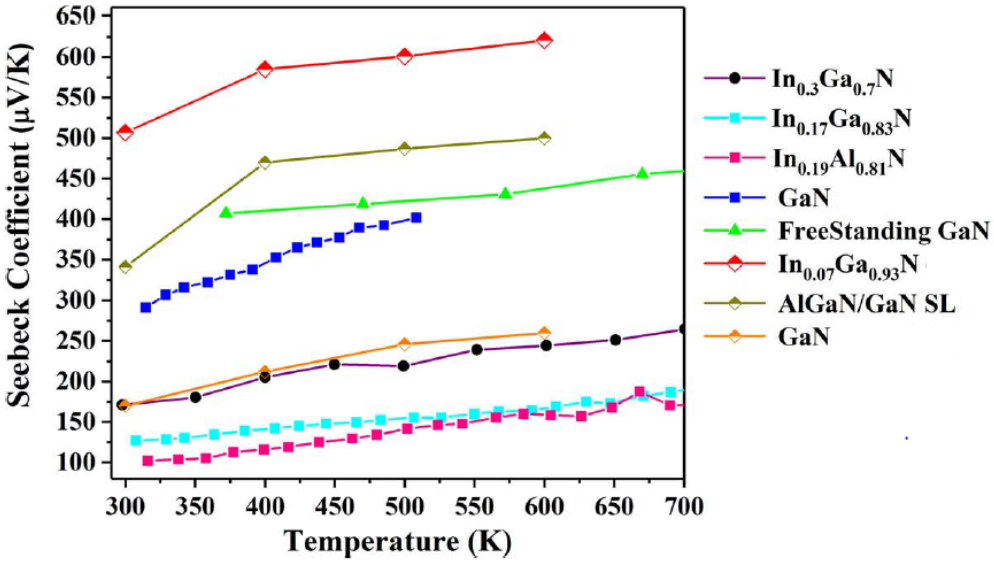

Figure 1.15 Seebeck coefficients of GaN based materials[100].

1.5.4. Light Emitting Diodes. GaN has been one of the key materials in the development of light emitting diodes. Initial LEDs were built using MBE-grown GaN, but an improvement in the quality was seen with MOCVD-grown GaN[100]. Heterostructures of GaN alloyed with Al and In could be developed to tune the output properties of LEDs. Patterned sapphire substrates, electron/hole blocking layers in the quantum wells, control over polarization, and reduction of crystal defects and nonradiative recombination could help towards enhancing LEDs' quality.

A high free exciton binding energy of 60 meV, tunable bandgap, and high carrier concentration, also makes ZnO a narrowband emitter, and a potential add-on to GaN as a typical semiconductor material for light emitting diode (LED)[111,202–204]. ZnO LED was built from MOCVD-grown p-n junction. A turn on voltage of 3.3 V and reverse breakdown voltage of 10 V was reported, which shows a low defect density[111]. An electroluminescence peak at 384 nm appears due to a recombination of the nitrogen luminescent centers (p-type dopant) and shallow donors in n-type ZnO. ZnO could either be used as a homojunction LED, or could even be interfaced with other p-type material, for example, p-GaN/n-ZnO LED[204]. Some other configurations include ZnO on Si, ZnO on SiC, nanowire and quantum dots LEDs wherein the nanostructure-related properties would append to the inherent ZnO characteristics that are conducive for LEDs' operations.

1.5.5. Neutron Detection. Neutron detection and scintillating materials are important in nuclear fusion and fission reactions, sensing high energy radiations in space and materials, medical imaging, non-destructive testing, geological purposes, and energy characterization[105,117,142,205]. There has been an increasing interest in new materials for neutron detection especially after the recognition of a scarcity of materials to build ^{3}He detectors[206,207]. Scintillators absorb high energy radiation and emit radiation that are lesser energetic and could be processed by optical detectors. Neutrons do not carry charge or ionization capabilities, which makes their detection complicated.

GaN and ZnO has been explored for scintillation applications due to their large cross-section to interact with neutrons particles, and a high exciton binding energy. GaN is an effective neutron and gamma detector and its properties could be enhanced with doping

Gd, In, B, and Li[100]. GaN detectors have shown scintillation response proportional to the incident reactor power level.

MOCVD-grown ZnO has been reported to undergo carrier recombination during scintillation with a rise and decay time of 30 ps and 0.65 ns respectively[117]. Cu-doped ZnO grown by a liquid phase epitaxy method on ZnO substrates was also explored for neutron detection[142]. A scintillation light yield that is 140% times more than commonly used BiGeO scintillator was achieved. Cu-doped ZnO films had a decay time of 21500 nm, as compared to 2300 ns for un-doped ZnO. Photoluminescence spectra, as well as radioluminescence responses when irradiated with ^{241}Am 5.5 MeV showed emission at 450-650 nm. These states could be the results of recombination of oxygen vacancy donor states with deep acceptor-type energy states of Cu^{2+}.

1.5.6. Other Applications. GaN has also been applied in RF propagation, photonics ad plasmonics, and water splitting.

A high breakdown voltage of over 2000 V, power density of 10.3 W/mm, carrier concentration in orders over 10^{19} cm^{-3}, and mobility of more than 1250 cm^2/V-s has made GaN a candidate for high power electronics and RF propagation. GaN could help towards miniaturization and improve efficiency of high-power devices such as DC-DC converters, buck and boost converters, transistors, rectifiers, and batteries, and could operate at higher frequency (over 18 GHz) range[100]. GaN alloyed with InGaN has been used in water splitting applications due to its potential for redox reactions and charge separations. Emission characteristics of GaN could be used in photonics and plasmonics applications and for tuning light absorption, scattering, and confinement[100].

ZnO has potential applications in flexible electronics considering its tunable bandgap, exceptional electrical characteristics, physical flexibility, transparency, bio-compatibility and low temperature synthesis[208–210]. ZnO (grown by sputtering) based thin film transistors (TFTs) exhibited a field-effect mobility up to 50 $cm^2V^{-1}s^{-1}$, current on/off ratio in the order of 10^6, threshold voltage of ~0 V, and sub-threshold slope of 3 V/decade [211]. ZnO based TFTs could have a threshold voltage up to 5.4 V[208]. These characteristics could be enhanced by alloying ZnO with indium[212]. Field-effect properties of ZnO were also improved through the formation of heterostructures such as ZnO/ZnMgO with a two-dimensional electron gas at the interface, resulting in a mobility up to 9.1 $cm^2V^{-1}s^{-1}$, current on/off ratio up to 10^8, turn on voltage of -2.75 V, and a sub-threshold slope of 0.78 V/decade [105,213]. The non-linear current-voltage characteristics (turn-on voltage, breakdown voltage, current-voltage slope) of ZnO ceramics are also utilized to build varistors[214–216].

ZnO could be used in gas sensing, pharmaceuticals, cosmetics, and textile industries[103,217–219]. ZnO nanostructures are permeable, block UV-radiation, and can be used as textile coating materials. Antibacterial and disinfecting properties of ZnO make it a component of medicines, creams, medication to heal wounds, dental pastes, and dietary supplements[103,219–221]. ZnO nanoparticles could be incorporated in food packaging material to inhibit the growth of microorganisms on the food surface[217]. ZnO nanoparticles are also explored for antitumor activities, antidiabetic activities, therapies for lung cancer, gastric cancer, hepatocarcinoma, cervical cancer, ovarian cancer, breast cancer, colon cancer, leukemia, functionalizing nano-elements and carriers to target cancer cells, and biomedical imaging[217,222–226].

1.6. SPINTRONICS AND COMPOUND SEMICONDUCTORS SUMMARY

Spintronics, photovoltaics, compound semiconductors, gallium nitride, and zinc oxide are introduced in this section. GaN and ZnO have potential applications in various areas of electronics and energy harvesting such as spintronics, photovoltaics, thermoelectrics, neutron detection, light emitting diodes, power electronics, flexible electronics, and bio-medicine.

Spintronics could be an enabling technology for the next generation of computing such as quantum information, neuromorphic computing, and artificial intelligence. Spintronics could result in high speed miniaturized devices with a low power consumption. However, a major challenge in spintronics is that materials show spin functionality at low temperatures, and the root causes for room temperature spin properties are not clear. Dilute magnetic semiconductor GaN doped with Gd has shown ferromagnetism at RT, but the underlying mechanism is not completely understood. It is imperative to understand the mechanism of spin functionalities to be able to control and manipulate it at RT and help towards the development of spintronic devices and applications.

2. GADOLINIUM-DOPED GALLIUM NITRIDE FOR ROOM TEMPERATURE SPINTRONICS

2.1. GADOLINIUM-DOPED GALLIUM NITRIDE

Dilute magnetic semiconductors (DMS) are interesting materials for spintronic applications due to an integration of magnetic, electrical and optical properties, and their functioning based on exchange mechanisms[227–230]. Magnetic elements could be doped in non-magnetic semiconductors in dilute amounts so that the resulting material shows magnetic and semiconductor properties, that is necessary for spintronic applications[157,231–233]. Alternative spin injection structures consisting of stacked magnetic and semiconductor films encounter challenges of interface-related defects, mismatches in electrical and optical properties, and scattering, which are reduced in DMS. Interactions of a doped transition metal or rare earth element with the host material and resulting properties depend on the exchange interaction mechanism[234–237].

The most straight-forward but less likely mechanism is a direct exchange between dopant carriers or atoms that have in-phase wave functions. These atoms could have their spins aligned in a parallel or anti-parallel orientation resulting in a net magnetic moment. Indirect exchange mechanisms are more common as dopant atoms typically do not have sufficiently overlapping wavefunctions. In carrier-mediated mechanism, ferromagnetism is rendered by the interaction of carriers from the dopant with the host material. d- or f-orbitals of a transition metal or rare earth element could interact with the s and p-orbitals of host material, resulting in ferromagnetism. Double exchange mechanism involves interaction of dopant-related carriers from d- or f- orbitals through the host material's p-orbitals. Super-exchange mechanism is the transfer of spin-polarized electrons between

magnetic elements in semiconductors through anions or cations such as group III-material vacancies in III-V semiconductors. Some of these exchange mechanisms are illustrated in Figure 2.1. Crystal defects and vacancies, interstitials, and unintended doping could also result in ferromagnetism in DMS. Carrier-mediated is a preferable mechanism in DMS as the ferromagnetism could be better controlled with the carrier concentration and the mobility, and the nature (p-type or n-type) of the host material.

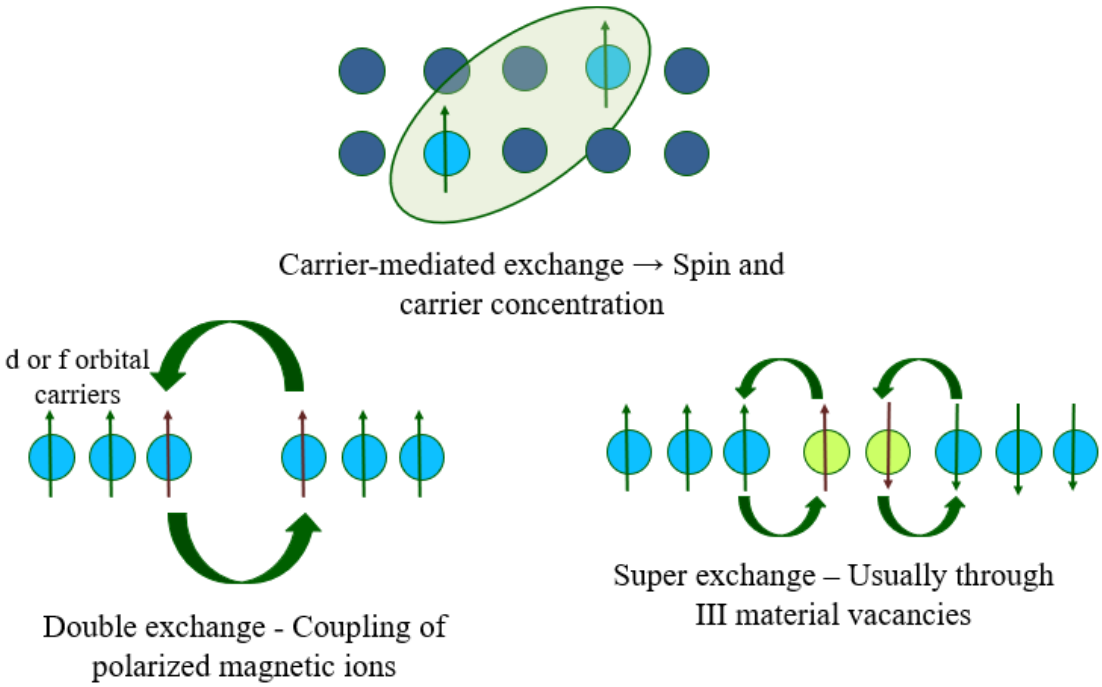

Figure 2.1 Indirect exchange mechanisms in dilute magnetic semiconductors[238].

Theoretical modeling based on Zener model have shown predictions of ferromagnetism in semiconductors doped with transition metal Mn and with carrier concentration of 3.5 x 10^{20} holes/cm^3, as shown in Figure 2.2[57]. Commonly used semiconductors such as silicon and gallium arsenide have a Curie Temperature (T_C) below

room temperature. For practical and commercial applications such as quantum computing, it is necessary to investigate semiconductors that could show ferromagnetic properties at room temperature (RT). Gallium nitride (GaN) and zinc oxide (ZnO) showed a potential for room temperature ferromagnetism. GaN and ZnO have smaller lattice constants, which is conducive for spin-related interactions between the dopant and the host material[175,239–247]. High quality growth of p-type zinc oxide is still a challenge considering the existence of n-type native defects in ZnO[248,249]. On the other hand, GaN could be doped to be both p-type or n-type and could be a candidate for room temperature spintronic applications[166].

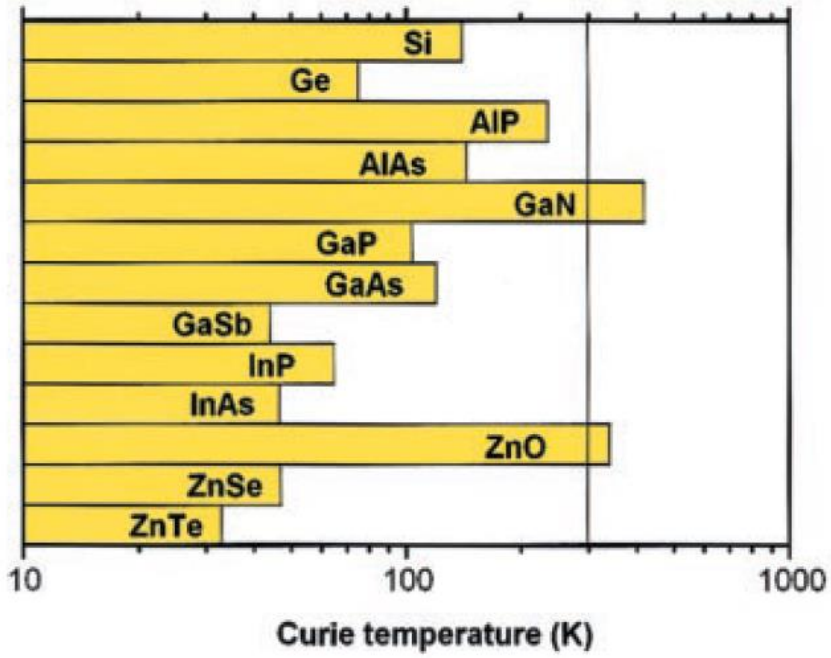

Figure 2.2 Computed Curie Temperature of dilute magnetic semiconductors (Mn as a transition metal dopant)[57].

Gallium nitride doped with Mn showed ferromagnetism at room temperature. The ferromagnetism increased with an increase with Mn doping, and the samples were highly resistive. The effect of co-doping (at a lower temperature) is shown in Figure 2.3[247].

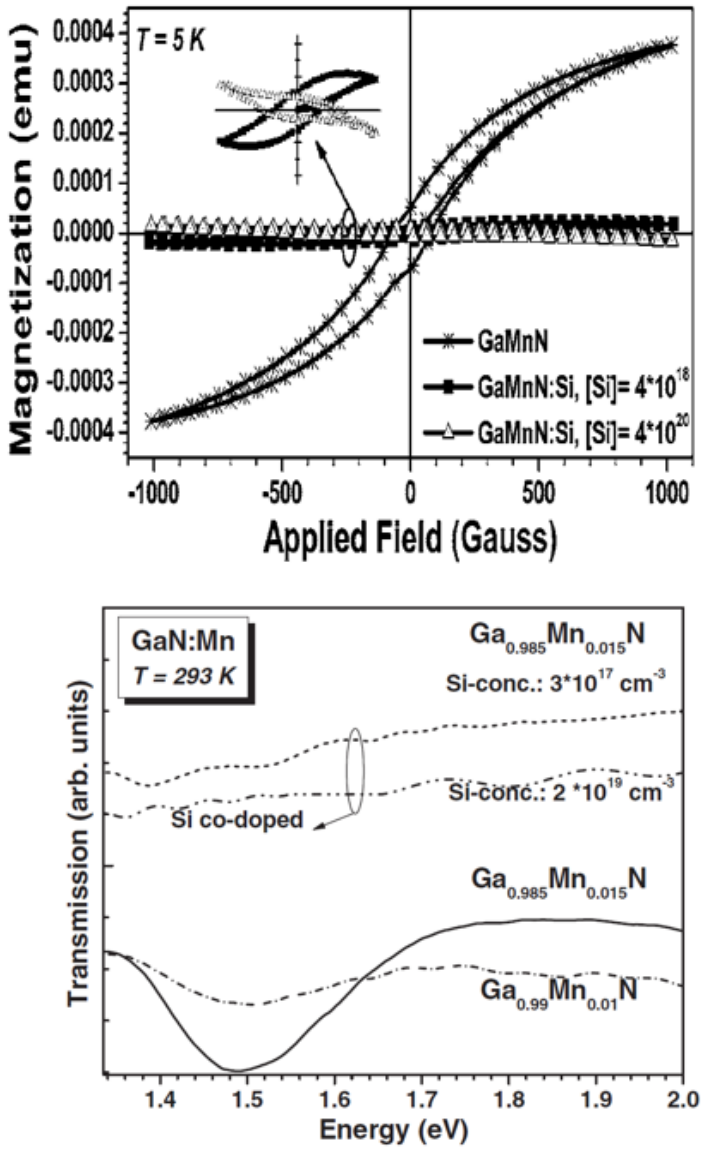

Figure 2.3 Magnetization response of GaMnN:Si at 5 K and effect of Si-codoping, and transmission spectra of GaMnN and GaMnN at 293 K[247].

The ferromagnetic signal reduced with silicon doping, and with annealing. A broad absorption band was detected at ~1.5 eV in GaMnN which is due to the interstate transitions of Mn ions[229]. The peak broadened and increased in intensity with an increase in Mn content. Such an absorption dip was not seen in Si-codoped GaMnN or un-doped GaN. Si-codoping increases the free carrier concentration and results in a shift of the Fermi level towards the conduction band and could compensate the acceptor-like impurities states introduced by Mn-doping that are responsible for the ferromagnetism[230,245,247]. This pointed towards a ferromagnetism in GaMnN mediated by deep impurity states introduced by Mn-doping, which lowers the chances for a carrier-mediated mechanism in transition-metal doped GaN.. A related coordination diagram is shown in Figure 2.4.

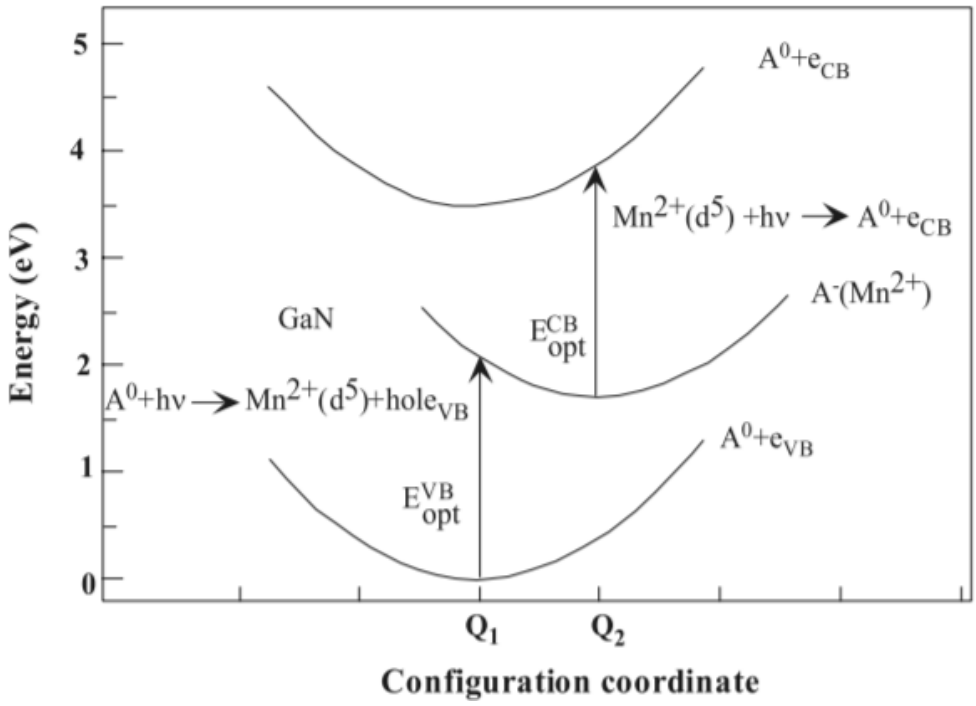

Figure 2.4 Energy and configuration coordinate figure of Mn-related transitions in GaMnN[229].

Rare earth elements have a partially filled f-orbital and a potential to interact with GaN and render ferromagnetism[166,250–252]. Gadolinium is an interesting dopant in gallium nitride due to its partially filled d- and f-orbitals, and hence a potentially large magnetic moment that could hybridize with carriers in the host compound semiconductor. Density of states corresponding to Ga, N and Gd (4f) are shown in Figure 2.5[253]. An exchange or split of ~4.5 eV is observed between the Gd-4f spin-up and spin-down states. Gd substituting Ga in GaGdN is isovalent but could introduce magnetism and a spin polarization. This shows a potential for carrier-related mechanism in GaGdN.

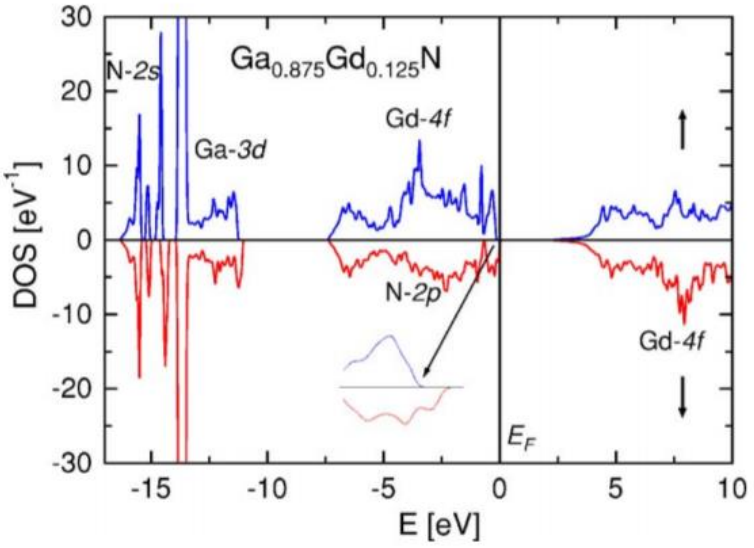

Figure 2.5 Electronic structure density of states of Gd-doped GaN[253].

A large magnetic moment was seen in GaGdN grown by molecular beam epitaxy on silicon carbide substrates, with varying Gd concentrations, as shown in Figure 2.6[252]. The ferromagnetic signal reduced upon co-doping showing lesser chances of a carrier-related mechanism.

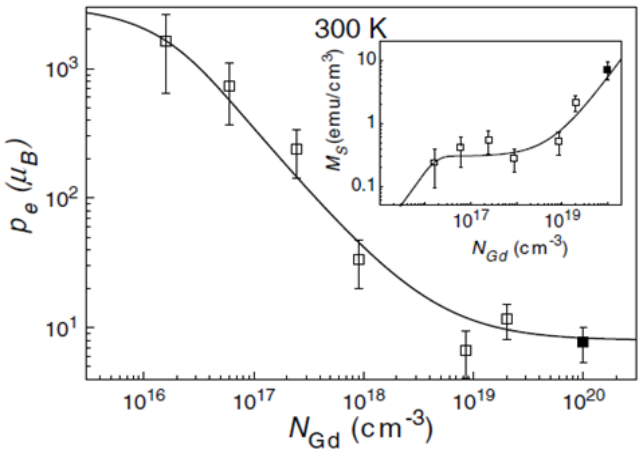

Figure 2.6 Room temperature ferromagnetism in MBE-grown GaGdN[252].

Similarly, a magnetic moment was observed in Gd-implanted GaN layers grown on silicon substrates, as shown in Figure 2.7[254]. The samples did not show signs of hysteresis, and the saturation magnetization increased with the implantation dose. Implantation could also introduce defects (such as Ga vacancies) that result in the paramagnetic behavior in GaGdN in the presence of Gd atoms.

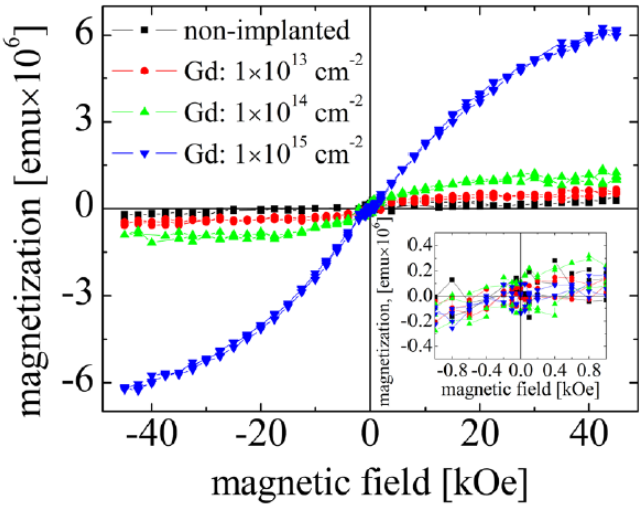

Figure 2.7 Magnetic characterization of GaN grown by molecular beam epitaxy on silicon substrates and implanted with Gd[254].

Upon annealing MBE-grown samples implanted with Gd, the ferromagnetism reduced, and the effect was different in different samples, as seen in Figure 2.8 where the two plots correspond to samples grown under similar conditions[255]. Additional X-ray diffraction peaks were seen upon annealing, which are signs of gallium and nitrogen interstitial defect states. Such a spin polarization could be the result of a long-range interaction of the Gd atoms with the GaN host material. The ferromagnetism in GaGdN synthesized by MBE or implantation seem to be mediated by defects in the GaN structure but this is not very clear.

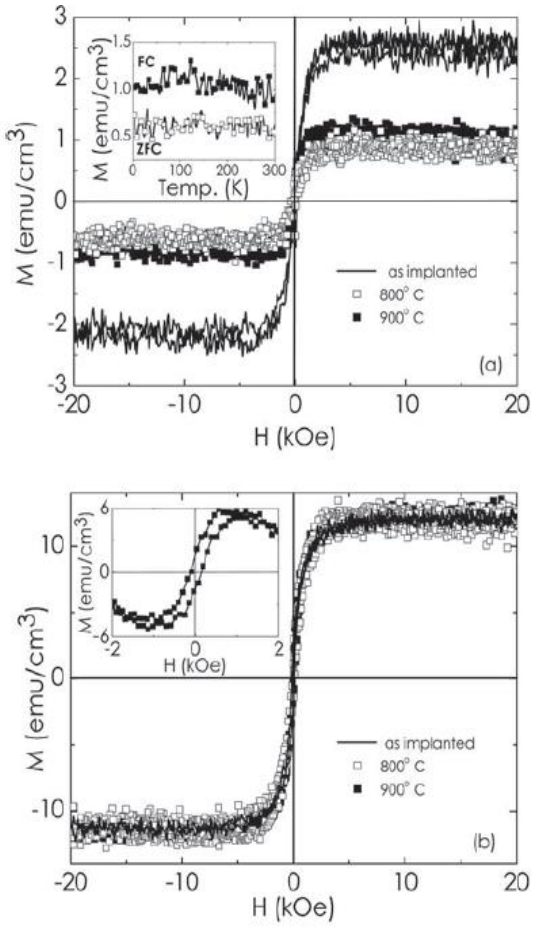

Figure 2.8 Effect of annealing on Gd-implanted GaN[255].

In this section, magnetic properties of GaGdN grown by metal-organic chemical vapor deposition (MOCVD) technique are discussed to get a better understanding for the mechanism for spin-related properties in GaGdN and its suitability for room temperature spintronics.

2.2. METAL-ORGANIC CHEMICAL VAPOR DEPOSITION GROWTH OF GADOLINIUM-DOPED GALLIUM NITRIDE

Metal-organic chemical vapor deposition (MOCVD) is a widely used technique for the growth of GaN at a laboratory as well as commercial scale for the development of light emitting diodes, solar cells, photodetectors, and transistors[256,257]. It involves chemical reactions of metal-organic sources and hydrides under optimum growth conditions, resulting in a well-controlled GaN thin film deposition. MOCVD growth sequence consists of a controlled vaporization of metal-organic precursors, their transport to the reaction chamber, reaction with a hydride (or similar), surface reactions and adsorption on a substrate, and desorption and exhaust of by-products. Figure 2.9 provides an illustration of the growth process. Non-optimum growth conditions could affect the thermodynamics and kinetics of the growth and result in a reduced adsorption of reactants and surface diffusion, and a lower growth rate. Maximum growth rate is limited by the free energy and thermodynamic potential of the system, while it is optimized (towards the lower end) by the mass transport which is controlled by the growth conditions and precursor flows, and reaction kinetics. Fluid dynamics depends on the reactor design. Boundary conditions properly satisfied and a laminar flow is required for the precursors to react in the gas phase and adsorb on the substrate. A limit on the lower end of an optimum temperature is set by the kinetics while an upper limit by the thermodynamics of the growth system.

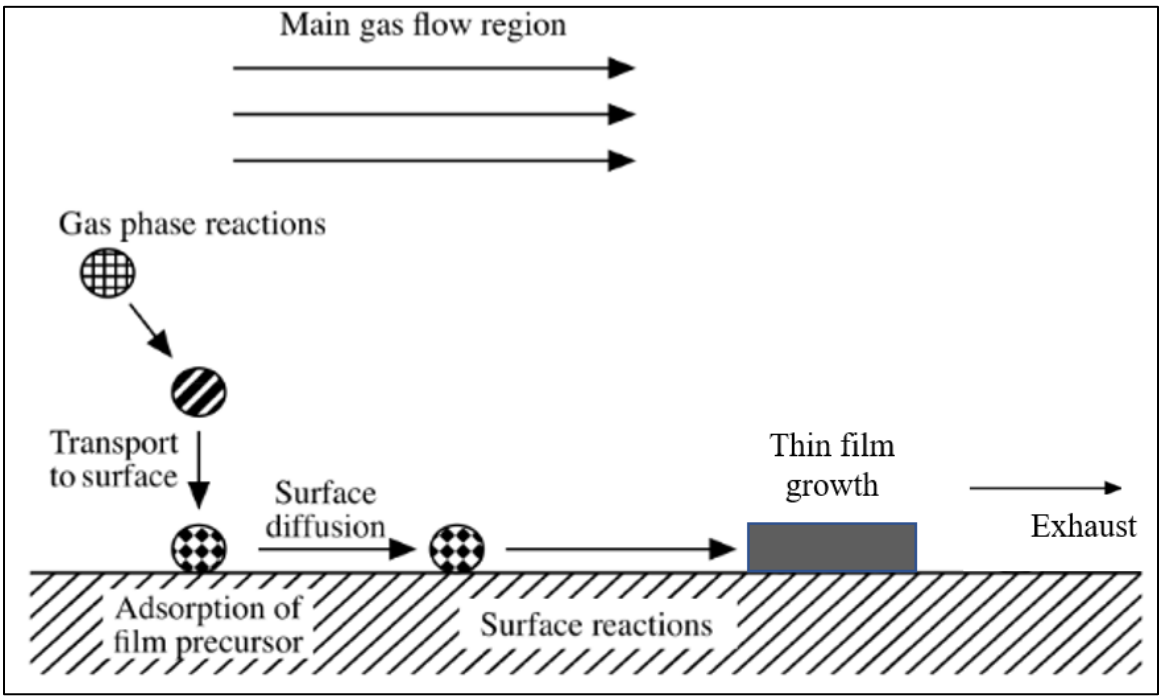

Figure 2.9 Schematics of metal-organic chemical vapor deposition (MOCVD) process [from "Chemistry of Electronic Materials" by Andrew R. Barron at https://cnx.org/contents/EJYWe4UY@9.4:uF0G3M7o@6/Mechanism-of-the-Metal-Organic-Chemical-Vapor-Deposition-of-Gallium-Arsenide (04-16-2020), adapted from K. F. Jensen and W. Kern, in Thin Film Processes II, Eds. J. L. Vossen and W. Kern, Academic Press, New York (1991)].

Figure 2.10 shows the MOCVD system that was used to Gd-doped GaN. It is a vertical configuration based rotating disk reactor with temperature capabilities up to 1200 ^{o}C.

Trimethyl gallium (TMGa) was used as a gallium precursor. Two Gd precursors were used – Tris(2, 2, 6, 6 – tetramethyl-3, 5 – heptanedionato) gadolinium ($(TMHD)_3Gd$) and tris(cyclopentadienyl) gadonlinium (Cp_3Gd). The major difference is in the composition of the Gd precursors as seen in Figure 2.11; $(TMHD)_3Gd$ contains oxygen in its organic ligand while Cp_3Gd does not contain oxygen.

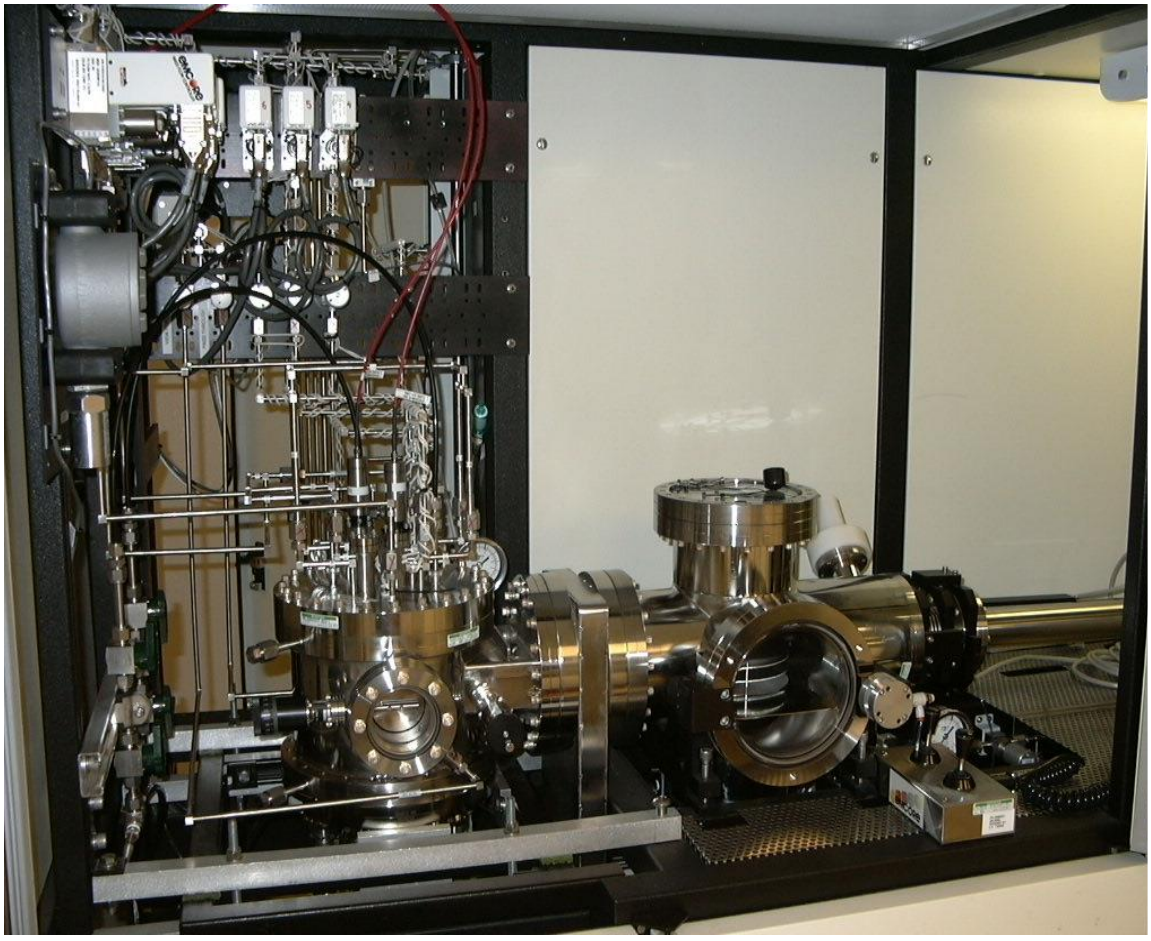

Figure 2.10 Metal-organic chemical vapor deposition (MOCVD) tool used for the growth of GaGdN

Silane and bis(cyclopentadienyl) magnesium (Cp_2Mg) were used as Si and Mg precursors for n-type and p-type doping respectively. Ammonia was a nitrogen source. Ammonia also helps to restrict decomposition of deposited films. Sapphire was used as a substrate considering a crystal structure match with GaN, thermal expansion coefficient, good crystal quality, low cost, and stability at high temperature and pressure. Using optically transparent sapphire as a substrate also provides opportunities to stack other

lattice matched thin films such as AlGaN, ZnO, InGaN on GaN and apply it as a dual-sided photodetector or absorber.

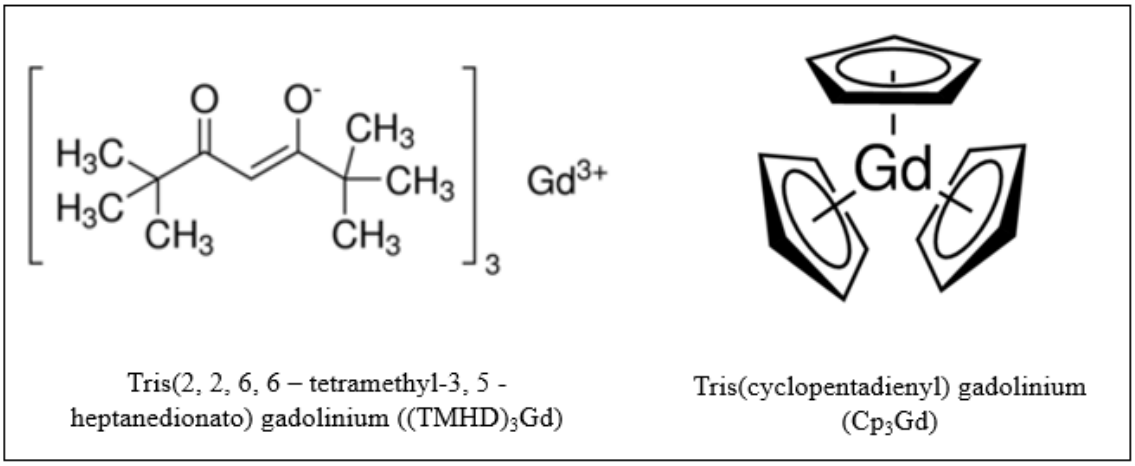

Figure 2.11 Chemical formulas of gadolinium precursors – $(TMHD)_3Gd$ and Cp_3Gd [Figures from Millipore Sigma website (04-16-2020)].

The growth process consists of a GaGdN layer deposition on sapphire with buffer layers. The substrate is baked or pre-heated to 1000 ^oC and exposed to ammonia for 3-10 minutes to improve the overall quality and reduce defects in the resulting thin films deposition. A buffer layer is grown at a low temperature (500 ^oC) for about 3 minutes to enhance the growth and create low energy centers with the desired crystal orientation and smoothness. The buffer layer is crystallized by increasing the chamber temperature to 1000 ^oC in an ammonia environment, which also relatively expands and roughens the GaN buffer layer. As the nucleation centers coalesce at the high temperature, growth of a 2 µm GaN layer is performed at 1050 ^oC. A V/III ratio of 2000-3000 is used to ensure cracking of NH_3 sufficient nitrogen. A GaGdN layer of 500 nm thickness is then grown on the buffer

layers. A summary of the growth process and a schematic of the deposited thin films structure is shown in Figure 2.11.

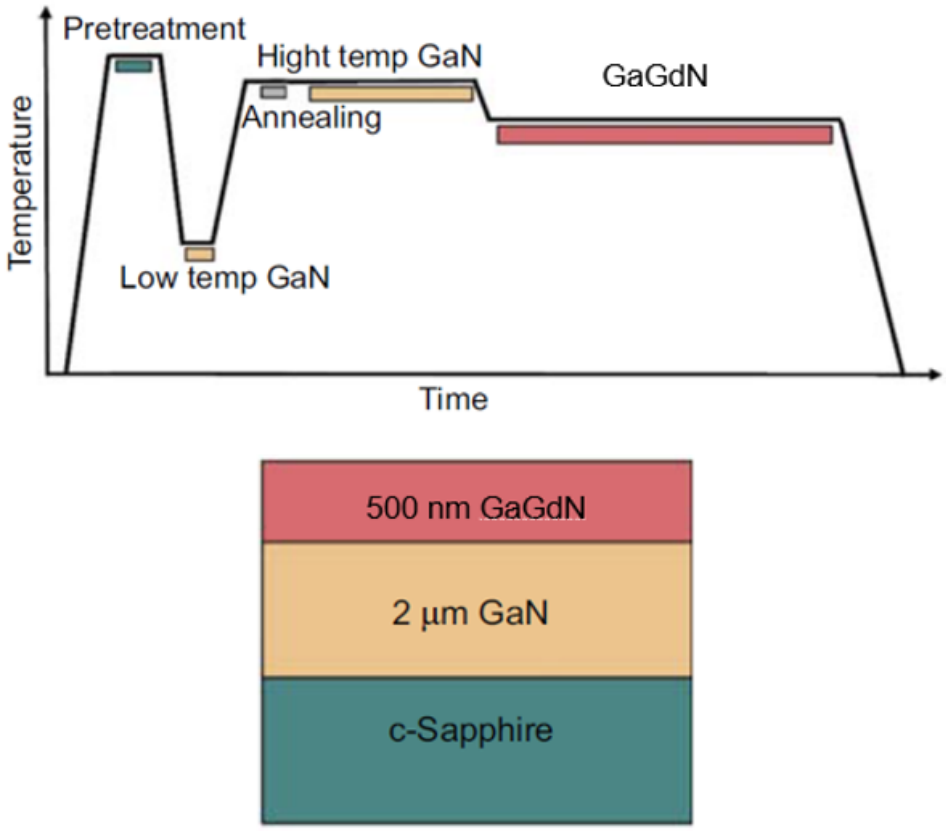

Figure 2.12 Summary of GaGdN MOCVD growth process and schematic of the deposited structure[238].

As-grown GaN and GaGdN films are typically n-type, hence p-type doping requires a post-growth annealing step at 800 ^{o}C for 4 mins in N_2 environment, to active the Mg acceptors.

2.3. STRUCTURAL PROPERTIES OF GADOLINIUM-DOPED GALLIUM NITRIDE

Structural properties of GaGdN were studied using X-ray diffraction (XRD) and energy-dispersive X-ray spectroscopy (EDS) techniques[258–261]. GaGdN from both the Gd precursors showed a good crystal quality and a crystal orientation in the (002) direction, as shown in Figure 2.12.

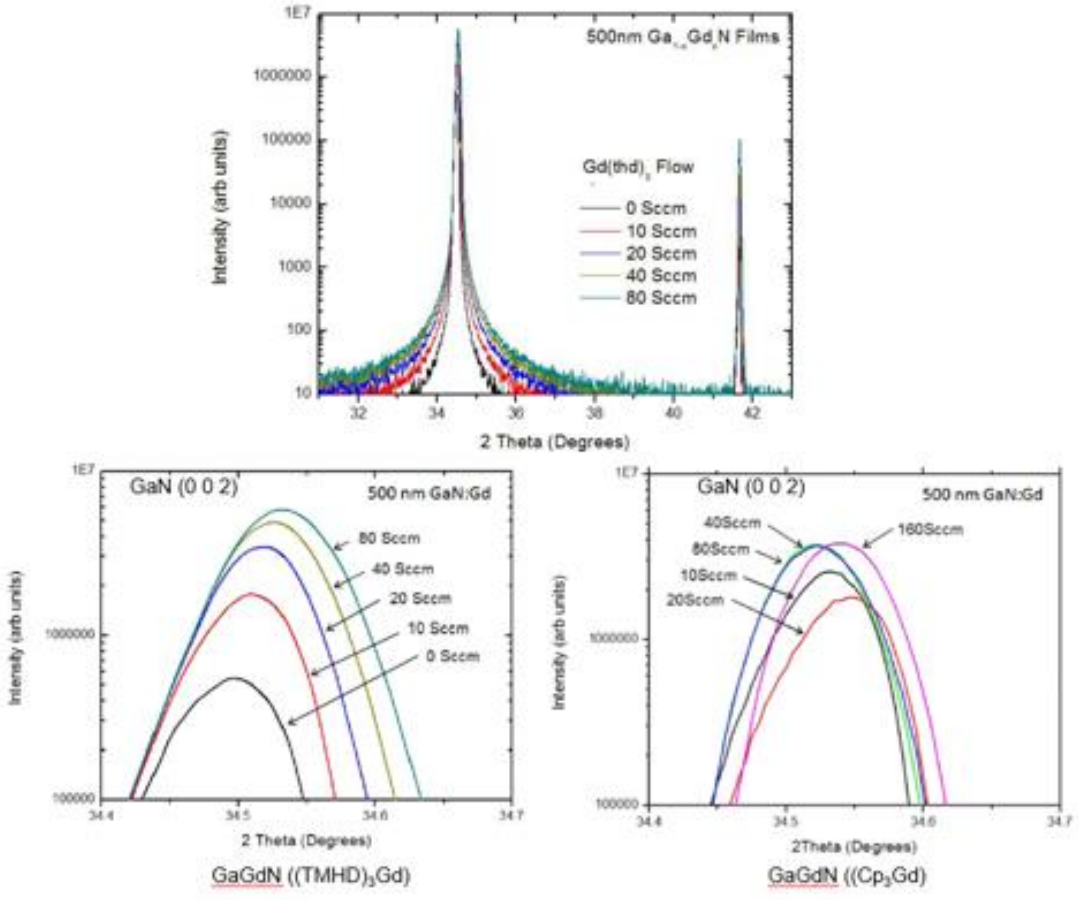

Figure 2.13 XRD of MOCVD-grown GaGdN from $(TMHD)_3Gd$ precursor over a wide and short range, and GaGdN from Cp_3Gd precursor over a short range[262].

In GaGdN grown from $(TMHD)_3Gd$, a peak shift towards higher 2θ with an increase in the Gd content was observed. On the other hand, GaGdN from Cp_3Gd precursor showed a nearly consistent peak position with Gd incorporation. A peak shift towards higher diffraction angles indicates a reduction in lattice size of GaN with Gd precursor's flow. As seen in Figure 2.11, using a $(TMHD)_3Gd$ precursor could result in oxygen incorporation in GaGdN which is not a possibility in GaGdN from Cp_3Gd. Oxygen has atomic radius lower than nitrogen (as well as Ga) and could result in a reduced lattice size upon being incorporated in GaGdN. This was also reflected in EDS measurement as shown in Table 2.1. GaGdN from $(TMHD)_3Gd$ source showed oxygen content while no oxygen is detected in GaGdN from Cp_3Gd source.

Table 2.1 Energy-dispersive X-ray scattering spectroscopy results of GaGdN samples grown by MOCVD[238]

Precursor flow	Ga%	N%	Gd%	O%
$TMHD_3Gd$, 10 sccm	44.46	44.41	0.06	1.18
$TMHD_3Gd$, 40 sccm	49.07	48.46	0.01	0.88
$TMHD_3Gd$, 80 sccm	47.74	48.61	0.01	1.55
Cp_3Gd, 10 sccm	46.51	47.03	0.35	0.00
Cp_3Gd, 80 sccm	46.33	46.37	0.34	0.00
Cp_3Gd, 160 sccm	47.48	46.34	0.53	0.00

Williamson-Hall plot analysis was done for GaGdN grown from both the Gd precursors, as shown in Figures 2.14 and 2.15. Vertical correlation lengths and strain

factors could be determined from wide range 2θ-ω scans, so corresponding (002), (004), and (006) corresponding to GaN-based materials are detected.

The FWHM in 2θ-ω scans represent the size broadening $\beta_{2\theta\text{-}\omega\text{–}1}$, and is related to the incident X-ray wavelength λ, vertical correlation length $L_{\|}$, and diffraction angle θ by Equation (1), where A is a constant[263–265].

$$\beta_{2\theta-\omega-1} = A\frac{\lambda}{L_{II}\cos(\theta)} \quad (1)$$

Peak broadening $\beta_{2\theta\text{-}\omega\text{–}2}$ due to strain is given by Equation (2), where ε represents a strain distribution, and B is a constant

$$\beta_{2\theta-\omega-2} = B\,\varepsilon\tan(\theta) \quad (2)$$

Total FWHM is a summation of $\beta_{2\theta\text{-}\omega\text{–}1}$ and $\beta_{2\theta\text{-}\omega\text{–}2}$ (considering a relatively negligible instrument-related broadening) as shown in Equations (4) and (5).

$$\beta_{2\theta-\omega} = \beta_{2\theta-\omega-1} + \beta_{2\theta-\omega-2} \quad (3)$$

$$\beta_{2\theta-\omega} = A\frac{\lambda}{L_{II}\cos(\theta)} + B\,\varepsilon\tan(\theta) \quad (4)$$

Multiplying throughout by cos(θ)/λ and rearranging, results in Equation (5).

$$\frac{\beta_{2\theta-\omega}\cos(\theta)}{\lambda} = A\frac{1}{L_{II}} + \frac{B\,\varepsilon\sin(\theta)}{\lambda} \quad (5)$$

Equation (5) looks like a straight line equation, and by plotting (sin(θ))/λ on the x-axis, and $\beta_{2\theta\text{-}\omega}\cos(\theta)/\lambda$ on the y-axis, an intercept on the y-axis gives an inverse of the vertical correlation length and intercept on x-axis gives the strain component.

Such Williamson-Hall analysis of GaN and GaGdN samples was performed as shown in Figure 2.13. A vertical correlation length of 64-82 nm and a strain component of $1.9\text{-}3.4\text{x}10^{-4}$ were obtained, and crystal quality of GaGdN samples was comparable to un-doped GaN.

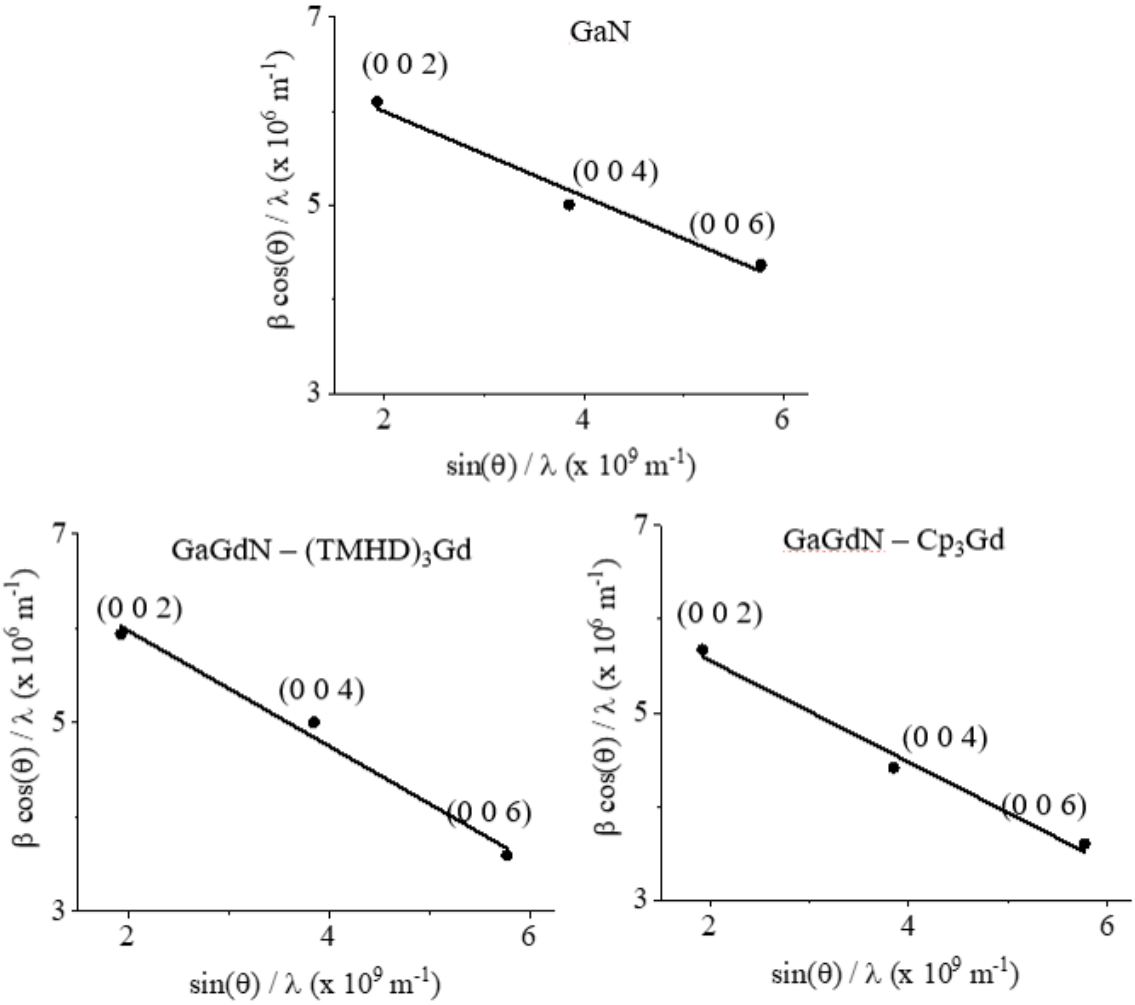

Figure 2.14 Williamson-Hall plot analysis of MOCVD-grown un-doped GaN, and Gd-doped GaN from $(TMHD)_3Gd$ and Cp_3Gd precursors to determine vertical correlation lengths and strain.

Horizontal correlation lengths were determined by measuring ω-rocking curves for (002), (004), and (006) peaks, and plotting $\beta_{\omega\text{-RC}}/\lambda$ vs $(\sin(\theta))/\lambda$, as shown in Figure 2.14. The y-axis intercept gives inverse of the horizontal correlation length, and x-intercept gives tilt angle. A horizontal correlation length of 638-1790 nm and tilt angle of 8.7-11.1 arcmin were calculated. The FWHM of the peaks ranged from 430 to 690 arcsec. The measured crystal properties of GaN and GaGdN were similar.

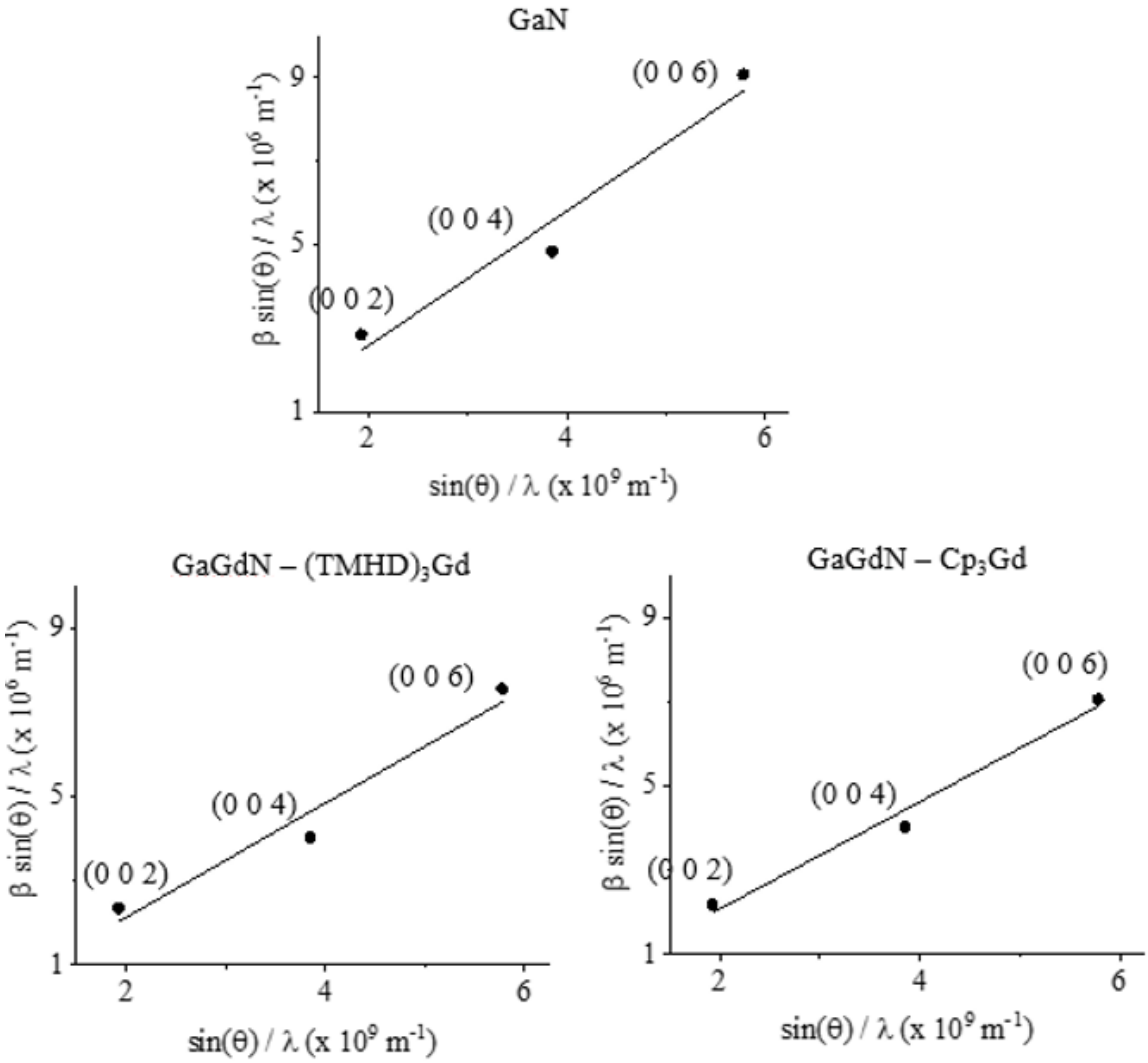

Figure 2.15 Williamson-Hall plot analysis of MOCVD-grown un-doped GaN, and Gd-doped GaN from $(TMHD)_3Gd$ and Cp_3Gd precursors to determine horizontal correlation lengths and tilt angles.

2.4. MAGNETIC PROPERTIES OF GADOLINIUM-DOPED GALLIUM NITRIDE

Magnetic properties of GaGdN grown by MOCVD were measured at RT using vibrating sample magnetometer (VSM)[230], as seen in Figure 2.16. A shift from a diamagnetic to ferromagnetic behavior was seen with Gd doping in GaGdN from $(TMHD)_3Gd$ source. GaGdN samples from Cp_3Gd precursor did not show signs of

ferromagnetism. Based on the basic difference between the two Gd precursors, it seems that oxygen incorporation helped in mediating the ferromagnetism, but this is not clear.

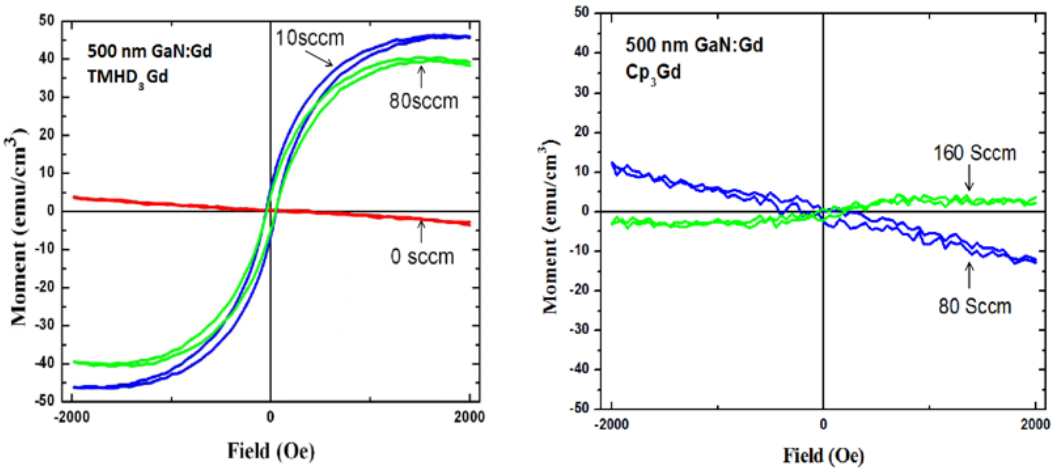

Figure 2.16 Magnetic properties of MOCVD-grown GaGdN grown from two Gd precursors – $(TMHD)_3Gd$ and Cp_3Gd[230].

GaN-based materials need to be typically doped with silicon and magnesium to induce n-type and p-type conductivity respectively, and GaGdN doped with Si and Mg both showed ferromagnetism[166]. The magnetization increased with the co-doping systematically as shown in Figure 2.17.

Spin light emitting diodes (SpinLEDs) were fabricated to understand the magnetic properties of MOCVD-grown GaGdN, as seen in Figure 2.18[238]. A GaN based LED showed lower turn-on voltage and resistance as compared to the GaGdN-based LED, due to a higher resistance of GaGdN as compared to GaN. Electroluminescence measurement of GaGdN spinLED showed variation in the polarization of light emission with applied magnetic field. GaN LED did not show differences in the light emission polarization with magnetic field. The difference between right and left circularly polarized light was

calculated and plotted as shown in Figure 2.18. Spin polarization up to 14.6% was observed, with a remnant polarization at 0 Gauss. The sign of the spin polarization stayed constant under different directions of the magnetic field.

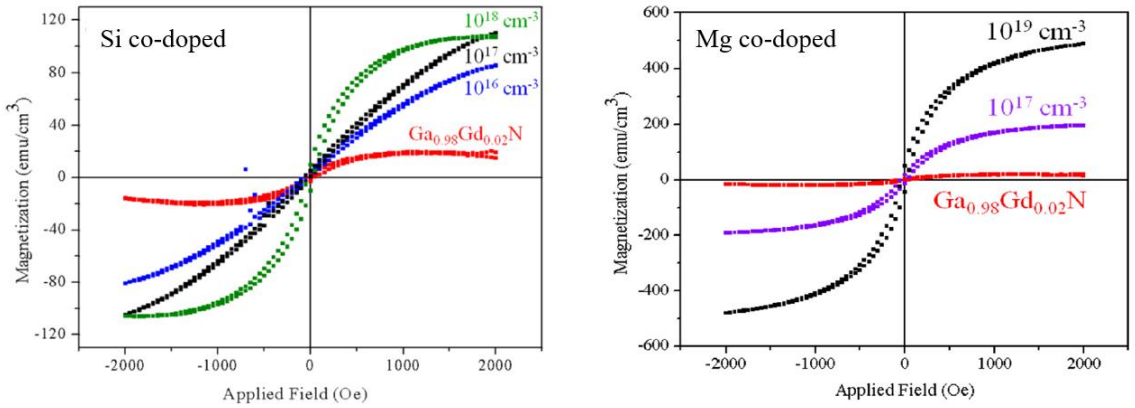

Figure 2.17 Room temperature magnetic characterization of GaGdN from $(TMHD)_3Gd$ precursor with Si and Mg co-doping[166].

2.5. ELECTRICAL CHARACTERIZATION OF GADOLINIUM-DOPED GALLIUM NITRIDE

Electrical characterization of MOCVD-grown GaGdN and reference GaN samples was performed using Hall effect measurement in a Van der Pauw geometry[266,267]. Longitudinal 4-point resistivity (ρ_{4pt}) of the samples was measured in a configuration as shown in Figure 2.18.

A standard resistivity calculation equation is shown in Equation (6), where ρ_{xx} is the sample's resistivity, and other resistances in the equation correspond to the applied currents and measured voltages along the sample's edges as shown in Figure 2.19.

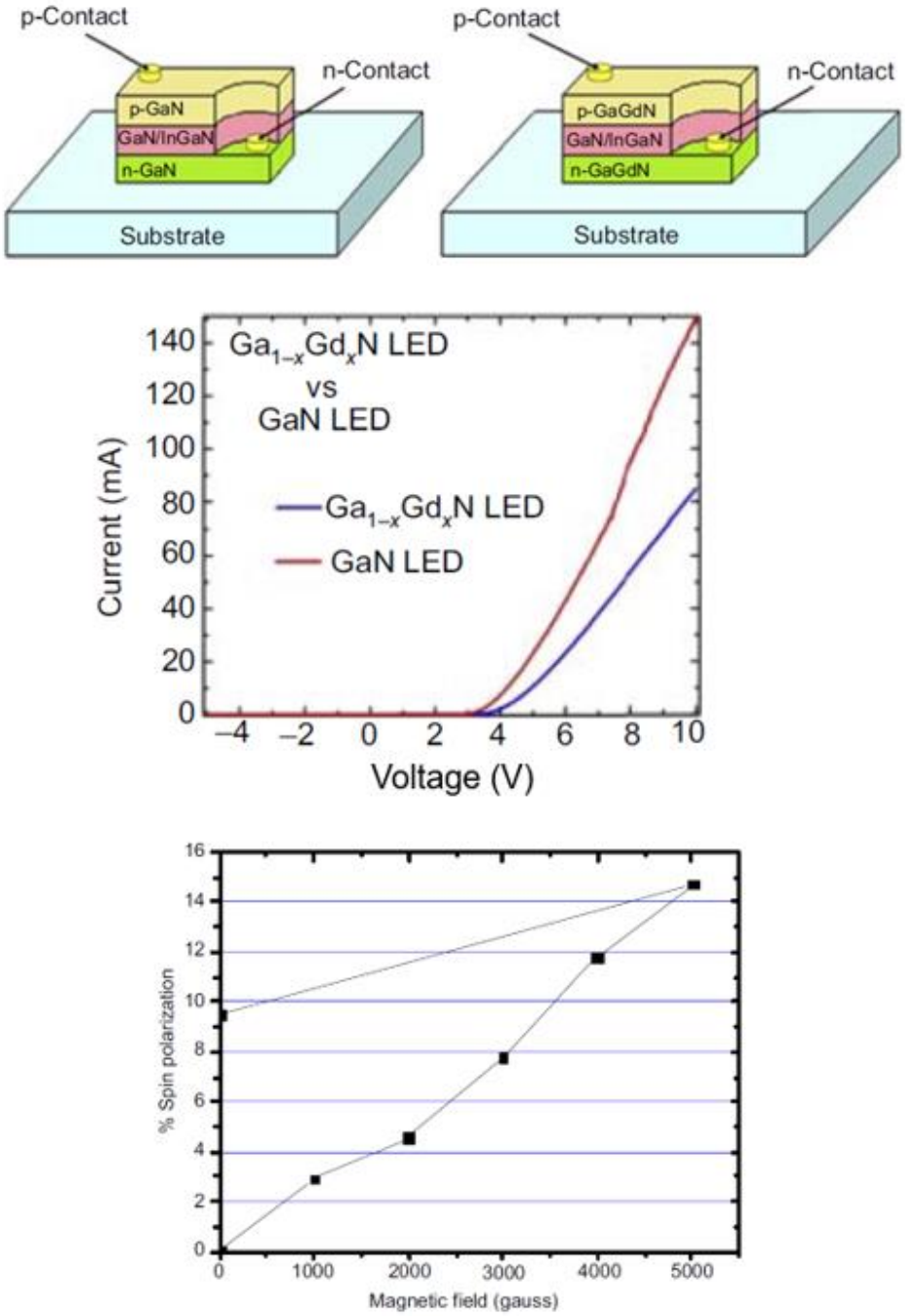

Figure 2.18 MOCVD-grown GaN and GaGdN Spin-light emitting diodes schematics and characteristics – Current-voltage, and spin polarization[238].

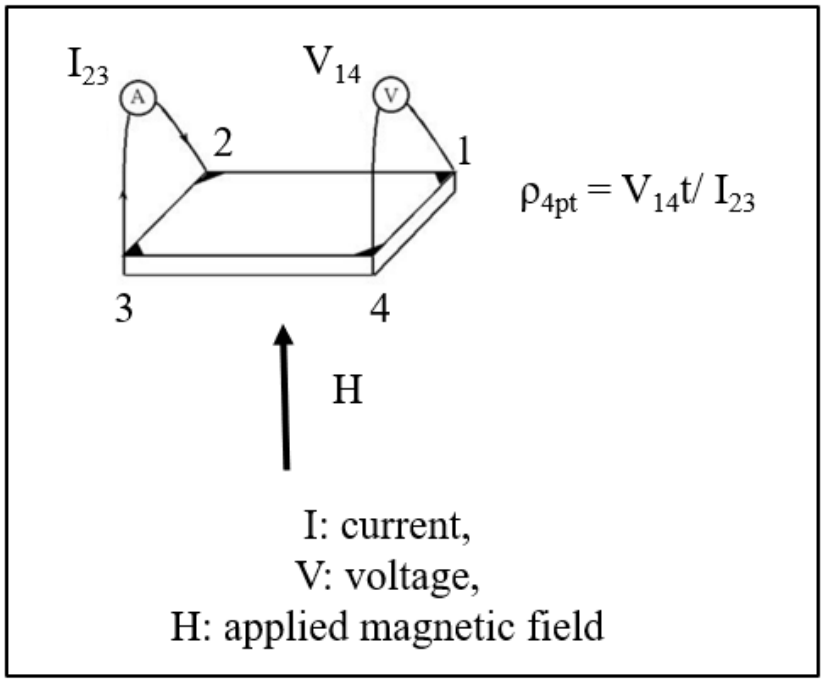

Figure 2.19 Van der Pauw geometry configuration to measure resistivity of MOCVD-grown GaGdN and reference GaN samples. [From " Hall Effect Measurements", NIST website, https://www.nist.gov/pml/nanoscale-device-characterization-division/popular-links/hall-effect (06-06-2020)]

$$e^{\left(\frac{-\pi t R_{12}}{\rho_{xx}}\right)} + e^{\left(\frac{-\pi t R_{23}}{\rho_{xx}}\right)} = 1 \qquad (6)$$

Resistivity of un-doped GaN samples ranged from 8 to 283 mΩ-cm. Resistivty of GaGdN from $(TMHD)_3Gd$ and Cp_3Gd sources were 190-3240 mΩ-cm and 20-90 mΩ-cm respectively. A high resistivity was observed in GaGdN samples grown using $(TMHD)_3Gd$ precursor, possibly due to additional energy states introduced by components such as oxygen from the precursor.

Carrier concentration and mobility of GaGdN and reference GaN samples was measured using Hall Effect. Upon application of a perpendicular current i or electric field E and perpendicular magnetic field H_z, charge carriers q in the thin films start traveling

along curved paths (unlike straight lines under no magnetic field), as shown in Figure 2.20, resulting in a Hall voltage perpendicular to the applied current and magnetic field.

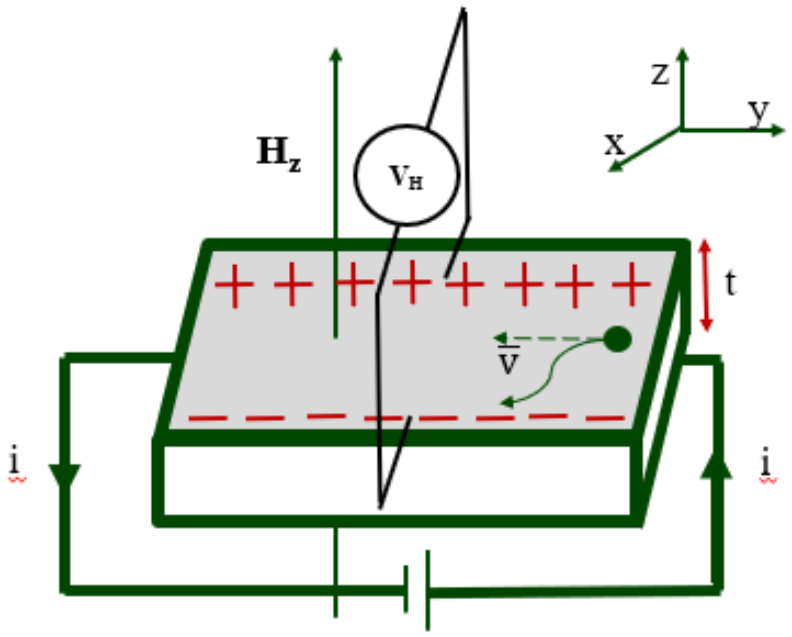

Figure 2.20 Hall Effect measurement schematic with an applied current i and magnetic field H_z and measured voltage V_H.

The force on the charge carriers F, is given by Equation (7), where $B=H_z$ in this section, and v is the charge carrier velocity.

$$F = qE + q\,v \times B \tag{7}$$

Hall resistances were measured in a configuration shown in Figure 2.21. Hall voltages were measured across both diagonal directions in positive and negative directions of applied magnetic field and current both, and then processed to determine the carrier density and mobility.

The carrier density and mobility can also be determined using Equations (8) and (9) respectively.

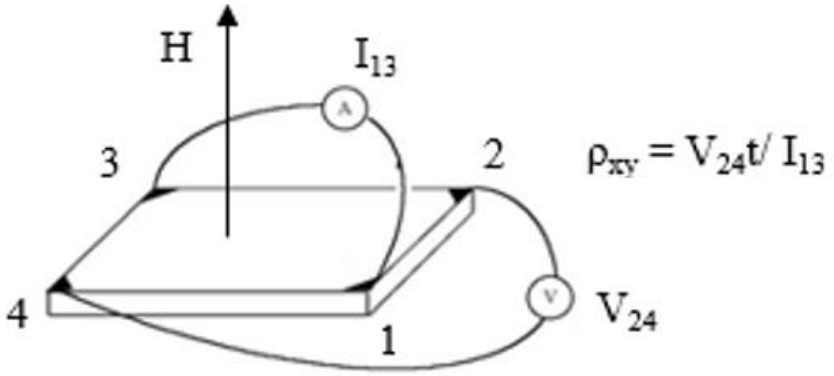

Figure 2.21 Hall Effect measurement configuration. [From " Hall Effect Measurements", NIST website, https://www.nist.gov/pml/nanoscale-device-characterization-division/popular-links/hall-effect (06-06-2020)].

$$n_s = \frac{iB}{qV_H}t \tag{8}$$

$$\mu = \frac{1}{qn_sR_{xx}} \tag{9}$$

Carrier density and mobility characterization of MOCVD-grown and n-type GaGdN and reference GaN samples is shown in Figure 2.22. A constant reference thickness was considered for comparison, as the samples were grown under similar conditions. GaN, and GaGdN from Cp_3Gd showed high carrier concentration and mobility as expected. On the other hand, GaGdN samples from $(TMHD)_3Gd$ source showed a low carrier concentration and mobility. This, accompanied with a high resistivity in GaGdN from $(TMHD)_3Gd$ source shows signs of deep level acceptor states incorporated in GaGdN, that compensate the n-type conductivity.

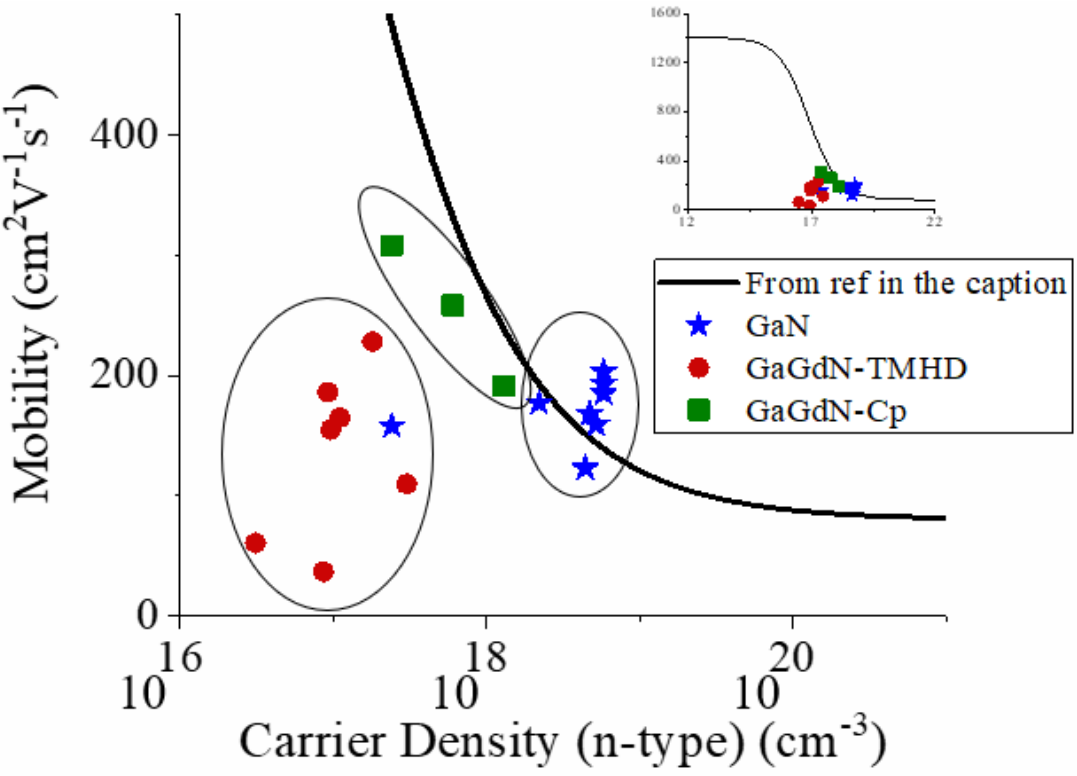

Figure 2.22 Mobility and carrier density of MOCVD-grown GaGdN and reference GaN.

2.6. ANOMALOUS HALL EFFECT CHARACTERIZATION OF GADOLINIUM-DOPED GALLIUM NITRIDE

Anomalous Hall Effect characterization of GaGdN is discussed in this sub-section.

2.6.1. Hall Effect. Hall Effect has been discussed in the previous Section 2.5 in the context of electrical characterization. Hall effect also provides information of the magnetic properties of thin films materials. As seen in Equations (7), (8), and (9), the Hall voltage is a function of magnetic field across the sample. For typical samples (that not have ferromagnetism), the Hall resistivity response as shown in Figure 2.23 is observed. Hall resistivity (ρ_{Hall}) changes linearly with the applied magnetic field with negative and positive slopes for n-type and p-type materials respectively.

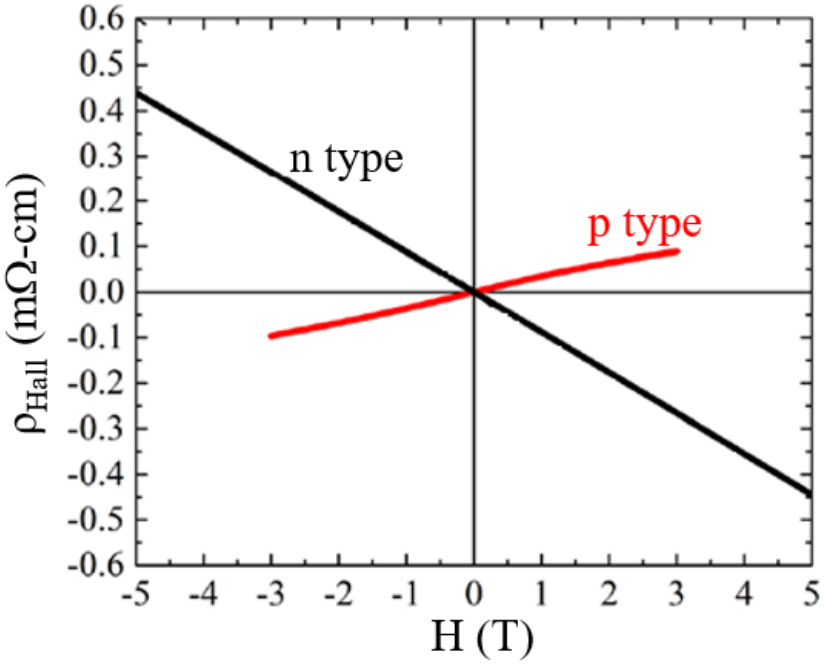

Figure 2.23 Typical Hall Effect response[268].

2.6.2. Anomalous Hall Effect. Anomalous Hall effect (AHE), also called as extraordinary Hall Effect (EHE) is a phenomenon observed in ferromagnetic materials wherein the Hall voltage shows anomaly in its typical linear trend with magnetic field. In case of ferromagnetic materials, the change in Hall voltage with variation in magnetic field is linear at high fields, but this becomes anomalous especially at some ranges of fields[269–272]. Usually at lower fields, the Hall voltage and resistivity could be a superposition of the materials' properties and the applied magnetic field.

Magnetization measurement typically include effects of defects in the substrates, clusters, and parameters that could not be directly related to a thin film. In ferromagnetic materials, the total magnetic field in the material is the result of the applied field and the magnetization in the material. At applied fields comparable to the magnetization of the material in Hall Effect analysis, the hall resistivity (ρ_{xy}) is not linear with the applied field

which results in AHE. Analyzing AHE in materials helps towards qualitatively determining the mechanism that is responsible for their magnetic behavior.

In AHE, the Hall resistivity consists of two components, the ordinary Hall component that is dominant at high fields and the anomalous Hall component that contributes to Hall resistivity at least at lower fields[269–272]. Conventionally, relation between the Hall resistivity and sample's resistivity provides information about mechanisms for magnetic properties in the material. In intrinsic mechanism, the Hall resistivity is proportional to the square of the longitudinal resistivity. Intrinsic mechanism is based on the band structure which is a characteristic of the material and wherein an anomalous velocity is added to the group velocity of the carriers under an applied magnetic field and current, and the net sum of these anomalous velocities could be non-zero when applied magnetic field is removed. Extrinsic mechanism could be based on carrier scattering and impurities in the material that induce magnetic properties. In skew scattering, asymmetric scattering of carriers from impurities such as spin waves or phonons or crystal disorders in the material causes spin-orbit interaction and results in ferromagnetism; Hall resistivity is directly proportional to longitudinal resistivity in this case. In side jump mechanism, anomalous Hall voltage is observed due to the scattering of carriers from spin-orbit coupled impurities, and the Hall component is proportional to the square of the longitudinal component of the resistivity. Intrinsic and side-jump mechanisms could be inter-related and one could result into another, hence separating or distinguishing these two mechanisms could be complicated. Figure 2.24 gives a broad summary of mechanisms that could be understood using AHE.

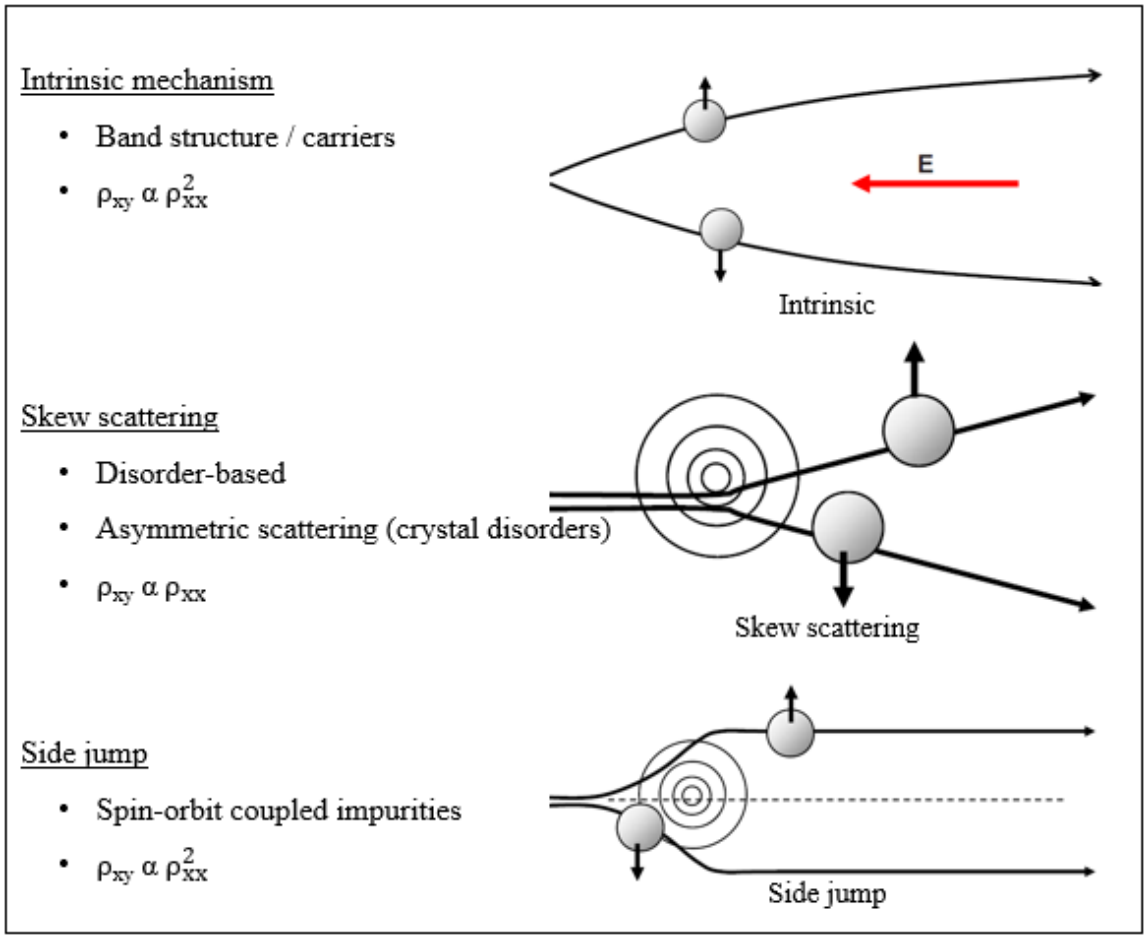

Figure 2.24 Summary of determination of mechanisms based on relationship between Hall resistivity and sample's net resistivity[270].

With recent developments and efforts towards better understanding Anomalous Hall Effect, mechanisms for ferromagnetism have been studied by identifying contributions to the anomalous Hall conductivity (σ_{AHE})[269–272]. The dependence of σ_{AHE} on longitudinal conductivity (σ_{xx}) is characteristic of different mechanisms as well as conductivity regime of σ_{xx}. Skew scattering dominates in a highly conductivity region ($\sigma_{xx} > 10^6$ $(\Omega\ cm)^{-1}$) and the anomalous Hall conductivity varies linearly with the samples' conductivity. In an intermediate conductivity region ($10^6 > \sigma_{xx} > 10^4$ $(\Omega\ cm)^{-1}$), if the

mechanism is purely intrinsic, the anomalous Hall conductivity is independent of the samples' conductivity. A low conductivity region ($\sigma_{xx} < 10^4$ $(\Omega\ cm)^{-1}$) shows a super-linear scaling of the anomalous Hall conductivity and the mechanism could be metallic conduction or hopping. This understanding of AHE, as summarized in Table 2.2 could be directly applicable to dilute magnetic semiconductor materials which can be tuned to have conductivity in varying ranges by tuning temperature, carrier concentration or impurities.

Table 2.2 Anomalous Hall Effect mechanisms based on conductivity regimes and relationships between anomalous Hall conductivity and sample's net conductivity[270].

Conductivity Regime	**Relation between σ_{AHE} and σ_{xx}**	**Mechanism for ferromagnetism**
$\sigma_{xx} > 10^6$ $(\Omega\ cm)^{-1}$	$\sigma_{AHE} \propto \sigma_{xx}$	Skew Scattering
$10^6 > \sigma_{xx} > 10^4$ $(\Omega\ cm)^{-1}$	σ_{AHE} independent of σ_{xx}	Intrinsic mechanism
$\sigma_{xx} < 10^4$ $(\Omega\ cm)^{-1}$	$\sigma_{AHE} \propto \sigma_{xx}^{a}$ $(1.6 < a < 2)$	Metallic Conduction / Hopping

Figure 2.25 shows a summary of the mechanisms' dependence on the conductivity ranges. At low temperature, skew scattering could be dominating with presence of intrinsic mechanisms. At low conductivity region, the intrinsic mechanism starts fading and carrier-hopping mechanism starts contributing towards the AHE.

AHE in DMS such as GaMnAs and InMnAs is reported to be scattering-independent[251,269,270]. AHE at temperatures up to 210 K was seen in ZnMnO grown by pulsed laser deposition with 26% Mn, and the resulting mechanism was reported to be a

side jump mechanism with contributions from localized magnetic moments and spin carriers[273]. High Mn concentration could result in carrier deflection, a short mean free path, and oxygen vacancies. Similar mechanism was observed in Mn_4N grown by MBE and the effects of side-jump and intrinsic mechanisms were complicated to be well-separated[274]. AHE was also seen in ZnO codoped with Co up to 3.5%, and native defects such as oxygen vacancies or zinc interstitials seemed to mediate the AHE[275]. In the case of TiO_2, only films with high carrier concentration showed signs of AHE, which showed the effects of carriers (and possible compensation of defects states) on the Hall effect results[276,277]. In MBE-grown InMnP:Zn, a hole-mediated AHE was observed at temperatures below 200 K[278]. AHE was observed in Gd-implanted GaN/AlGaN heterostructures grown by MBE, but its origin and relation to magnetic properties is not clear[251]. MBE-grown GdN (111) on GaN (002) showed signs of AHE, but the T_C observed was 70 K[279].

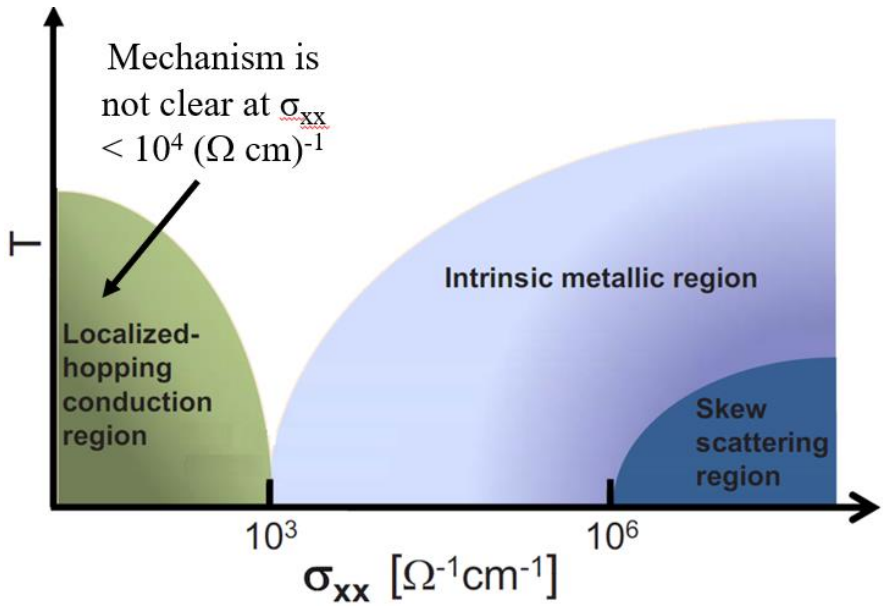

Figure 2.25 Summary of Anomalous Hall Effect mechanisms based on the conductivity range of the samples[270].

As discussed in the previous sections, MOCVD-grown GaGdN has shown structural, magnetic, and electrical properties that could be conducive for RT spintronic applications. However, the mechanism for the magnetic properties is not clear and needs more investigation. In the next sub-section, Hall Effect analysis of GaGdN and reference GaN samples has been performed to achieve an insight into the magnetic properties.

2.6.3. Anomalous Hall Effect Characterization of GaGdN. Hall measurements were performed on MOCVD-grown GaN and GaGdN samples at RT using Van der Pauw configuration. Longitudinal resistivity (ρ_{xx}) and transverse resistivity (ρ_{xy}) were measured in perpendicular magnetic fields ranging from 0 to ±1.4 T. An MMR-Technologies H5000 controller was used to read and apply current and voltages, and control the magnetic field. Magnetic fields were swept and applied between +1.4 T and -1.4 T and transverse and longitudinal voltages were measured[228].

Hall effect analysis of three sets of samples was conducted - a.) un-doped GaN, b.) GaGdN grown using a Cp_3Gd precursor and c.) GaGdN grown from a $((TMHD)_3Gd)$ precursor. Hall measurement of a GaN sample that does not contain Gd is shown in Figure 2.26.

Variation in resistivity with magnetic fields is shown in the ±1000 Gauss region where the anomalous Hall effect could be better seen even though measurement were taken over a larger range of fields (up to 1.4 T). The transverse resistivity (ρ_{xy}) has linear variation with applied magnetic field (H) as expected. The change in the measured four-point resistivity ρ_{4pt} (measured in a direction parallel to the applied current) with H was negligible relative to the variation in ρ_{xy} with H. The field-independent component of ρ_{xy} was subtracted from ρ_{xy} to analyze the Hall effect. This sample only showed the ordinary

Hall effect (OHE) and was not ferromagnetic. GaN samples with range of n-type carrier density from $2x10^{17}$ cm^{-3} to $5x10^{18}$ cm^{-3} and mobility from 123 $cm^2V^{-1}s^{-1}$ to 193 $cm^2V^{-1}s^{-1}$ were measured and OHE was observed.

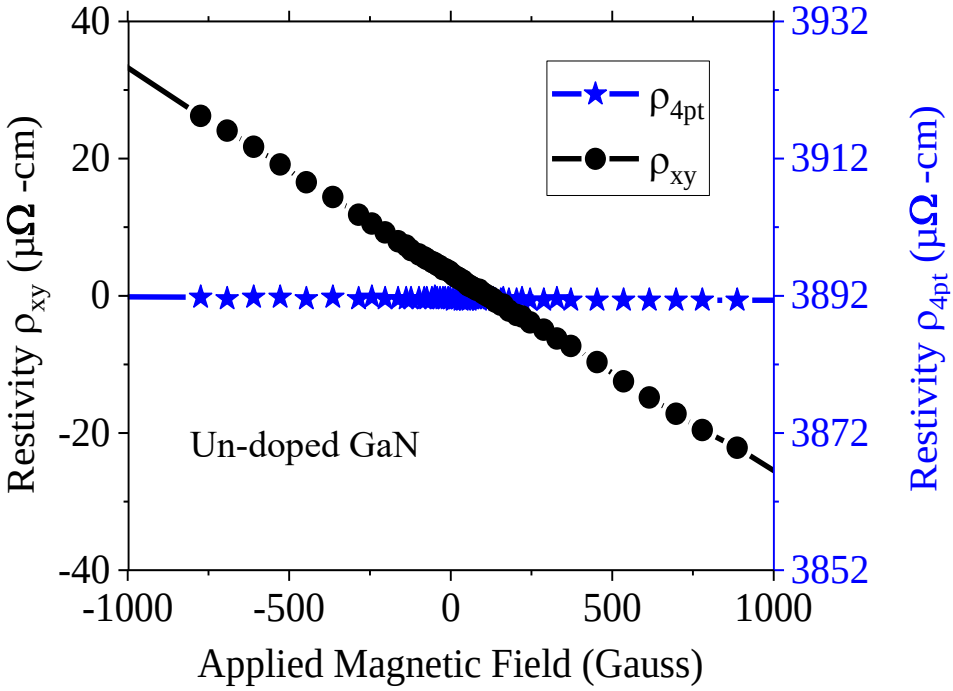

Figure 2.26 Transverse and longitudinal resistivity of un-doped GaN[228].

The second set of samples consisted of GaGdN grown using a Cp_3Gd precursor as shown in Figure 2.27. These samples showed OHE similar to GaN, and no sign of ferromagnetism. The samples had n-type carrier concentration in the order of 10^{17} cm^{-3} and 10^{18} cm^{-3} and mobility from 190 $cm^2V^{-1}s^{-1}$ to 300 $cm^2V^{-1}s^{-1}$.

In the third set of samples, AHE was observed in GaGdN grown using the $((TMHD)_3Gd)$ precursor as seen in Figure 2.28. The behaviour was consistent in several

samples with range of n-type carrier density from 3 x 10^{16} cm^{-3} to 3 x 10^{17} cm^{-3} and mobility from 37 $cm^2V^{-1}s^{-1}$ to 228 $cm^2V^{-1}s^{-1}$.

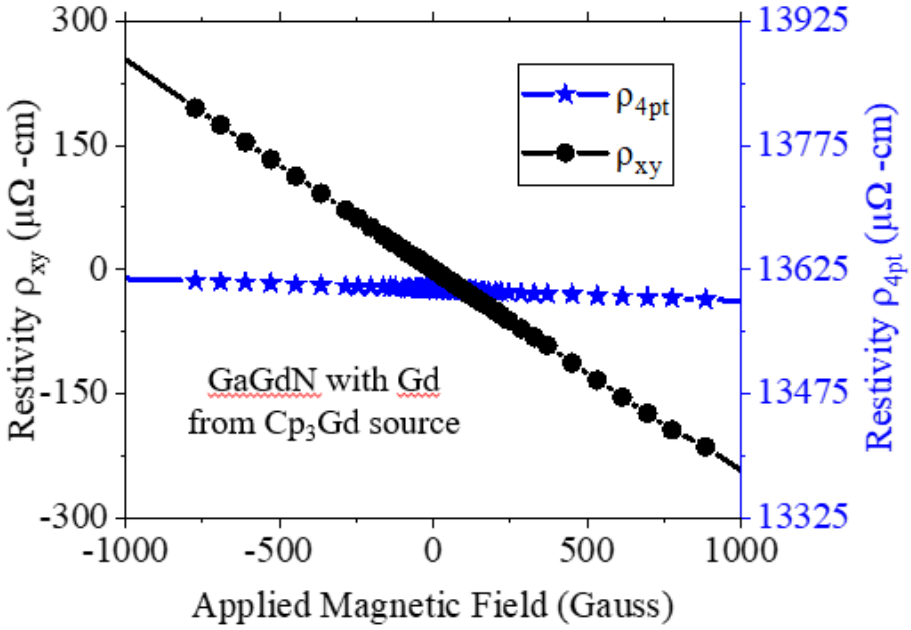

Figure 2.27 Transverse and longitudinal resistivity of GaGdN from Cp_3Gd precursor[228].

AHE was only observed in GaGdN grown using a $(TMHD)_3Gd$ source and not in GaGdN grown using Cp_3Gd and un-doped GaN. This is in agreement with the relatively bulk magnetic characterization from vibrating sample magnetometer which showed ferromagnetism only in GaGdN from $(TMHD)_3Gd$ source but not in GaGdN from Cp_3Gd.

2.6.4. Mechanism for Anomalous Hall Effect in GaGdN. Proceeding towards determining the mechanism, early theories were based on relation between ρ_{xy} and longitudinal resistivity (ρ_{xx}). As per recent exploration of experimental and theoretical models, responsible mechanisms can be identified by finding relationship between

anomalous Hall conductivity (σ_{AHE}) and longitudinal conductivity (σ_{xx}), as discussed in Section 2.6.2.

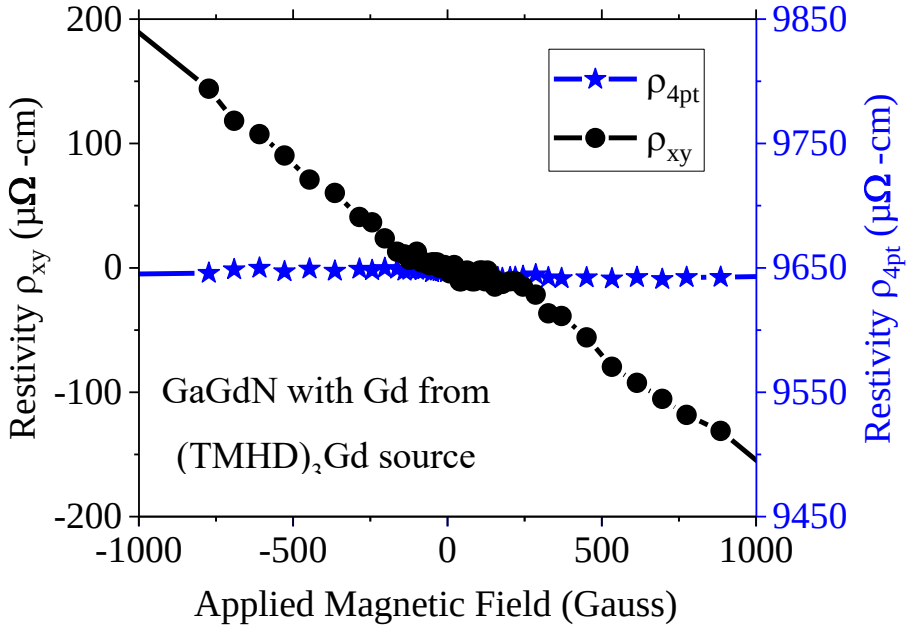

Figure 2.28 Transverse and longitudinal resistivity of MOCVD-grown GaGdN from $(TMHD)_3Gd$ precursor[228].

The measured value of ρ_{xy} is convolution of both the anomalous Hall component (ρ_{AHE}) and ordinary Hall component. The OHE and AHE components need to be separated to explicitly study the AHE. The ordinary Hall coefficient (R_o) can be determined by calculating the slope of ρ_{xy} versus H at high magnetic fields, typically over 0.5 T. The anomalous Hall component ($\rho_{AHE} = R_{AHE}M$) was calculated as shown in Equation (10),

$$R_{AHE}M = \rho_{xy} - R_o \tag{10}$$

where R_{AHE} is the anomalous Hall coefficient and M is the magnetization in the sample which should saturate at high fields for perfectly ferromagnetic materials. ρ_{AHE} is plotted

in Figure 2.29 (for the best GaGdN from $(TMHD)_3Gd$ sample) which can be seen to follow an S-shape, similar to that usually observed in bulk magnetization measurements.

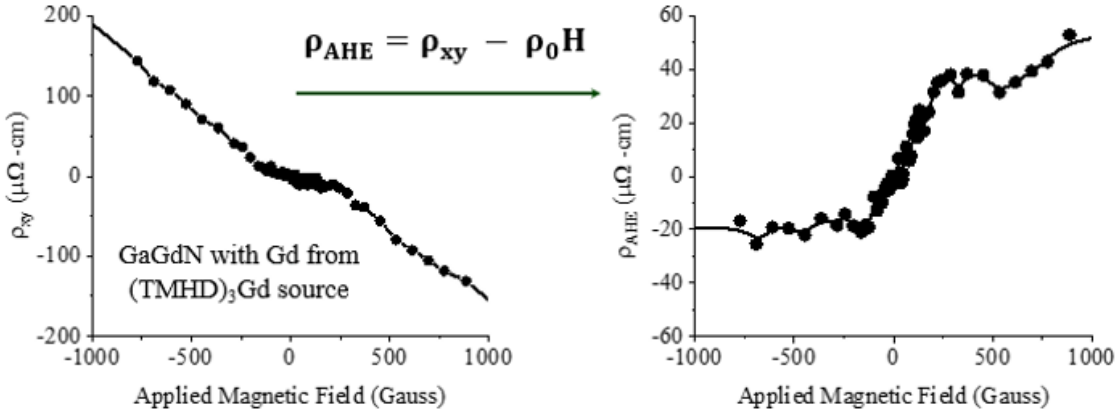

Figure 2.29 Transverse resistivity of GaGdN from $(TMHD)_3Gd$ source processed to determine the anomalous Hall component[228].

The potential mechanism for the observed ferromagnetism in GaGdN is further investigated. σ_{AHE} and σ_{xx} were calculated using Equation (11) and relationship between them at 1 T was determined[269–272].

$$\sigma_{AHE} = \frac{\rho_{AHE}}{(\rho_{xx}^2 + \rho_{AHE}^2)}, \qquad \sigma_{xx} = \frac{\rho_{xx}}{(\rho_{xx}^2 + \rho_{AHE}^2)} \tag{11}$$

It was found that σ_{AHE} increased compared to σ_{xx} at a rate that was superlinear. On fitting, a relation $\sigma_{AHE} \propto \sigma_{xx}^{1.78}$ was found, Figure 2.30. The exponent with value between 1.6 and 1.8 is typically observed in ferromagnetic materials in the low conductive regime which would be expected for wideband gap semiconductor materials such as GaN.

The observation of ferromagnetism in semi-conducting GaGdN and the scaling of σ_{AHE} with σ_{xx} indicates the mechanism for the ferromagnetism is scattering-independent. The potential mechanisms for this type of behavior are metallic conduction or localized

hopping and partially intrinsic; the intrinsic mechanism dampens as the conductivity range reduces as shown in Figure 2.24. These mechanisms are based on the interaction and flow of carriers that result in spin-polarization in the material. The metallic conduction and/or hopping of carriers may depend on the localized states near the Fermi level of GaGdN that are introduced by oxygen interstitials from the Gd precursor. Theoretical calculations indicate that Gd atoms in GaGdN interact to exhibit ferromagnetic behavior in the presence of a split-interstitial oxygen with a total energy difference of over 100 meV.

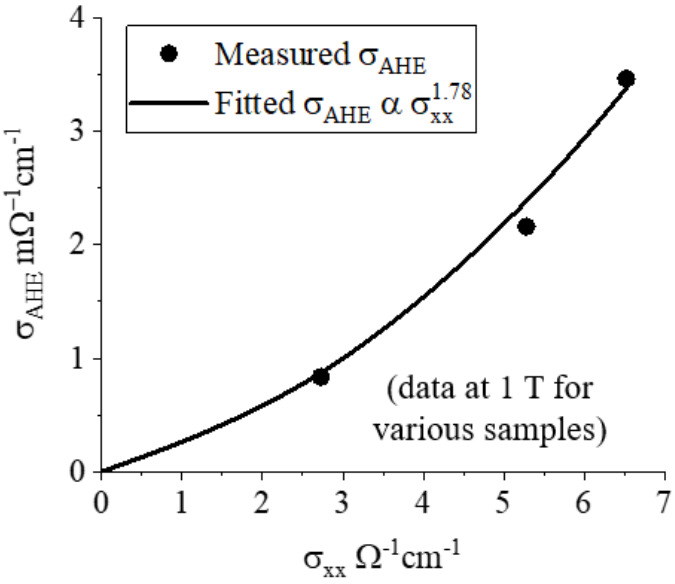

Figure 2.30 Relationship between Anomalous Hall conductivity and longitudinal conductivity for MOCVD-grown GaGdN from $(TMHD)_3Gd$ precursor[228].

2.7. MECHANISM FOR SPIN PROPERTIES OF GADOLINIUM-DOPED GALLIUM NITRIDE

Anomalous Hall Effect characterization showed the mechanism in GaGdN thin films grown by MOCVD to be a combination of carrier-hopping, metallic conduction, and intrinsic mechanisms. Bulk magnetization measurement showed a scaling of magnetization

with co-doping and with the carrier density. AHE and ferromagnetism at RT show that GaGdN grown by MOCVD could have a free-carrier related spin mechanism conducive for RT spintronic applications.

However, AHE and ferromagnetism were only observed in GaGdN grown using a $(TMHD)_3Gd$ source and not in GaGdN grown using Cp_3Gd and un-doped GaN. This could be attributed to the presence of oxygen in GaGdN from $(TMHD)_3Gd$, that is not seen in Cp_3Gd. XRD and EDS measurement indicated that only GaGdN from $(TMHD)_3Gd$ contain oxygen. Electrical characterization showed that GaGdN from ($TMHD_3Gd$ precursor has a high resistivity and a lower carrier density, which points towards the existence of deep level acceptor states from oxygen.

Density functional theory calculations show that oxygen interstitials introduce localized states close to the Fermi level of GaGdN which couples with the partially filled states of the dopant to render ferromagnetism that can be observed at RT[280]. Strong p-d and/or p-f coupling could exist between oxygen interstitials and Gd in the host GaN material, resulting in the spin-related properties.

In summary, Gadolinium-doped gallium nitride (GaGdN) grown by MOCVD was explored in this section and spin-related properties were studied. GaGdN was grown using two precursors - ($TMHD_3Gd$ that contains oxygen in its organic ligand, and Cp_3Gd that does not contain oxygen. GaGdN from $(TMHD)_3Gd$ showed clear signs of ferromagnetism and anomalous Hall effect at RT, mediated by metallic conduction, carrier-hopping and partly intrinsic mechanisms which points towards a free carrier-mediated mechanism, and makes GaGdN an interesting material for RT spintronics.

Un-doped GaN and GaGdN from Cp_3Gd showed Ordinary Hall Effect and no signs of ferromagnetism, which shows a contribution of oxygen in GaGdN from $(TMHD)_3Gd$. The presence of oxygen and related deep acceptor or interstitial states seem play a significant role in GaGdN, but this is not clear and needs further investigation to precisely understand the mechanism for spin-related properties of GaGdN at RT.

3. ROLE OF OXYGEN AND CARBON IN GADOLINIUM-DOPED GALLIUM NITRIDE FOR SPINTRONICS

3.1. SPIN-RELATED ELEMENTS IN GaGdN

Gallium nitride doped with gadolinium has been a candidate material for spintronic applications at RT mainly due to its lattice size which enables exchange interactions between the carriers of spin-related energy states more than spin-orbit couplings, and experimental results showing RT ferromagnetism. Colossal magnetic moments were reported in Gd-doped GaN (GaGdN) grown by molecular beam epitaxy (MBE), but the mechanism for ferromagnetism seems to stem from defects and vacancies and not carriers as the ferromagnetism reduced with co-doping and enhanced with implantation. GaGdN grown by metal-organic chemical vapor deposition (MOCVD) also showed RT ferromagnetism which enhanced with co-doping. The mechanism for the ferromagnetism is based on intrinsic mechanisms and combinations of carrier hopping and metallic conduction which involves interactions of carriers in GaGdN and is a conducive underlying mechanism for spintronic applications.

MOCVD-grown GaGdN exhibited RT ferromagnetism and Anomalous Hall Effect (AHE) only when grown using a $(TMHD)_3Gd$ precursor. $(TMHD)_3Gd$ precursor contains oxygen in its organic ligand. GaGdN from Cp_3Gd precursor which does not contain oxygen showed Ordinary Hall Effect (OHE). In the latter case, ferromagnetism was not observed even in the presence of Gd atoms in GaN. Oxygen from the $(TMHD)_3Gd$ precursor could be incorporated in the GaGdN structure and could play a role in rendering ferromagnetism. These results are summarized are in Figure 3.1. Also, GaGdN from $(TMHD)_3Gd$ precursor had smaller lattice sizes with at high Gd source flows and presence of O while GaGdN

from Cp_3Gd did not exhibit systematic changes in lattice sizes and did not show any O content. GaGdN from $(TMHD)_3Gd$ was resistive with a lower carrier concentration as compared to GaGdN from Cp_3Gd precursor.

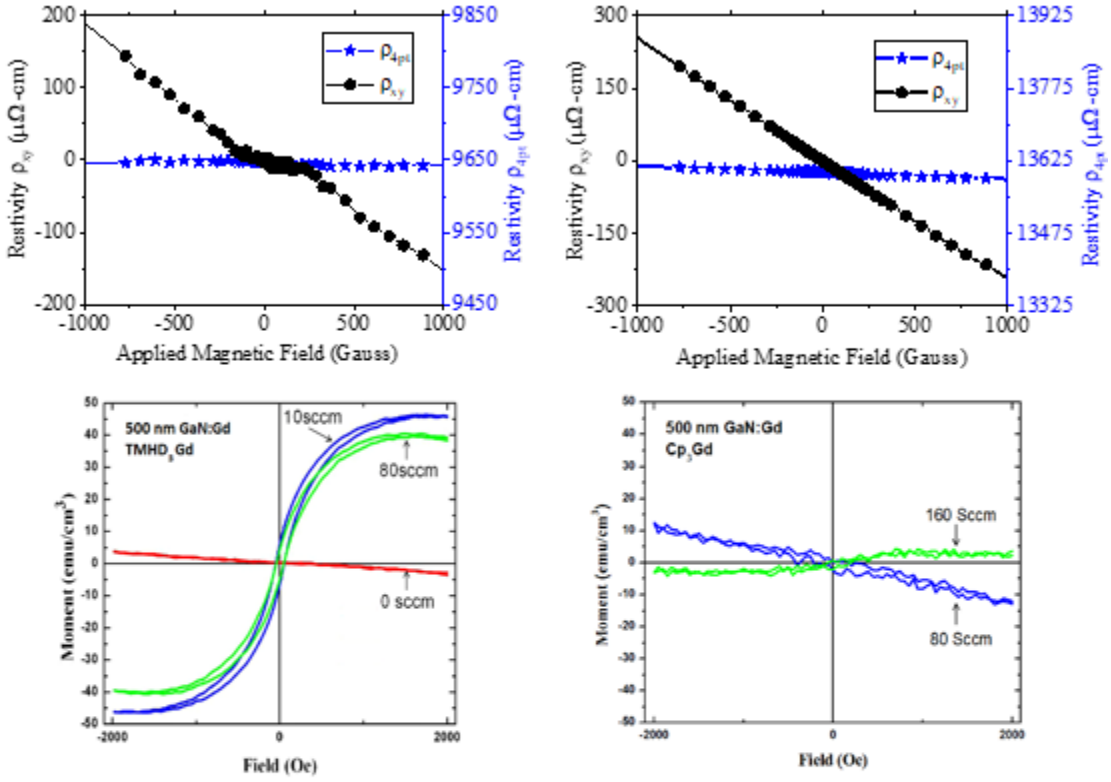

Figure 3.1 Summary of magnetic measurement results of MOCVD-grown GaGdN and chemical composition of the two Gd precursors $(TMHD)_3Gd$ and Cp_3Gd that were used[228,238] [$(TMHD)_3Gd$ and Cp_3Gd precursors' chemical composition figures from Millipore Sigma website (04-16-2020)].

X-ray magnetic circular dichroism (XMCD) measurement of MBE-grown GaGdN on SiC showed a very small signal for Gd and discrepancies as compared to measurement of GaGdN from superconductive quantum interference device measurements (SQUID)[281]. XMCD signal from Gd is significantly smaller than SQUID measurement of GaGdN, as seen in Figure 3.2.

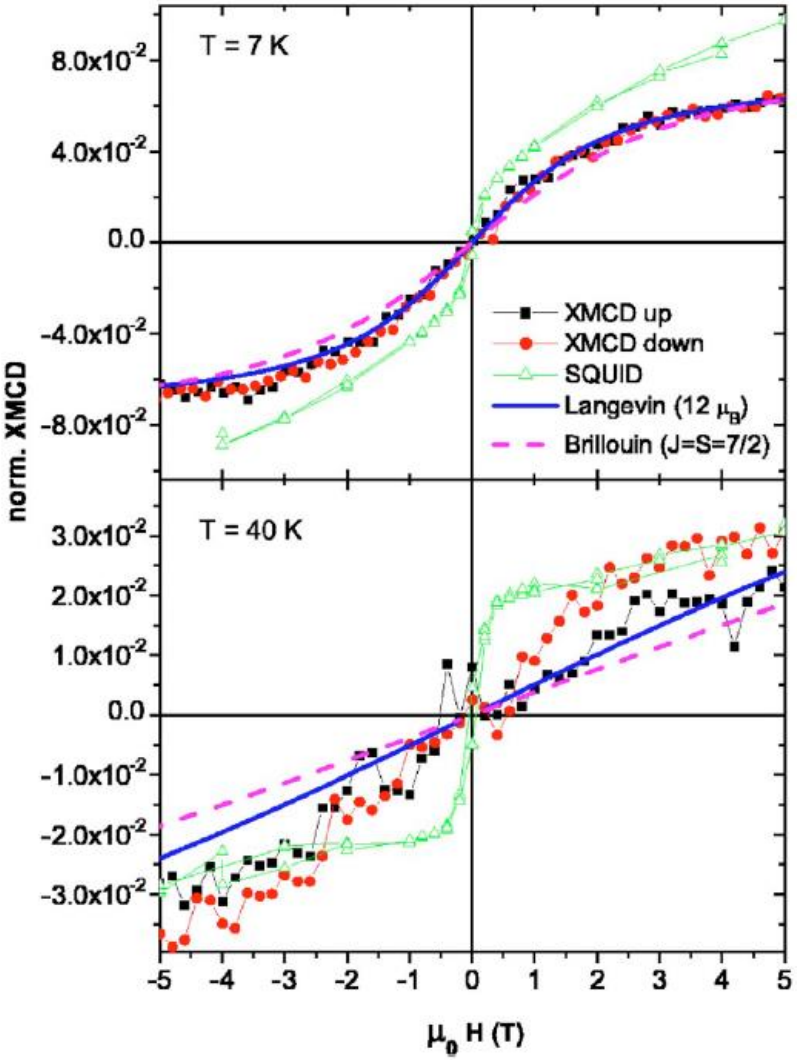

Figure 3.2 X-ray magnetic circular dichroism (XMCD) at Gd and superconducting quantum interference device (SQUID) measurement of MBE-grown GaGdN on SiC[281].

Thermally simulated current spectroscopy (TSC) performed on Gd-doped GaN grown by MBE on SiC substrates showed a reduction in O- and Gd-related defect states upon annealing[282]. Figure 3.3 illustrates the TSC response where TSC-1 is attributed to oxygen donors (or related states), TSC-2 to Gd-related defects, and TSC-D is a peak from signal resulting from difference of TSCs of as-grown GaGdN and annealed sample. Reduction in O- and Gd-states upon annealing reduced the magnetization in the sample.

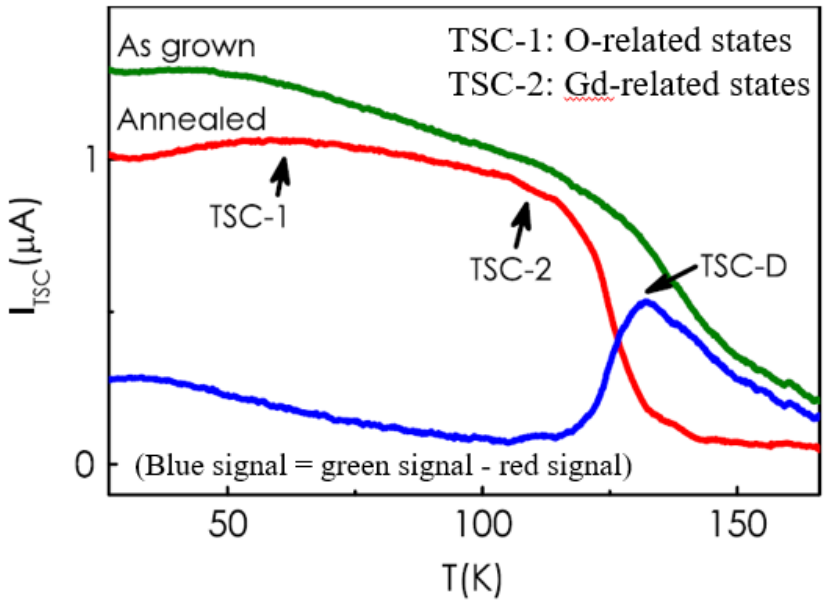

Figure 3.3 Thermally simulated current spectroscopy profile of MBE-grown GaGdN[282].

Gd does not induce ferromagnetism in GaGdN but acts as an activating element in the presence of the host GaN. This points towards the importance of the role of other possible constituent elements of GaGdN in the magnetic properties[282].

In oxygen and gadolinium-implanted GaN samples, superparamagnetism was observed[251]. GaN grown by MOCVD and implanted with Gd showed no net magnetization.

Even upon oxygen implantation, no magnetization was seen but after annealing, the oxygen and gadolinium-implanted GaN showed superparamagnetism. Annealing helps the oxygen and gadolinium to settle in the most favorable energy site in GaGdN and also removes any hydrogen if present. The annealing was performed on Gd and O- implanted GaGdN, so it is not clear if the resulting magnetic behavior was due to the relaxation of defects due to Gd- implantation or O-implantation or activation of Gd or O or other rmechanisms.

Calculations based on local spin density functional calculations with Coulomb interactions dependent on orbital show that spin-splitting takes place in the presence of oxygen-related defect states[242] . Corresponding density of states are shown in Figure 3.4.

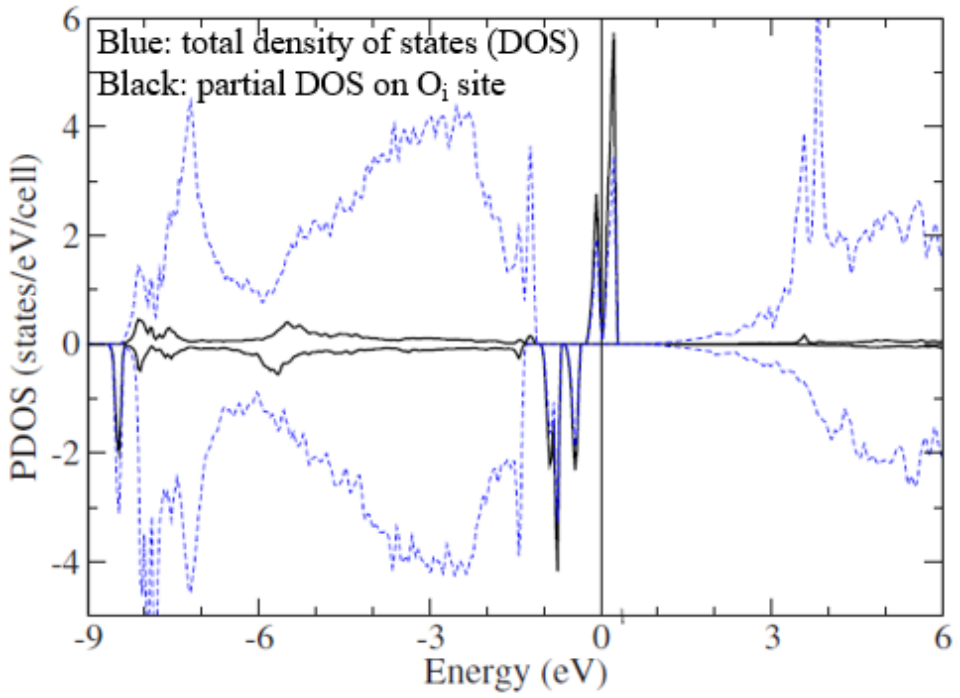

Figure 3.4 Total density of states in GaGdN and partial density of states related to oxygen interstitial site[242].

Calculations performed using a Vienna ab-initio simulation package show that distance between Gd and O interstitial could be 2.25 Å in the case of an octahedral O interstitial site and 6.67 Å in tetrahedral O interstitial site.[283]. Corresponding total and partial density of states are shown in Figure 3.5. p-orbitals related to tetrahedral O interstitial shift Fermi level above the valence band maximum, while octahedral O interstitials results in a spin-splitting and ferromagnetism.

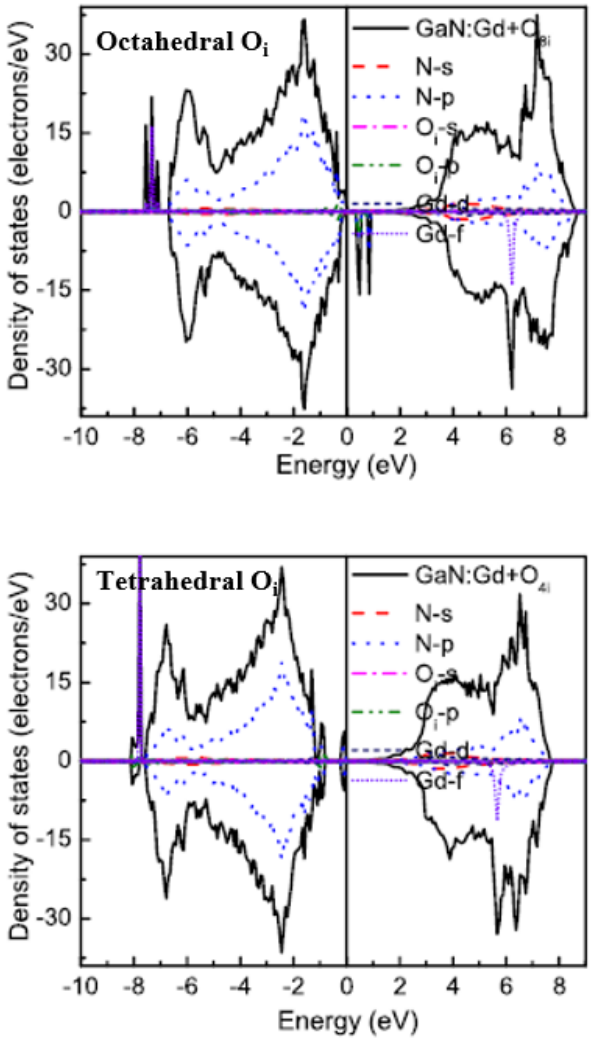

Figure 3.5 Total and partial density of states of GaGdN with O interstitial incorporation at octahedral and tetrahedral sites[283].

Spin-up states are in minority and located near and within the conduction band while spin-down states are located towards the valence band and are typically filled[242]. The spin splitting is a result of oxygen interstitials and 2p orbitals. These O-related states are localized and can results in a long-range ferromagnetic interaction with Gd atoms. O substituting N could also have lower energy by migrating to interstitial sites in GaGdN.

Density functional theory calculations based on a Vienna ab initio simulation package and local density approximations was performed to understand the role of split-interstitial and channel center sites introduced by O in GaGdN[280]. Band structure of O-related split-interstitial sites in GaGdN is shown in Figure 3.6.

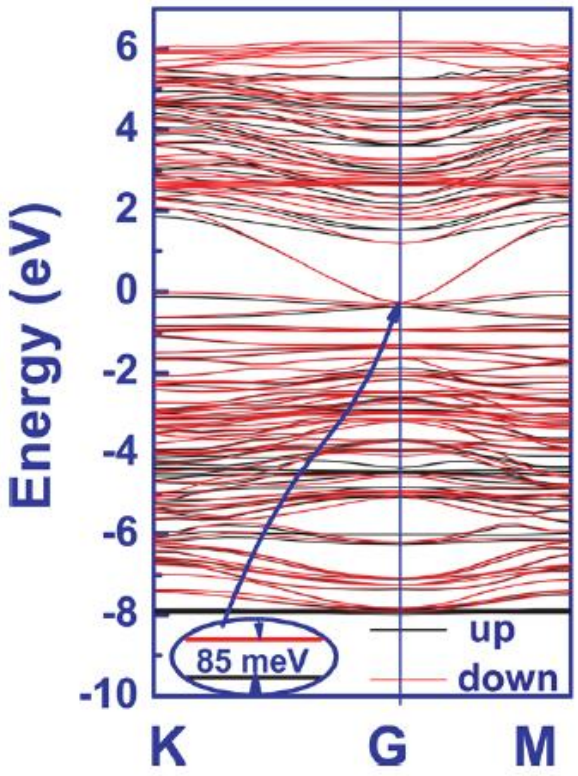

Figure 3.6 Band structural of oxygen split interstitial sites in GaGdN[280].

Partially filled f and d orbitals of Gd are far from the Fermi level and hence cannot render ferromagnetism in the absence of O; O introduces localized energy states near the Fermi level in GaGdN and results in the ferromagnetism. 4f and 5d energy states from Gd split into threefold and singlet states and overlap with the 2p orbitals of O, as shown in Figure 3.7[280]. Formation energy of O-induced split-interstitial sites that result in a coupling of the O-2p orbitals with Gd-5d/4f orbitals is positive and about 113 meV. The relative position of O-related energy states could vary as per the 5d and 4f orbitals of Gd but could still couple to render ferromagnetism.

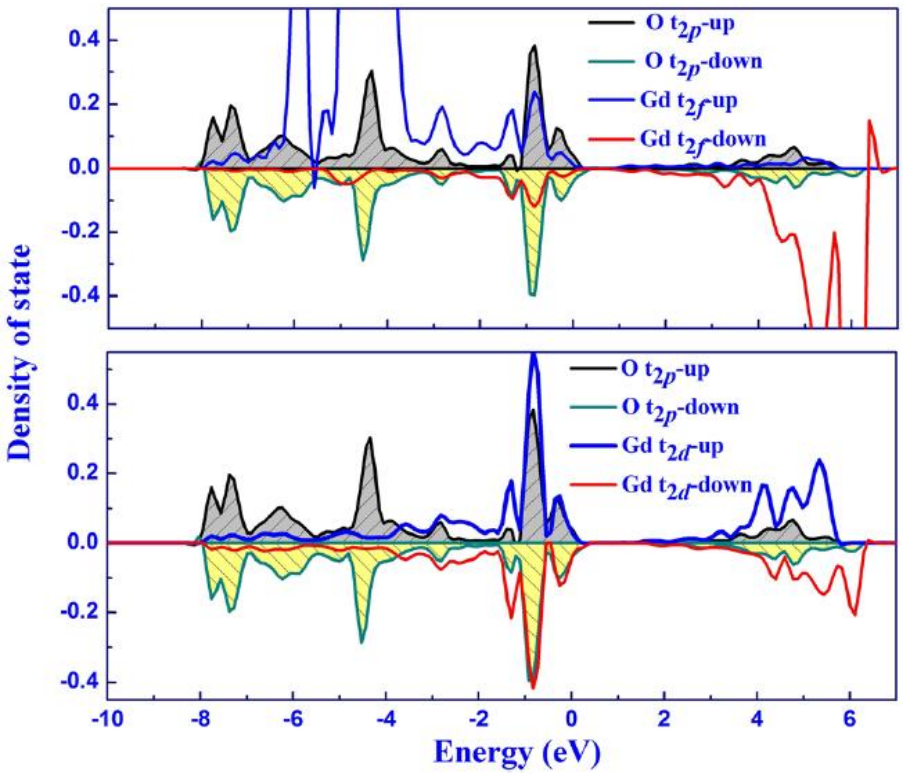

Figure 3.7 Projected density of states of 4f and 5d orbitals of Gd, and 2p orbitals of O in GaGdN[280].

Similar to oxygen, a group IV element carbon could also play a role in rendering magnetic properties in GaGdN[100,284–286]. Spin polarized density functional theory was used to understand the substitution of Ga and N sites by C in GaGdN nanowires, as seen in Figure 3.8[250]. Ferromagnetism could occur only when C and Gd atoms are close to each other. Curie temperature (T_C) of 436.8K was calculated for configuration (a). A band structure of GaGdN doped with C is shown in Figure 3.8 wherein localized energy states are introduced by C within the bandgap of GaGdN[250].

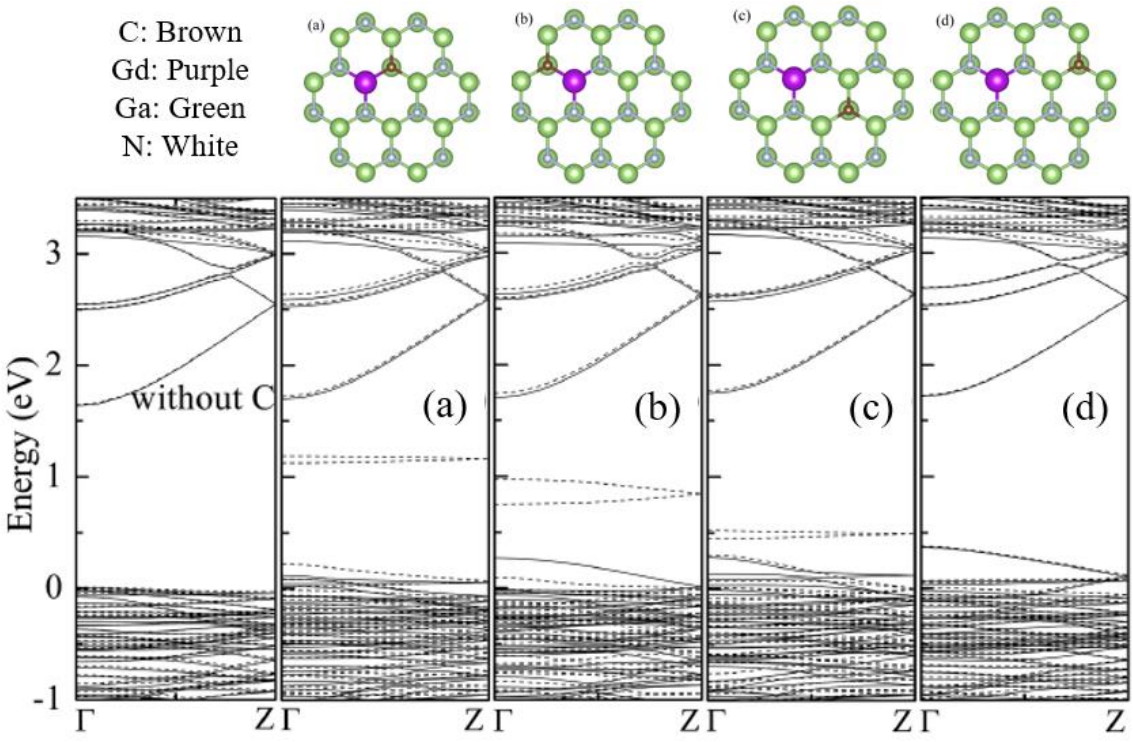

Figure 3.8 Configuration of C-doped GaGdN nanostructures with different locations of C and Gd atoms in GaGdN, and related band structure (Continuous lines show spin-up and dashed lines show spin-down energy states)[250].

A p-d exchange between C and Gd atoms along with Ga vacancy could be responsible for the theoretical ferromagnetism in C-doped GaGdN as per density functional theory based on a full-potential linear augmented plane wave method[246], and illustrated in Figure 3.9.

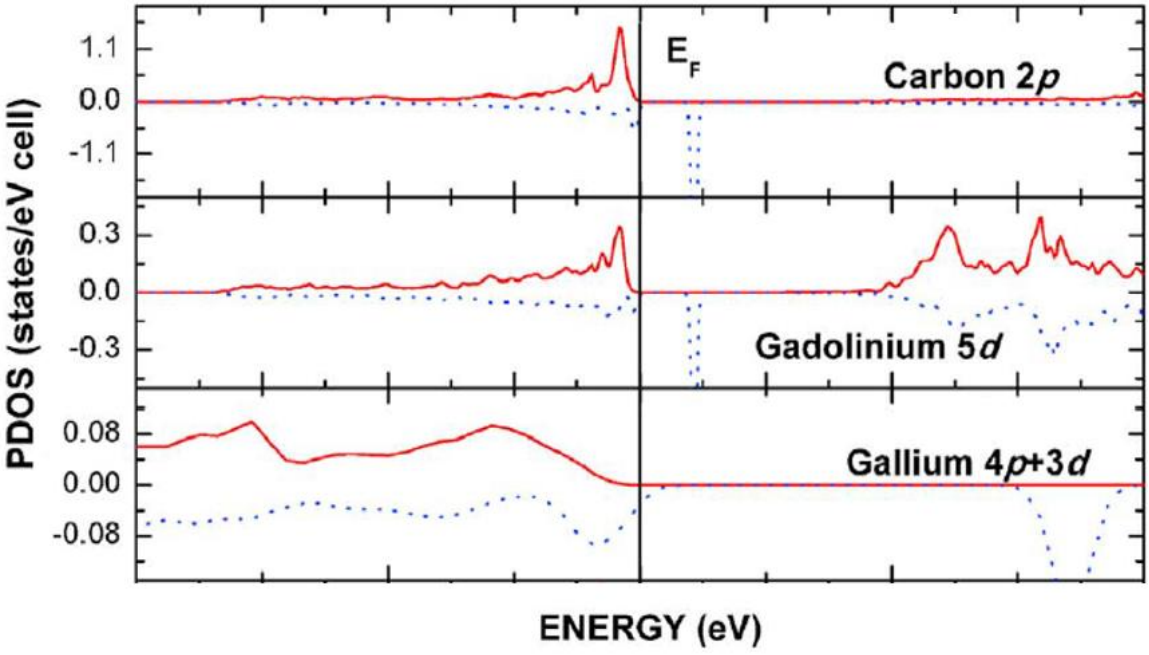

Figure 3.9 Density of states of C, Gd, and Ga[246].

Oxygen and carbon could have a role in the magnetic properties of Gd-doped GaN. As seen in Figure 3.1, RT ferromagnetism and Anomalous Hall Effect based on intrinsic mechanisms is observed in MOCVD-grown GaGdN. It is imperative to understand the role of O and C in order to control and manipulate spin-related properties of GaGdN. This is investigated by doping MOCVD-grown GaGdN from Cp_3Gd that initially does not contain any oxygen, with oxygen or carbon.

3.2. ION IMPLANTATION OF OXYGEN AND CARBON IN GaGdN

Ion implantation is an effective technique to controllable introduce O or C in GaGdN from Cp_3Gd that does not contain oxygen or carbon as-grown[251,287–293]. It involves bombardment of solid substrates with ions of intended dopants. Table 3.1 reviews some of the existing works about implantation of O (or similar) in GaN based materials.

Table 3.1 Literature review of O implantation in GaN based materials[251,287–292].

Growth Technique	Dose (cm^{-2})	Energy (keV)	Temp (K)	Depth profile (nm)	Final O conc	Anneal temp (^0C)	Anneal duration	Anneal envt
MOCVD	5e+14	70		100		1050	10-15 s	N_2
(Halogen CVD)	1e+16	80	RT			900	0.5-1 h	Ammonia
MBE	1e+15	40				650	1 h	
MOVPE	5e13 - 5e16	600 (60^0)	190-210			300-970	20 mins each step	liquid N_2
MOCVD (GaGdN)	6.7e+12	40		50-100	1e+18	1000	10 mins	
Hydride VPE	2e+17	80	RT ($2e^{-4}$ Pa)	17-165				
Unspecified	5e14 to 4e16	150 to 50	RT	200	3e19 to 7e21			

Key parameters in the implantation process are the dopant dose and energy. These parameters determine the depth and concentration of the dopant. As implantation could cause lattice-defects due to the ions' bombardment, a post-implantation annealing is typically done to recover the lattice structure as well as to activate the dopant as necessary, as listed in Table 3.1.

Dopants' dose is calculated so that optimum O or C is implanted in GaGdN to potentially render magnetic properties. As O content of 1-2% was observed in GaGdN grown from $(TMHD)_3Gd$ precursor that were ferromagnetic and showed Anomalous Hall Effect, O or C content of 1-2% is intended to be implanted in GaGdN from Cp_3Gd which do not originally contain any O or C. The distribution of implanted dopants is typically Gaussian, and there is a trade-off between the target concentration and the depth at which the target concentration is achieved. Hence, a thickness such as sufficient doped area is available for thin film measurement such as Anomalous Hall Effect, structural measurement such as X-ray diffraction and other similar measurement should be chosen. Two approaches for implantation dose calculations were used – (a) based on GaGdN unit cell volume, and (b) based on Avogadro number. Both calculations are elaborated below and result in a dose requirement of ~2×10^{16} cm^{-2}.

a. O or C dose calculations based on GaGdN unit cell volume:

- Thickness of GaGdN where O or C is most implanted (t): 200 nm
- Unit cell volume of GaN (V_{unit_cell}) : 46.6×10^{-24} cm^3
- Number of unit cells in 1 cm^2 (n_{unit_cell}) = $\frac{1}{V_{unit_cell}} \times t$ = ~4.3×10^{17} cm^{-2}
- A unit cell contains 2 Ga and 2 N atoms
- Number of Ga atoms (n_{Ga}) = N atoms (n_N) = $2 \times n_{unit_cell}$ = 8.6×10^{17} cm^{-2}

- Dose for 1 - 2% O or C in $Ga_{100-x}Gd_xN$ = 1–2% of ($n_{Ga} + n_N$) = ~2 x 10^{16} cm^{-2}

b. O or C dose calculations based on Avogadro number:

- Thickness of GaGdN where O or C is most implanted (t): 200 nm
- Mass of 200 nm thick GaGdN with area of 1 cm^2

  m = density of GaN x Volume = 6.15 $g.cm^{-3}$ x t x 1 cm^2 = 1.23 x 10^{-4} g
- Molecular weight of $Ga_{100-x}Gd_xN \cong GaN \cong 84$ g (x from 0% to 4%)
- 84 g of GaN contains 6.022 x 10^{23} atoms of GaN
- Number of GaN atoms in m gm per cm^2 = $\frac{m \times 6.022 \times 1023}{84}$ = n = 8.8 x 10^{17} cm^{-2}
- Dose for 1 - 2% O or C in $Ga_{100-x}Gd_xN$ = 1-2% of n = ~2 x 10^{16} cm^{-2}

Energy of implantation for O and C were determined and the ion implantation process was emulated using stopping and range of ions in matter (SRIM) simulation and results from literature, as seen in Figure 3.10. Implantation energies for O and C for the same depth profiles are different due to differences in their atomic weights. Implantation could result in channeling effect wherein the dopants could travel through specific directions determined by the crystal structure of GaGdN or tubes/ holes in the material. This could result in changes in the depth profile, hence a tilt angel of ~7-12^o was used in the implantation process. The implantation in this work was performed at Innovion Ion Implantation Foundry.

3.3. STRUCTURAL STUDY OF OXYGEN AND CARBON-IMPLANTED GADOLINIUM-DOPED GALLIUM NITRIDE

Structural characterization of O and C-implanted GaGdN was performed using X-ray diffraction technique and compared with as-grown GaGdN from Cp_3Gd source. Most

peaks in O- and C-implanted GaGdN overlap with as-grown GaGdN as seen in Figure 3.11. GaN-related (002), (004), and (006) directions still define the primary crystal orientations in the material. A GaN (001) peak is observed at a 2θ of ~17°. Other peaks arise from the c-plane sapphire substrate. The overall crystal structure of GaGdN from Cp_3Gd is maintained and comparable to as-grown GaGdN after O- or C-implantation. Peak broadening at lower intensities are identified in the diffraction peaks after O- and C-implantation, which confirm the incorporation of O and C in the lattice structure of GaGdN. The broadening increases as the crystal planes' size reduce from (002) to (006).

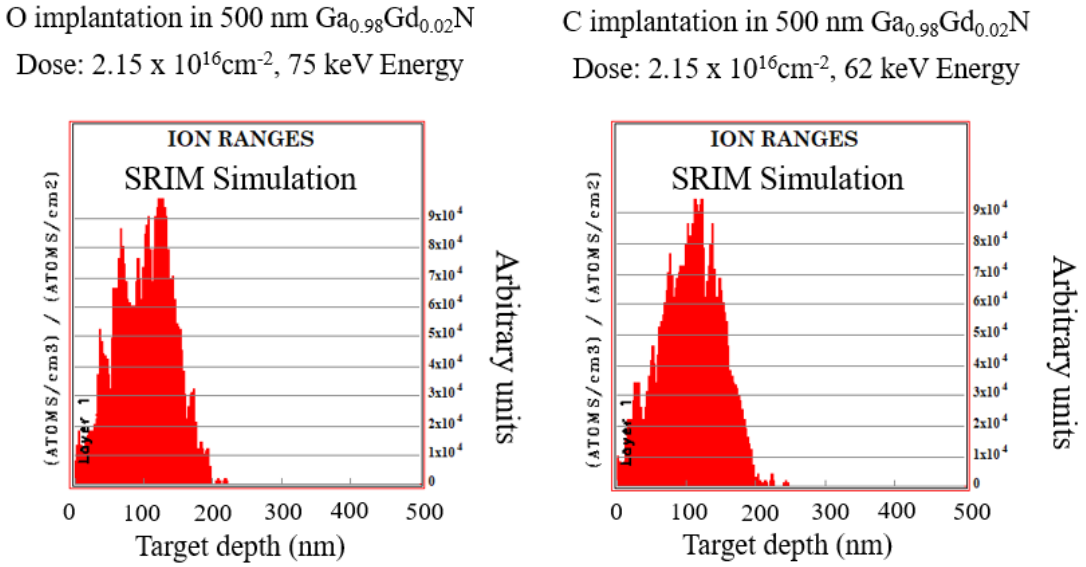

Figure 3.10 Stopping and range of ions in matter (SRIM) simulation of implantation parameters of O and C in GaGdN.

X-ray diffraction results of the (002) peaks are illustrated in Figure 3.12. The crystal quality of O- and C-implanted GaGdN is comparable to as-grown GaGdN from Cp_3Gd source. Both implanted GaGdN show peak shift to higher diffraction angles as a result of

implantation. The peak shift is larger in O-implanted GaGdN, as O has a smaller covalent radius than N and C, and could substitute N resulting in a small lattice size. However, C has a larger covalent radius than both O and N. A peak shift in O- and C-implanted GaGdN towards higher diffraction angles with the largest shift in O-implanted GaGdN implies that O and C could occupy other sites such as interstitials along with substitutional sites in GaGdN upon implantation.

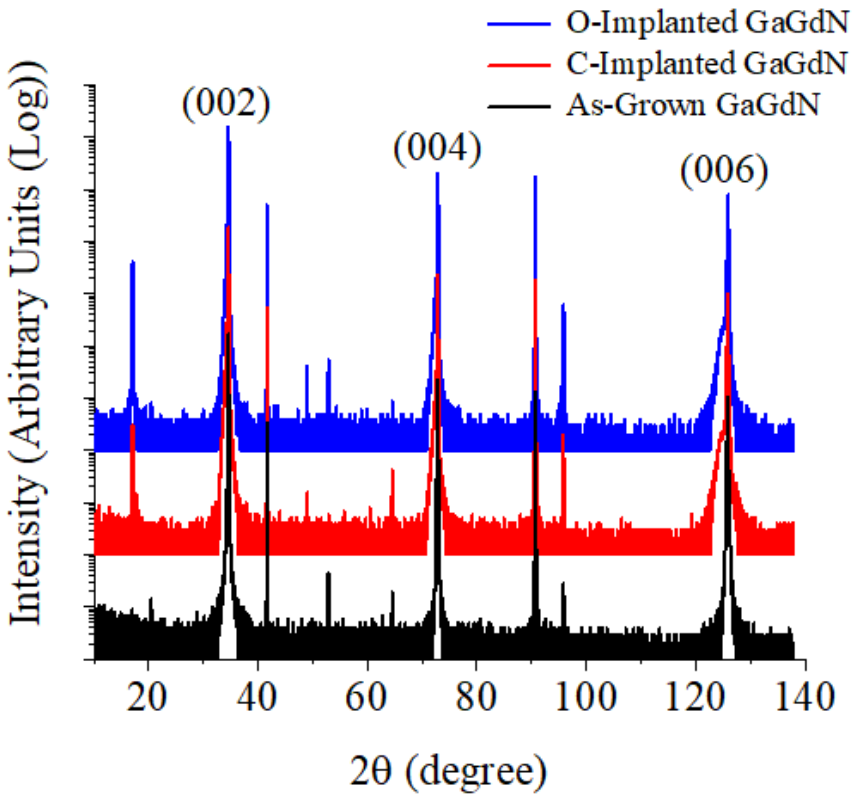

Figure 3.11 Long range 2θ-ω scans of O- and C-implanted GaGdN and comparison with as-grown GaGdN from Cp_3Gd source.

Table 3.2 shows a summary of the X-ray diffraction of measurement of O- and C-implanted GaGdN samples. The trend of peak shifts is similar as (002) for (004) and (006)

crystal orientations. The FWHM of O- and C-implanted samples is comparable with as-grown samples. O- and C- implantation did not cause any alteration in the crystal properties or quality of GaGdN, even though are slight signs of implantation-induced defects as per peak broadening at lower intensities as seen in the plots with X-ray diffraction intensities on a log scale.

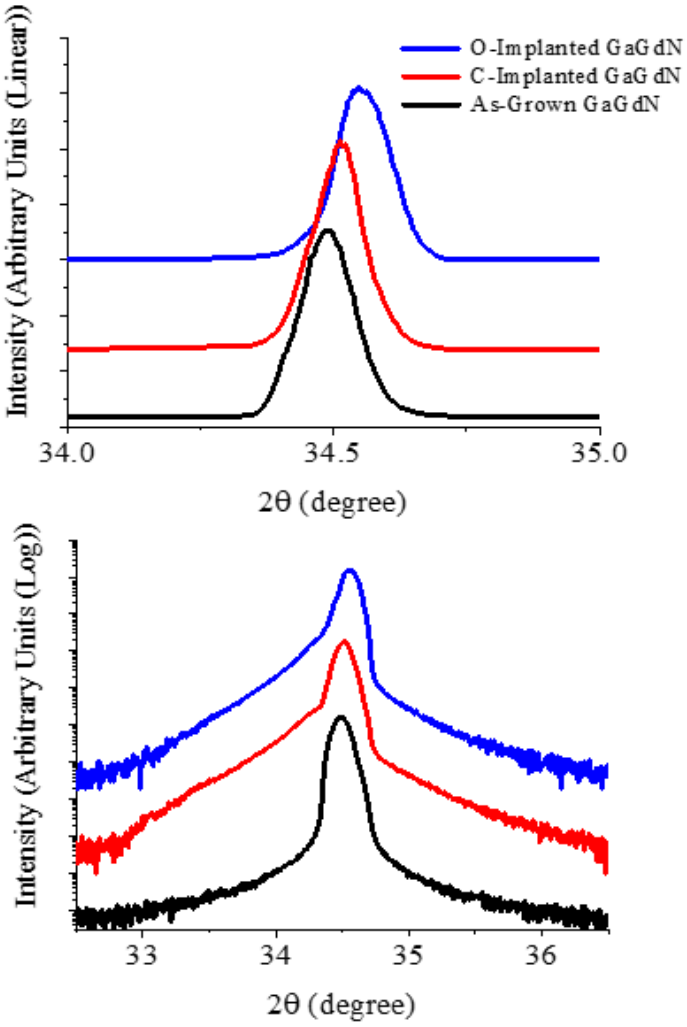

Figure 3.12 X-ray diffraction 2θ-ω scans of (002) peaks of O- and C-implanted, and as-grown GaGdN with vertical axes on linear and log scales.

Table 3.2 Summary of X-ray diffraction results of O- and C-implanted GaGdN.

Sample #	(002) 2θ peak position (°)	(002) peak FWHM (arcsec)	(004) 2θ peak position (°)	(004) peak FWHM (arcsec)	(006) 2θ peak position (°)	(006) peak FWHM (arcsec)
GaGdN as-grown (Cp_3Gd)	34.49	453	72.78	417	125.85	520
GaGdN:O as-implanted	34.55	432	72.86	408	128.91	545
GaGdN:C as-implanted	34.51	435	72.81	389	125.87	508

3.4. ANOMALOUS HALL EFFECT CHARACTERIZATION OF OXYGEN AND CARBON-IMPLANTED GADOLINIUM-DOPED GALLIUM NITRIDE

Magnetic characterization of O- and C-implanted GaGdN was performed using Anomalous Hall Effect (AHE). AHE is an effective technique to understand the spin-related properties of thin films and related mechanisms. Effects from defects, interfaces, and substrates are significantly suppressed so that the mechanism for spin-related properties of thin films could be studied.

As-grown GaGdN sample from Cp_3Gd source that does not contain oxygen or carbon showed Ordinary Hall Effect (OHE) as seen in Figure 3.13. No signs of spin-related characteristics are seen even though the sample contains Gd.

Hall Effect characterization of O-implanted GaGdN is shown in Figure 3.14. Anomaly is observed at lower magnetic fields starting at ~200 Gauss. Oxygen implantation resulted in AHE, and a slightly noisy signal as compared to as-grown GaGdN without O. GaGdN:O has a higher resistivity and a high Hall coefficient. Presence of AHE in

GaGdN:O points to the existence of O interstitials in GaGdN:O which is also apparent from XRD results. GaGdN:O has a lower carrier concentration of $9.5x10^{17}$ cm^{-3} as compared to as-grown GaGdN with $3.7x10^{18}$ cm^{-3}, which implies introduction of acceptor type energy bands with O incorporation in GaGdN. Observed results are consistent with density functional theory calculations that acceptor type oxygen interstitials could render spin-related properties in GaGdN.

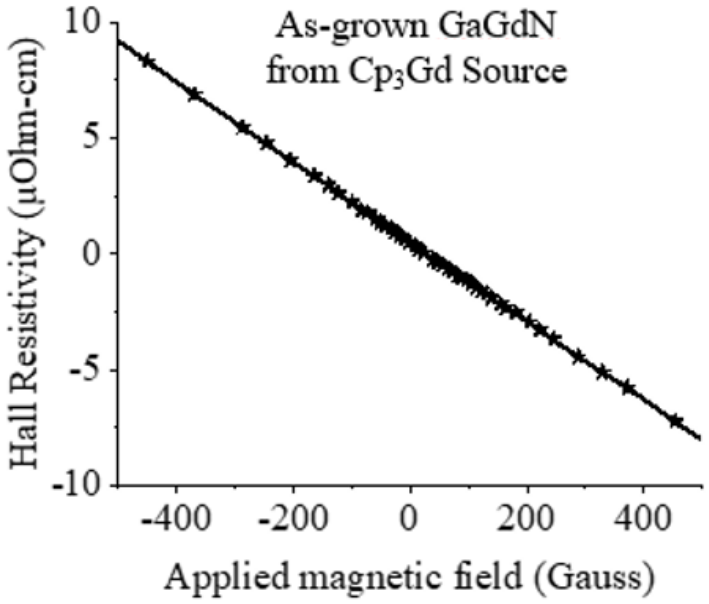

Figure 3.13 Hall Effect analysis of as-grown GaGdN from Cp_3Gd source.

Anomalous Hall Effect was observed in C-implanted GaGdN as shown in Figure 3.15. The Hall resistivity shows anomalies at lower fields starting at ~500 Gauss, which confirm the existence of spin-related carriers in the material and could be related to their stability or fluctuations. GaGdN:C showed a higher resistivity and lower carrier concentration as compared to as-grown GaGdN. GaGdN:C has a lesser resistivity and

higher carrier density than GaGdN:O. Mobility of GaGdN:O and GaGdN:C was higher in implanted GaGdN. The electrical characterization and Hall Effect-related results of as-implanted GaGdN are shown in Table 3.3.

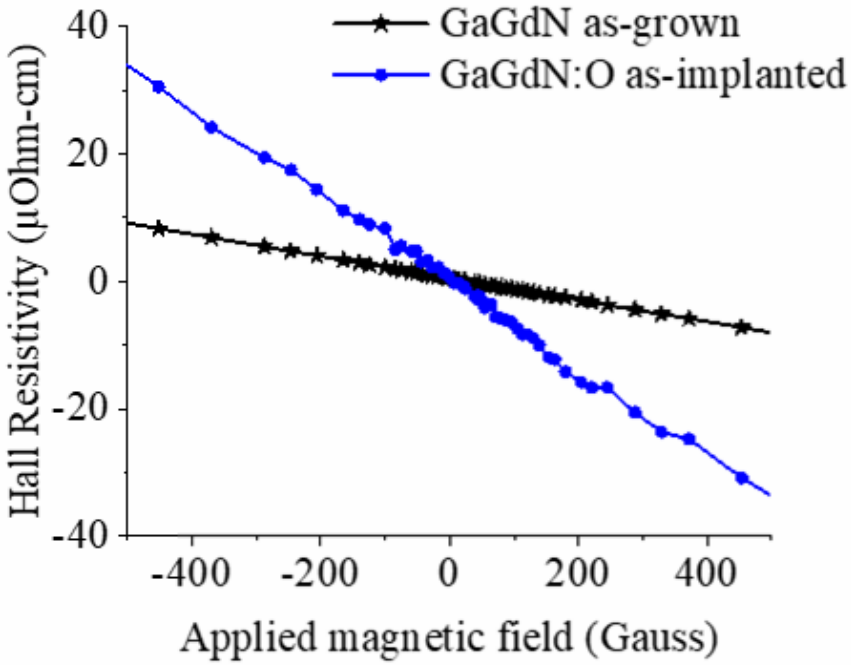

Figure 3.14 Anomalous Hall Effect in O-implanted GaGdN from Cp_3Gd source.

A larger peak shift in XRD measurement, which could be associated with a combination of substitutional and interstitial sites occupied by the dopant corresponds in a higher resistivity as per electrical characterization. Oxygen at substitutional sites acts as a donor, but the carrier concentration in GaGdN reduced upon O-doping. Hence, the proportion of interstitial O compared to substitutional O is more in GaGdN:O which is in coherence with density functional theory calculations that the formation energy of O interstitials could be lesser or comparable to O substitutional sites[280,283].

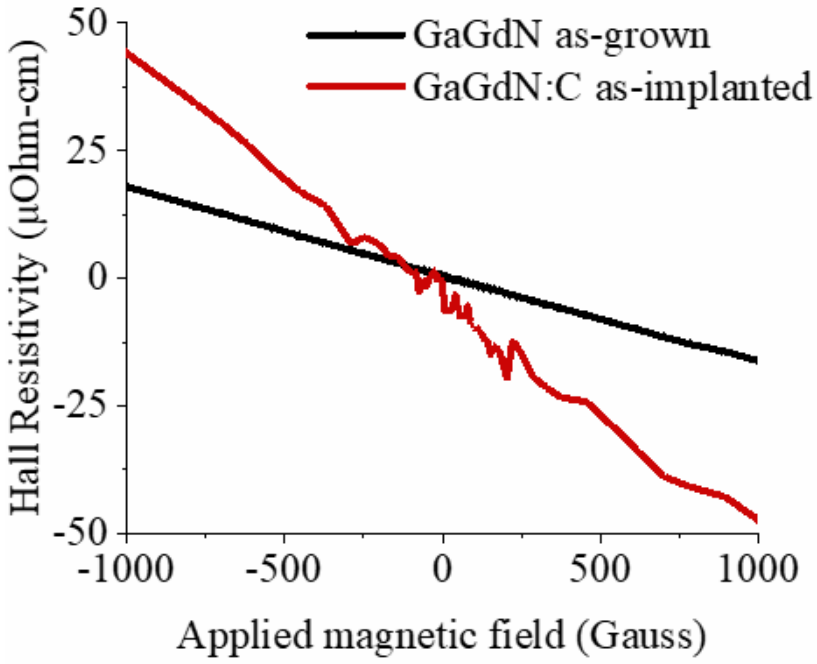

Figure 3.15 Anomalous Hall Effect in C-implanted GaGdN from Cp_3Gd source.

Table 3.3 Electrical and Hall Effect characterization results of O- and C-implanted GaGdN from Cp_3Gd source

Sample	Resistivity (mΩ-cm)	Density (cm^{-3})	Mobility ($cm^2V^{-1}s^{-1}$)	Hall coefficient (cm^3C^{-1})	Comments
GaGdN (Cp_3Gd)	8	3.7×10^{18}	213	1.7	OHE
GaGdN:O as-implanted	22	9.5×10^{17}	298	6.6	AHE
GaGdN:C as-implanted	17	1.4×10^{18}	262	4.5	AHE

Similar results are observed in GaGdN:C and energy states introduced by C-doping resulted in AHE. C plays the role of an acceptor if it substitutes N and would result in an increase in lattice size based on the covalent radii of C and N. X-ray diffraction results

show an overall reduction in lattice size of GaGdN:C with respect to as-grown GaGdN. Even though C reduces the n-type carrier density of GaGdN, the AHE could primarily be a result of defects or deep energy states introduced by C within the band gap of GaGdN, and secondarily substitutional sites occupied by C in GaGdN.

3.5. EFFECT OF ANNEALING ON OXYGEN AND CARBON-IMPLANTED GADOLINIUM-DOPED GALLIUM NITRIDE

Effect of annealing on the structural and spin properties of O- and C-implanted GaGdN is discussed.

3.5.1. Annealing O- and C-implanted GaGdN. Ion implantation of O and C results in incorporation of the dopants in GaGdN. However, implantation was performed at RT, and O and C atoms could migrate to more energetically favorable positions in GaGdN by applying a high temperature and suitable environment. Also, implantation results in defects as also evident from slight XRD peak broadening at lower intensities in implanted GaGdN. Annealing could help to activate or migrate O and C in GaGdN and also recover from implantation-induced defects.

Temperature and time in an optimum range are required for effective annealing. A lower temperature or time could result in insufficient activation of atoms in the material, while higher temperature or time could result in decomposition and formation of secondary phases[294–297]. A temperature ~2/3rd of the melting point is typically required for complete recovery of crystal structure. Considering a melting point of 2500-2800 ^{o}C for GaN based materials of, a temperature of 1600-1800 ^{o}C would be suitable for recovering GaGdN from implantation-related defects[294]. However, GaGdN could decompose at such a high

temperature and undergo a change in properties. An equivalent temperature with longer annealing time could be scaled using Arrhenius equation as stated in Equation 10.

$$t_2 = t_1 e^{\frac{E_a}{R}\left(\frac{1}{T_2} - \frac{1}{T_1}\right)} \tag{12}$$

where, T_1 and t_1 are reference temperature and times respectively (T_1 and t_1 are considered as 1800 ^oC and 15 sec respectively), T_2 is the applied annealing temperature, t_2 is activation time with a temperature of T_2, E_a is activation energy of dopant (113 meV for O in GaGdN[280]), and R is the Universal gas constant (86.16 μeV). Curve corresponding to Arrehenius equation is plotted in Figure 3.16. Literature review regarding of O-implanted GaN is provided in Table 3.1. For MOCVD-grown GaN, temperatures of 800-900 ^oC for 4-5 mins have resulted in successful activation of dopants.

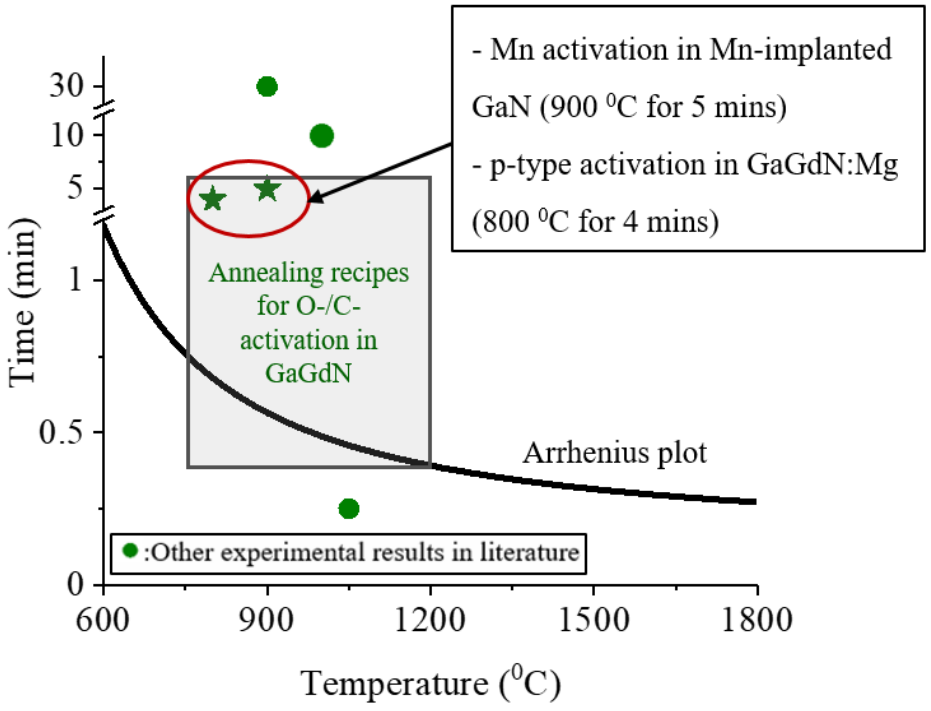

Figure 3.16 Annealing time and temperature for O- and C-implanted GaGdN.

Taking into account previous results of MOCVD-grown GaN, literature review, and Arrhenius relation, O- and C-implanted GaGdN were rapid thermally annealed at 1200 ^{o}C for 2 mins in N_2 environment. In order to further avoid the decomposition of GaN, a capping layer of un-doped GaN was placed on the samples during annealing in N_2 ambient to prevent loss of nitrogen atoms and was removed after annealing.

3.5.2. Structural Study of Annealed O- and C-implanted GaGdN. Long range XRD characterization of annealed O- and C-implanted GaGdN is shown in Figure 3.17. Overall crystal structure stays similar and no additional phases are observed after annealing.

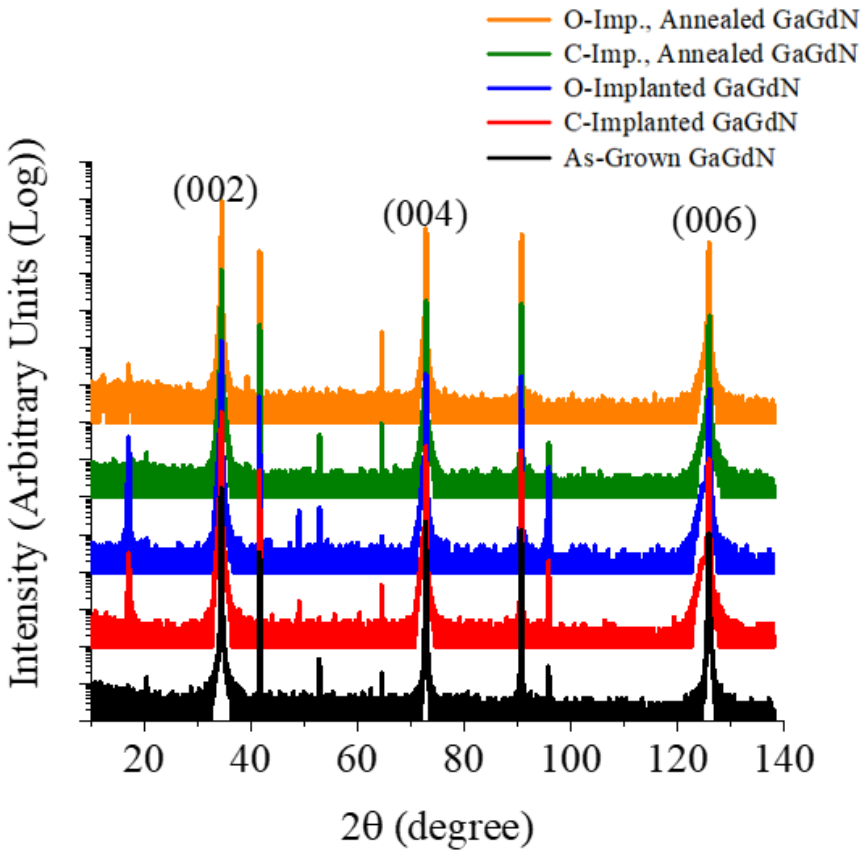

Figure 3.17 X-ray diffraction 2θ-ω scans of annealed O- and C-implanted GaGdN and their comparison with as-implanted GaGdN and as-grown GaGdN from Cp_3Gd source.

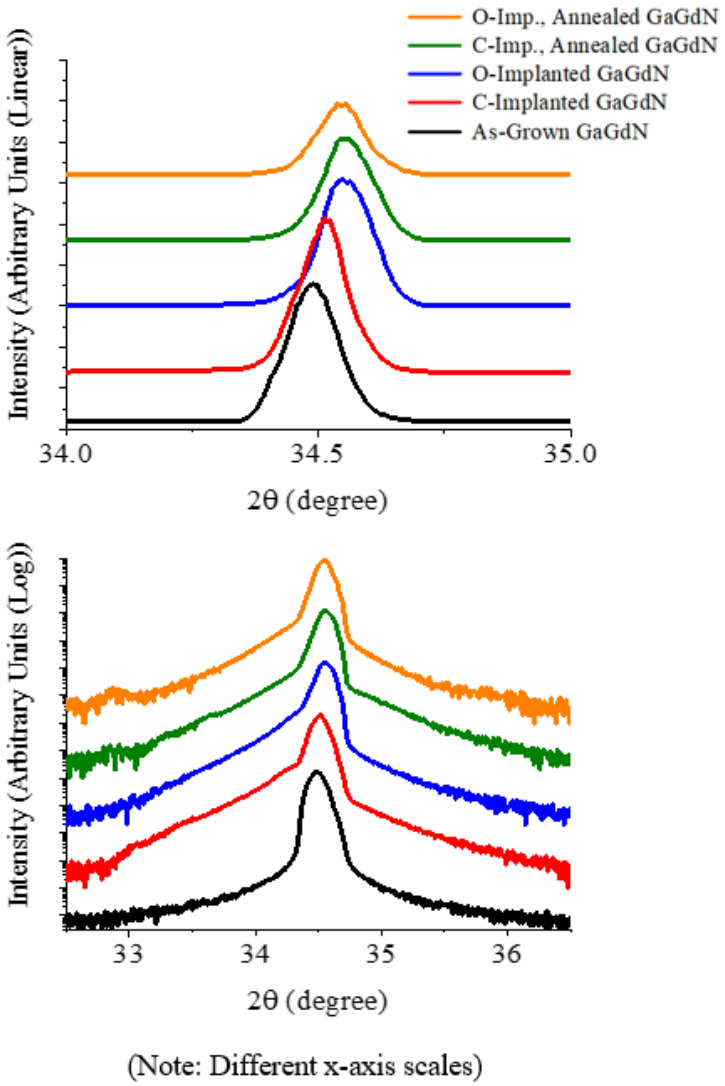

Figure 3.18 X-ray diffraction 2θ-ω scans of (002) peaks of annealed O- and C-implanted GaGdN and their comparison with as-implanted GaGdN and as-grown GaGdN from Cp_3Gd source with vertical axes on linear and log scales.

Figure 3.18 shows the (002) peak of annealed, implanted, and as-grown GaGdN from Cp_3Gd. Peak position of O-implanted GaGdN very slightly shifted to lower diffraction angles in (002), (004) and (006) crystal orientations, while C-implanted GaGdN has a noticeable peak shift towards higher diffractions angles. These peak shifts confirm that O and C do not occupy dominantly substitutional sites because O has a smaller

covalent radius than N and C has a larger covalent radius, which would result in a peak shift towards higher diffraction angles in GaGdN:O and lower diffraction angles in GaGdN:C, but complementary results are seen. O and C both likely primarily exists as interstitial sites in GaGdN. Details of (002), (004), and (006) peaks are mentioned in Table 3.4. The FWHM of O-implanted GaGdN reduces upon annealing which points towards a better incorporation of O in GaGdN. On the other hand, FWHM of C-implanted GaGdN stayed almost consistent or increased with annealing. The effects of annealing on O- and C-implanted GaGdN are different which points towards possible differences in their respective incorporation in the GaGdN lattice structure.

Table 3.4 Summary of X-ray diffraction results of annealed and implanted O- and C-implanted GaGdN and their comparison with as-implanted GaGdN and as-grown GaGdN from Cp_3Gd source.

Sample #	(002) 2θ peak position (º)	(002) peak FWHM (arcsec)	(004) 2θ peak position (º)	(004) peak FWHM (arcsec)	(006) 2θ peak position (º)	(006) peak FWHM (arcsec)
GaGdN as-grown (Cp_3Gd)	34.49	453	72.78	417	125.85	520
GaGdN:O as-implanted	34.55	432	72.86	408	125.91	545
GaGdN:C as-implanted	34.51	435	72.81	389	125.87	508
GaGdN:O annealed	34.55	394	72.85	394	125.90	540
GaGdN:C annealed	54.55	429	72.86	406	125.91	531

3.5.3. Anomalous Hall Effect Characterization of Annealed O- and C-implanted GaGdN. Annealing could activate energetically favorable sites for O and C in GaGdN and influence the spin-related properties. AHE measurement are performed to understand these effects and discussed in this section.

In O-implanted GaGdN, annealing resulted in AHE but anomaly of the signal seems different as compared to as-implanted GaGdN, as seen in Figure 3.19. Anomalies in both the cases start down from ~200 Gauss. The resistivity significantly reduced which points towards a better incorporation of O in GaGdN upon annealing. The carrier concentration only slightly increased due to an activation of n-type defects in GaGdN. Both interstitial and substitutional O states could be activated in GaGdN upon annealing along with a reduction in implantation-related defects. This is in agreement with XRD results as the FWHM reduced and the peak position very slightly shifted to lower diffraction angles. Energy sites such as O interstitials could be stabilized by annealing resulting in AHE.

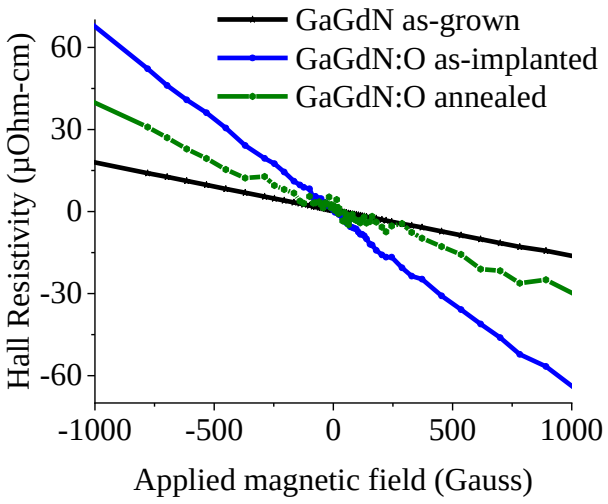

Figure 3.19 Anomalous Hall Effect in annealed and as-implanted GaGdN:O.

Similar results are seen in annealed C-implanted GaGdN; both as-implanted and annealed GaGdN:C show AHE but nature of AHE signals are different, as seen in Figure 3.20. As-implanted GaGdN showed a signal that represents spin in the material but has fluctuations. Annealing possibly resulted in a stabilization or relaxation of the spin constituents (yet have a net spin), and a smoother AHE signal.

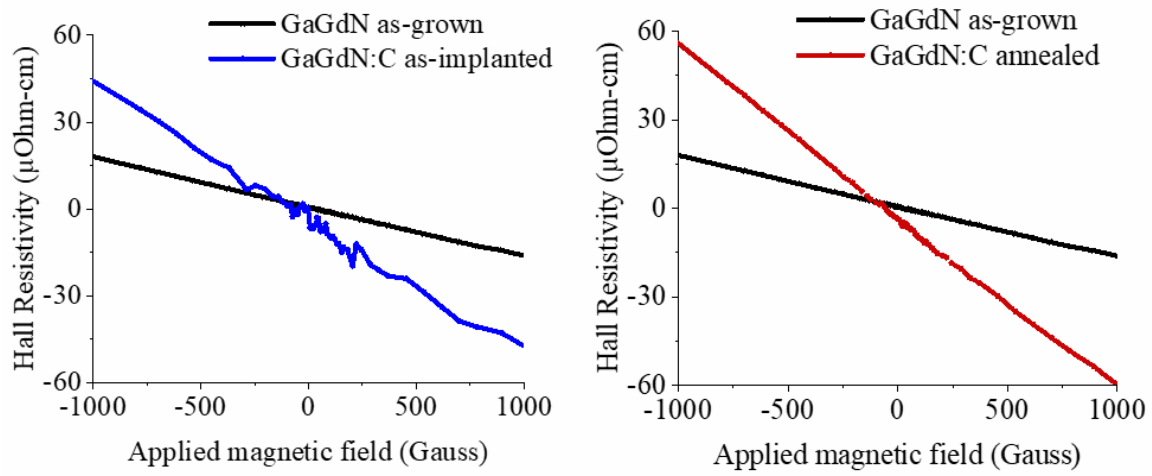

Figure 3.20 Anomalous Hall Effect in annealed and as-implanted GaGdN:C.

The resistivity of GaGdN:C increased, and carrier density reduced upon annealing. This points towards activation of additional deep acceptor energy states in GaGdN:C. As observed in the XRD results, annealing activated interstitial or related energy bands in GaGdN:C that resulted in a change in nature of the AHE signal. The change in resistivity of GaGdN:O and GaGdN:C could be corresponding to the FWHM in the XRD peaks and stability or incorporation of O and C in GaGdN. Also mobility of GaGdN:O and GaGdN:C further increased upon annealing. The net resistivity also has effects on the Hall coefficient. A summary of the Hall effect characterization is shown in Table 3.5.

Based on the XRD and AHE characterization results, as-implanted GaGdN:O showed both substitutional and interstitial O, and the O interstitial sites were stabilized upon annealing. On the other hand, as-implanted GaGdN:C has more interstitials as compared to substitutional sites in as-implanted form, and are activated more with annealing. An increase in the interstitial (or related) energy states' activation resulted in a change in the nature of signal, but still showed AHE.

Table 3.5 Summary of electrical and Hall Effect characterization annealed and implanted O- and C-implanted GaGdN and their comparison with as-implanted GaGdN and as-grown GaGdN from Cp_3Gd source.

Sample	Resistivity (mΩ-cm)	Density (cm^{-3})	Mobility ($cm^2V^{-1}s^{-1}$)	Hall coefficient (cm^3C^{-1})	Comments
GaGdN (Cp_3Gd)	8	3.7×10^{18}	213	1.7	OHE
GaGdN:O as-implanted	22	9.5×10^{17}	298	6.6	AHE
GaGdN:C as-implanted	17	1.4×10^{18}	262	4.5	AHE
GaGdN:O annealed	12	1.7×10^{18}	300	3.6	AHE
GaGdN:C annealed	19	1.1×10^{18}	300	5.75	AHE

3.6. MECHANISM FOR SPIN-RELATED PROPERTIES OF OXYGEN AND CARBON-IMPLANTED GADOLINIUM-DOPED GALLIUM NITRIDE

Anomalous Hall Effect was observed in O- and C-implanted GaGdN. As-grown GaGdN from Cp_3Gd that did not contain any O or C showed Ordinary Hall Effect. Gd

could have spin moments associated with partially filled d and f orbitals but these are activated in the presence of O or C.

O and C could occupy interstitial, substitutional and similar sites in GaGdN and proportion of interstitial sites relative to other energy states could increase with annealing. O is a donor when it substitutes N, but the carrier concentration of GaGdN:O has been lower than GaGdN. Also, C has a larger covalent radius than N, but the peak shifts in XRD measurement indicate a reduced lattice size in GaGdN:C as compared to GaGdN.

Evaluating the AHE results and reviewing density functional theory calculations of O and C incorporation in GaGdN, O or C exists in interstitial states in GaGdN, acts as acceptors, has energy states deep within the bandgap of GaGdN, and render spin characteristics in GaGdN. A p-d/f hybridization of the carriers is responsible for the AHE. This helps to clarify that O or C is essential in rendering spin-related characteristics in MOCVD-grown GaGdN.

The overall mechanism for spin-related properties in GaGdN at RT could be intrinsic and a combination of metallic conduction and variable range carrier hopping, is related with free carriers in the material, and activated in the presence of oxygen or carbon.

3.7. MECHANISM FOR SPIN IN GaGdN AT ROOM TEMPERATURE

The roles of oxygen and carbon in spin properties of GaGdN are investigated in this section. As-grown GaGdN from Cp_3Gd that did not contain O or C showed Ordinary Hall Effect. O- and C-implanted GaGdN exhibited Anomalous Hall Effect at RT. The incorporation of O and C in GaGdN and resulting signals were relatively different, but both exhibited AHE. A good crystal quality was maintained even after O- and C- incorporation

in GaGdN by implantation. X-ray diffraction peak shifts and FWHM confirmed the presence of interstitial and substitutional O- and C- sites in implanted GaGdN. Annealing stabilized the interstitial states and still exhibited AHE. O introduced more deep acceptor states in GaGdN than C but annealing activated more of C-related deep states while O-related states relaxed.

In summary, that O and C have a crucial role in rendering AHE in GaGdN at RT with a good crystal quality. A carrier-related mechanism in GaGdN and its activation by O or C shows a potential towards achieving tunable properties in GaGdN conducive for RT spintronic applications.

4. MOCVD GROWTH AND CHARACTERIZATION OF TRANSITION-METAL DOPED ZINC OXIDE

4.1. ZINC OXIDE FOR BANDGAP TUNABILITY

Zinc oxide has been one of the most versatile and multi-functional materials with applications in photovoltaics, photodetection, photocatalysis, thermoelectrics, spintronics, and biomedicine[58–68]. These functionalities of zinc oxide stem from a direct bandgap of ~3.4 eV, stability at high temperature and power, existence of an asymmetrical crystal structure, high exciton binding energy, high Seebeck coefficient, high chemical stability, broad radiation absorption spectrum, and ferromagnetism[104–106,114,118,201,204,215]. Absorption and emission characteristics in ultraviolet/blue light makes zinc oxide a good candidate for solar cells, photodetector, and light emitting diodes applications[138,150,200,298–300]. Zinc oxide is also suitable for electronics considering a tunable carrier mobility up to 200 $cm^2V^{-1}s^{-1}$ and carrier concentration up to 10^{20} cm^{-3} for n-type, and up to 50 $cm^2V^{-1}s^{-1}$ mobility and 10^{19} cm^{-3} carrier density for p-type. Along with semiconductor transport behavior, zinc oxide could be doped with transition metals in dilute amounts to induce magnetic properties for spintronic applications[57,125,131,132]. Also, low toxicity, biocompatibility, and biodegradability extends the applicability of zinc oxide to biomedical and environment-related purposes[217,219].

Zinc oxide could play various roles in photovoltaics, such as active layer, transparent conductive oxide, carrier blocking layer, interfacial or passivation layer, anti-reflection coating, or a substrate for other materials with similar crystal structure[116,301–307].

ZnO-based Schottky junction solar cells were built using MOCVD-grown ZnO as active layer[99]. Schottky junction solar cells can avoid p-doping and have a simple device structure and low cost. Figure 4.1 has insets that show the ZnO/Ag Schottky junction structure with Ti/Au ohmic contacts[200]. The current-voltage characterization exhibits diode-like rectifying behavior, and the open circuit voltage and short circuit current increase with an increase in the illumination intensities of solux lamp, confirming the photovoltaic performance. ZnO can also be used as a passivation layer component in multi-junction solar cells[191,195]. Passivation layers can reduce surface recombination, interface-related traps and dangling bonds, resulting in a better photovoltaic performance.

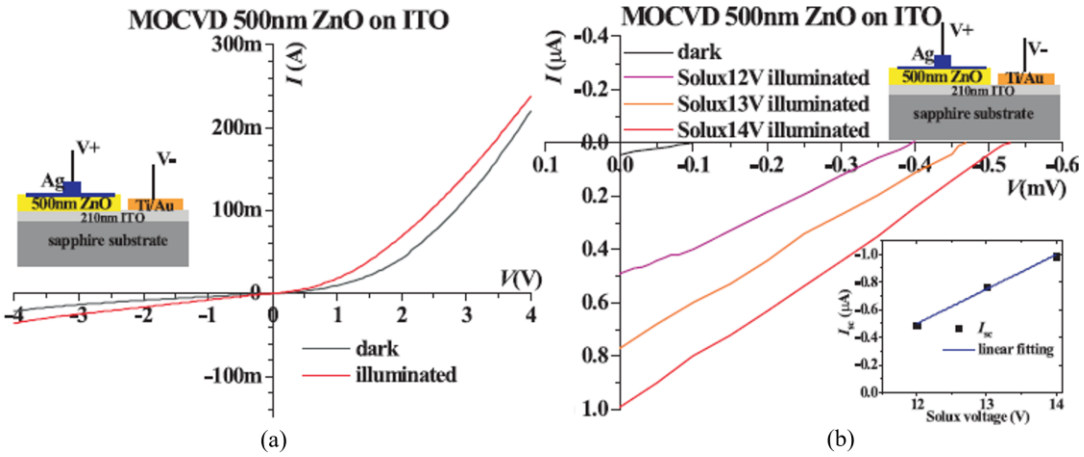

Figure 4.1 Current-voltage characterization of ZnO/Ag Schottky solar cell at different axes limits. Insets show device structures, and trend of short circuit current with solux voltages[200].

Power conversion efficiency of solar cells could be improved by using multi-junction solar cells over single-junction, with different bandgaps configured in a tandem structure. A heterojunction solar cell structure consisting of zinc oxide and silicon active layers, as shown in Figure 4.2 was theoretically studied[308]. Input characteristics of zinc

oxide for the simulation were experimentally acquired using MOCVD-grown ZnO. The refractive index of ZnO matches with anti-reflection requirement for silicon solar cells, so zinc oxide acts as an anti-reflection layer too. A reference external quantum efficiency measured for 0.5 µm thick ZnO. Short circuit current and the open circuit voltage depend on the thickness of ZnO, as shown in Figure 4.2. Optimized thickness and optical parameters of ZnO could be used in the development of multi-junction solar cells.

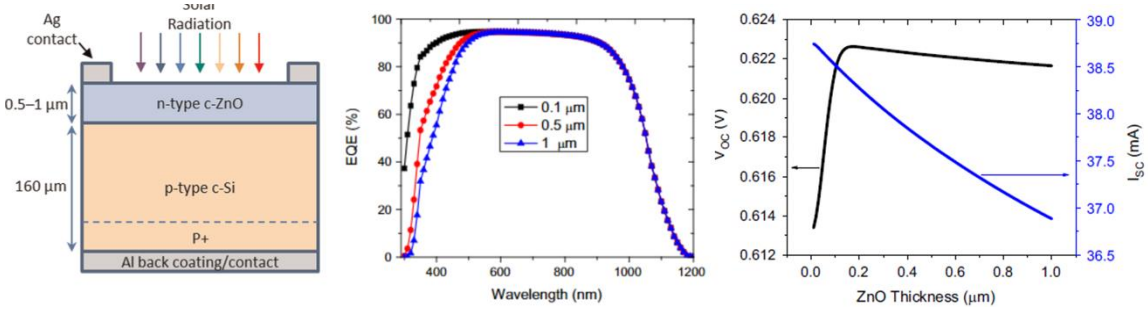

Figure 4.2 ZnO based tandem solar cell – (a) Schematic of a multi-junction solar cell with zinc oxide and silicon active layers, (b) External quantum efficiency of solar cells with varying ZnO thickness, (c) Current-voltage simulation result of ZnO/Si solar cell as a function of ZnO thickness[308].

Tunable bandgaps in the same material could reduce heterostructure-related interface traps or defects and enhance device performance. Such tunability in the optical absorption properties of zinc oxide could be achieved by doping it with transition metals such as nickel and manganese[299,309–316]. The resulting bandgap and related properties of transition metal-doped zinc oxide could depend on the growth techniques used[317–322]. Figure 4.3 shows a summary of growth techniques that could be used for thin film deposition for typical oxide materials[119,126,128,137,149,200,323,324].

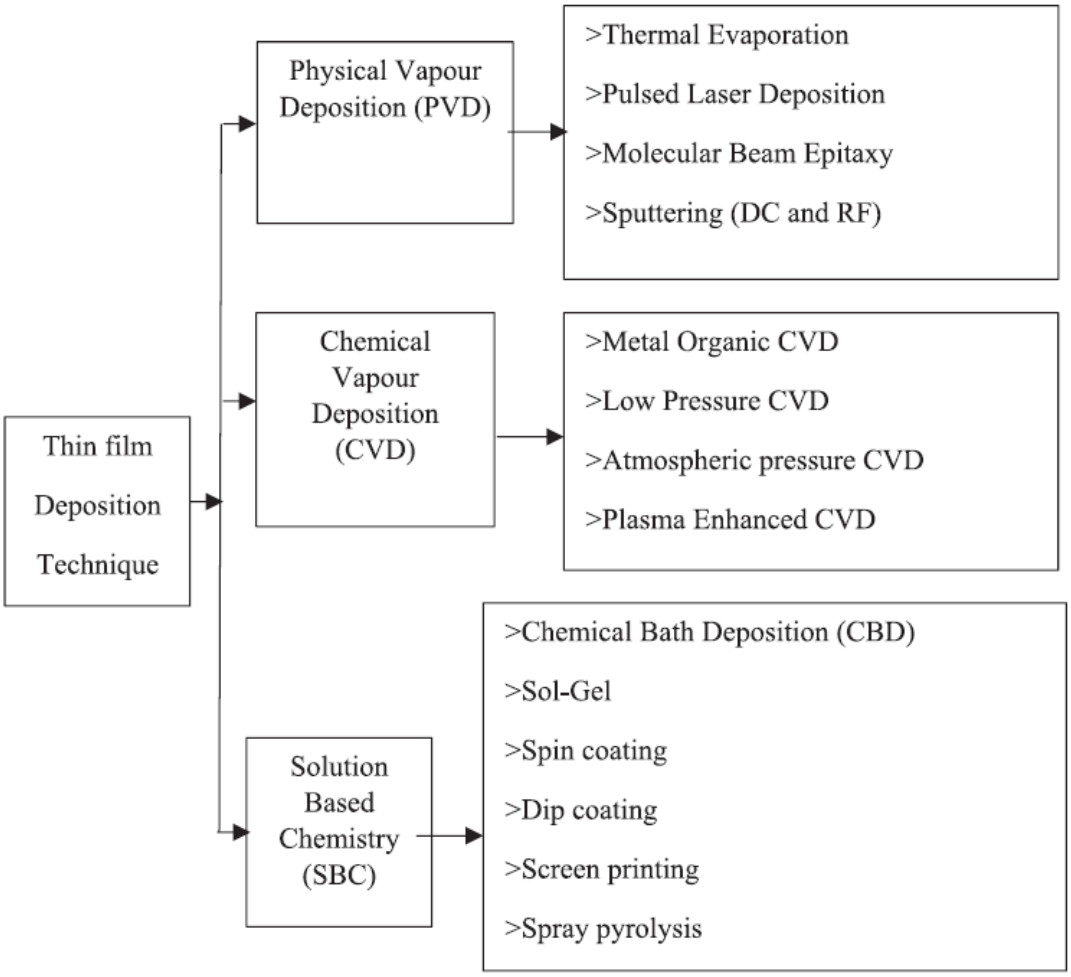

Figure 4.3 Summary of common thin film deposition techniques[325].

Nickel-doped zinc oxide grown by DC/RF magnetron sputtering showed a bandedge shift from 3.2 eV down to 1.4 eV with Ni doping up to 7%, as seen in Figure 4.4[326]. However, transmittance reduced with Ni doping, which could be due to lattice defects introduced by sputtering.

For nickel-doped zinc oxide, different results are reported depending on the material growth and processing. Zinc nickel oxide grown by spray pyrolysis deposition on quartz substrates showed a reduction in bandgap with Ni content up to 10%; however,

another work using a similar growth method observed an initial decrease and then an increase in the band edge with added Ni content up to 4%[312,316,327]. Bandgap reduction from 3.22 eV to 3.11 eV was seen in zinc oxide doped with 10% Ni and grown by precipitation method[328]. Ni-doped ZnO nanoplatelets synthesized by chemical reactions of aqueous solutions of Zn, Ni, and O precursors in polymer micelles also resulted in a red shift from 3.25 eV to 3.19 eV with 10% Ni[314]. On the other hand, zinc nickel oxide nanoparticles prepared by sol-gel technique showed an increase in band edge from 3.29 eV to 3.32 eV with Ni content up to 6% as shown in Figure 4.5[329]. Ni-doped ZnO nanoparticles grown by chemical solution deposition method showed a consistent near band edge of 3.22 eV with Ni doping, but mid absorption bands in the visible region were observed[313].

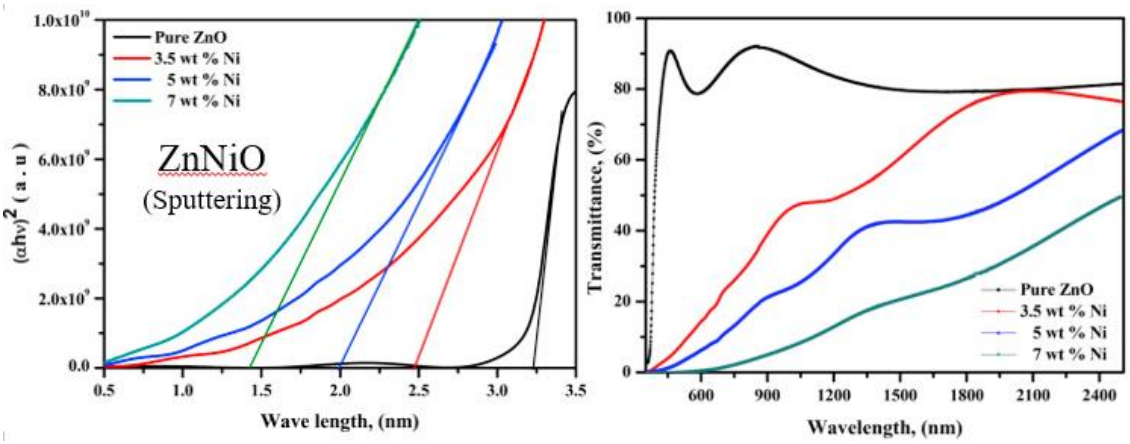

Figure 4.4 Bandgap and transmittance of un-doped and Ni-doped ZnO thin films grown by a DC/RF magnetron sputtering method[326].

Zinc oxide doped with manganese also has a potential for bandgap tunability[330–332]. As seen in Figure 4.6, transition metals such as Mn could exist different ionic states in zinc oxide and result in variations in the bandgap. Zinc manganese oxide nanoparticles grown

by a sol-gel like technique showed a bandgap reduction from 3.34 eV to 3.22 eV with 5% Mn. In another study based on sol-gel technique, Mn- and Ni-doped ZnO nanopowders also exhibited a reduction in bandgap but the reflectance reduced significantly with doping, as shown in Figure 4.7.

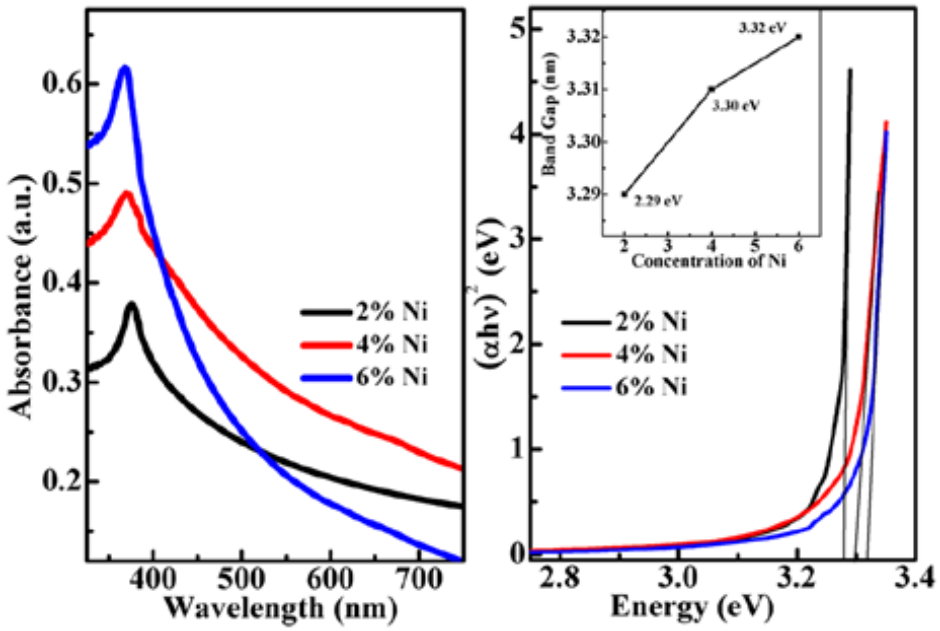

Figure 4.5 Absorption spectra of Ni-doped zinc oxide with different nickel content[329].

Bandgap tunability could add to optical and magnetic functionalities of zinc oxide and result in better energy harvesting / electronic devices[329,333–336]. Transition-metal doped ZnO has a potential for spintronic applications as transition metals have unpaired electrons in the d-orbitals, and could form magnetic clusters or interact with carriers in ZnO to render ferromagnetism; also, ZnO doped with transition metals has provided signs of enhancing the thermo-emf and possibly thermoelectric-related properties in ZnO[313,329,330,338–342].

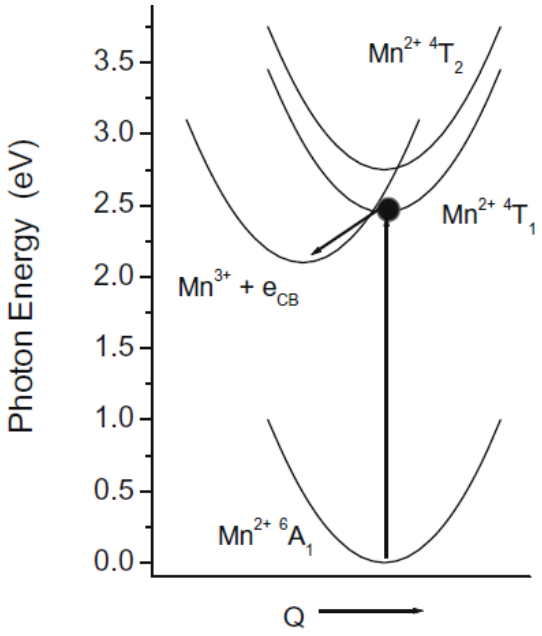

Figure 4.6 A configuration coordinate model of ionization of Mn^{2+} states and related transitions in a hypothetical ionic system[337].

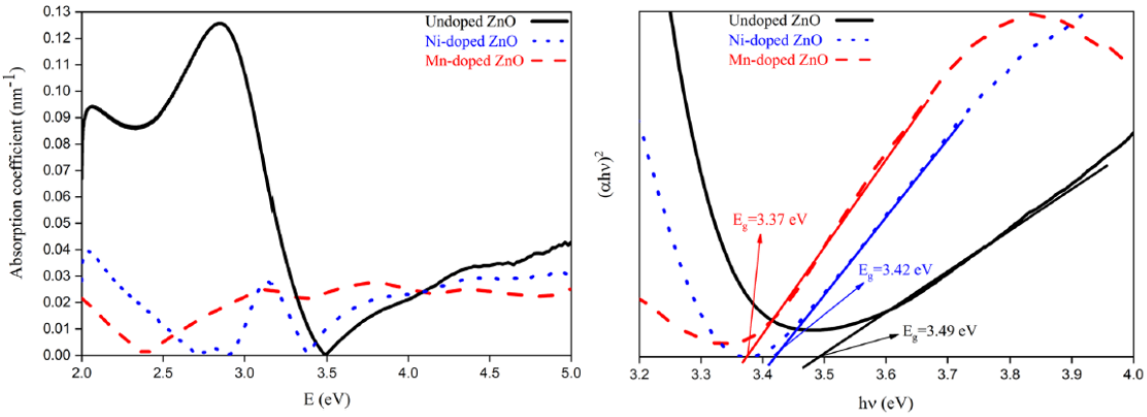

Figure 4.7 Absorption spectra of un-doped, Ni- and Mn-doped ZnO nanopowders by sol-gel technique, and their bandgap determination using Kramers-Kronig method[332].

Metal-organic chemical vapor deposition (MOCVD) has been one of the established techniques for the growth of compound semiconductors with high

controllability and good crystal quality[124,200,323,343,344]. These thin films could be used as active layers in solar cells, at a laboratory as well as commercial scale. Material properties could be systematically tuned in MOCVD growth with changes in conditions such as temperature, pressure, precursors' flows, etc. However, bandgap-related properties of MOCVD-grown zinc oxide doped with transition metals have not been sufficiently investigated. In this section, MOCVD growth of transition-metal doped zinc oxide and their resulting properties with varying dopant concentration and MOCVD growth conditions are discussed.

4.2. METAL-ORGANIC CHEMICAL VAPOR DEPOSITION OF ZINC OXIDE

Metal-organic chemical vapor deposition (MOCVD) involves deposition of thin films on substrates or surface sites in a suitable mass transport regime, by a controlled vaporization and chemical reaction of precursors.

Figure 4.8 is a picture of the MOCVD tool that was used for growth of zinc oxide-based materials, and Figure 4.9 shows the control unit arrangement for the MOCVD system.

Diethyl zinc (DEZn) is used as the zinc precursor with a vapor pressure of 4-10 Torr in temperature range of 5-16 ^{o}C.. A thermal refrigerator / circulator is used to maintain a suitable source-bubbler temperature. Pure oxygen is the oxide source, and nitrogen is the carrier gas. The flow rates and vertical injection of the source materials in the reaction chamber are controlled using mass flow controllers (MFCs) and needle valves.

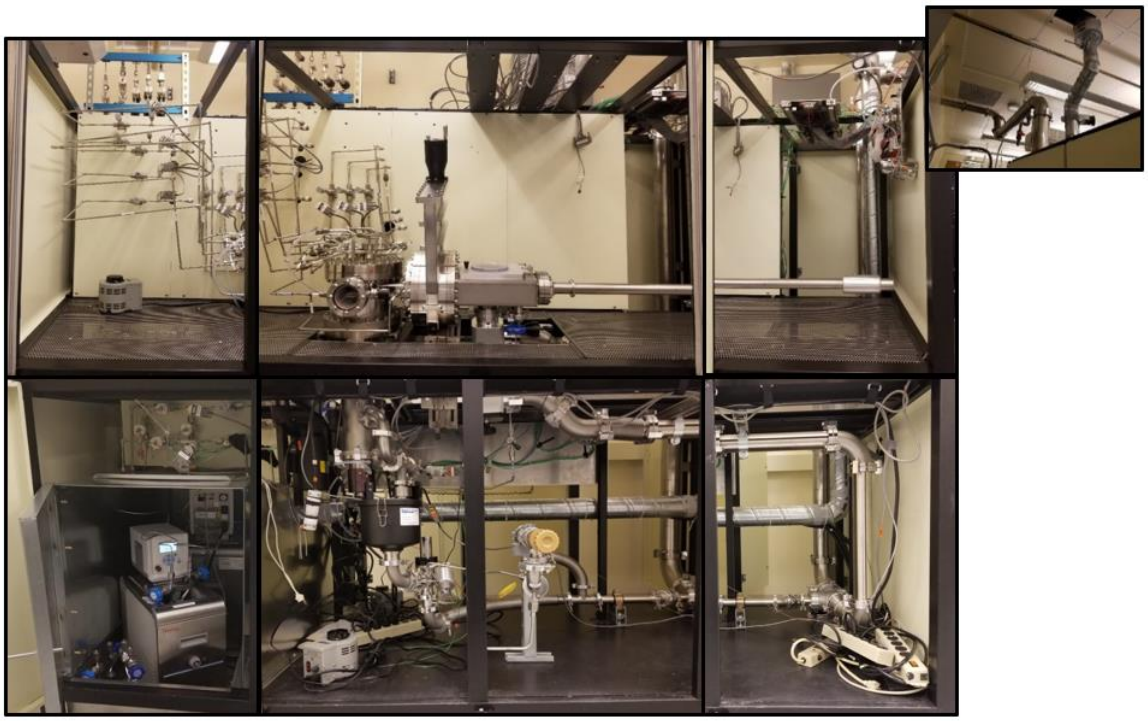

Figure 4.8 Metal-organic vapor deposition system for growth of un-doped and transition-metal doped zinc oxide.

Purposes or types of mass flow controllers include carrier gas flow mass flow controllers connected with the material sources to control the sources' injection in the reaction chamber, push and double dilution MFCs to further tune the flow rates. The reaction chamber flow flange has 8 metal-organic source lines, 4 oxygen, and 5 nitrogen lines getting into the chamber, to ensure a proper gas flow through the system. A butterfly valve is used to control the pressure in the reaction chamber. The chamber is maintained at room temperature at standby by a water circulation arrangement. A load-lock setup is used to load and remove samples from the chamber. The chamber and the load-lock arrangement have exhausts' arrangements consisting of a throttle valve, drystar vacuum pump, and

related filter. The temperature, pressure, and substrate-holder rotation speed are set through a computer and control unit shown in Figure 4.9.

Figure 4.9 Metal-organic vapor deposition system for growth of un-doped and transition-metal doped zinc oxide – Control panel.

Figure 4.10 illustrates a schematic of the system. Sources with a controlled flow rate enter the chamber through a pneumatic valves logic arrangement. This arrangement helps to route the sources' flow through desired push and double dilution MFCs. 4 double dilution MFCs for metal-organic sources are used, with a single MFC and a group of 3

MFCs. Oxygen and selected nitrogen lines enter the chamber through their individually allocated valves and MFCs. MFCs' flow rates vary from 100 to 2000 sccm for the sources, and up to 5000 sccm for the direct nitrogen lines. A more detailed and simplified arrangement of the sources' flow is shown in Figure 4.11.

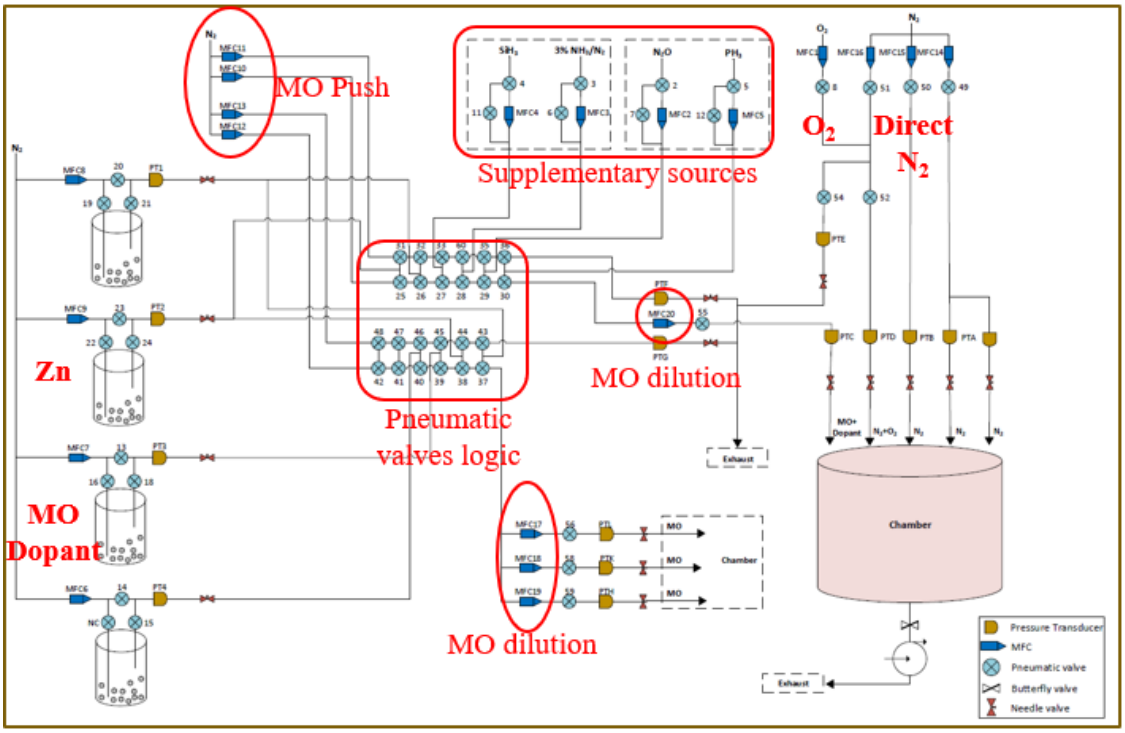

Figure 4.10 Schematic of metal-organic chemical vapor deposition system for growth of un-doped and transition-metal doped zinc oxide [from database / documents of the equipment system].

The net flow rate of DEZn entering the chamber is given by Equation (13).

$$FR_{DEZn} = FR_{Dilution}\left(\frac{FR_{DEZn_MFC}}{FR_{DEZn_MFC}+FR_{Push}}\right)\left(\frac{P_{DEZn_Vaporpressure}}{P_{DEZn_bubblerline}+P_{DEZn_Vaporpressure}}\right) \quad (13)$$

where FR_{DEZn} is the net DEZn flow rate entering the chamber, $FR_{Dilution}$ is the flow rate at the double dilution MFC, FR_{DEZn_MFC} is the carrier gas flow rate through the DEZn bubbler,

FR_{Push} is the flow rate at push MFC, $P_{DEZn_vaporpressure}$ is the vapor pressure of DEZn, and $P_{DEZn_bubblerline}$ is the pressure at the DEZn bubbler/line.

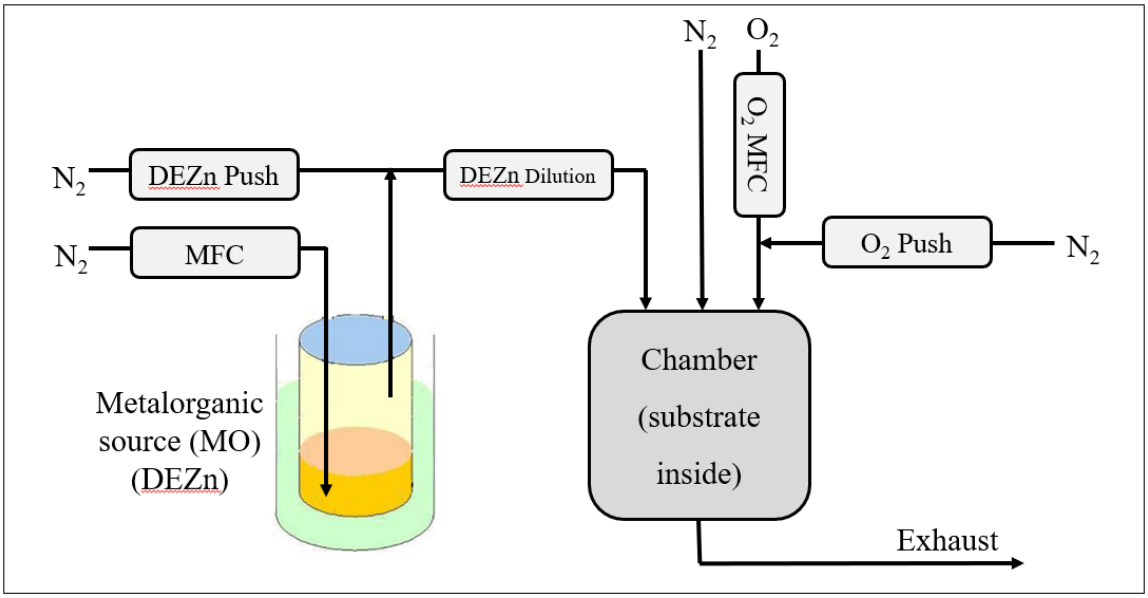

Figure 4.11 A simplified block diagram (mass flow controllers, sources, reaction chamber) of zinc oxide growth.

The mass flow controllers and temperature are controlled, and pressure transducers read, through a control software, as shown in Figure 4.12. Suitable pneumatic valves could be opened and closed depending on the growth parameters, and if the tool is in growth, N_2 purging, or idle mode.

Zinc oxide with varying precursor flow rates were grown on sapphire substrates. Zinc oxide could have native defects and sites that are deficient in oxygen or zinc, zinc interstitials, and other possible defects. Their effects on the resulting properties could be understood by varying the flow rates of the sources, as summarized in Table 4.1. Chamber temperature and pressure were maintained at 550 ^{o}C and 30 Torr respectively, with a

substrate disk rotation of 800 rpm. DEZn push was set at 200 sccm, and double dilution MFC was set at a summation value of the push MFC and the DEZn carrier MFC.

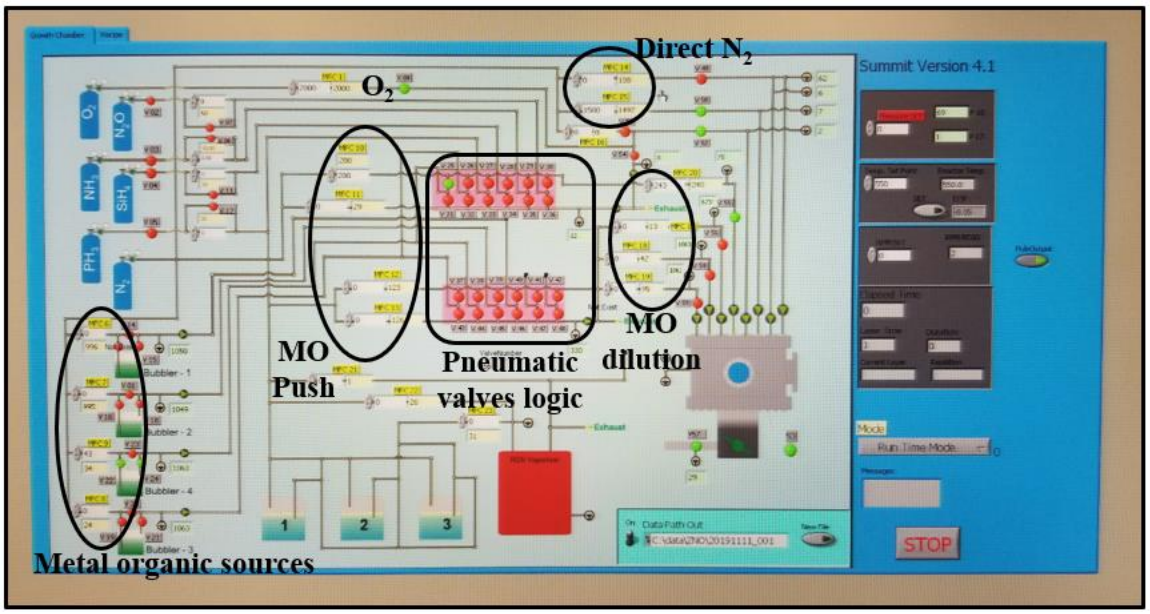

Figure 4.12 Software control of metal-organic chemical vapor deposition system for growth of un-doped and transition-metal doped zinc oxide.

4.3. STRUCTURAL AND OPTICAL CHARACTERIZATION OF ZINC OXIDE

Initial characterization of un-doped zinc oxide was performed with X-ray diffraction (XRD) and energy dispersive X-ray spectroscopy (EDX) techniques. As seen in Figure 4.13, a ZnO (002) peak is observed as expected. The sapphire substrate is c-plane and hence an epitaxial growth of zinc oxide with a hexagonal crystal structure was observed. A phase of ZnO (100) is also apparent. A minor peak at a 2θ of ~37^{o} could be due to residuals / memory effect of materials having cubic phases in the system.

Table 4.1 MOCVD growth / precursors' flow details of un-doped zinc oxide

Sample #	DEZn Temp. (^{0}C)	DEZn MFC FR (sccm)	DEZn flow rate (sccm)	O_2 MFC flow rate (sccm)	VI/II ratio	Direct N_2 flow (sccm)
Pr 1001	16	75	1.5	300	204	4000
Pr 1002	16	75	1.5	150	102	4000
Pr 1003	16	75	1.5	600	410	3600
Pr 1004	16	50	1.0	2000	2043	1000
Pr 1005	16	43	0.9	2000	2309	1500
Pr 1011	5	100	1.0	150	150	3500
Pr 1012	5	50	1.5	225	150	3500
Pr 1013	5	200	2.0	300	150	3500
Pr 1014	5	50	1.5	2000	1336	200
Pr 1015	5	200	2.0	2000	1002	200

Elemental composition study of ZnO by EDX showed zinc and oxygen peaks as seen in Figure 4.14. Also, an increase in the thickness is observed with an increase in the DEZn flow rate, as seen in Figure 4.15, but relatively stayed consistent with O_2 flow rate. XRD, EDX, and thickness characterization confirmed a successful growth of zinc oxide.

Considering the goal to investigate the effects of transition-metal doping on the optical and structural properties of ZnO, the bandgap of un-doped zinc oxide was measured under different precursor flow rates. Figure 4.16 shows photoluminescence measurement

results of un-doped ZnO samples. A dominant peak at ~3.3 eV is observed, as expected. Minor peaks at ~2.2 eV could be due to the lamp source.

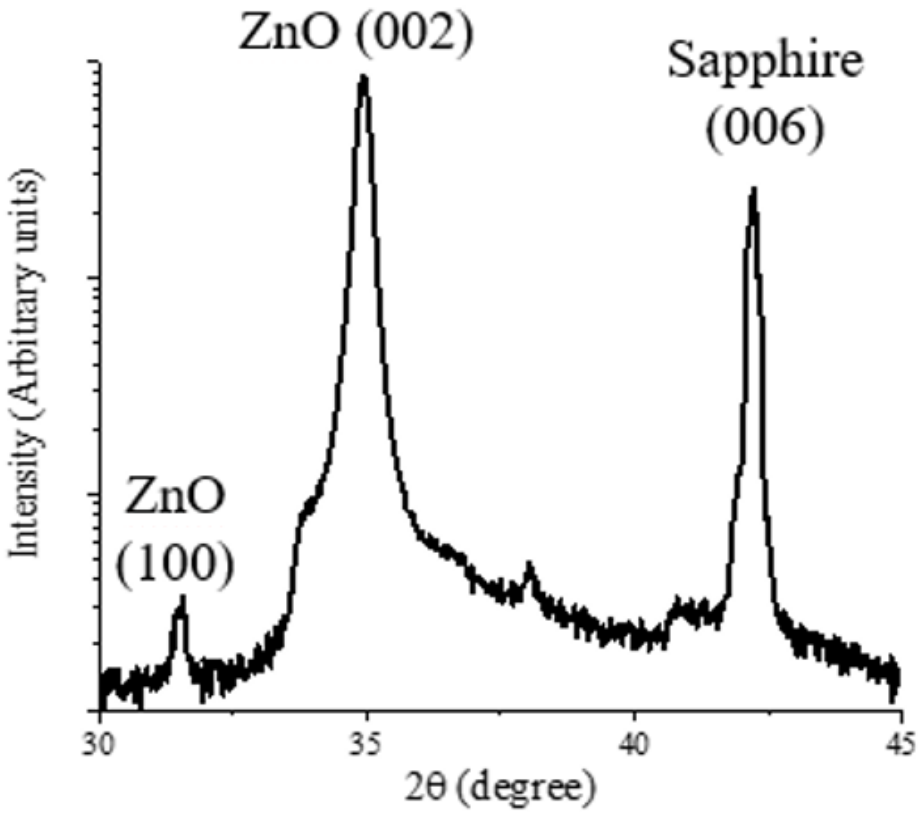

Figure 4.13 X-ray diffraction results of an un-doped ZnO sample (Pr 1002).

Variation in bandgap with varying precursor flows, that is, possibly varying vacancy or interstitial defects is studied as shown in Figure 4.17. The bandgap stays consistent in all the un-doped zinc oxide irrespective of variations in the flow rates. Following this, in the next section, transition metal doping of zinc oxide is done and resulting properties investigated.

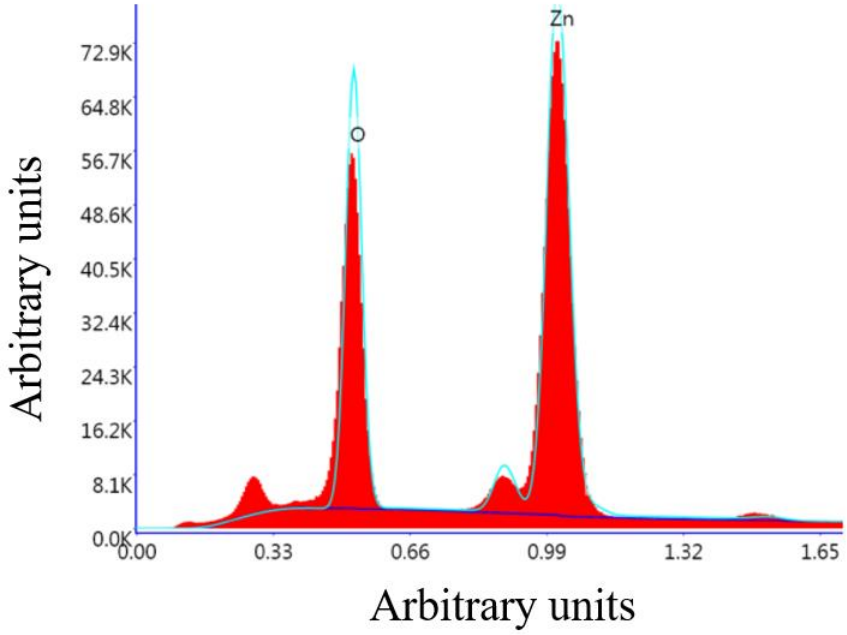

Figure 4.14 Energy-dispersive X-ray characterization results of un-doped ZnO (Pr 1002).

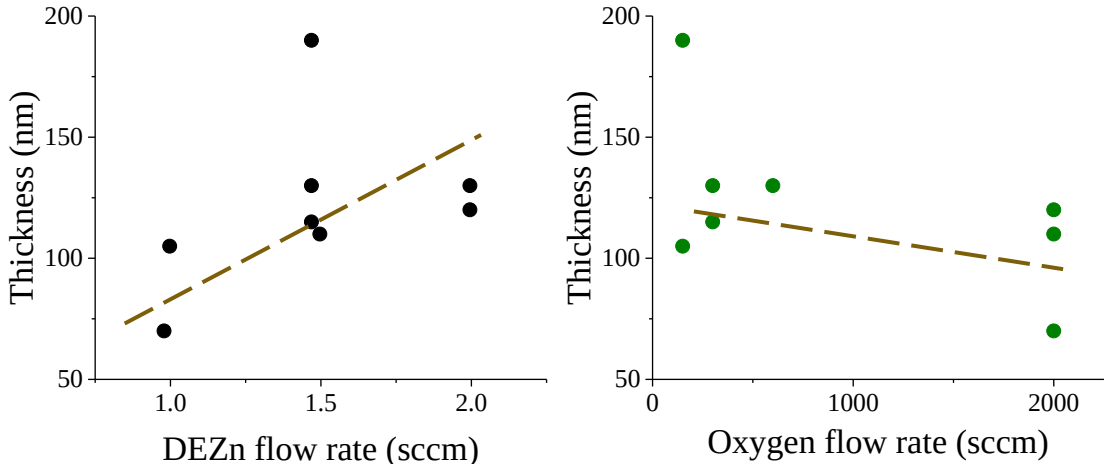

Figure 4.15 Effect of precursors' flows on the thickness of un-doped ZnO.

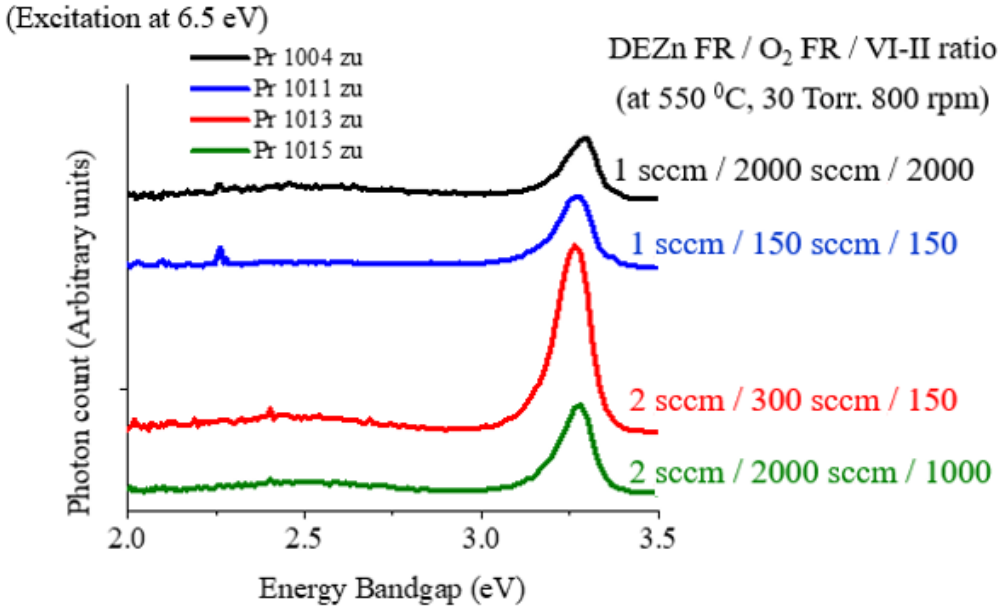

Figure 4.16 Photoluminescence characterization results of un-doped ZnO.

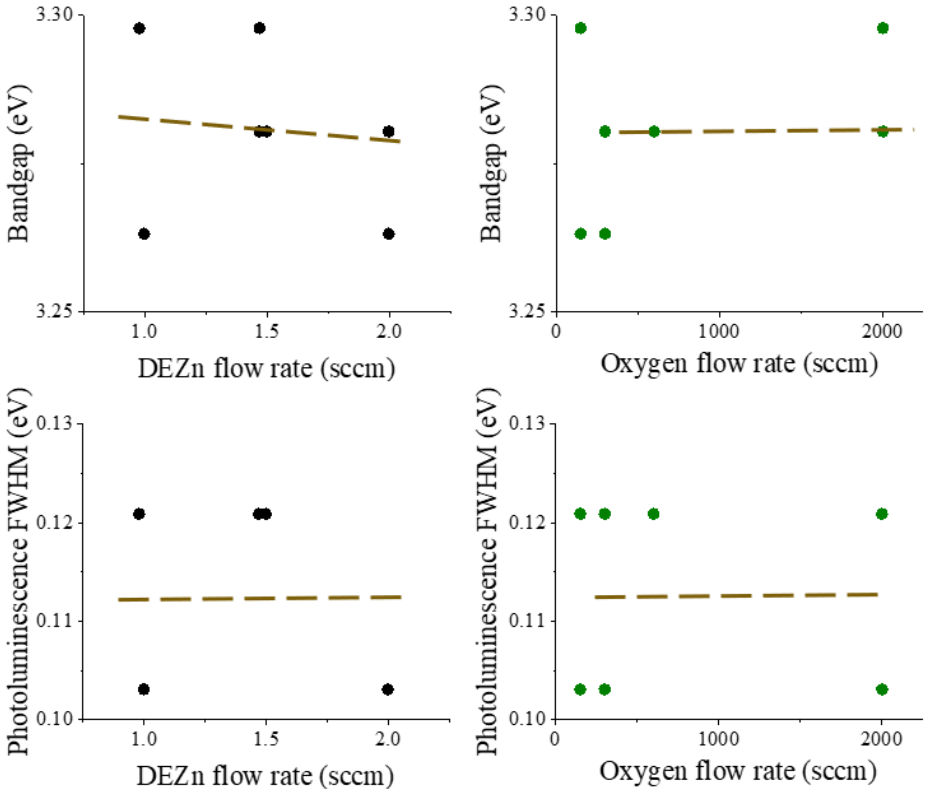

Figure 4.17 Effect of precursors' flows on the bandgap of un-doped ZnO.

4.4. METAL-ORGANIC CHEMICAL VAPOR DEPOSITION OF ZINC NICKEL OXIDE – PHASE I : EFFECTS OF NICKEL CONCENTRATION

Prior to growing nickel-doped zinc oxide, the injection of nickel in the chamber is tested. Bis-cyclopentadienyl nickel (Cp_2Ni) is a nickel precursor and was maintained at 90-95 ^oC with a vapor pressure of 3-7 Torr. As seen in Figure 4.18, broad peaks are observed in nickel oxide sample that were not observed on sapphire. These peaks are broad; the growth conditions optimized for zinc oxide were used to grow nickel oxide, while nickel oxide could have different optimum conditions than zinc oxide.

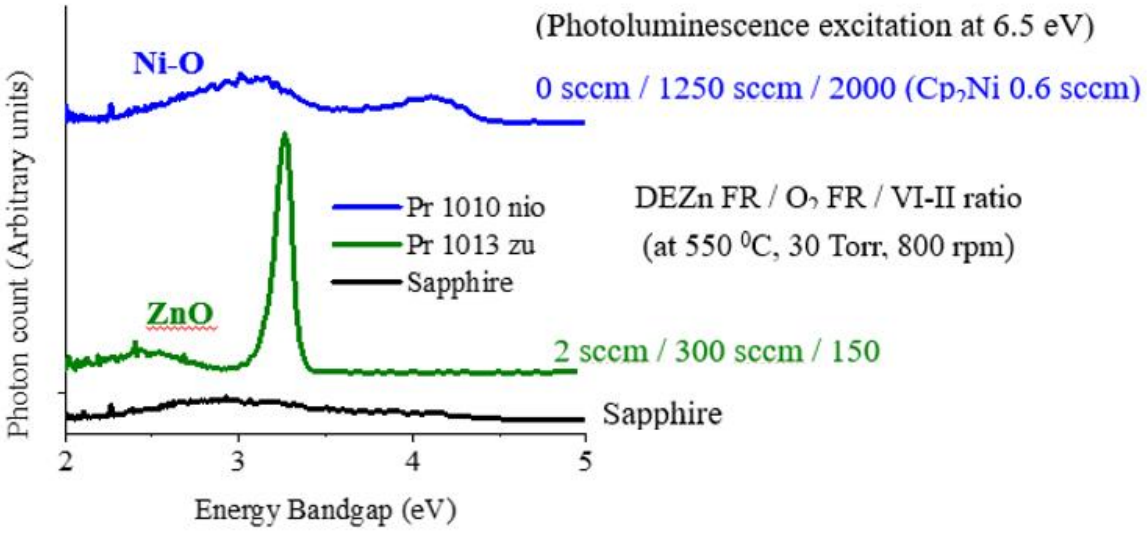

Figure 4.18 Photoluminescence characterization of sapphire, un-doped zinc oxide and nickel oxide.

Even though sapphire is a preferred substrate with a hexagonal crystal structure and lesser lattice mismatch with zinc oxide, a set of Ni-doped ZnO was grown on silicon as shown in Table 4.2 to understand the sources' injection and thin films' deposition.

DEZn was maintained at 5 ^{0}C with a carrier flow rate of 100 sccm, and Cp_2Ni at 95 ^{0}C with a carrier flow rate of 400 sccm.

As seen in Figure 4.19, samples with different growth conditions show different colors. Variation in nickel content, oxygen content, and growth condition could result in varying properties. For example, sample S-1 with no nickel injection appears bluish than sample S-2 with nickel injection.

Table 4.2 MOCVD growth parameters of set S of Ni-doped ZnO on silicon.

Sample #	Growth temp.	Growth pressure	DEZn FR (sccm)	O_2 MFC flow rate (sccm))	Cp_2Ni MFC flow rate (sccm)	VI/II ratio
S-1	450	30	1	150	0	150
S-2	450	30	1	150	5.4	150
S-3	450	30	1	2000	5.4	2000
S-4	550	100	1	150	5.4	150
S-5	550	30	1	150	5.4	150

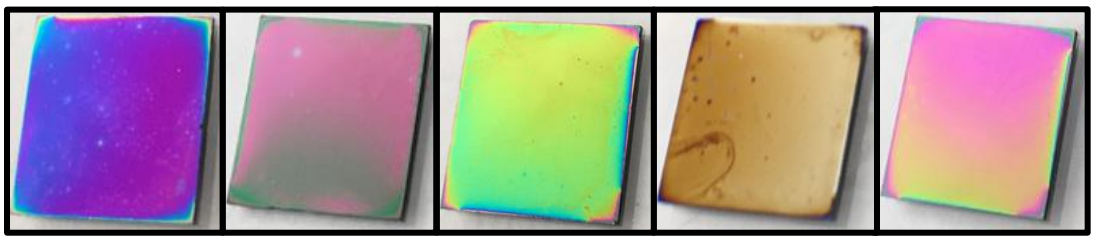

S-1 S-2 S-3 S-4 S-5

Figure 4.19 Ni-doped ZnO on silicon samples.

Following the initial growth tests, Ni-doped zinc oxide were grown on sapphire substrates. Diethyl zinc (DEZn) was maintained at 5 ^{o}C. Bis-cyclopentadienyl nickel (Cp_2Ni) is a nickel precursor and was maintained at 90-95 ^{o}C with a vapor pressure of 3-7 Torr and varying flow rates. Two sets of samples were grown, set A at 400 ^{o}C, 100 Torr, with a net DEZn flow of 2 sccm; and set B at 450 ^{o}C, 30 Torr, with a net DEZn flow of 1 sccm, both for 90 minutes. Oxygen flow rate was maintained at 300 sccm and 150 sccm for sets A and B respectively resulting in VI/II ratio of 150. Direct N_2 flow rate for the chamber ranged from 3000 to 5000 sccm. Substrate rotation speed was maintained at 800 rpm for all samples. Table 4.3 shows a summary of the conditions applied to grow Ni-doped ZnO.

Table 4.3 MOCVD growth details of Ni-doped ZnO on sapphire – Phase I.

Sample #	Temp. (^{o}C)	Pressure (Torr)	DEZn flow rate (sccm)	Cp_2Ni flow rate (sccm)	O_2 flow rate (sccm)
A-1	400	100	2	0	300
A-2	400	100	2	0.62	300
A-3	400	100	2	1.24	300
A-4	400	100	2	1.86	300
B-1	450	30	1	0	150
B-2	450	30	1	2.48	150
B-3	450	30	1	5.42	150

Reynolds numbers for the metal-organic precursors in sets A and B ranged about 2650-2250 and 650-850 respectively; which result in a stable and uniform laminar gas flow for adsorption of reactants on the sapphire substrates. Cp_2Ni flow rate is higher than DEZn flow rate in some samples, considering the possibility of a low adsorption or decomposition rate of the Cp_2Ni precursor.

Figure 4.20 shows the grown samples (of set A for reference (with similar case for set B)). Differences in color with an increase in Ni injection is seen in the samples due to changes in light absorption properties and introduction of defect states. Thicknesses of the samples were ~150 nm and ~500 nm for sets A and B respectively, and samples with the highest Ni content were the thickest in the respective sets.

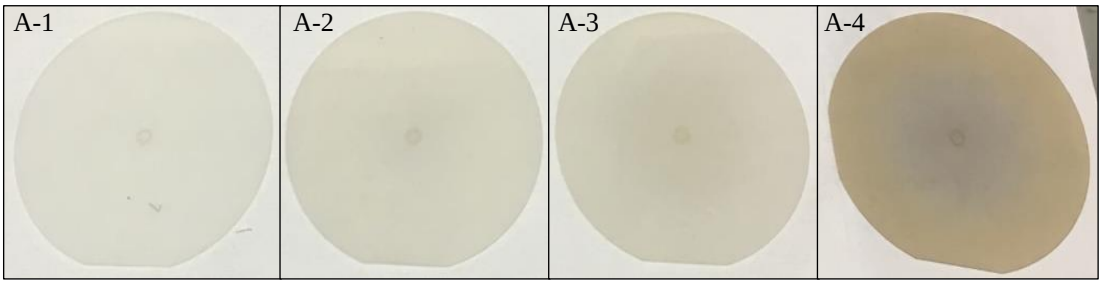

Figure 4.20 Ni-doped ZnO on sapphire (Phase I) Samples A-1 to A-4 with an increase in the Ni content (from left to right).

4.5. STRUCTURAL AND OPTICAL PROPERTIES OF ZINC NICKEL OXIDE – PHASE I : EFFECTS OF NICKEL CONCENTRATION

Structural properties of MOCVD-grown ZnNiO were studied under varying Ni concentration.

4.5.1. Structural Properties. Elemental composition characterization and X-ray diffraction measurement were performed to determine the incorporation of nickel in zinc

oxide and identify the crystal structures in ZnNiO. Figure 4.21 shows a sample EDX measurement, and Table 4.4 is a summary of the results.

EDX results agree with the growth parameters used, and the zinc content in samples of set B is less due to a lower zinc precursor input flow relative to Cp_2Ni flow. (In addition to Zn, Ni, and O, small amount of carbon impurities (unlabeled peak) is also detected). Ni percentage was calculated from the ratio of Ni to the total of Ni and Zn weights, as Ni typically substitutes Zn[11,17].

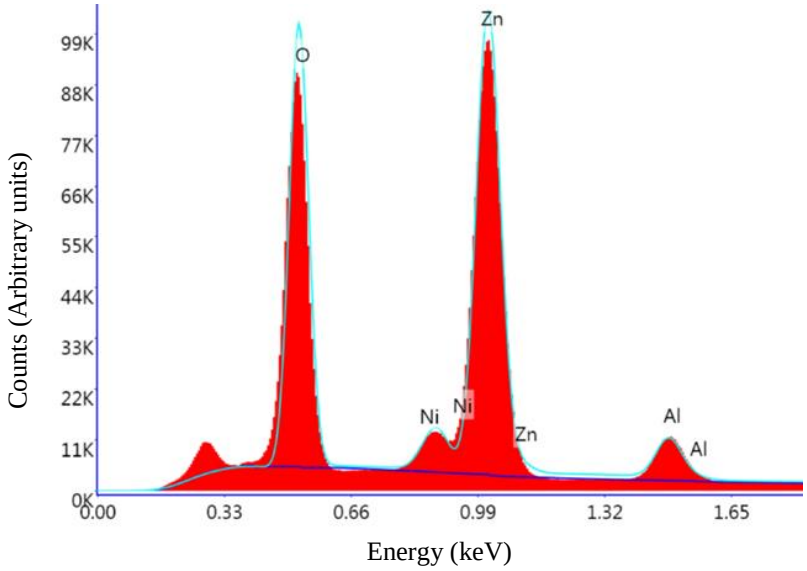

Figure 4.21 Energy-dispersive X-ray spectroscopy results of a Ni-doped ZnO sample on sapphire (Phase I) (sample# A-4).

Un-doped ZnO #B-1 contains small amount of Ni even though Ni precursor flow rate was 0 sccm, due to memory effect in the chemical vapor deposition system, as the samples were grown back to back. It can be seen from Table 4.4 that Ni incorporation not

only affects Zn content but also oxygen in ZnNiO, which could be the result of defect states or interstitial states or oxygen vacancies introduced or occupied by Ni in ZnNiO.

Table 4.4 Energy dispersive X-ray spectroscopy results of MOCVD-grown ZnNiO on sapphire (Phase I).

Sample #	Zn weight %	Ni weight %	O weight %	Ni % in ZnNiO
A-1	68.37	0	24.32	0.00
A-2	64.12	0.08	26.07	0.12
A-3	61.81	0.14	27.29	0.23
A-4	69.38	1.54	24.26	2.17
B-1	36.21	0.01	23.36	0.03
B-2	59.07	0.29	17.93	0.49
B-3	63.43	0.75	19.87	1.17

X-ray diffraction 2θ-ω measurement is shown in Figure 4.22. A hexagonal crystal structure in (002) direction is observed, along with secondary phases. The (002) peak shifts towards lower and higher diffraction angles relative to an un-doped ZnO upon Ni doping. Ni^{2+} has a smaller ionic radius than Zn^{2+} which results in a reduction in the lattice size and a peak shift towards higher diffraction angles. However, this could also be convoluted with other sites that Ni can occupy in ZnO, as also observed in EDX results. Detailed information of the (002) peak is presented in Table 4.5. A better full width half maximum (FWHM) with Ni doping shows that the overall crystal quality of the thin films is not affected with Ni doping. Vertical correlation length is determined (approximately) using

Scherrer equation (crystallite size = ~0.9 λ / β cos(θ), where λ is wavelength of the X-ray source, β is FWHM of the (002) peak, and θ refers to the incident X-ray angle), to understand the relative variation in crystallite size with Ni doping. The crystallite size increased with Ni doping in ZnO, which could be due to a larger atomic radius of nickel than zinc, and possibilities of nickel occupying substitutional or interstitial sites in zinc nickel oxide.

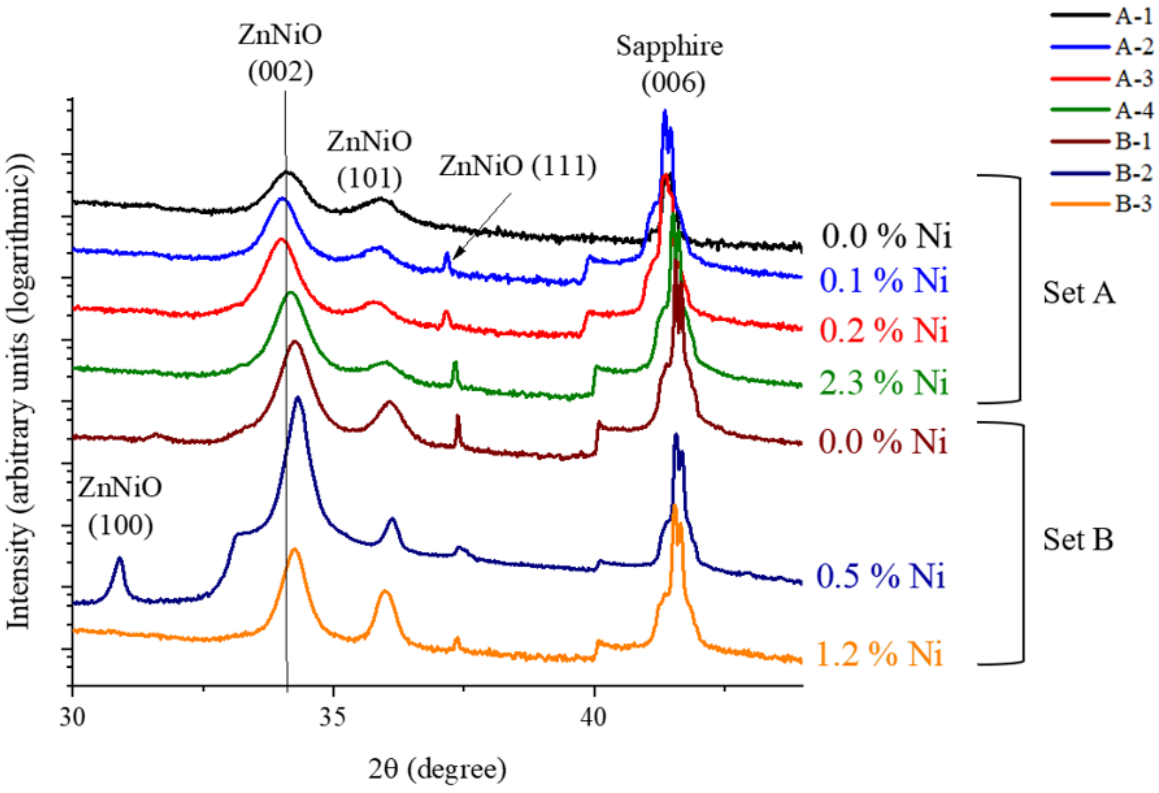

Figure 4.22 X-ray diffraction results of MOCVD-grown ZnNiO on sapphire (Phase I).

A ZnNiO (100) phase was identified in a Ni-doped ZnO sample due to polycrystallinity in the films. ZnNiO (101) peaks at ~36^0 2θ are relatively higher in intensity with reference to the (002) peaks in set B, which could be the result of different

growth conditions. The peak at ~37.4^0 could be a combination of a ZnNiO (111) phase and sapphire (110), but ZnNiO (111) is the dominant one considering that the peak does not appear in un-doped ZnO sample# A-1 and shifts in position with Ni doping. Un-doped ZnO B-1 still shows the (111) peak due to memory effect; as also seen in the EDX results. Shoulders at some diffraction peaks could be due to Laue-like oscillations or interface defects introduced by Ni doping.

Table 4.5 X-ray diffraction results of MOCVD-grown ZnNiO on sapphire (Phase I).

Sample #	Ni % (EDX)	(002) 2θ peak position (^{o})	(002) peak FWHM (arcsec)	Lattice constant c (Å)	~ Vertical correlation length (Å)
A-1	0.00	34.08	2484	5.256	118
A-2	0.12	34.02	1764	5.265	170
A-3	0.23	34.02	1620	5.265	186
A-4	2.17	34.18	1620	5.240	186
B-1	0.03	34.26	1332	5.228	227
B-2	0.49	34.32	792	5.219	372
B-3	1.17	34.26	1080	5.228	273

Occurrence of (111) phase with slight shifts in (002) peak, accompanied with Ni detection in EDX measurement, show that nickel was incorporated in zinc oxide without significantly effecting the crystallinity relative to un-doped ZnO.

4.5.2. Optical Properties. Optical properties of Ni-doped ZnO on sapphire were studied using photoluminescence and absorption measurement.

Photoluminescence measurement of Ni-doped ZnO samples on sapphire were performed (with an excitation energy of ~6 eV), as shown in Figure 4.23. All the samples showed photoluminescence at or below ~3.3 eV. Set B grown at 450 ^{0}C and 30 Torr showed narrow UV emission peaks. Broad peaks were observed in set A samples grown at 400 ^{0}C and 100 Torr, due to a low signal to noise ratio in the measurement or a lower quality at higher pressure / lower temperature as also seen from the XRD peak intensities and FWHM, or an inter-mix of the UV emission peak and defects-related broad peak in the yellow luminescence wavelengths.

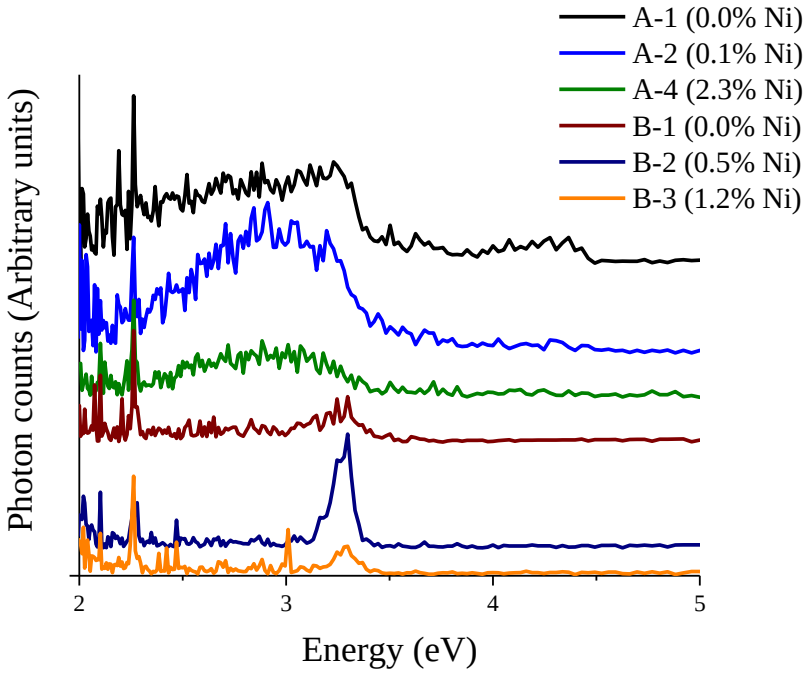

Figure 4.23 Photoluminescence diffraction results of MOCVD-grown ZnNiO on sapphire (Phase I).

Absorption spectrum measurement was performed to determine band edge related properties of MOCVD-grown ZnNiO samples. Near band edge characterization could be

crucial especially in photovoltaic and sensing applications. Figure 4.24 shows the absorbance spectra of ZnNiO with varying nickel content. For sample# A-4 with Ni content of 2.3%, an increase in the absorbance, and a red shift in band edge (also sample# A-2), are observed relative to other samples in the respective set. Set B also shows a red shift and increase in absorbance with nickel doping in zinc oxide. The step at ~3.5 eV is due to switching of lamps in the measurement equipment.

Energy band gap of Ni-doped ZnO was determined using Tauc plots. Absorption coefficient (α = Absorbance/thickness) was calculated and $(\alpha hv)^2$ plotted as seen in Figure 4.24. Considering a direct bandgap in zinc oxide-based materials, linear lines (dashed lines in the figures) were extrapolated on the x-axis, and corresponding intercepts were determined. In set A, the band gap reduced from 3.276 eV in un-doped ZnO to 3.269 eV in ZnNiO with 2.3% Ni. Set B showed more reduction in the band gap from 3.287 eV to 3.260 eV with an increase in the Ni-doping up to 1.2%.

Figure 4.25 depicts the reducing trend in the band gap with Ni content in ZnNiO, which is consistent in both the samples' sets. The rate of bandgap reduction is more in set B. From X-ray diffraction results, it could be understood that crystallinity is relatively better in samples of set B based on the FWHM of the (002) peak. Relative to the (002) peak of un-doped ZnO, it seems that a peak shift towards higher diffraction angles (on average) in ZnNiO, is preferable for bandgap reduction rate. Also, as seen in Table 4.4, samples with lower oxygen content showed lower bandgaps. Substitution of Zn^{2+} with Ni^{2+}, and oxygen vacancies caused by Ni doping, could be primarily responsible for the bandgap reduction. A sample with lower Ni content (for example, sample# B-3) can possibly have a lower bandgap (more bandgap reduction) than a sample with relatively higher Ni content

(for example, sample# A-4), if it has more incorporation of Ni at sites that favor band gap reduction in ZnNiO. As the rate of band gap reduction with Ni-doping is different under the two growth conditions, it can be said that energy sites occupied by Ni are influenced by growth parameters. Different growth conditions could activate different sites for dopant incorporation during growth and affect the resulting band edge of the material.

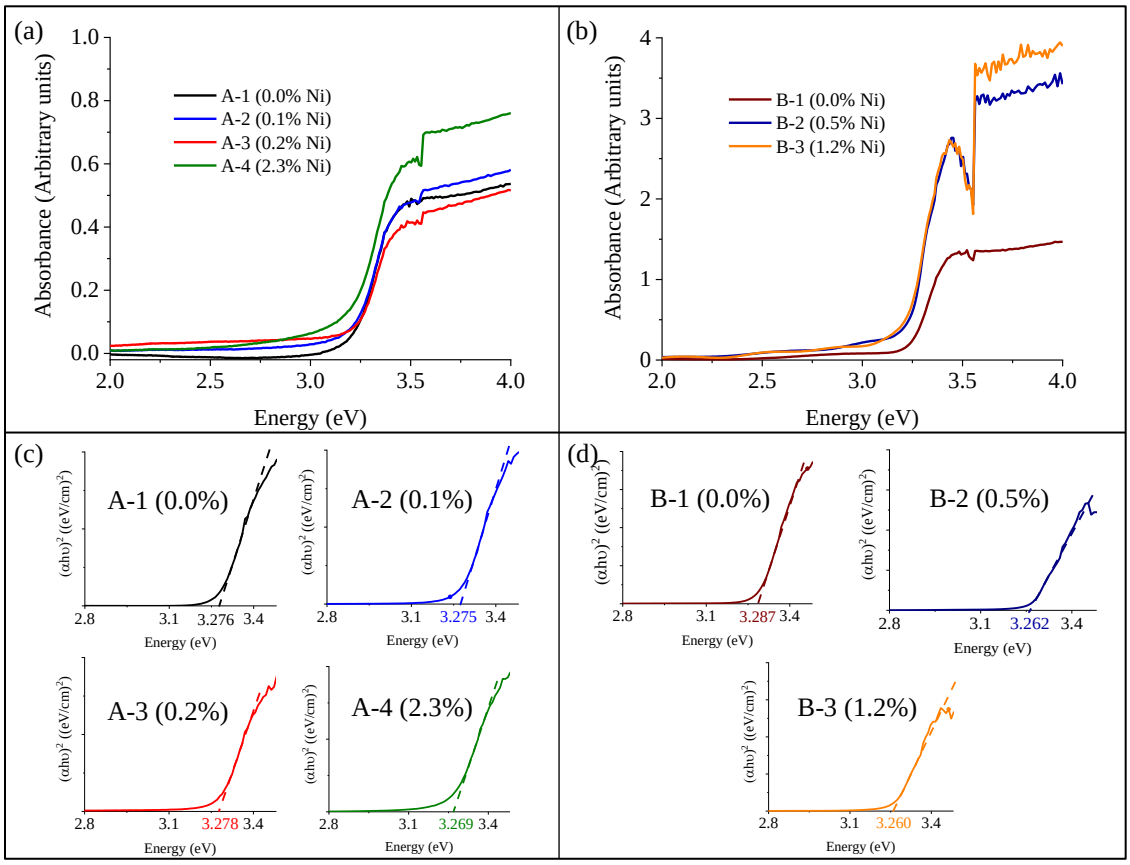

Figure 4.24 Absorbance spectra and Tauc plots of MOCVD-grown ZnNiO on sapphire (Phase I) (a) Absorbance spectra - Set A, and (b) Absorbance spectra - Set B, (c) Tauc plots - Set A, and (d) Tauc plots - Set B.

Overall absorption spectrum results show a potential of band gap tunability of zinc oxide by doping with nickel. Ni would p-dope ZnO and could introduce shallow energy

states near the valence band causing the bandgap reduction. In addition to controllably manipulating the band edge; energy states activated in zinc oxide by Ni-doping, could also interact with the energy bands or defects in the host material, resulting in a coupling of the Ni *d* orbitals within (Ni-Ni), and with the *s* or *p* orbitals of ZnO, to potentially also render magnetic and thermo-electric properties.

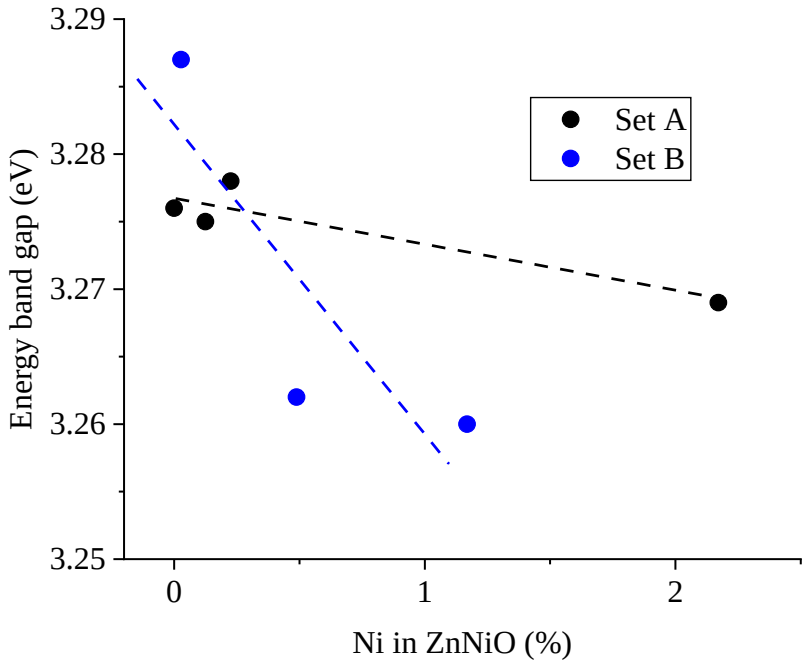

Figure 4.25 Trend of variation in band gap of MOCVD-grown Ni-doped ZnO on sapphire (Phase I) with Ni content.

4.6. METAL-ORGANIC CHEMICAL VAPOR DEPOSITION OF ZINC NICKEL OXIDE – PHASE II : EFFECTS OF GROWTH CONDITIONS

Phase II growth of zinc nickel oxide involved a systematic study of the effect of growth conditions – temperature and pressure on the nickel incorporation and resulting optical and structural properties. DEZn and Cp_2Ni sources were maintained at 5 ^oC and 90-

95 ^{o}C respectively. Two sets of samples were grown, set C at 450° C and set D at 550° C with a chamber pressure-range of 22-100 Torr, and a substrate disk rotation speed of 600 rpm. DEZn and oxygen net flow rates were maintained at 1 sccm and 300 sccm with a VI/II ratio of 300. Cp_2Ni flow rate was maintained at 2.7 sccm considering a possibility of low decomposition / adsorption rate of the dopant. N_2 flow rate directly into the chamber ranged from 500 to 4000 sccm. Table 4.6 summarizes the growth conditions.

Table 4.6 MOCVD growth details of Ni-doped ZnO on sapphire – Phase II

Sample #	Temp. (^{o}C)	Pressure (Torr)	DEZn flow rate (sccm)	Cp_2Ni flow rate (sccm)	O_2 flow rate (sccm)
C-1	450	22	1	2.7	300
C-2	450	30	1	2.7	300
C-3	450	100	1	2.7	300
D-1	550	22	1	2.7	300
D-2	550	30	1	2.7	300
D-3	550	100	1	2.7	300

4.7. STRUCTURAL AND OPTICAL PROPERTIES OF ZINC NICKEL OXIDE – PHASE II: EFFECTS OF GROWTH CONDITIONS

ZnNiO grown by MOCVD with varying growth conditions are characterized.

4.7.1. Structural Properties. Elemental composition of selected samples was studied using EDX, as shown in Figure 4.26, and details are provided in Table 4.7.

The zinc and nickel content in sample grown under a high pressure at 550 ^{o}C showed a significant reduction as compared to samples with lower pressure. Oxygen to zinc weight ratio for samples C-1, C-2, and D-3 are 0.64, 0.35, and 9.36 respectively. The oxygen peak in D-3 is primarily from the sapphire substrate, as the sample was only a few nanometers thick.

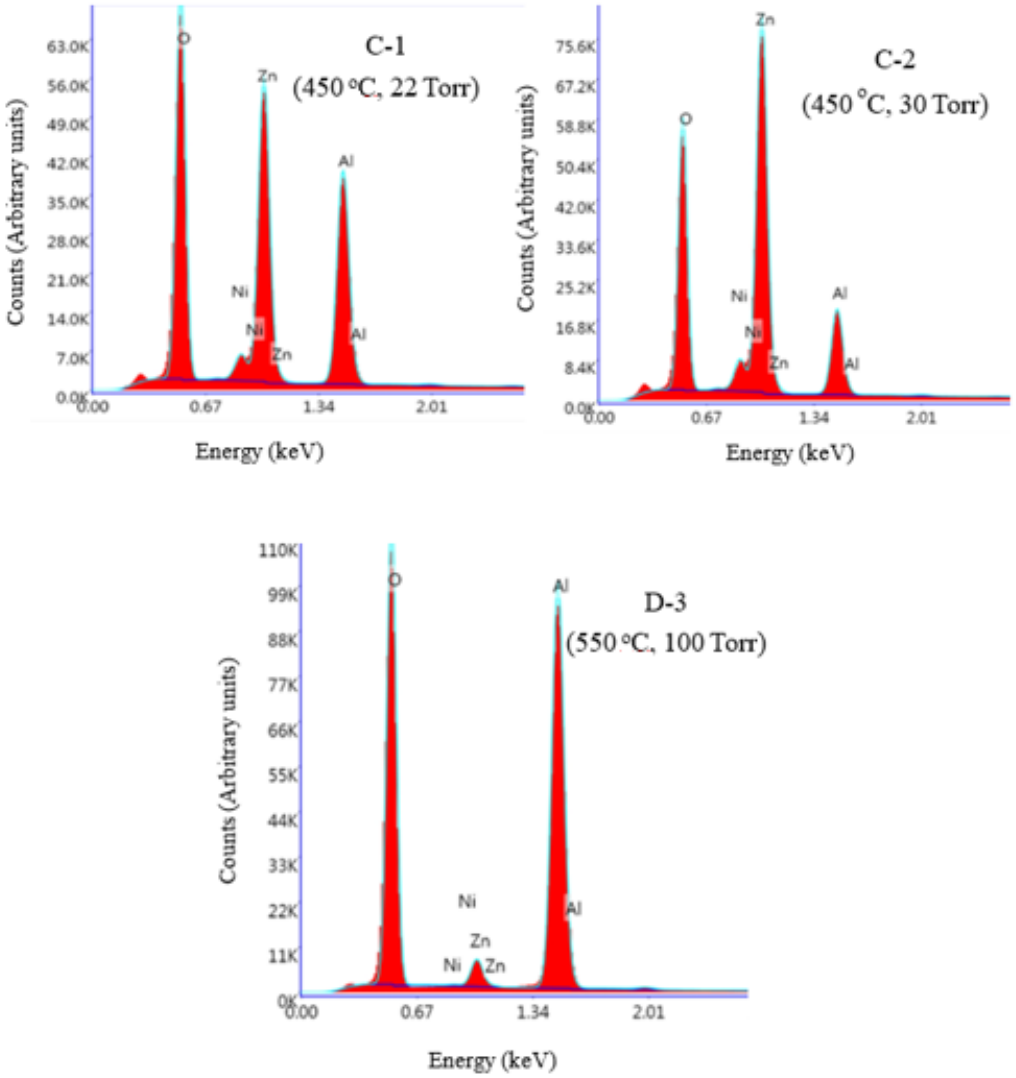

Figure 4.26 Energy-dispersive X-ray diffraction spectroscopy of Ni-doped ZnO on sapphire samples (Phase II).

Table 4.7 Energy-dispersive X-ray spectroscopy results of ZnNiO on sapphire (Phase II).

Sample #	Zn weight %	Ni weight %	O weight %	Ni % in ZnNiO
C-1	44.80	1.03	28.89	2.2
C-2	63.91	1.34	22.91	2.05
D-3	4.48	0.00	41.97	0.0

Figure 4.27 shows the X-ray diffraction plots of the samples. A hexagonal crystal structure with (002) orientation (at 2θ = 34°) is observed, along with ZnO like (100) phase at 2θ = 31° and (101) phase at 2θ = 36°. NiO like cubic phase is observed at 2θ = 37°.

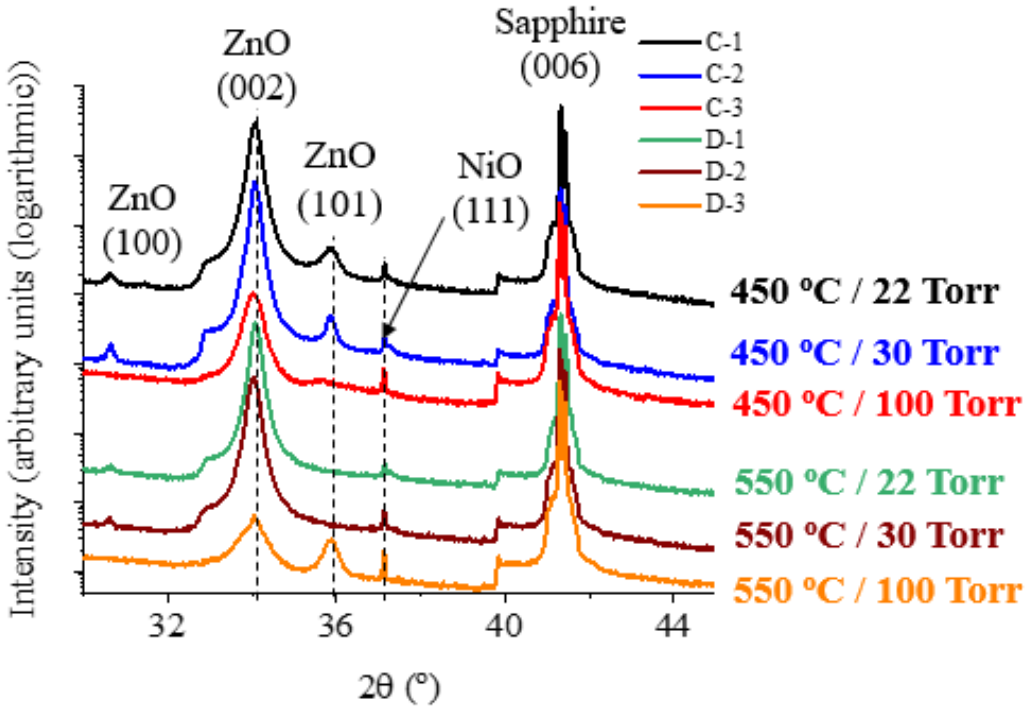

Figure 4.27 X-ray diffraction results of Ni-doped ZnO on sapphire (Phase II).

Details of the (002) peak are summarized in Table 4.8. The peak intensity and the vertical correlation length decrease with an increase in the chamber pressure. The FWHM of the (002) peaks increase with the pressure. The crystal quality of Ni-doped zinc oxide seems better at lower pressure.

Table 4.8 X-ray diffraction results of Ni-doped ZnO on sapphire (Phase II).

Sample #	(002) 2θ peak position (°)	(002) peak FWHM (arcsec)	Lattice constant c (Å)	~ Vertical correlation length (Å)
C-1	34.06	864	5.258	346
C-2	34.06	864	5.258	346
C-3	34.02	1440	5.264	208
D-1	34.32	720	5.219	415
D-2	34.26	864	5.228	346
D-3	34.06	1728	2.258	173

4.7.2. Optical Properties. Photoluminescence and absorption properties of Phase-II ZnNiO were studied.

As seen in the photoluminescence spectra with an excitation wavelength of ~6 eV, in Figure 4.28, all the samples show photoluminescence peak around 3.3 eV. Samples growth at a 450 ^{0} and lower pressure have stronger ultra-violet emission peaks. Samples at

a higher temperature of 550 ^{o}C or higher pressure show broad peaks, which could be due to defects or energy states introduced by Ni incorporation under the specific growth conditions. Peak around 4 eV could be due to a NiO like (111) phase which is also reflected in the X-ray diffraction results.

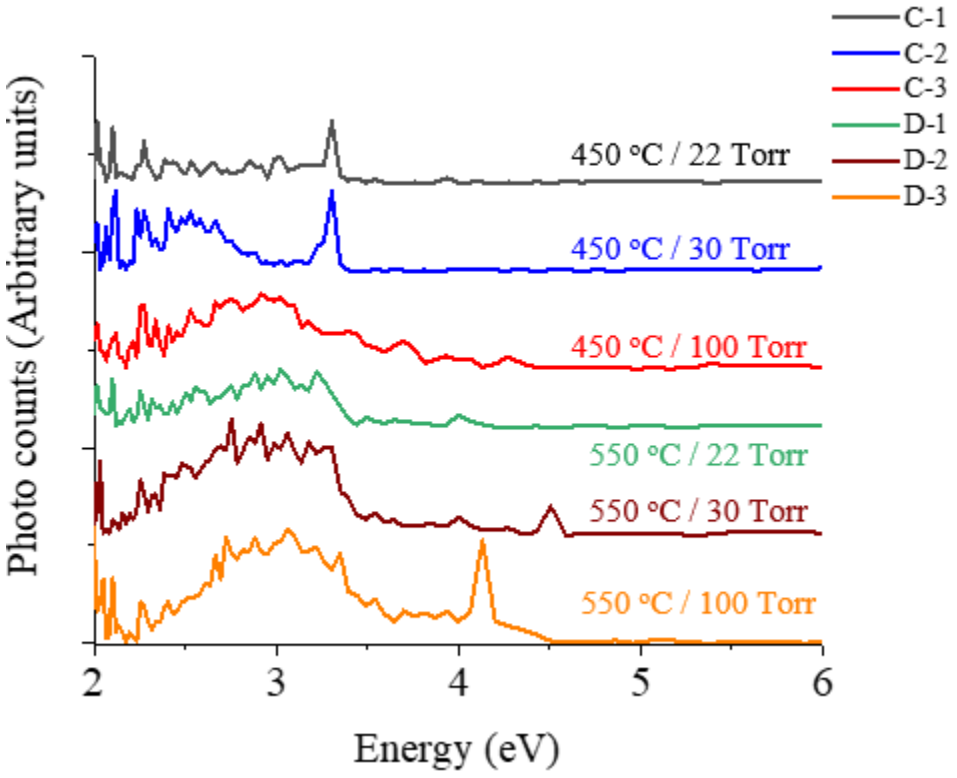

Figure 4.28 Photoluminescence spectra of ZnNiO on sapphire growth at different growth conditions (Phase II).

Absorbance spectra plots of the ZnNiO samples are shown in Figure 4.29. The step at 3.5 eV is due to a switching of lamps in the spectrophotometer. All the samples grown show a bandgap around 3.3 eV which is in agreement with the photoluminescence results. In set C, the absorption intensity of sample with high pressure is significantly lower than the samples at low pressure. Sample D-3 did not exhibit band-edge.

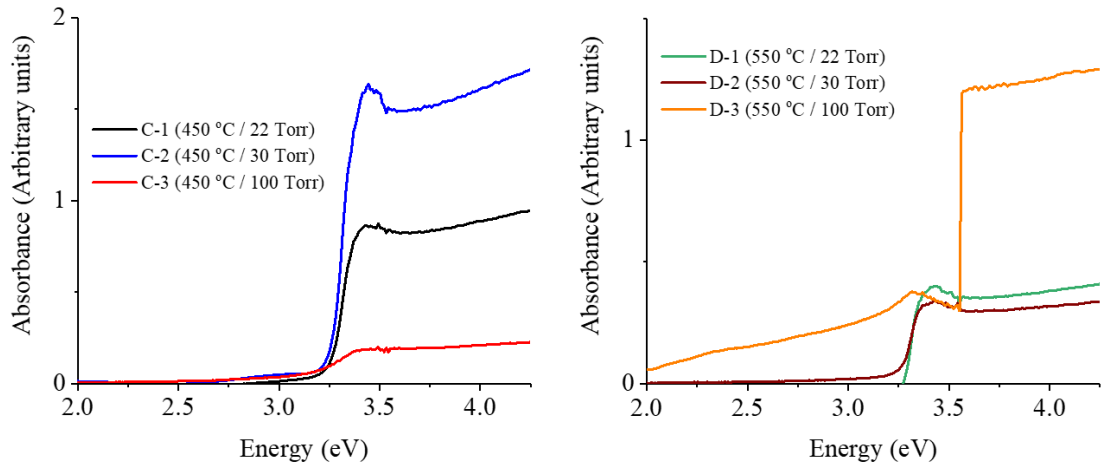

Figure 4.29 Absorption spectra of ZnNiO on sapphire grown under varying temperature and pressure conditions (Phase II).

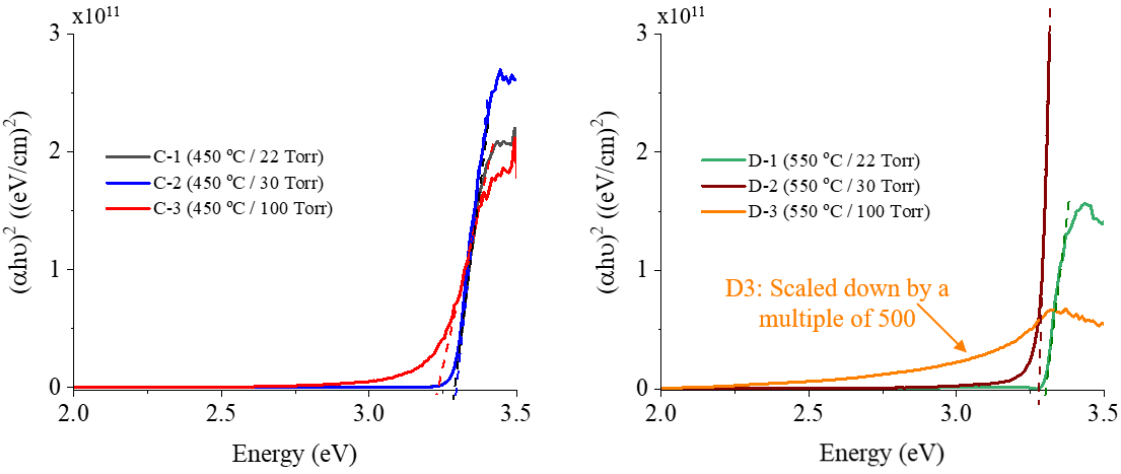

Figure 4.30 Tauc plots of ZnNiO on sapphire grown under varying temperature and pressure conditions (Phase II).

Figure 4.30 shows the Tauc plots of ZnNiO that are used to determine the band edges of ZnNiO. Samples grown at both the growth temperature show sharper band edges of 3.3 eV at low pressures, as compared to high pressure.

4.7.3. Effects of Annealing. Post-growth processing of ZnNiO could effect their properties. Annealing could activate energy sites or help the movement of Ni ions or atoms towards energy sites that are favorable for a reduction in bandgap. ZnNiO as-grown at 450 ^{o}C / 30 Torr was annealed in air at 1000 ^{0}C for 30 mins.

Figure 4.31 shows the photoluminescence spectra of the as-grown and annealed samples. As-grown sample shows UV emission peak and broad yellow peak around 2.3 eV. The peak intensities significantly reduced in the annealed sample. It still shows a broad peak (from ~2.5 eV to ~3.3 eV) and a bandgap around 3.3 eV, but the quality is deteriorated, which could be due to the activation of impurity (non-luminescent) centers.

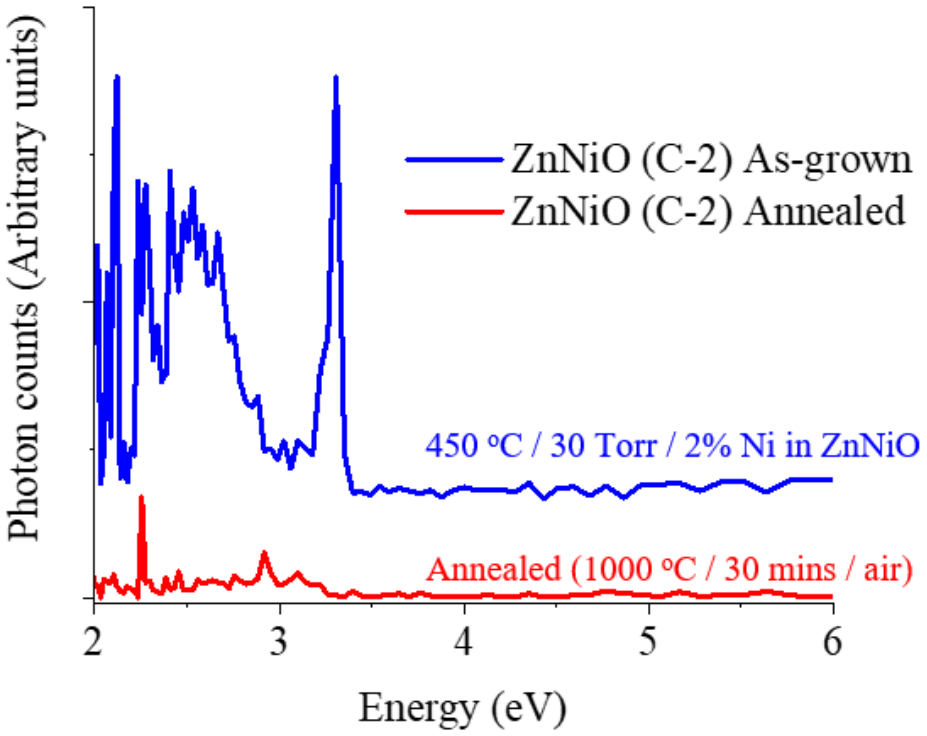

Figure 4.31 Photoluminescence spectra of as-grown and annealed ZnNiO.

Absorption spectra of as-grown and annealed samples are shown in Figure 4.32. The absorption intensity reduced with a slight reduction in the band edge sharpness, as also indicated in the photoluminescence spectra.

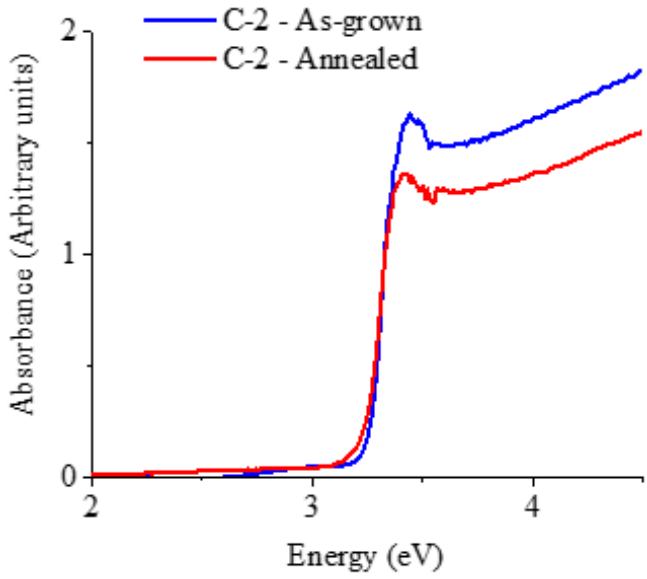

Figure 4.32 Absorption spectra of as-grown and annealed ZnNiO.

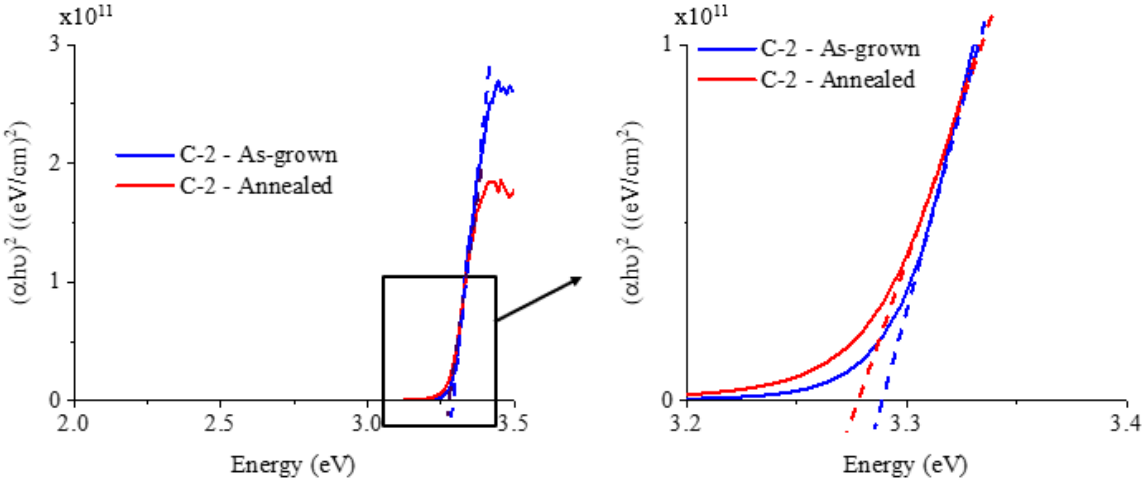

Figure 4.33 Tauc plots of as-grown and annealed ZnNiO.

Tauc plots are illustrated in Figure 4.33 to determine the bandgaps. The as-grown sample has a bandgap of 3.289 eV, while annealed sample showed a bandgap of 3.277 eV. Annealing resulted in a reduction in the bandgap and a possible activation of energy states conductive for bandgap reduction.

In summary of the phase-II growth of ZnNiO, MOCVD growth conditions effect the structural and optical properties of Ni-doped ZnO. Energy bands introduced in zinc oxide with dopant incorporation depend on the growth conditions such as temperature and pressure. Samples grown at a lower pressure of 22-30 Torr showed better crystal quality, and sharp optical properties, unlike 100 Torr. Growth conditions with a low chamber pressure (≤ 30 Torr) and a temperature close to the decomposition temperatures of the metal-organic sources within a mass transport regime, exhibited a good crystalline quality, and sharp band edges. Post-growth annealing has a potential to further reduce the bandgap of ZnNiO.

4.8. METAL-ORGANIC CHEMICAL VAPOR DEPOSITION OF ZINC MANGANESE OXIDE

Zinc oxide doped with manganese also has a potential for a reduction in bandgap, as discussed in Section 4.1. In this section, MOCVD growth of Mn-doped ZnO is investigated. A DEZn source maintained at 5 ^{o}C with a vapor pressure of ~5 Torr had a net flow rate of 1-2 sccm with the actual carrier gas flow rate of 100-200 sccm. A VI/II ratio of 150 was maintained with oxygen flow rates of 150-300 sccm. A bis(cyclopentadienyl) manganese (Cp_2Mn) precursor was used as Mn source. The Cp_2Mn bubbler is maintained at a temperature in a temperature range of 150-162 ^{o}C for a vapor pressure of 0.55-0.85 Torr. The source's flow rates and temperature could be tuned to achieve source injection

in the reaction chamber. Growth temperature and pressure were varied in the initial growth runs and then optimized at 550 ^{o}C and 25 Torr, with a disk rotation speed of 600 rpm. Table 4.9 provides a summary of the growth condition of ZnMnO samples.

Table 4.9 MOCVD growth details of ZnMnO on sapphire.

Sample #	Temp. (^{o}C)	Pressure (Torr)	DEZn flow rate (sccm)	O_2 flow rate (sccm)	Cp_2Mn injection (%)
E-1	550	25	2	300	0
E-2	450	22	2	300	11
E-3	550	30	2	300	11
E-4	550	25	2	300	14
E-5	550	25	2	300	18/
E-6	550	25	2	300	23
E-7	550	25	1	150	25

Figure 4.34 shows picture of a ZnMnO sample (E-6) along with a sapphire substrate and an Mn-doped ZnO sample. The ZnMnO sample seems to reflect an orangish-yellow tinge in response to the incident white light.

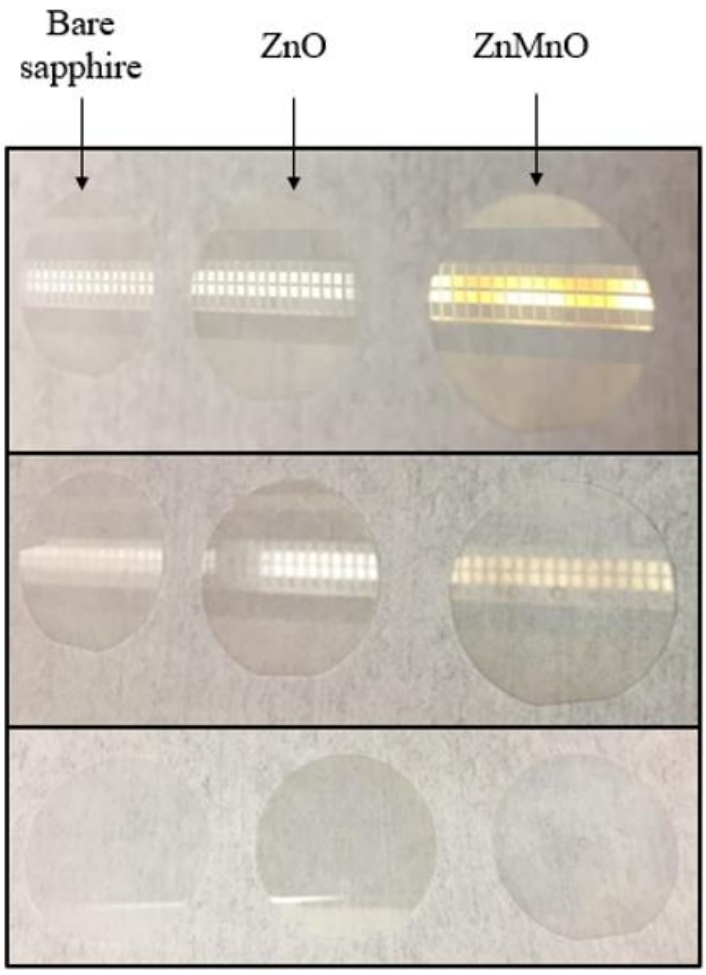

Figure 4.34 Pictures of 3 samples – sapphire, un-doped ZnO and ZnMnO (with 3 different background light conditions for the photos).

4.9. STRUCTURAL AND OPTICAL PROPERTIES OF ZINC MANGANESE OXIDE

Characterization of MOCVD-grown ZnMnO was performed and is discussed.

4.9.1. Structural Properties. Structural and crystal properties of ZnMnO were investigated using XRD and EDX.

Figure 4.35 shows an X-ray diffraction pattern of ZnMnO samples E-2, E-3, and E-5. A dominant peak at a 2θ of ~34.5^{o} is observed. Considering sapphire substrate

orientation in the (006) direction, the primary crystal growth or orientation is (002). Slight variations in the peak position and FWHM were observed among these samples as summarized in Table 4.10, could be due variations in Mn source injection or changes in the growth conditions. However, the samples show similar phases and crystal orientations. The peak at (002) could be a combination of the primary ZnO like (002) structure with Mn_2O_3 (222), Mn_3O_4 (211) Mn_3O_4 (103), MnO (111), and Mn_2O_3 (222) structures. The diffraction peak at ~31.7° could be from a ZnO-like (101) structure, and the peak at ~37° could be a combination of ZnO-like (101), MnO_2 (211), Mn_2O_3 (400), and Mn_3O_4 (004) structures.

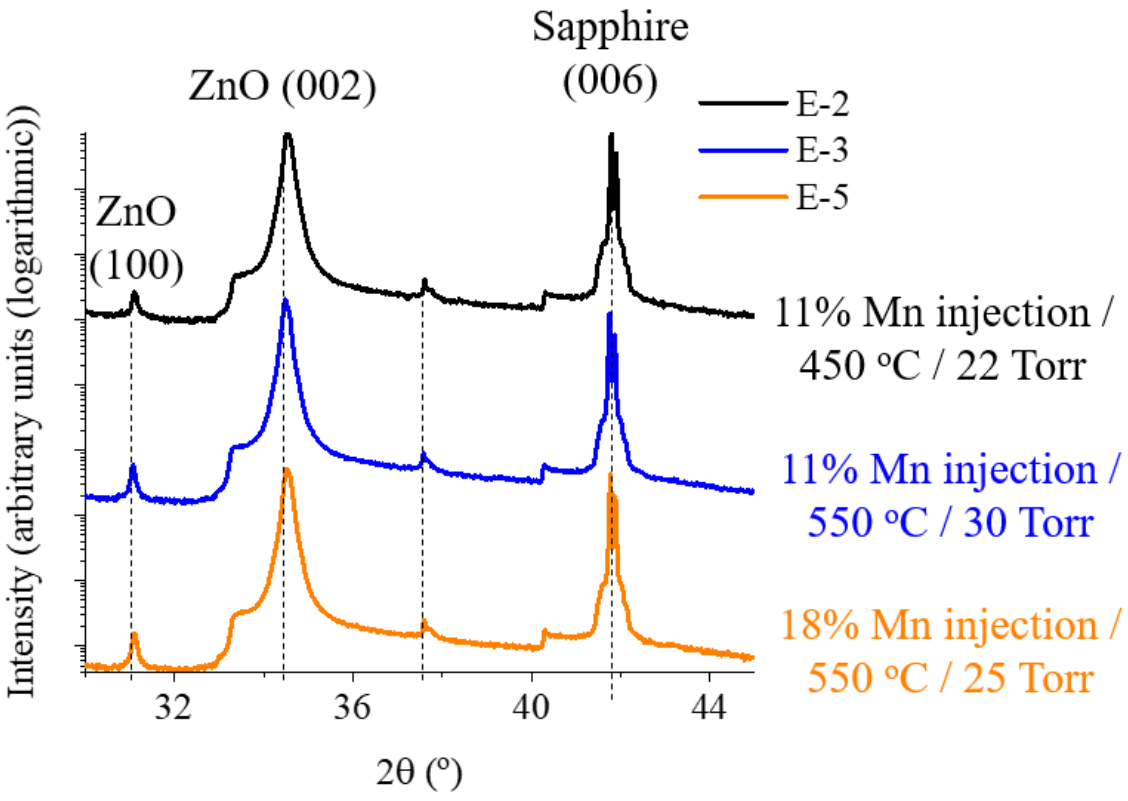

Figure 4.35 X-ray diffraction results of MOCVD-grown ZnMnO.

ZnMnO seem to exhibit peaks that could be a combination of several oxidation states of Mn. Mn^{4+} and Mn^{3+} have ionic radii of 0.54 Å and 0.64 Å respectively and are smaller than Zn^{2+} (0.74 Å), while Mn^{2+} has a larger ionic radius of 0.80 Å, hence a systematic peak shift could not be seen due to a mix of several phases of Zn-Mn-O. As compared to ZnNiO samples of Section 1.5, ZnMnO samples showed a higher correlation length.

Table 4.10 X-ray diffraction results of ZnMnO on sapphire

Sample #	(002) 2θ peak position (°)	(002) peak FWHM (arcsec)	Lattice constant c (Å)	~ Vertical correlation length (Å)
E-2	34.54	694	5.187	431
E-3	34.48	603	5.196	496
E-5	34.52	674	5.190	444

EDX spectra (Figure 4.36) showed Mn content of 0.28 weight % and 0.34% atomic in ZnMnO growth with 11% Mn source injection (sample # E-3). Zn weight and atomic % were 77 and 47 respectively, and oxygen weight and atomic % were 20 and 50 respectively. A reduced incorporation, as compared to the Mn source injection, could be due to a low decomposition / adsorption rates of the reactants, at the specific growth conditions. Mn content in ZnMnO with up to 25% Mn source injection could then be estimated to be in a range of 0.4-0.6%.

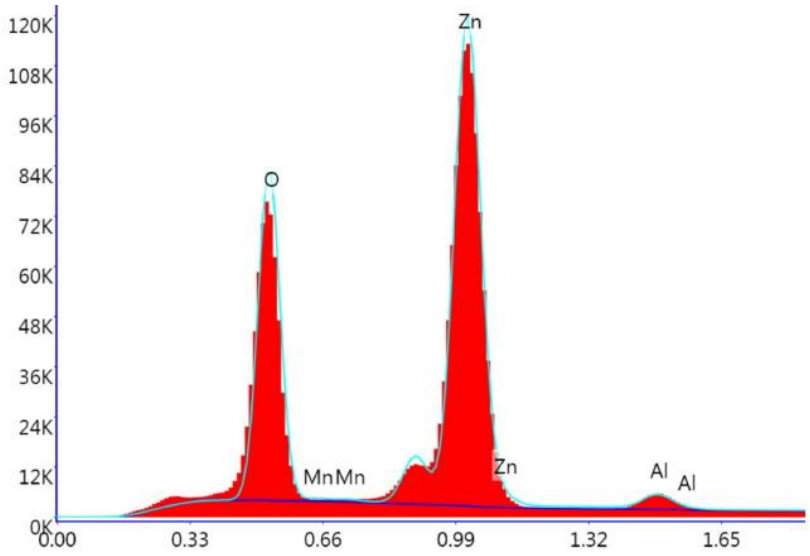

Figure 4.36 Energy dispersive X-ray spectroscopy of MOCVD-growth ZnMnO.

4.9.2. Optical Properties. Photoluminescence and absorption measurement were performed to investigate the optical properties of MOCVD-grown ZnMnO.

As shown in Figure 4.37, photoluminescence results showed clear UV emission peaks in all the samples. Intensity of the peak significantly reduced in sample E-7 with Mn source injection of 25%. Some of the samples show low intensity broad bands around 2.2 eV due to oxygen vacancies, zinc interstitials, or other defects.

Figure 4.38 shows the absorption spectra of ZnMnO samples. All the samples show sharp absorption edges. The sites occupied by Mn in ZnMnO could vary as per the growth conditions, and Mn content, and could result in varying absorbance intensities.

Tauc plots were plotted and bandgaps of ZnMnO samples were determined as shown in Figure 4.39. Lowest and highest band-edges observed are 3.275 eV with 25% Mn source injection and 3.291 eV with 0% and 11% Mn source injection in ZnMnO.

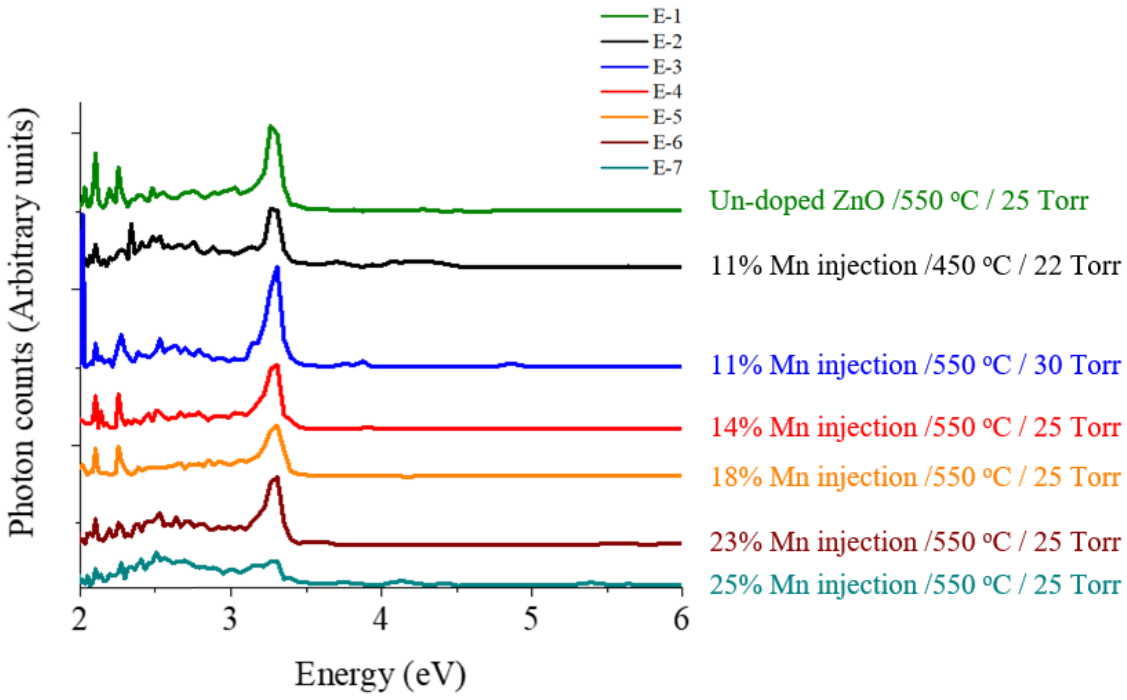

Figure 4.37 Photoluminescence spectra of MOCVD-grown ZnMnO.

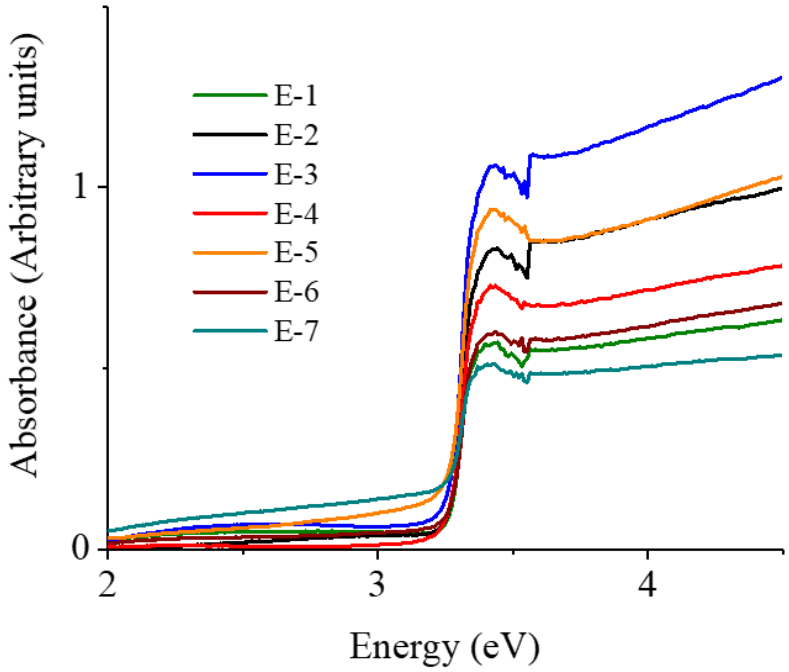

Figure 4.38 Absorption spectra of MOCVD-grown ZnMnO.

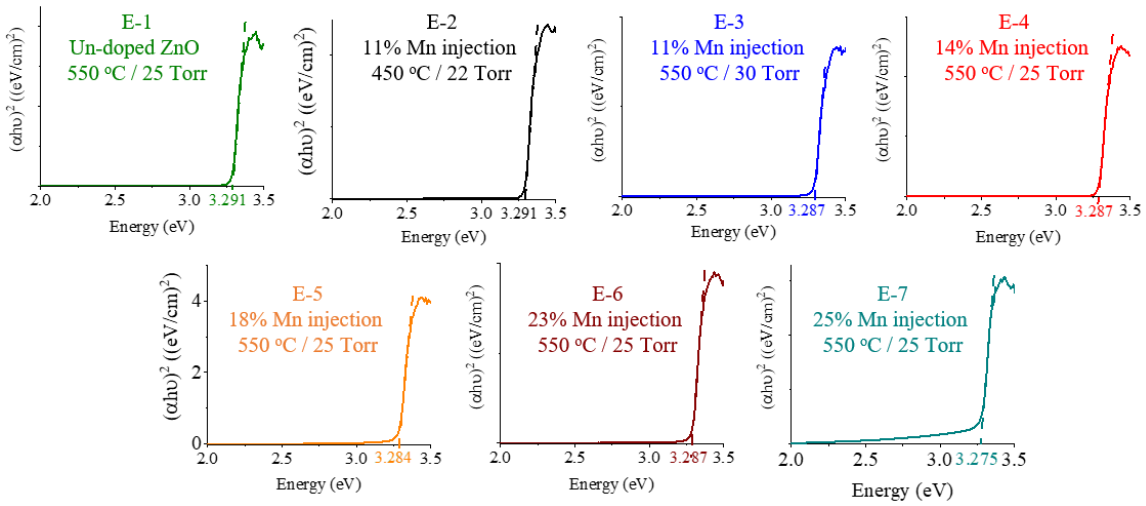

Figure 4.39 Tauc plots of MOCVD-grown ZnMnO.

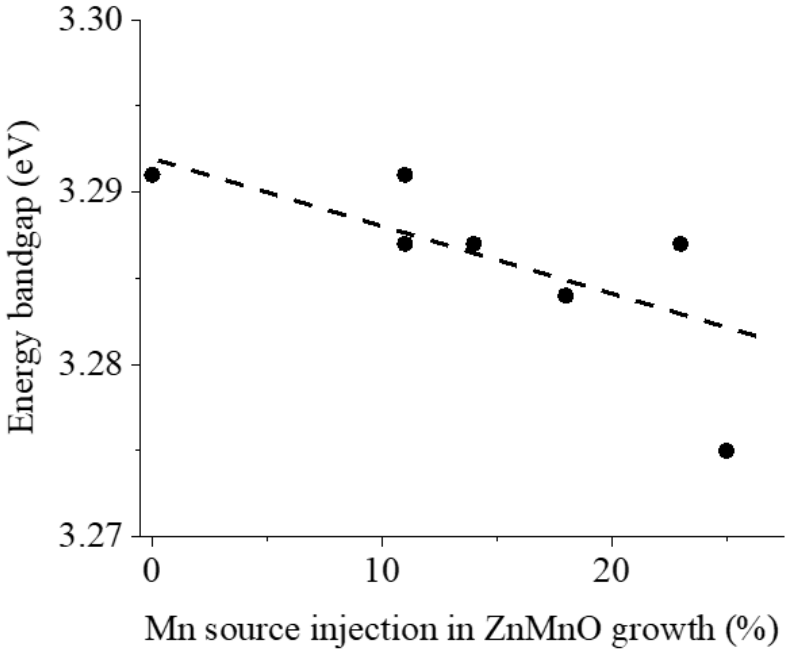

Figure 4.40 Variation in band gap of MOCVD-grown ZnMnO with Mn source injection in ZnMnO growth at varying growth conditions (Dotted line: Guide to the eyes).

Figure 4.40 shows the variation and overall trend of bandgap of ZnMnO with Mn source injection. Mn dopant could introduce energy states close to the valence band (or activate energy states close to conduction band) in zinc oxide resulting in the red-shift.

4.9.3. Effects of Annealing. Post-growth annealing was done at 1000 ^{0}C for 30 mins in air to possibly activate energetically favorable sites for Mn that could further reduce or tune the bandgap.

X-ray diffraction results of as-grown and annealed ZnMnO samples with 11% Mn source injection are shown in Figure 4.41 and summarized in Table 4.11.

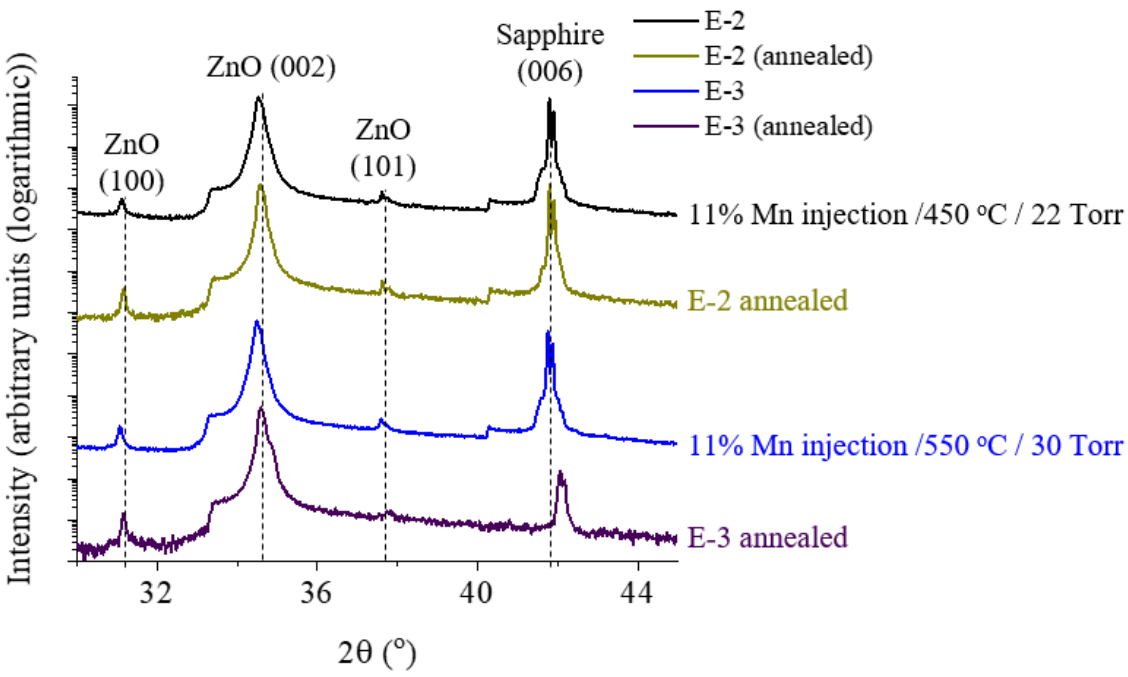

Figure 4.41 X-ray diffraction results of as-grown and annealed ZnMnO.

No significant variation in the peaks and phases or crystal structure is observed upon annealing. The FWHM reduced and vertical correlation lengths increased upon

annealing. An improvement in the crystal quality of ZnMnO upon annealing points towards a better intermix of ZnO-like phases (especially (002)) with Mn_xO_y related phases which is also correlated with the crystal structure better.

Table 4.11 X-ray diffraction results of as-grown and annealed ZnMnO.

Sample #	(002) 2θ peak position (°)	(002) peak FWHM (arcsec)	Lattice constant c (Å)	~ Vertical correlation length (Å)
E-2	34.54	694	5.187	431
E-2 annealed	34.56	600	5.184	500
E-3	34.48	603	5.196	496
E-3 annealed	34.58	584	5.181	512

Photoluminescence spectra as acquired in Figure 4.42 show a reduction in the peak at ~3.3 eV with onsets of peaks at ~4 eV with annealing. Annealing could result in introduction of non-luminescent impurity states and luminescent defect centers. This could be caused by possible phases of Mn with O or Zn or related defects in zinc oxide.

While photoluminescence spectra at ~3.3 eV is deteriorated, absorption spectra as shown in Figure 4.43 showed higher intensities in annealed samples. In addition to non-luminescent centers, Mn incorporation could also introduce energy states near the valence or conduction band in ZnMnO resulting in sharp absorption around 3.3 eV.

Figure 4.44 shows the Tauc plots that were used to calculate the bandgaps of annealed samples. A reduction in bandgap with annealing is seen in samples that were grown with 11% Mn source injection. As-grown samples have bandgap of 3.29 eV and annealing reduced it to 3.27 eV.

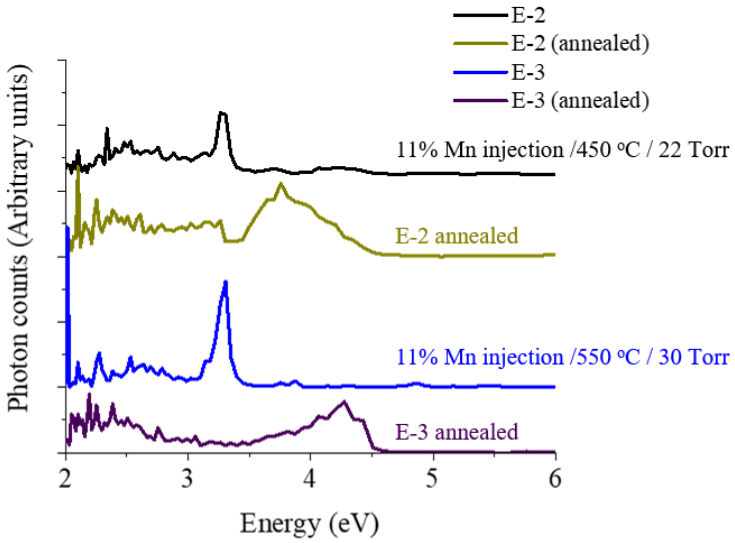

Figure 4.42 Photoluminescence spectra of as-grown and annealed ZnMnO.

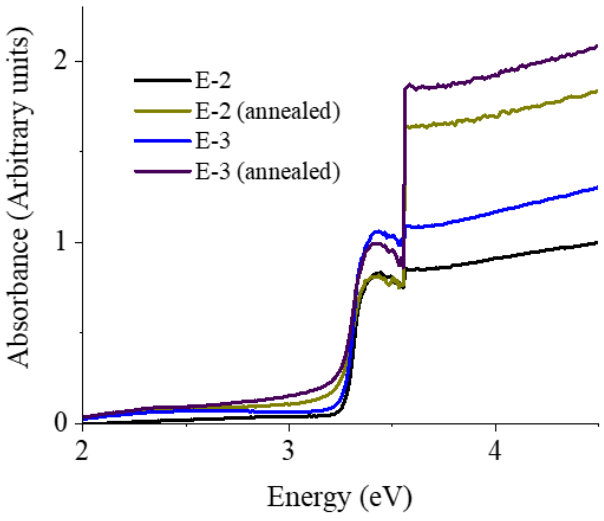

Figure 4.43 Absorption spectra of as-grown and annealed ZnMnO.

Annealing ZnMnO favors the intermixing of ZnO like phases with possible Mn-related phases resulting in a better crystal quality. Energy states near the valence or conduction band are introduced or activated which result in a reduction in the bandgap. Also, centers that affect existing luminescence, along with introduction of additonal luminescent defect centers are activated with annealing.

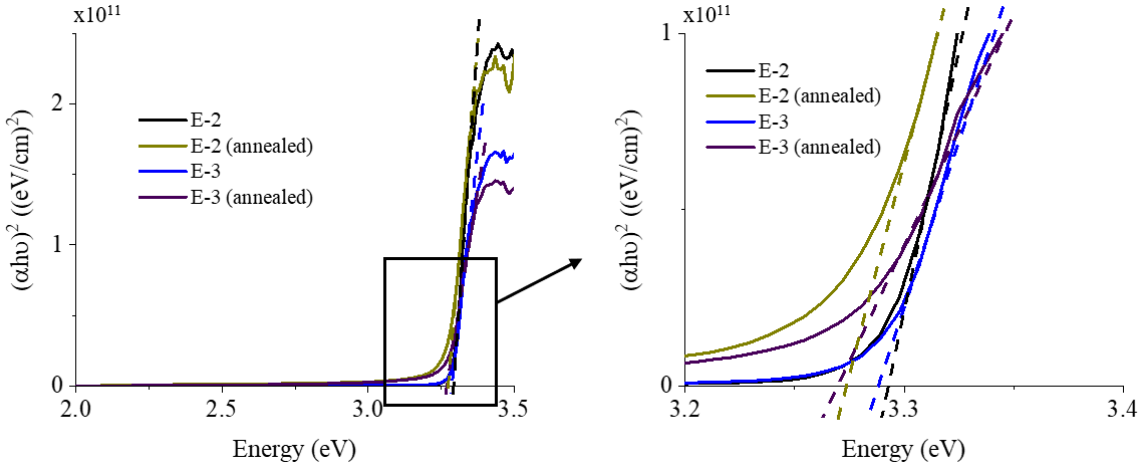

Figure 4.44 Tauc plots of as-grown and annealed ZnMnO.

4.10. HALL EFFECT ANALYSIS OF TRANSITION-METAL DOPED ZINC OXIDE

Initial Hall Effect analysis of Ni-doped ZnO (C-2) (450 ^{o}C/30 Torr) was performed. Electrical characterization showed a carrier density of 2.5 x 10^{16} cm^{-3}, variable mobility range from -200 to -50 $cm^2V^{-1}s^{-1}$ and a resistivity of 3 Ω-cm. Hall Effect results (normalized) are shown in Figure 4.45. The Hall resistivity and 4-point Van der Pauw resistivity showed similar trend and had similar changes with applied magnetic field. Hall Effect is not clearly observed. However, response to applied magnetic fields is seen. This points towards the presence of scattering centers in Ni-doped ZnO due to Ni-related phases

which were also detected in X-ray diffraction measurement. Carrier-mediated mechanism seems less likely in such cases.

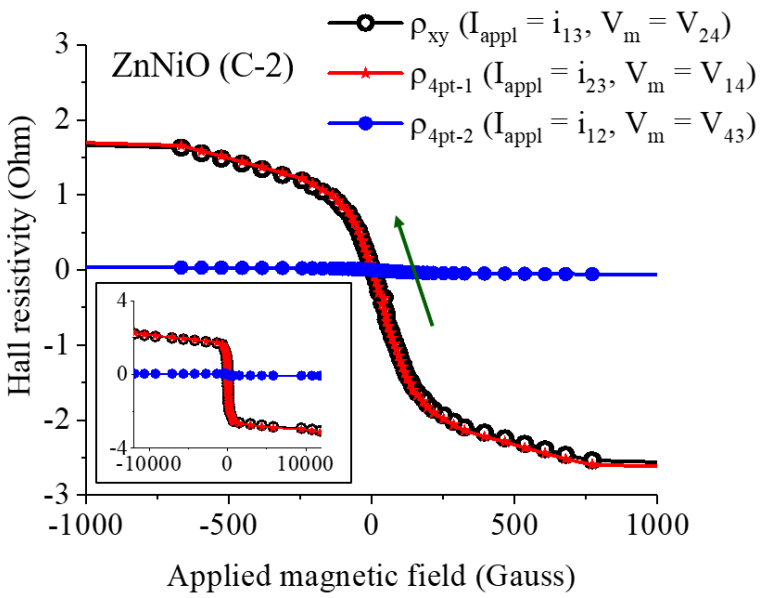

Figure 4.45 Initial Hall Effect analysis of Ni-doped zinc oxide

Measurement and analysis of Ni and Mn-doped ZnO grown under different growth conditions and pos-processed, for example by annealing, are needed to clearly understand the magnetic properties and their mechanism in transition-metal doped zinc oxide.

4.11. CONCLUSION – TRANSITION METAL DOPED ZINC OXIDE

Transition metal-doped zinc oxide are grown by metal-organic chemical vapor deposition and their structural and optical characteristics are investigated in this section. MOCVD resulted in a good crystal quality and sharp absorption band edges. Un-doped

zinc oxide showed a consistent bandgap with varying precursors' flow rates, and with varying possible vacancy and interstitial related native defects.

Ni and Mn were doped in ZnO. Ni-doped zinc oxide showed a reduction in bandgap down to 3.26 eV (1.2% Ni). Reduction in bandgap depends on the growth conditions; low pressure ($\leq$ 30 Torr) and a temperature close to the decomposition temperature of the metal-organic precursors (and in a mass-transport regime) result in better crystal quality, sharp band-edges and are optimum for the growth of ZnNiO. Annealing deteriorated the photoluminescence spectra but resulted in a bandgap reduction in ZnNiO.

Mn-doped ZnO showed a peak shift relative to un-doped ZnO with a good crystal quality possibly, due to intermixing of ZnO like crystal structure with Mn-related phases. Bandgap of ZnMnO reduced down to 3.275 eV with Mn source injection up to 25%, and down to 3.271 eV in annealed sample that was grown with 11% Mn injection. Annealing improved the crystal quality and reduced the bandgap which points to a better intermix of Mn in ZnO. However, photoluminescence response deteriorated due to incorporation luminescent defect centers, and impurities that affected existing luminescence.

Doping zinc oxide with transition metals by MOCVD does show a potential for bandgap tunability and annealing could further help to control it. Several types of energy states depending on the oxidation states of the dopant could be introduced in ZnO leading to bandgap tunability properties. A controllable introduction or activation of energy states in zinc oxide by transition-metal doping could enable the development of multi-junction solar cells with minimum interface related defects and better efficiency, along with potential spintronic and thermoelectric devices wherein dopant-induced properties could make ZnO more suited for the various applications.

5. FIELD-EFFECT SCHOTTKY SOLAR CELLS

5.1. SOLAR CELLS

There has an increasing need and interest in the development and optimization of solar cells targeted towards a high conversion of solar energy into electricity, with a low cost and simple devices fabrication process[345–352]. Silicon has been extensively used to build solar cells, and the devices fabrication technology for silicon solar cells is well developed, however, the power conversion efficiency is practically limited to ~25%, as seen in Figure 5.1. An indirect band gap of 1.1 eV in silicon introduces a limiting factor on the photon absorption and on the resulting energy difference between the valence band and conduction band edges typically responsible for open circuit voltages[353–357]. Using alternative materials for silicon and developing multi-junction solar cells with silicon as one of the active layers, could help address the power conversion efficiency related limitations in solar cells.

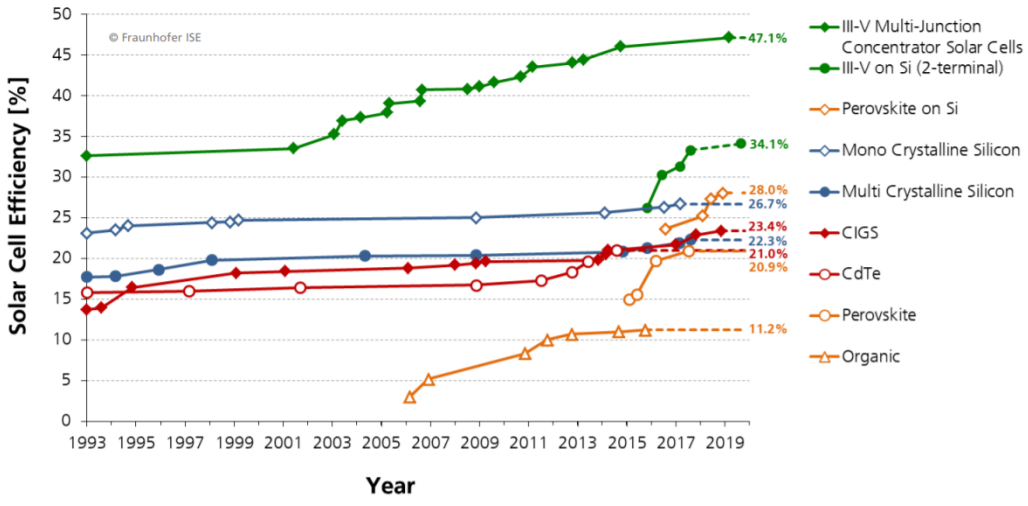

Figure 5.1 Efficiency of solar cells with different active layer materials[358].

Alternative materials to silicon such as III-V and II-VI compound semiconductors, for example, gallium arsenide (GaAs) and zinc oxide (ZnO), have a direct bandgap and a potential for tunability in the bandgap making them also suitable for tandem structures[359–367]. Figure 5.2 shows possible variations in bandgaps of compound semiconductors with alloying. For example, GaAs has a bandgap of 1.4 eV and AlAs of 2.2 eV and doping Al in GaAs could result in intermediate bandgaps. Moreover, these materials have a minimum lattice mismatch which minimizes the losses associated with crystal and interfacial defects[368–370]. The number of interfaces and layers in devices structures increase as passivation, anti-reflection, transparent conductive materials, and carrier-blocking are added; existence of more lattice matched layers could help towards maintaining a good solar cell's efficiency[371–376].

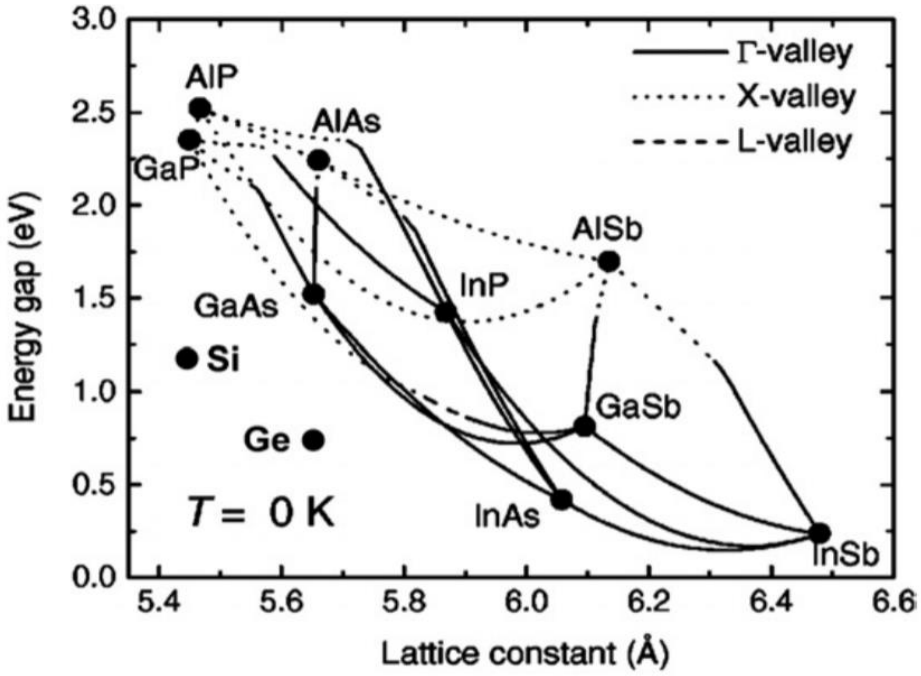

Figure 5.2 Energy gap and lattice constants of selected compound semiconductors[377].

Another way to achieve better solar cells performances is multi-junction solar cells[365,366,378]. In single-junction solar cells, material used as an active layer absorbs energy equivalent to its energy bandgap from the incident energy. The excess energy is lost as heat, and low energy incident waves are transmitted. Using several active layers in a tandem structure could help to achieve better efficiency as each of these layers have different bandgaps[379–381]. Material with the highest bandgap could be the top layer, and transmitted energy could be absorbed by lower energy bandgap materials towards the bottom of a tandem structure. Compound semiconductors such as GaAs could be used as top or intermediate layers in multi-junction solar cells. One of the challenges in using compound semiconductors as active layers are the difficulties in producing high quality p-type materials, due to native defects that could deteriorate the efficiency of solar cells.

Schottky junction solar cells, built by a junction of n-type semiconductor and metal could be an optimum choice, as they do not involve a p-type layer, and also provide a necessary space-charge region and photo-current that is necessary for a photovoltaic response[200,382]. Also, fabrication of Schottky-junction solar cells is cost-effective and involves simple device processing. However, the depletion region in Schottky solar cells is narrower than p-n junction solar cells, that could affect the effective performance of a solar cell.

The Fermi levels of semiconductors needs to be matched with the metals so that suitable energy barrier heights are achieved at the interfaces. Figure 5.3 shows Schottky barrier heights formed using commonly used metal contacts with Si and GaAs.

Metal contact	Work function ($q\phi_m$; eV)	n-Type semiconductor: Barrier height ($q\varphi_{Bn}$; eV) GaAs	Ge	Si	p-Type semiconductor: Barrier height ($q\varphi_{Bp}$; eV) GaAs	Ge	Si
Ag	4.26	0.88	0.54	0.78	0.63	0.50	0.54
Au	4.80	0.90	0.59	0.80	0.43	0.30	0.34
Al	4.25	0.80	0.48	0.72	0.61[f]		0.58
Pt	5.30	0.98[a]		0.90			0.22
Cr	4.50	0.80[b]		0.61			0.50
Ni	4.50	0.83[c]		0.61			0.51
Pd	5.12	0.78		0.81			0.42
Ti	4.33	0.75[d]					
W	4.60	0.90[e]	0.48	0.67			0.45

Figure 5.3 Table showing Schottky barrier heights of junctions made of common metals with Si, Ge, and GaAs[377].

In this section, a strategy called as Isolated Collection and Biasing Solar Cells (ICBS) to increase the solar cell efficiency, especially of Schottky junction solar cells is investigated. A gate contact is introduced in the Schottky junction solar cells, that induces an external electric field in the space-charge region but stays isolated from the carrier collection layer. Optimizing this biasing layer or gate contact could effectively enhance the performance of cells.

5.2. FIELD-EFFECT SCHOTTKY SOLAR CELLS THEORY

Field-effect passivation involves design and development of Schottky solar cells in which an external gate contact is introduced and applying a gate voltage could increase the

Schottky barrier height and the resulting solar cell performance. In addition to serving a strategy for general solar cells, it helps to overcome challenges such as thermionic emissions or tunneling of carriers in reverse or undesired direction that affect solar cells performances and happen to reduce the barrier height.

In this work, Isolated Collection and Biasing Solar Cells (ICBS) are developed in which a bias layer is added to the Schottky solar cell and is isolated from the collection contact to induce external band bending within the depletion region, thereby maintaining (or increasing) the Schottky barrier height. Contacts and circuits are connected to the collection layer while the bias layer is floating. The external band bending introduces additional electron-hole pair separations that result in a higher photo-current as compared to conventional Schottky solar cells. The band-bending in a typical n-type Schottky junction solar cell is shown in Figure 5.4 (a), wherein a load resistor reduces the barrier height and potentially deteriorates the solar cell's performance. Effect of external band-bending in an ICBS solar cell is shown in Figure 5.4 (b). As seen, the Schottky barrier height is still maintained due to the external bias layer, which also results in more electron-hole pairs due to the field-effect. Irrespective of the barrier height under the collection contact which could reduce when connected to resistors and other circuits, the bias layer maintains the necessary barrier height.

Figure 5.5 shows the schematic of an ICBS solar cell. The collection layer and ohmic layer are probed to electrically integrate the solar cell in external systems. The performance of the solar cell could be further improved by adding interfacial layers such as passivation layers to reduce interface defects (that could trap carriers) and increase the solar spectrum absorption.

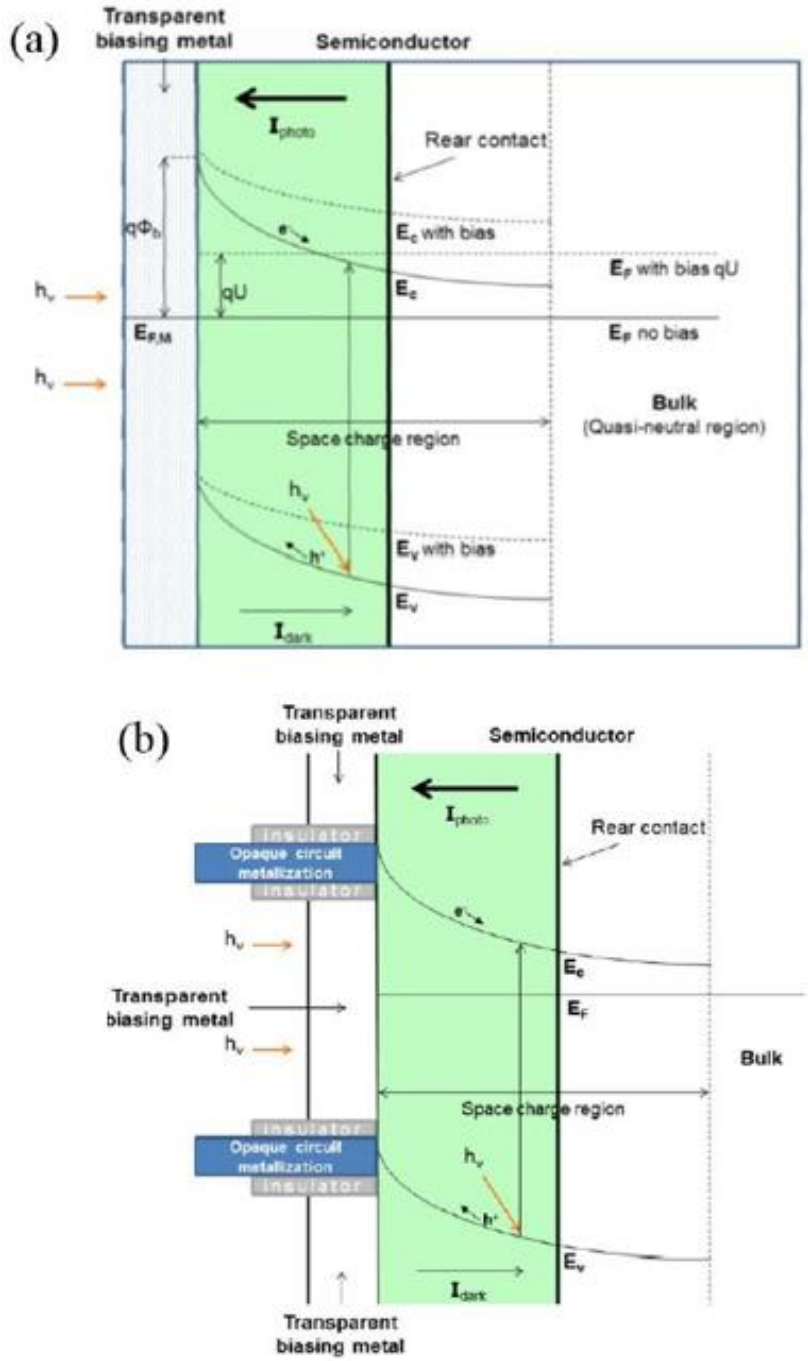

Figure 5.4 (a) Band-bending in n-type Schottky junction cell under illumination with carrier collection contact in the space charge region, and (b) Effect of isolated bias layer and external band-bending in ICBS solar cell [from Proposal "Development of Next General Multijunction Solar Cells", Copyrights by Columbus Photovoltaics LLC, not allowed for distribution].

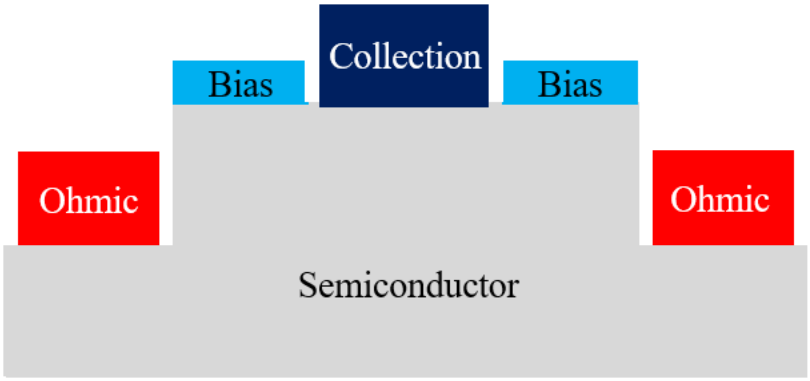

Figure 5.5 Schematic of an ICBS solar cell.

Theoretical modeling of an ICBS solar cell using COMSOL's semiconductor module is shown in Figure 5.6. The effect of isolation of the biasing layer from carrier collection layer is understood. As seen in Figure 5.6 (a), a Schottky barrier height of 0.5 eV is maintained when there is no external resistor or circuit that could affect the barrier height under collection contact. A potential of 0.5 eV is constant for both, the biasing and collection layers. To emulate a scenario of a solar cell being connected in an external circuitry, an external voltage drop is applied to the collection layer in Figure 5.6 (b). It is observed that a reduction in barrier height is seen under the collection layer due to the applied voltage drop. On the other hand, the barrier height at the bias layer stayed consistent irrespective of an external circuitry.

5.3. FABRICATION OF GALLIUM ARSENIDE FIELD-EFFECT SCHOTTKY SOLAR CELLS

This section discusses about the fabrication process of the ICBS GaAs-Ag solar cells. The overall process of building a quasi-vertical structure ICBS solar cells consist of photolithography using appropriate masks and deposition of intended metal layers step by

step, in a clean environment. GaAs was the semiconductor, Ag was the Schottky contact, and Au was the metal contact used. Two sets with different passivation layer thicknesses were built, one with ZnO/Al_2O_3 2nm/18nm and other with 2nm/8nm.

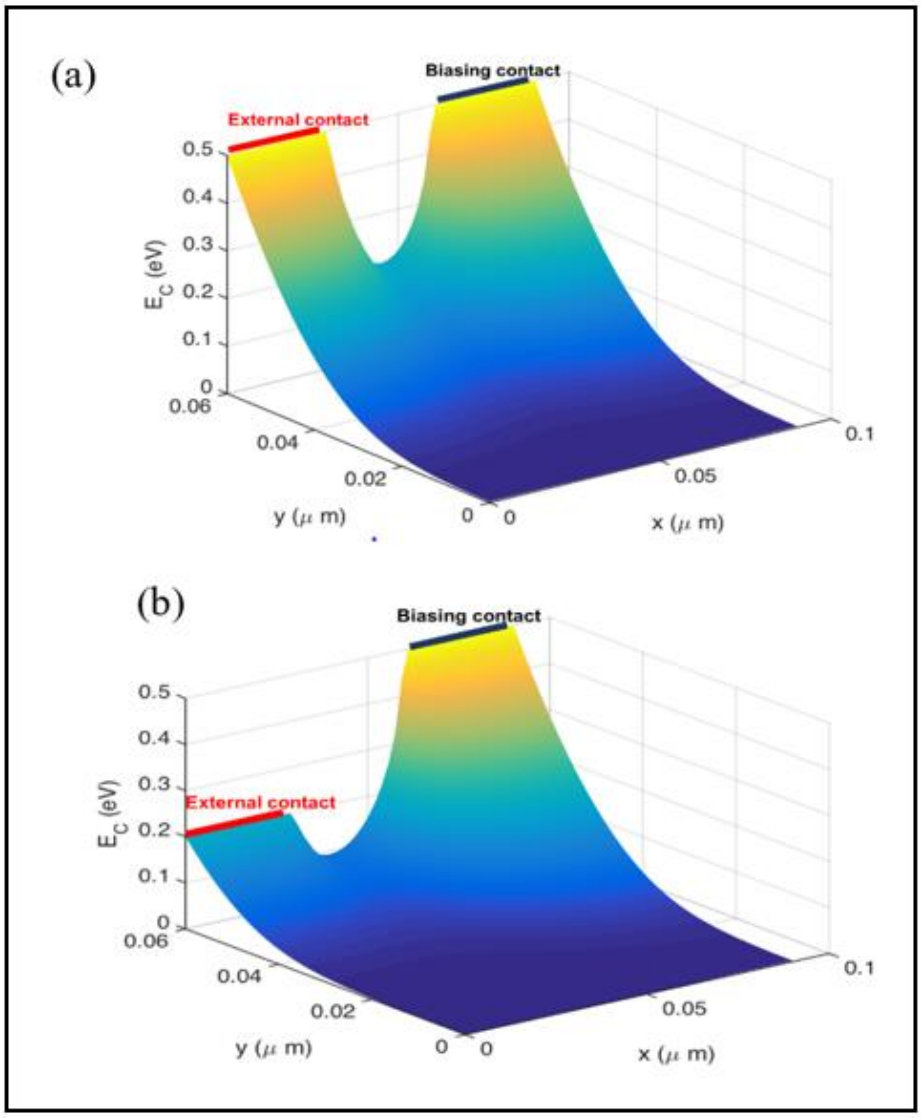

Figure 5.6 Theoretical modeling of energy band structure of ICBS solar cell (a) No load resistor or external circuit connected to the collection layer, (b) An external voltage drop of 0.3 V at the collection contact [from Proposal "Development of Next General Multijunction Solar Cells", Copyrights by Columbus Photovoltaics LLC, not allowed for distribution].

Several photomasks are used in this device fabrication process depending on the intended pattern, and desired layer to be deposited. Figure 5.7 shows examples of photomasks that could be used in the device fabrication process. Different masks are used for mesa etch of bare GaAs substrate, ohmic contact, bias, and Schottky layers. These masks have patterns consisting of fingers slots and designed in various geometries. Two types of configurations are used in this work – asymmetric collection layer geometry with a contact probe towards one end, and symmetric collection layer with a contact probe area at the center with fingers protruding perpendicular from this area. More and thinner fingers result in a better contact area of the Schottky metal layer with semiconductor substrate. On the other hand, a larger area of contact of the bias layer with semiconductor is conducive for photovoltaic response but increasing the number of fingers could lower this. 5 and 15 fingers were determined to result in an optimum configuration and used for the devices. An optimum gap between the biasing and Schottky contacts on the semiconductor is crucial for proper isolation, such as the generation of localized electron-hole pairs is maximized while the shunt and leakage currents are minimum. An optimum gap of 10 μm between the Schottky or collection and biasing layer fingers was used.

Figure 5.8 shows an overview of ICBS solar cells fabrication. GaAs with n-type carrier density in the order of 10^{17} cm^{-3} and a thickness of 400 μm was used as the semiconductor substrate. 1x1 cm^2 size pieces are cut and cleaned using a routine of acetone, methonal and native oxide etch using dilute HCl. A Shipley S1813 positive photoresist is spun on the samples at 4000 rpm and then baked. Mask aligner MA/BA6 is used to selectively expose the piece to UV light using a mesa etch mask. H_3PO_4:H_2O_2:H_2O in

proportion of 3:1:40 for 120 seconds was used for the mesa etch resulting in a structure with step size of about 200 nm, as shown in Figure 5.8.

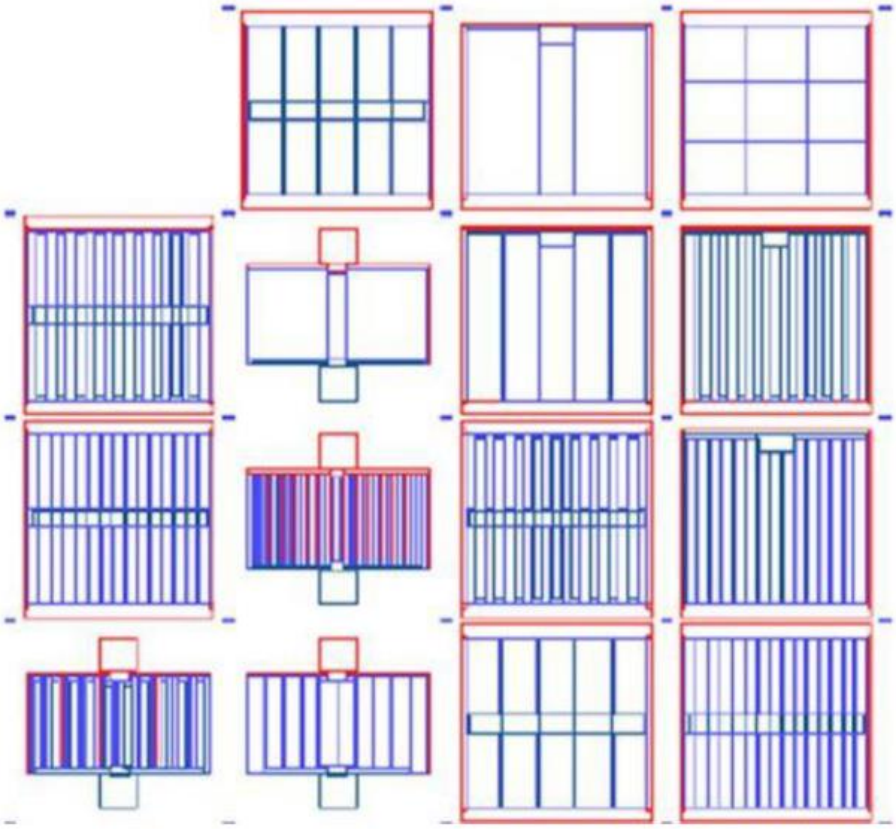

Figure 5.7 Geometries of photomasks [from Proposal "Isolated Collection and Biasing Solar Cells", Copyrights by Columbus Photovoltaics LLC, not for distribution].

An ohmic contact layer is deposited on the samples using e-beam evaporation. Ni/AuGe/Ni/Au with thicknesses of about 5/100/35/50 nm were deposited, as shown in Figures 5.8. The samples were annealed using a rapid thermal annealer MILA-5000 at 440 ^{o}C in forming gas (95% N_2, 5% H_2) environment for 90 seconds.

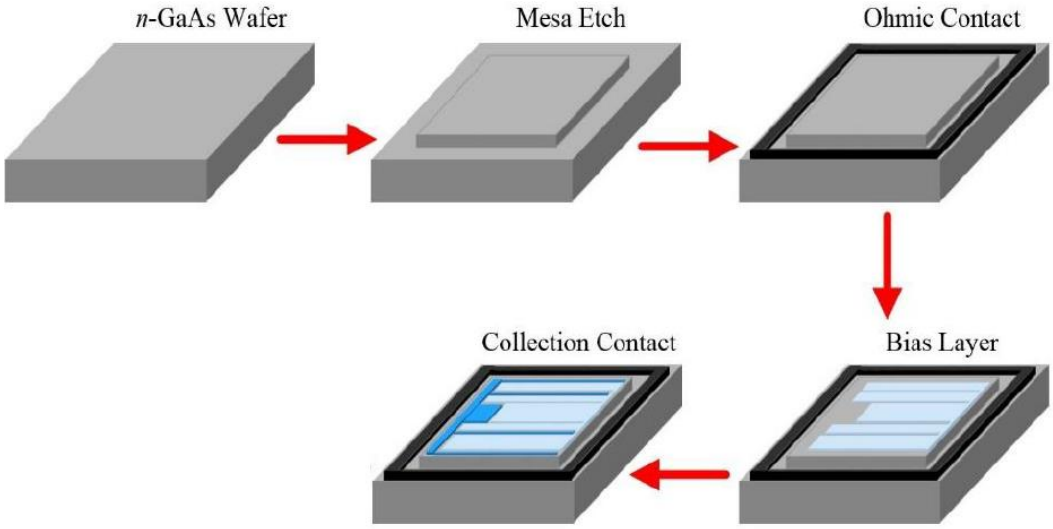

Figure 5.8 Illustration of a typical ICBS device fabrication process [from Proposal "Next General Multijunction Solar Cells", Copyrights by Columbus Photovoltaics LLC, not for distribution].

Surface passivation is achieved by depositing ZnO/Al_2O_3 layer on the samples using atomic layer deposition (ALD) at 200 ^oC in vacuum conditions. Surface passivation could reduce dangling bonds, interface traps, leakage currents, and help towards achieving a better solar cell performance[376,383–385]. Al_2O_3/ZnO has a high dielectric constant and thermal stability and is transparent. Al_2O_3 combined with ZnO could reduce the non-radiation recombination centers at the interfaces, and also maintain a necessary dielectric constant[386–388]. Two sub-sets of solar cells were made, one had a passivation later of 2nm/8nm ZnO/Al_2O_3 and other with 2nm/18nm ZnO/Al_2O_3.

ALD also known as atomic layer epitaxy or molecular layering is an effective technique to grow conformal and uniform oxide layers with thickness of 10 nm or even lower, at low temperatures of 100-400 ^oC. The process is self-limiting, sequential and a

slow reaction kinetics gives control over the properties of the deposited layers[389–393]. Figure 5.9 shows a schematic of an ALD process[390].

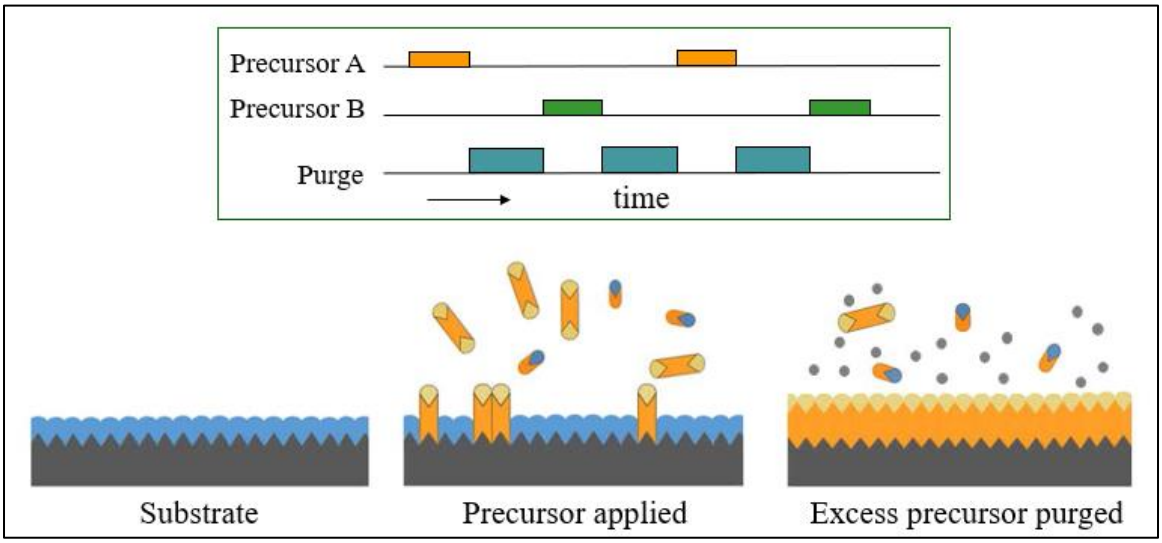

Figure 5.9 Working principle of atomic layer deposition with a sequential flow of two precursors and carrier gas[390].

Following deposition of the passivation layer, a bias layer of 5 nm Ag is deposited using the respective masks and photolithography steps. A pre-treatment to etch native oxide is performed in Piranha solution H_2SO_4:H_2O_2:H_2O (1:1:50) and HCl:H_2O (1:1) for 5 seconds before Ag deposition.

A Schottky collection pattern is developed and the Ag and ZnO/Al_2O_3 layer is etched as shown in step (4) of Figure 5.10, to make an undercut and deposit Schottky layer directly on the semiconductor substrate. HNO_3:HCl:H_2O (1:0.5:2) (10 seconds) and 5% H_2O_2 (60 seconds) were used to etch Ag and Al_2O_3/ZnO respectively. Schottky Ni/Au of 5/100 nm layer is deposited as shown in step (5) of Figure 5.10 after a pre-treatment step of H_2SO_4:H_2O_2:H_2O (1:1:50) and HCl:H_2O (1:1). At the last step, a bias contact layer of

100 nm is deposited using a bias contact mask and a pre-treatment dip in HCl:H_2O (1:1). The step by step device fabrication process is summarized in Figure 5.10.

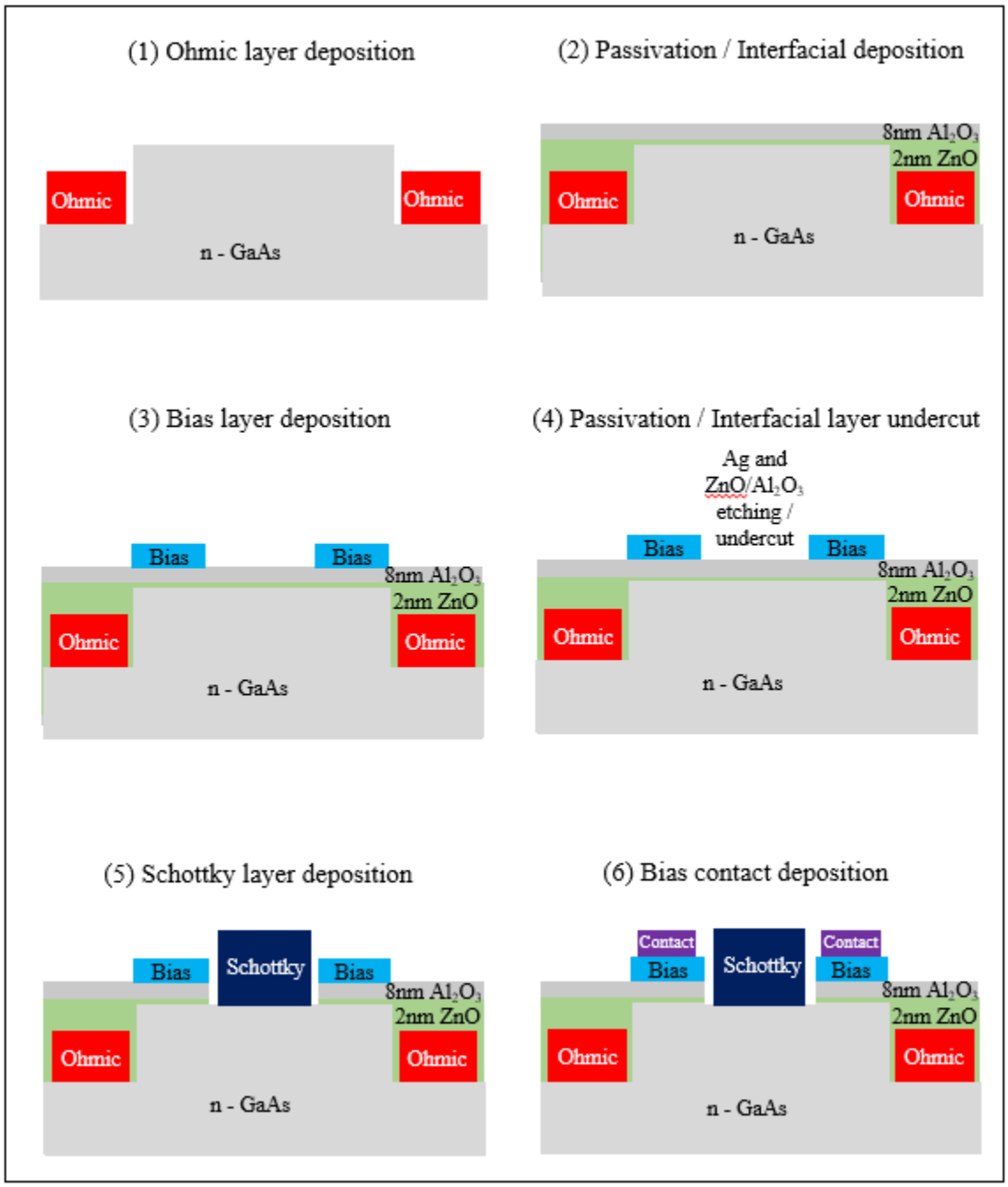

Figure 5.10 Overview of ICBS device structures through the fabrication process.

5.4. GALLIUM ARSENIDE FIELD-EFFECT SCHOTTKY SOLAR CELLS CHARACTERIZATION AND RESULTS

Electrical characterization of developed ICBS solar cells was performed to evaluate the diode-like behavior and photovoltaic response with the gate effect. Current-voltage between Schottky collection and ohmic contacts were probed as shown in Figure 5.11, under dark and illumination conditions. The illumination system was calibrated, and power used was 100 mW/cm^2 equivalent to 1 sun AM1.5. I-V characteristics of the best performing ICBS solar cells are shown in Figure 5.12.

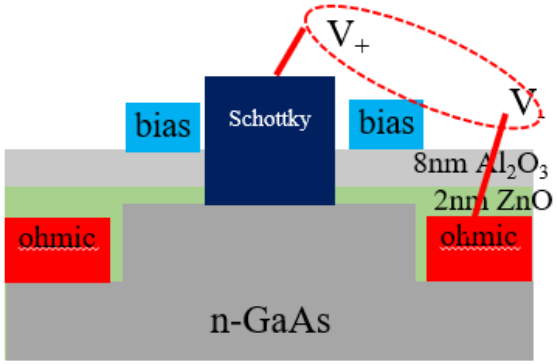

Figure 5.11 ICBS solar cells for electrical characterization.

The solar cells clearly show diode behavior under both dark and illumination conditions. Response under illumination confirms the photovoltaic properties of the built devices. Open circuit voltage (V_{OC}) up to 150 mV, and short circuit current (I_{SC}) up to 5 µA were observed. The response was similar for devices with ZnO/Al_2O_3 layer of 2nm/18nm and 2nm/8nm thicknesses. The GaAs substrate in the solar cells had a carrier concentration on a higher end, which could result in a reverse breakdown at 2-3 V and shows signs of a high reverse saturation current density.

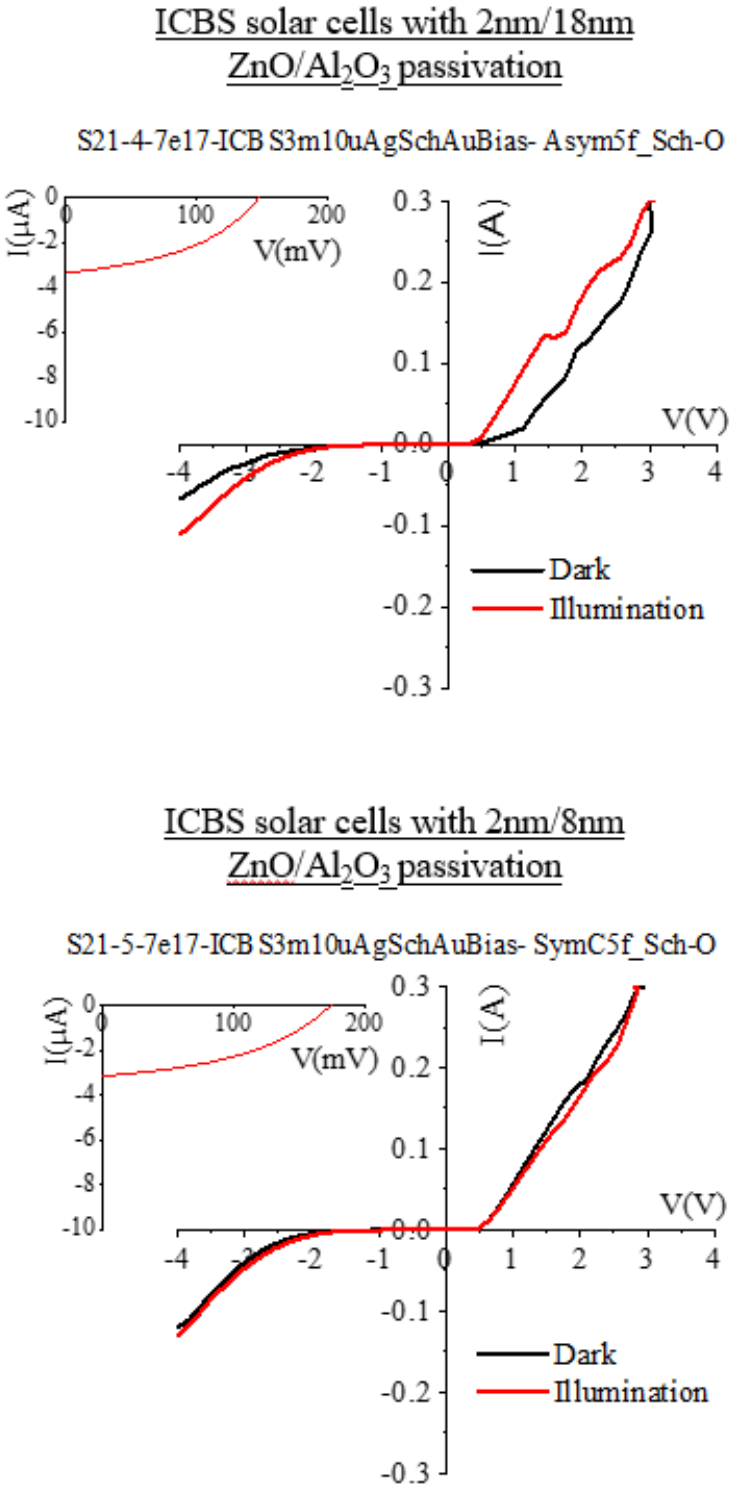

Figure 5.12 Current-voltage characterization results of developed ICBS solar cells.

The device structure could be optimized and depletion region under the external bias layer could be widened by slight variations in material and device structure properties. For example, a GaAs semiconductor substrate with lower carrier concentration in the order of 10^{16} cm^{-3} could be an alternative that could help enhance the performance. The primary objective of this work has been to address a narrower depletion region in Schottky solar cells and understand the gate effect.

A gate voltage is applied to external bias layer and carriers are collected at the Schottky collection layer, as shown in the device structure in Figure 5.13. The setup is updated to add an additional external bias across the gate and ohmic connection through a DC power supply. Measurement were acquired across the Schottky collection and ohmic contact under dark and illumination conditions, as shown Figure 5.13., and external biases (V_{bias}) ranging from -600 to 600 mV were applied. It can be observed that variations in externally applied voltages show changes in the current-voltage characteristics in the reverse as well as forward directions.

The short circuit current and open circuit voltage increase with a positive bias and reduce with a negative bias at the gate contact and stay consistent in the range of -200 to 200 mV applied voltages.

The trend of short circuit current with applied gate voltage is shown in Figure 5.14. The total current collected is the sum of photo-generated current in the solar cell, and a current resulting from a forwards biased bias-ohmic junction. The bias-ohmic contact is rectifying and resulted in an increased carrier flow towards the collection contact, which varied directly with the applied gate voltage.

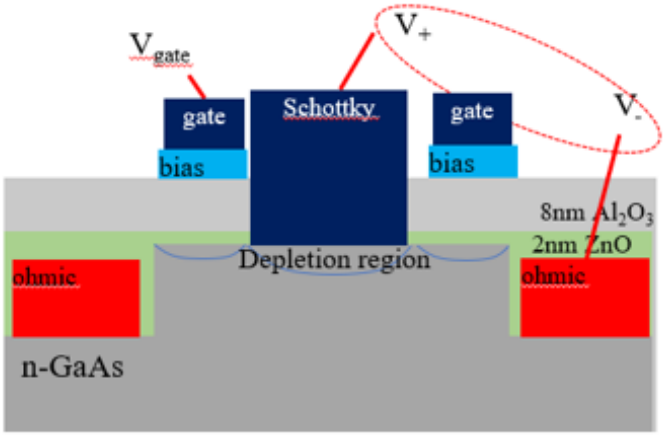

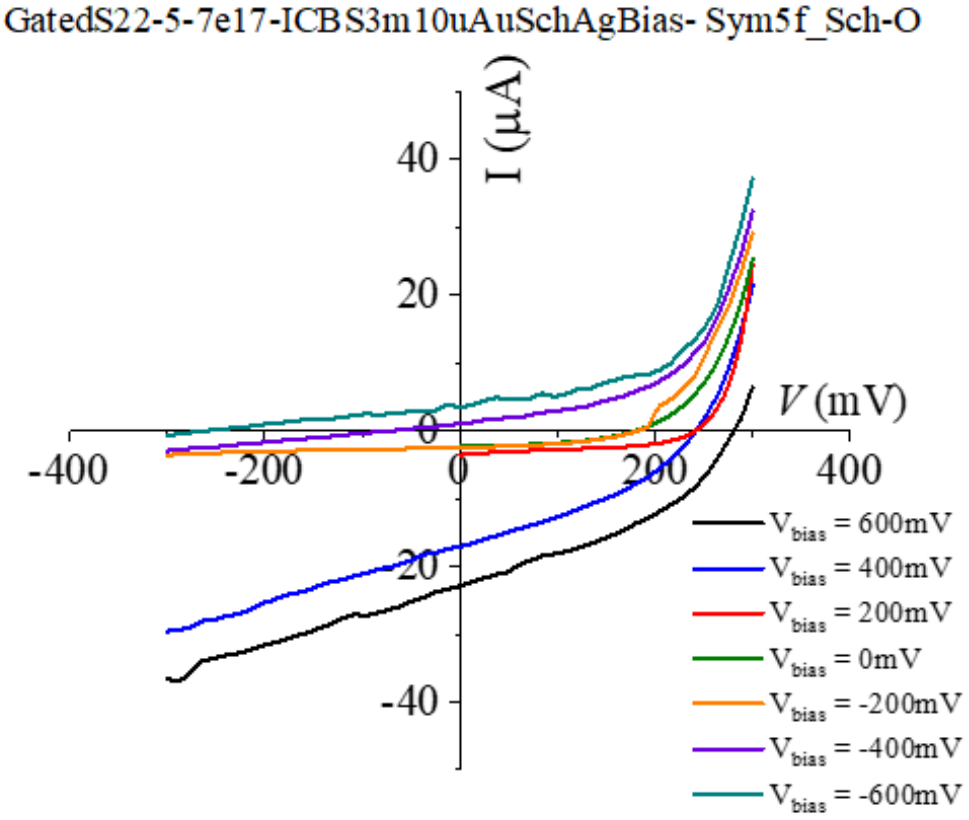

Figure 5.13 Device structure and current-voltage characteristics of gate-effect solar cells under the application of external voltage at the gate.

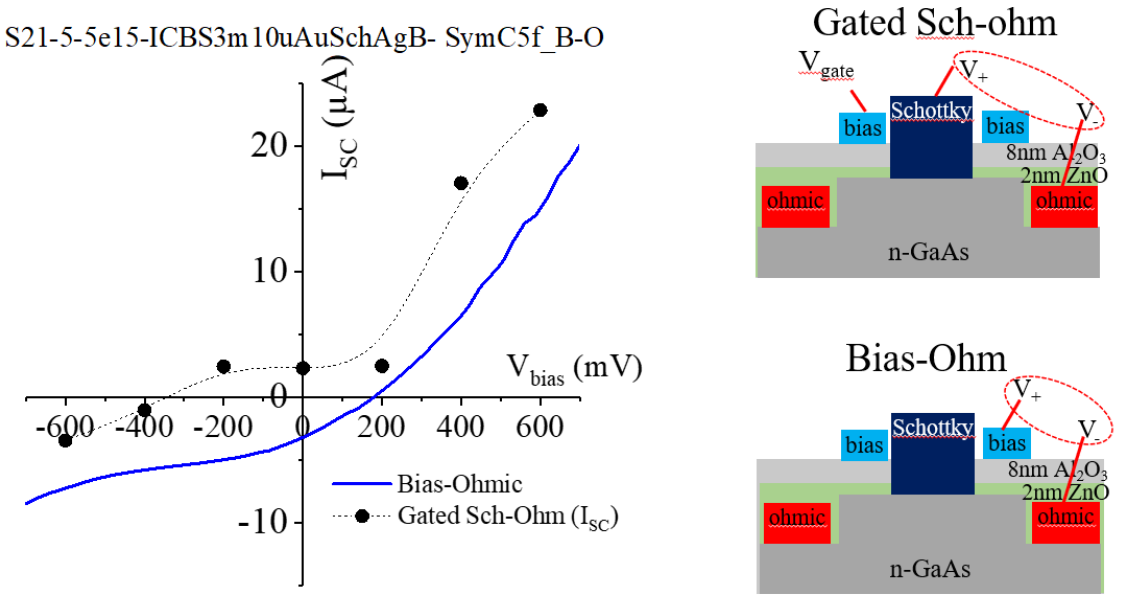

Figure 5.14 Effect of applied gate voltages on the short circuit current in field-effect Schottky solar cells.

5.5. FIELD-EFFECT SCHOTTKY SOLAR CELLS SUMMARY

Field-effect in GaAs/Ag Schottky solar cells was investigated by fabrication of ICBS solar cells and then characterizing the effect of externally applied bias voltages on the solar cell's performance. These device structures help to encounter the p-type doping related challenges faced by compound semiconductors in Schottky junction solar cells, and are cost-effect and relatively easier to build. GaAs/Ag based solar cells were built with ZnO/Al_2O_3 passivation layers of 10-20 nm thickness. The devices showed a photovoltaic response. Application of external gate voltage resulted in an increase in the short circuit current density and open circuit voltage, with contributions from the forward bias-ohmic component and the photogenerated current.

6. EQUIVALENT CIRCUIT MODELING OF INFRARED FREQUENCY SELECTIVE SURFACES

6.1. FREQUENCY SELECTIVE SURFACES

Frequency selective surfaces (FSS) are networks of antenna-like elements that permit electromagnetic scattering from an engineered structure. FSS are been used in microwave range as ground planes and in radome design, photonic crystals, RF interference mitigation, strain sensing and structural health monitoring[394–398]; FSS can be readily scaled down to THz, infrared and even optical frequencies[234,399–404]. There is an increasing interest in the infrared applications of FSS for narrowband and broadband filters[405–409]. They can be used in thermal sensing and imaging applications[402]. Cross shape, metallic ribbons, and square elements have been used as perfect absorbers[405,410–412]. FSS thermo-photovoltaic applications include transmitting solar energy that can be converted to electricity and reflecting other wavelength waves as per the respective engineering[413,414]. FSS act as daytime radiative coolant for buildings and decrease the heating loads[415,416]. Passive radiating surfaces that are not dependent on any active devices help in minimizing energy consumption. Chemical, biochemical sensors, pollutant and refractive index sensing elements can be developed using the infrared FSS technology[410,416–418]. Other applications include spacecraft temperature control, beam-splitters, Fabry-Perot interferometers, polarizers, laser couplers, and infrared sources with unique emission spectrum[410,413–419].

FSS are typically designed using simulation software and complex numerical techniques based on finite element method and finite difference time domain methods[420–422]. These three-dimensional numerical approaches result in accurate modeling and design

of FSS but are computationally intensive and slow down the process of designing[411,413,423–426]. Equivalent circuit models on the other hand, provide an immediate knowledge of the electromagnetic behavior of FSS that is necessary for quick design[413,418]. A change in the behavior of FSS is linked to the corresponding geometrical or functional change using an intermediate circuit model[427,428]. An FSS is considered as an inductor or capacitor or resistor or a combination of these elements depending on its geometry type being patch or slot, and its neighboring FSS elements[411,423–430]. Such modeling typically includes steps by which a simple circuit model is first made and then modified or updated to achieve specific characteristics such as broader band absorption or multiple absorption peaks.

Use of transmission lines to represent dielectrics embedded between several FSS structures or ground planes enhances the accuracy of the equivalent circuit models and helps in understanding the response to waves incident even at off-axis angles[428]. Transmission line based equivalent circuit method (ECM) provides a quick solution for designing an FSS and has an essential physical understanding that, relates electrical or optical characteristics of the FSS to its geometrical structure and material properties[431]. Although the ECM for FSS at microwave frequencies has been extensively studied, it was only recently demonstrated that the lumped-element concept of ECM can be transferred to optical FSS[425,432,433]. The ground plane at microwave frequency typically behaves like a short circuit and does not absorb any electromagnetic waves[429,434]. At infrared frequencies, the dissipative resistance produced by electron gas collision resists the current flow which results in a penetration of more energy into the metal which can no longer be modeled just as a surface resistance[434].

An ECM model for a simple cost-effective infrared FSS absorber which consists of aluminum disk-based Hexagonal Close Packed Array (HCP), dielectric, and ground plane has been developed[399–401]. Overviewing the section, an equivalent circuit model of the HCP FSS at infrared frequencies allows characterization of the lumped parameters, and determining the absorptivity, resonant wavelength and quality factor in the wavelength range of thermal infrared from 8 μm to 14 μm[412]. The influence of geometric parameters on inductance, capacitance, and resistance, extracted by fitting with High frequency structure simulator (HFSS) simulation results, are studied. The resonant wavelengths and corresponding quality factor and absorptivity are investigated by tuning these parameters for impedance matching and comparing those with HFSS results. A baseline ECM is developed in this paper considering normal incident data case.

6.2. HEXAGONAL CLOSE PACKED DISK (HCP) INFRARED FREQUENCY SELECTIVE SURFACE (FSS)

A 2D disk patch FSS illuminated by a normal incident wave is shown in Figure 6.1. The top FSS layer and ground plane is made of aluminum and the intermediate dielectric layer is a polycrystalline silicon[402]. ANSYS HFSS for unit cell is used to obtain the reflection coefficient over an infrared range of 8-14 μm. Geometric parameters of unit cell are shown in Figure 6.1, in which p is periodicity of FSS and d is diameter of FSS disk. Absorption remains stable when incident angle is less than 40^{o} (not shown here), so no significant difference in the values of the circuit elements would be expected.

When the wavelength is equal to the period of FSS, higher order diffraction is observed, so lower periodicity values are considered. The 1-2 μm diameter range of FSS disk is in accordance with the resonant wavelength in order to get resonance in an infrared

range. Since a wavelength range of 8-14 μm is considered, the minimum dielectric thickness for quarter wave mode is $\lambda/4\sqrt{\varepsilon_r}$ = 0.585 μm at 8 μm, where ε_r = 11.7 is the relative permittivity of crystalline silicon dielectric that is used. This quarter wave mode peak has enough width to couple with the closed FSS mode at 8 μm, which is not desirable in the FSS design. Therefore 0.5 μm was chosen as the maximum critical value of thickness to avoid more than one propagation mode-coupling situation. Based on the above discussion, three practical ranges of 0.05 μm ≤ h ≤ 0.5 μm, 2 μm ≤ p ≤ 4 μm and 1 μm ≤ d ≤ 2 μm are applied for the absorber model.

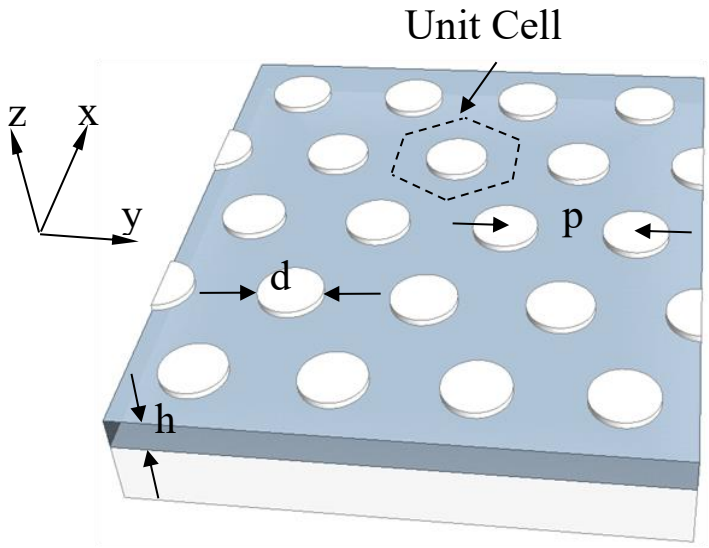

Figure 6.1 Hexagonal close packed array frequency selective surface (*h* ranges from 0.05 to 0.5 μm, *d* ranges from 1 to 2 μm, and *p* ranges from 2 to 4 μm).

6.3. HCP FSS EQUIVALENT CIRCUIT MODEL (ECM)

The FSS array exhibits two dominant responses, mutual inductive response between ground plane and FSS and a capacitive response between adjacent disks of FSS which form a resonant circuit. Also, there is a capacitance caused by the charges induced

on the edges of adjacent disks and the charges induced at the surface of ground plane and bottom of FSS layer. The equivalent impedance of an infrared FSS can be represented through a series of R_2, L_2 and C_2 three elements, as shown in Figure 6.2. A series of two elements R_1 and L_1 is used to represent ground plane. The dielectric layer is represented by propagation constant γ, impedance Z_{si} and thickness h. At infrared frequencies, the loss tangent of polycrystalline silicon approaches zero and hence is modeled as lossless dielectric.

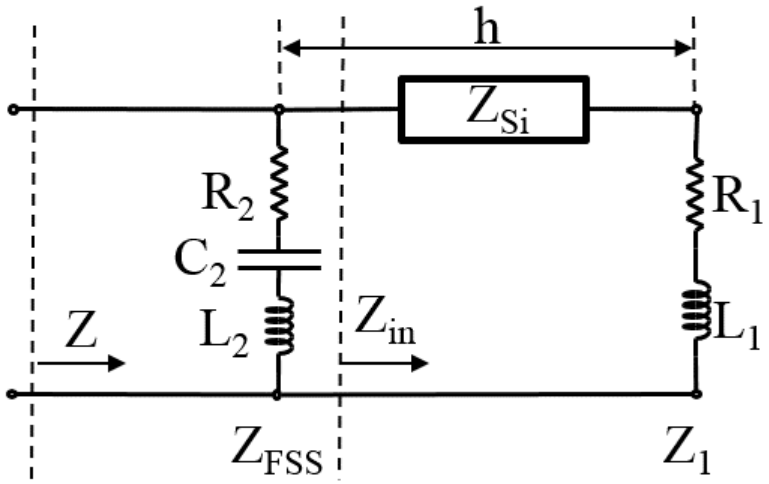

Figure 6.2 Equivalent circuit model of hexagonal close packed array frequency selective surface.

6.4. OPTIMIZED EQUIVALENT CIRCUIT OF INFRARED HCP FSS

After HFSS simulations for different geometric parameter combinations, circuit models with varying assigned values of R_1, L_1, R_2, L_2 and C_2 were evaluated to obtain reflection coefficients closest to the one obtained by HFSS. MATLAB optimization toolbox is used to minimize the function defined as mean value of absolute difference

between reflection coefficient obtained by HFSS and circuit model. Real and imaginary parts of the reflection coefficients were considered in MATLAB optimization toolbox, and interior point method-based algorithm was found to be most effective for these optimizations.

The reflection coefficient of the FSS is calculated such as in Equation (14), where Z_0 is the free space impedance, and Z is the input impedance of the overall FSS structure as shown in Equation (15). Z_{FSS} is the characteristic impedance of FSS layer, such as in Equation (16), and Z_{in} is the input impedance for elements towards the ground as shown in Figure 6.2 and Equation (17), where k_0 is a wave vector and Z_1 is the characteristic impedance of the Al substrate (Equation (18)).

$$\Gamma = \frac{Z - Z_0}{Z + Z_0} \tag{14}$$

$$\frac{1}{Z} = \frac{1}{Z_{FSS}} + \frac{1}{Z_{in}} \tag{15}$$

$$Z_{FSS} = R_2 + jL_2\omega + \frac{1}{jC_2\omega} \tag{16}$$

$$Z_{in} = Z_{Si}\frac{Z_1 + jZ_{Si}\tan(k_0 h)}{Z_{Si} + jZ_1\tan(k_0 h)} \tag{17}$$

$$Z_1 = R_1 + jL_1\omega \tag{18}$$

These circuit parameters were determined and fitted in accordance with the HFSS simulation results of the FSS with a threshold R^2 of 0.95. Formulas for the circuit elements were determined and are shown in Equations (19)-(23).

$$R_1 = a_0 \tag{19}$$

$$L_1 = (A_1 d^2 + A_2 d + A_3) e^{\left(A_4 h e^{(A_5 d)}\right)} \tag{20}$$

$$L_2 = (B_1 h + B_2)[p - (B_3 h + B_4)]^{\left(B_5 h^2 + B_6 h + B_7\right)} \tag{21}$$

$$R_2 = a_{27} h^{a_{28}} p^{a_{29}} d^{a_{30}} \tag{22}$$

$$C_2 = a_{31} h^{a_{32}} p^{a_{33}} d^{a_{34}} \quad (23)$$

where, $A_1 = a_1p + a_2$, $A_2 = a_3p + a_4$, $A_3 = a_5p + a_6$, $A_4=a_7p^2 + a_8p + a_9$, $A_5=a_{10}p^2 + a_{11}p + a_{12}$, $B_1 = a_{13}d^{a14}$, $B_2 = a_{15}d + a_{16}$, $B_3 = a_{17}d + a_{18}$, $B_4 = a_{19}d + a_{20}$, $B_5 = a_{21}d + a_{22}$, $B_6 = a_{23}d + a_{24}$, $B_7 = a_{25}d + a_{26}$. The values of all constants are shown in Table 6.1. As a result, all of the equivalent circuit elements values can be predicted from geometric parameters.

Table 6.1 Constants in equivalent circuit model formulas.

a_0	3.878	a_7	-0.377	a_{14}	-1.235	a_{21}	-2.846	a_{28}	0.254
a_1	-7.869	a_8	1.981	a_{15}	85.118	a_{22}	3.342	a_{29}	2.395
a_2	30.740	a_9	-1.230	a_{16}	-4.475	a_{23}	1.916	a_{30}	-2.311
a_3	24.819	a_{10}	0.329	a_{17}	-0.450	a_{24}	-1.622	a_{31}	17.491
a_4	-9.477	a_{11}	-2.064	a_{18}	0.357	a_{25}	-0.697	a_{32}	-0.910
a_5	-4.422	a_{12}	3.629	a_{19}	1.226	a_{26}	2.450	a_{33}	-2.111
a_6	76.616	a_{13}	1696	a_{20}	-0.375	a_{27}	5.126	a_{34}	3.563

Figure 6.3 shows the modulus and phase of S_{11} obtained by HFSS simulation and equivalent circuit model (ECM) for three of the cases. The results are in good agreement with each other and could be applied to obtain an insight into the FSS behavior. Frequency responses in the discussed geometry parameters range of 0.05 μm ≤ h ≤ 0.5 μm, 2 μm ≤ p ≤ 4 μm and 1 μm ≤ d ≤ 2 μm were obtained.

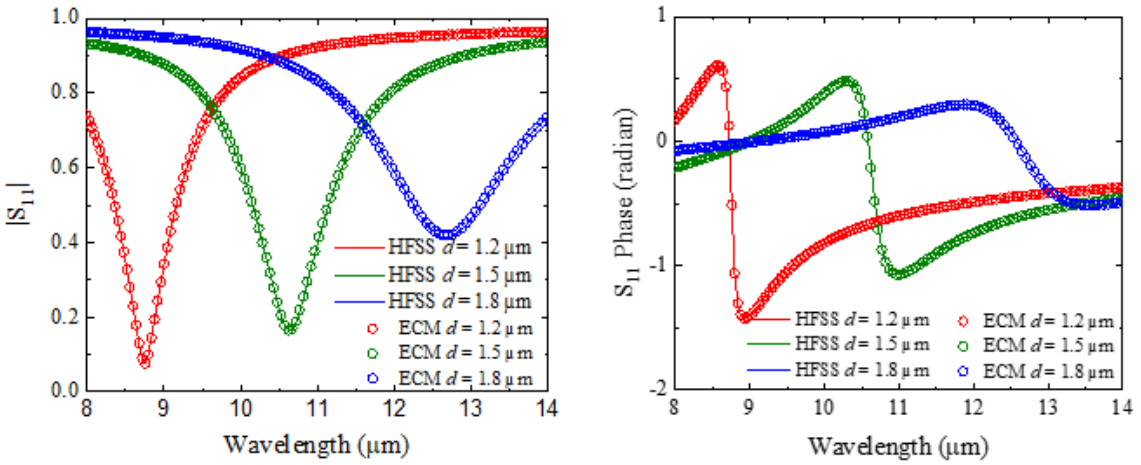

Figure 6.3 Comparison of S_{11} magnitude and phase from HFSS simulation and equivalent circuit model. (Red: p = 3 μm, h = 0.3 μm, Green: p = 2 μm, h = 0.2 μm, Blue: p = 2.8 μm, h = 0.2 μm).

6.5. GEOMETRY-DEPENDENCE OF THE FSS FREQUENCY RESPONSE

Absorption curves for wavelengths in 8-14 μm range were obtained using the model in Equations (1)-(10). The behaviors of equivalent circuit model elements L_1, L_2, C_2, R_1 and R_2 are investigated with changes in the geometric parameters in this section.

The inductance L_1 of equivalent circuit model corresponding to varying geometric parameters is shown in Figure 6.4. Since L_1 represents the inductance of the ground plane and between the ground plane and disk, the properties of ground plane and disk material play key roles. L_1 is affected by coupling between ground plane and the metal disks; a lower period leads to stronger mutual coupling and contributes to a higher L_1. In the infrared region, the kinetic inductance term is negligible compared to the Faraday inductance, since the incident frequency is not equal to aluminum plasma frequency[431]. The Faraday inductance is caused by phase delay, which is insensitive to thickness.

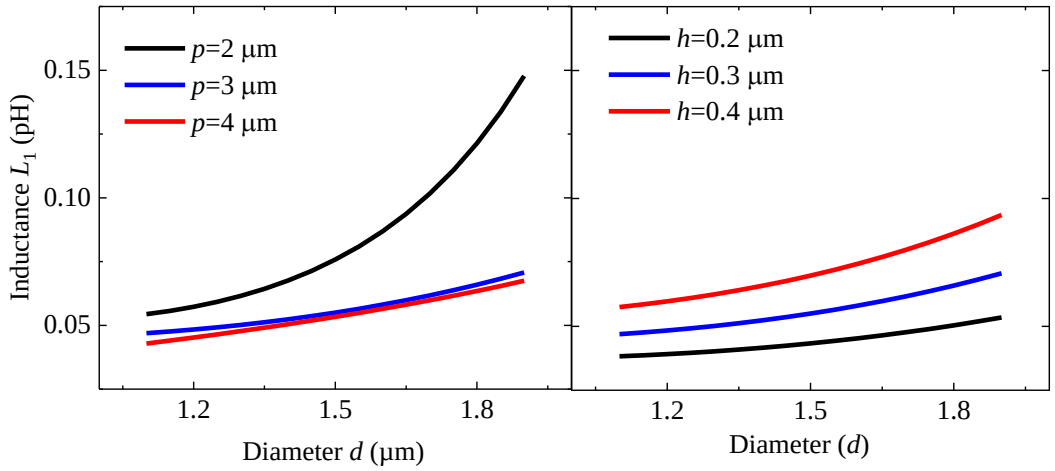

Figure 6.4 Ground inductance L_1 with variation in the disk diameter for different period values with h = 0.3 μm, and different thickness values with p = 3 μm.

The variation in the capacitance with changes in geometrical properties is shown in Figure 6.5. C_2 is directly proportional to the diameter of FSS disk and inversely proportional to the period and thickness. C_2 is produced by the charges induced on the edges of adjacent disk by incident electromagnetic waves when thickness is very large, hence a larger diameter and smaller period contribute to more charges' concentration and lead to a higher C_2. Also, smaller thickness concentrates more charges between ground plane and FSS layer, leading to a higher C_2.

The variation of inductance L_2 as represented in Figure 6.6 is complementary to the capacitance performance. The Faraday inductance dominates in this case, and surface plasmon modes are negligible. The Faraday inductance is equal to $\mu_o/(2kd)$ where μ_o is permeability, k is wave vector and d is the diameter of disk. This inductance is inversely proportional to diameter as shown in Figure 6.6. When the diameter is constant, L_2 is proportional to the period and thickness, leading to an increase in the mutual inductance between disks[434]. This behavior ties back to dependence of the mutual inductance between

adjacent disks, and between the disks and the ground on the FSS geometry. There is no induced current in the dielectric medium since the dielectric layer is modeled as lossless. With a decrease in the diameter and an increase in the period, C_2 and L_2 reach minimum and maximum values respectively such that $C_2 \times L_2 \approx$ constant.

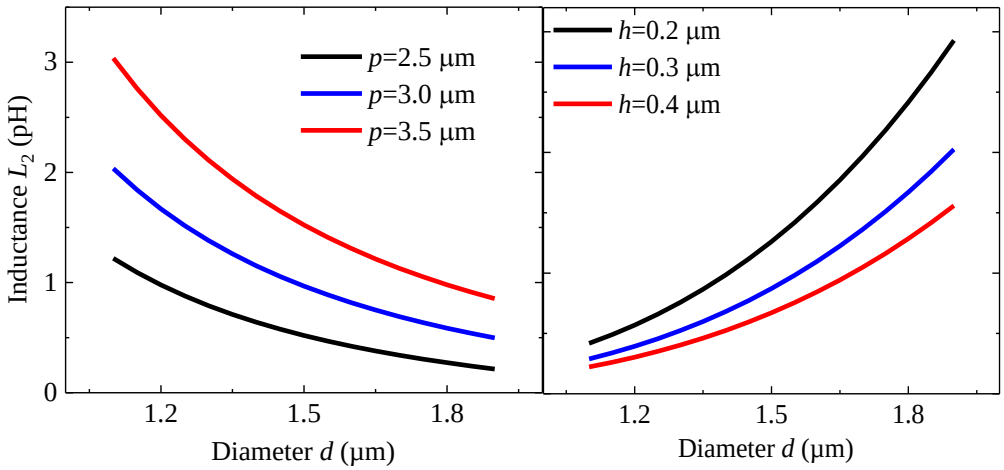

Figure 6.5 Capacitance C_2 with variation in the disk diameter for different period values with h = 0.3 μm, and different thickness values with p = 3 μm.

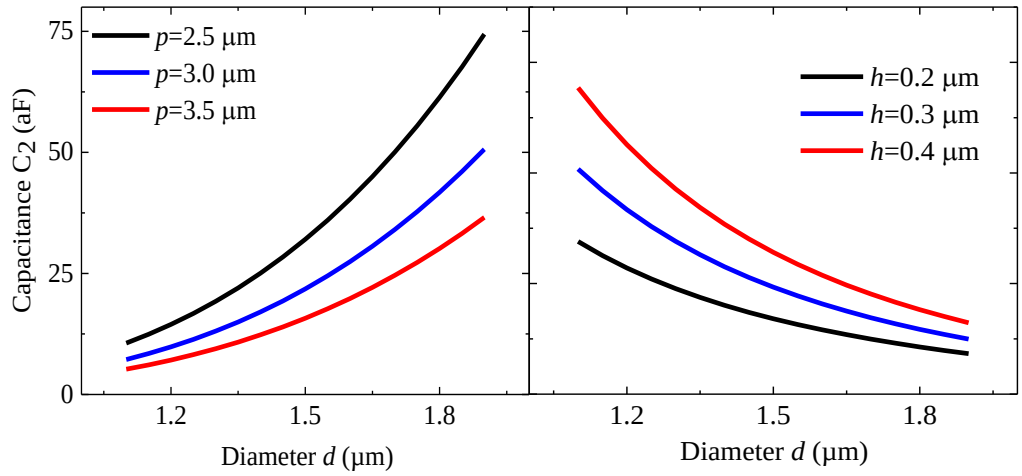

Figure 6.6 Inductance L_2 with variation in the disk diameter for different period values with h = 0.3 μm, and different thickness values with p = 3 μm.

Resistance R_1 of the ground remains constant throughout the considered wavelength range of 8-14 μm. Variation in the disk resistance with changes in the geometric parameters is shown in Figure 6.7. The resistance decreases with an increase in the cross-section area of the disk that is caused with an increase in the diameter, as expected. The variation of the disk resistance with change in period and height follows a similar trend as observed in L_2 and is a part of the internal or parasitic resistive part of L_2 and the disk impedance.

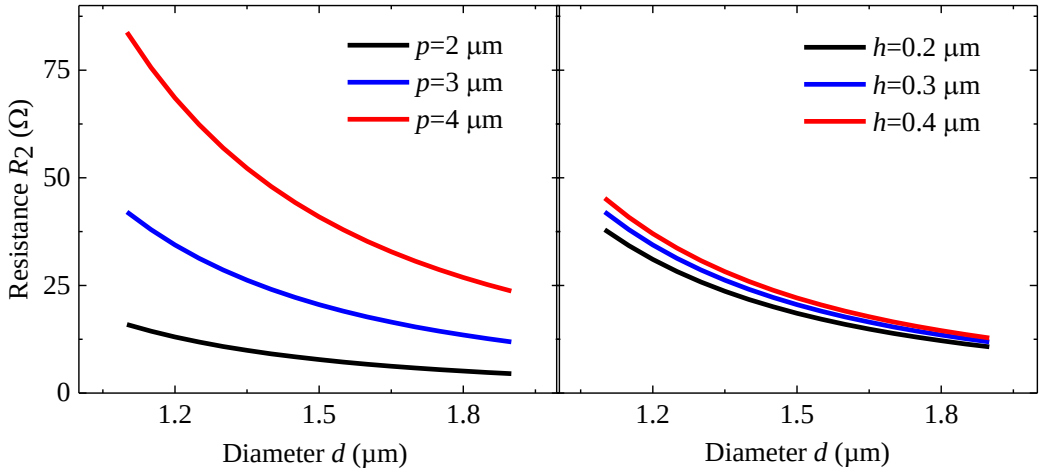

Figure 6.7 Resistance R_2 with variation in the disk diameter for different period values with h = 0.3 μm, and different thickness values with p = 3 μm.

6.6. MATERIAL-DEPENDENCE OF THE FSS FREQUENCY RESPONSE

Along with the geometric properties, the effect of material properties especially of the dielectric, on the frequency response was briefly investigated using the ECM. Dielectric constant or the relative permittivity (ε_r) typically affects the energy storage properties of the material and its frequency spectra characteristics. As the dielectric considered here is

crystalline, the change in ε_r would have negligible effect on the imaginary part of the permittivity and hence negligible effect on the resistors and inductors of the model. ε_r dominantly affects the equivalent capacitance, and accordingly tune the frequency response.

Values of ε_r ranging from 8 to 20 were simulated and lumped parameters for these models were determined by fitting using the procedure discussed previously. All lumped parameters except C_2 were kept constant. Changing C_2 did update the frequency response in the ECM and matched with the one from HFSS simulation. C_2 is seen to change proportionally with ε_r as expected and seen in Figure 6.8. Material with a higher dielectric point towards more electric field which is reflected in the capacitance associated partially with the FSS and partially with the transmission line.

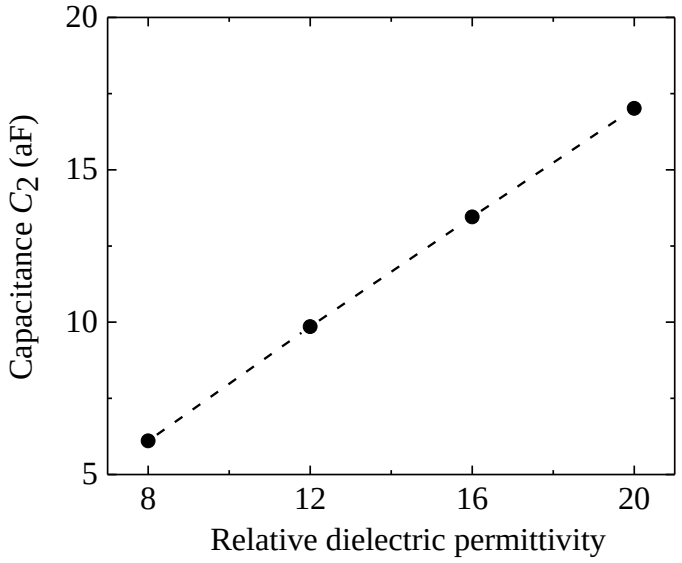

Figure 6.8 Capacitance C_2 with variation in dielectric permittivity of the layer between disks and ground (dotted line: guide to the eye)

This in agreement with the transmission line theories, strengthens and validates the model as a tool for designing and controlling the behavior of infrared FSS with an intuition. The primary effect of dielectric permittivity selectively on the capacitance, gives the flexibility to tune the capacitance of FSS without significantly affecting other lumped circuit elements. Designing an FSS configuration with different dielectric constants or refractive indices, and accordingly tuned geometrical parameters, could have applications in developing multi-functional FSS configurations as absorbers or transmitters. One of the advantages of a transmission-line based ECM is the accommodation of the effect of the dielectric constant between the disks and the ground (ε_r) on the impedance calculations and modeled lumped parameters.

6.7. PERFECT ABSORBER DESIGN USING ECM

Geometric parameters of the HCP disks to achieve perfect absorption in the 8-14 μm wavelength range were determined using the ECM and related equations. Absorption higher than 99.99% was the threshold for being a perfect absorber. Perfect absorbers in the range of 0.05 μm ≤ h ≤ 0.5 μm, 2 μm ≤ p ≤ 4 μm and 1 μm ≤ d ≤ 2 μm are studied.

The geometric parameter d dominates the extreme points of resonance wavelength. It can be seen in Figure 6.9 that the resonance wavelength is shifted toward higher values with an increase in the diameters. Data is plotted for p = 2 μm and p = 4 μm considering these as extreme periodicity values in this study, and other intermediate p's would have a similar trend. The resonant frequency would typically increase as the device or material size is reduced, which is seen in the case of the HCP disks. A reduction in disk size implies a reduction in capacitance with an increase in inductance. Resonant wavelength of disk

structures is inversely proportional to the square roots of inductance and capacitance. So, an increase in the resonant wavelength with diameter implies an off-balance change in capacitance and inductance with change in the disk size. The rates of increase in capacitance C_2 and reduction in inductance L_2 are different with change in the diameter which leads to the dependence of resonant wavelength on the disk diameter for perfect absorption. For a constant L_2, the capacitance C_2 is also increased by using a material with higher dielectric permittivity, which could add flexibility in FSS design. The focus of the current work is on tuning geometrical properties of the infrared FSS to develop the ECM and achieve perfect absorption.

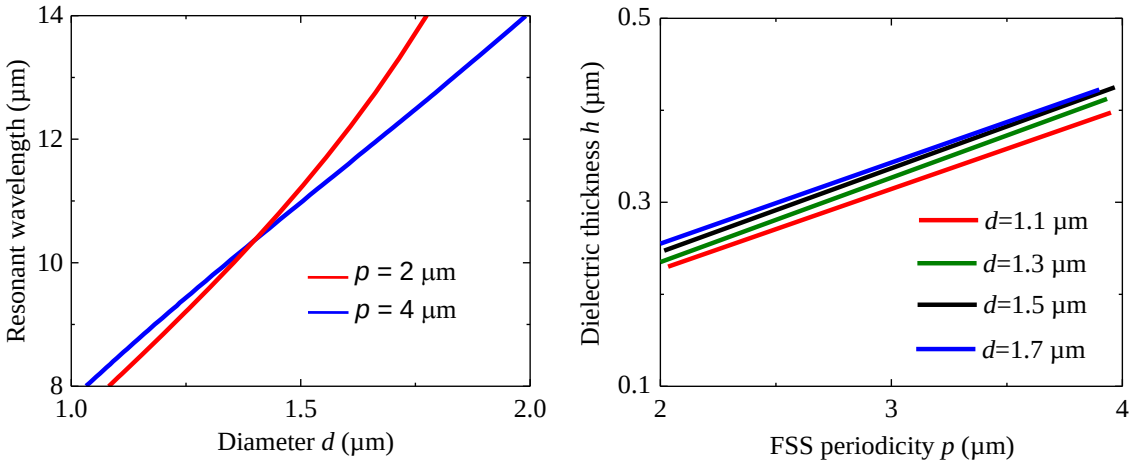

Figure 6.9 Conditions for perfection absorption by the hexagonal close packed array frequency selective surface: Diameter determines the resonant wavelength, and thickness and period determine absorptivity.

The relationship of thicknesses verses period with different diameters is shown in Figure 6.9 and it is seen that the period is proportional to thickness. Since the effect of period on L_2, C_2, and R_2 is similar as thickness, changing either one has similar effect on

the frequency response of perfect absorber FSS. This helps to find the correct period corresponding to a specific thickness, required to achieve perfect absorption. The height and period both also depend on the permittivity of the dielectric layer. A higher dielectric material has a higher capacitance and hence would result in an absorption and quality factor with higher dielectric height and periodicity. Therefore, to design perfect absorbers, the diameter of disks is proportional to the resonant wavelength and the thickness is proportional to the period.

The quality factor of an absorber further gives information about the frequency selectivity of the designed FSS. The quality factor (figures not shown here) is inversely proportional to resonance wavelength which relates to the onset of higher order at higher frequencies. Quality factor of an inductor circuit is typically proportional to the inductance, and that of a capacitor circuit is inversely proportional to the capacitance, at perfect absorption. For a higher quality factor, higher inductance L_2 and lower capacitance C_2 would be desirable. It is clear that enhancement in L_2 and reduction in C_2 could be achieved with a larger h or p, or a smaller d. The quality factor is enhanced with a higher h and smaller d. The inductor and capacitor seem to dominantly effect the quality factor. Since quality factor is the ratio of the energy stored in the absorber to the energy dissipated, thicker dielectric layer helps the absorber to store more energy and increases the quality factor.

(Also, as the quality factor would be greater when the absorptivity is lower than 1, the resistance would affect it. As a smaller disk with a larger dielectric height and periodicity results in a high quality factor, a higher disk resistance would be proportional

to the quality factor when the absorptivity is lower than 1, even though the focus here is on a perfect absorber case.)

6.8. TRANSMISSION LINE BASED MODEL FOR INFRARED FREQUENCY SELECTIVE SURFACES - SUMMARY

Equivalent Circuit Model of Infrared Frequency Selective Surfaces (FSS) provides an engineering insight into its frequency behavior and enables its rapid design. Hexagonal close packed array separated from a ground plane by a dielectric was considered here to formulate the equivalent circuit model consisting of circuit elements and transmission lines. Unlike microwave FSS, the ground plane in the infrared FSS had an impedance consisting of an inductor and a resistor. The dielectric was modeled as a transmission line and the disk array was represented as a combination of inductor, capacitor, and a resistor. The lumped circuit parameters effectively represented the FSS, characterized the frequency response, and their variation with the geometric and material properties of the FSS followed established electromagnetic relations and trends. In the case of analyzing perfect absorber condition, it is found that the resonant wavelength is directly proportional to the diameter of the HCP FSS, and the height and the period are inter-dependent and determine the absorptivity and the quality factor. A change in diameter changes the equivalent disk-related capacitance and inductance, which results in the tunability of resonant wavelength. A higher inductance and a lower capacitance results in an increase in the quality factor, which is achieved with an increase in dielectric thickness or the disks periodicity.

7. CONCLUSIONS AND FUTURE WORK

7.1. CONCLUSIONS

Wide bandgap compound semiconductors and their rare earth and transition metal doping is investigated in this work.

7.1.1. Mechanism for RT Spin Functionality in MOCVD-grown GaGdN. Gallium nitride has a small lattice size, potential for spin exchange interactions, and growth mechanisms that can result in p-type and n-type nature. While GaN doped with transition metal such as manganese has been explored in the literature, the mechanism for the RT ferromagnetism is based on deep impurity bands introduced by Mn within the bandgap of GaN, and the material is highly resistive. GaN doped with rare earth element Gd exhibits RT ferromagnetism and has relatively low resistance. The mechanism for the ferromagnetism and spin in GaGdN is investigated.

Hall Effect characterization was performed to achieve an understanding of MOCVD-grown GaGdN thin films on sapphire substrates and carrier-related properties. GaGdN samples were grown using two Gd sources, Tris (2, 2, 6, 6 – tetramethyl-3, 5 – heptanedionato) gadolinium ((TMHD)3Gd) and tris(cyclopentadienyl) gadolinium (Cp3Gd). Un-doped GaN showed Ordinary Hall Effect (OHE) clear and linear variation in Hall resistivity with sweeping magnetic field. GaGdN from Cp_3Gd precursor also showed OHE and no signs of spin. GaGdN grown using a $(TMHD)_3Gd$ precursor showed Anomalous Hall Effect (AHE), that is, the trend of Hall resistivity vs applied magnetic field was linear at high fields (above ~500 Gauss) but had anomaly at lower fields. This points towards a retainment of spin in GaGdN even after the removal of external magnetic

field. A coercive field of a few hundreds of Gausses could be in an optimum range such that the spin in GaGdN would not fluctuate with ambient fields and at the same time be tuned by external fields produced by current-carrying coils (or equivalent scalable magnets).

The Hall resistivity is a combination of ordinary Hall component that is dominant at high fields and anomalous Hall component which originates from GaGdN and superposes with the external magnetic field resulting in an AHE. Relationship between the Anomalous Hall conductivity and the samples' net conductivity help in the understanding of mechanism responsible for the spin in GaGdN. In GaGdN, the Anomalous Hall conductivity increased with samples' conductivity at a super-linear rate with an exponential factor of 1.8. Such a relationship in low conductivity regime shows signs of spin in MOCVD-grown GaGdN based on metallic conduction, localized carrier hopping and intrinsic mechanisms. All these phenomena are related with the carriers in GaGdN and on localized states present near the Fermi level.

The result that GaGdN from Cp_3Gd showed OHE even in the presence of Gd indicated that Gd as a dopant and GaN as host are not solely responsible for spin in GaGdN. Upon reviewing the chemical composition of $(TMHD)_3Gd$ and Cp_3Gd, a major difference between the two sources was that $(TMHD)_3Gd$ contains oxygen in its organic ligand while Cp_3Gd does not. Also, density functional theory suggest that oxygen could play a role in rendering magnetic properties in GaGdN[280]. Electrical characterization showed that GaGdN from $(TMHD)_3Gd$ precursor have a higher resistivity, and a lower carrier concentration and mobility as compared to GaGdN from Cp_3Gd. It seems that oxygen introduces energy states in GaGdN that reduce the n-type carrier concentration and increase

the resistivity. It was imperative to study the role of oxygen in GaGdN to sufficiently understand the mechanism for spin in GaGdN. Similar to oxygen, carbon could also introduce energy states in GaGdN that effect the spin functionality as per theoretical modeling[246,250].

GaGdN from Cp_3Gd that showed OHE and do not contain any O were implanted with O and C. Implantation dose, energy, and tile angle were determined so that implanted GaGdN would have O or C concentration equivalent to O present in GaGdN from $(TMHD)_3Gd$ precursor. O- and C-implanted GaGdN showed good crystalline quality even after implantation and no O- or C-related secondary phases. FWHM of X-ray diffraction (XRD) peaks in GaGdN stayed consistent after O- or C- implantation. Peak shifts in (002), (004), and (006) crystal directions, towards higher diffraction angles were observed in implanted GaGdN with more shift in O-implanted GaGdN. O has a smaller covalent radius than N, hence a smaller lattice size in GaGdN:O confirms incorporation of O in GaGdN and that part of implanted O substitutes N. C has a larger covalent radius than N but still had a peak shift towards higher diffraction angles, which shows that it could occupy more sites in GaGdN that are interstitial or similar as compared to substitutional sites.

As-grown GaGdN from Cp_3Gd precursor had shown OHE, but GaGdN implanted with O or C exhibited AHE. In O-implanted GaGdN, anomaly in Hall Effect response started down from ~200 Gauss, and from ~500 Gauss in C-implanted GaGdN. The AHE signal in O- and C-implanted GaGdN seemed different, but both showed AHE. GaGdN:O showed a smoother AHE while GaGdN:C showed AHE with more fluctuations in the spin at lower fields. Carrier concentration reduced and resistivity and mobility increased with implantation. These variations in electrical characteristics with respect to as-grown GaGdN

were more in O- than C- implanted GaGdN. O on substituting N acts as donor, so a reduction in the n-type carrier density indicated that O occupies acceptor-type interstitial or similar energy states in GaGdN along with substitutional sites. A peak shift towards higher diffraction angles along with reduction in carrier density also showed that C occupies interstitial or similar states in GaGdN.

O and C in GaGdN were further activated in GaGdN by annealing. O- and C-implanted GaGdN were annealed at 1200 ^{o}C for 2 mins with a cap un-doped GaN face down on the GaGdN samples. The samples showed good crystal quality and no secondary phases upon annealing. The (002), (004), and (006) in GaGdN:O showed a slight shift towards lower diffraction angles. Also, the FWHM reduced in GaGdN:O upon annealing. This shows that O stabilizes in interstitial (or similar) states in GaGdN. Peak shifts towards higher diffraction angles were observed in GaGdN:C upon annealing, which again pointed towards a favorable incorporation of C in interstitial or similar sites. Even after annealing, both GaGdN:O and GaGdN:C showed AHE. The nature of the signal changed upon annealing. Spin fluctuations increased in GaGdN:O but reduced in GaGdN:C upon annealing, but both had signs of spin functionality. Mobility of GaGdN:C and GaGdN:O increased upon annealing, which pointed towards a better carrier localization. Annealing reduced the resistivity of GaGdN:O but increased that of GaGdN:C; this was inter-related to the FWHM of the XRD peaks and differences in incorporation of the dopants. Also, the carrier concentration slightly increased in GaGdN:O due to activation of n-type defects in GaGdN and reduced in GaGdN:C due to activation of acceptor type defects.

O and C play a crucial role in rendering spin in GaGdN and are likely to occupy interstitial or similar sites. They introduce deep acceptor-type states within the band gap of

GaGdN resulting in a p-d/f exchange. Summarizing Sections 2 and 3, the mechanism for spin in GaGdN is a combination of intrinsic, metallic conduction and carrier-hopping, and spin states induced by Gd is activated by O or C at interstitial or similar energy states in GaGdN. A carrier-related mechanism enables control and manipulation of spin properties which could be applied in spintronic devices. This is a favorable mechanism for RT spintronics, and GaGdN could be a suitable material for future spintronic devices and applications.

7.1.2. Bandgap Tunability in MOCVD-grown Transition Metal-doped Zinc Oxide. Zinc oxide (ZnO) is a versatile and interesting material for applications in photovoltaics, spintronics, photodetection, thermoelectrics, and biomedicine. Transition metal doping could enhance and enable tunability in ZnO characteristics and result in variations in the bandgap. A study of bandgap tunability could help towards implementing ZnO in tandem solar cells, and also towards its understanding for spintronics. Metal organic chemical vapor deposition (MOCVD)-grown ZnO doped with Ni and Mn were investigated with emphasis on bandgap tunability.

Un-doped ZnO using diethyl zinc (DEZn) maintained at 5-16 ^{o}C and O_2 as Zn and O precursors with varying sources' flow rates was grown to firstly understand the effects of Zn and O-related possible defects on the bandgap of ZnO. Growth of good crystal quality in (002) orientation was achieved as observed in XRD results. The bandgap of un-doped ZnO stayed consistent with varying growth parameters.

Ni-doped ZnO was grown using bis-cyclopentadienyl nickel (Cp_2Ni) as a nickel source and maintained at 90-95 ^{o}C. Growth conditions were tuned so that reactions occur in a mass transport regime, and VI/II ratio of 150. Differences in color were observed with

varying Ni flow rates on silicon substrates. Sapphire was still a preferred substrate and used for most ZnO-based samples' epitaxial growth, considering its hexagonal structure, better lattice match, transparency, and thermal stability. The effects of Ni flow on the structural and optical properties of ZnNiO were studied by growing two sets of samples, set A at 400 ^{o}C and 100 Torr, and set B at 450 ^{o}C and 30 Torr, and varying Ni flow rates in each set.

An increase in Ni content with Ni flow rates in ZnNiO was seen as per energy-dispersive X-ray spectroscopy (EDX). Hexagonal crystal structure in (002) direction, and secondary Ni-related phases such as (Zn)NiO (111) were observed. (002) XRD peak shifted upon Ni-doping. Ni could occupy substitutional and other energy sites in ZnNiO. The FWHM reduced and crystallite size increased upon Ni-doping, which confirmed a good crystal quality. Set A (400 ^{o}C, too Torr) samples had a larger FWHM than Set B (450 ^{o}C, 30 Torr) which showed that a lower pressure and higher temperature resulted in a better crystal quality. The oxygen content was lesser than Set B (450 ^{o}C, 30 Torr) samples than Set A (400 ^{o}C, too Torr), hence Ni incorporation also influenced oxygen content due to defect states, oxygen vacancies, or interstitials. A red-shift in the band edge was observed in Ni-doped ZnO as compared to un-doped ZnO, as per absorption measurement. A bandgap reduction from 3.276 to 3.269 eV was observed in Set A (400 ^{o}C, 100 Torr) with Ni content up to 2.3%, and from 3.287 to 3.26 eV in Set B (450 ^{o}C, 30 Torr) with Ni content up to 1.2%. The bandgap reduction was more in Set B samples with a lower Ni incorporation. Growth conditions in Set B of 450 ^{o}C and 30 Torr resulted in more Ni-related energy states responsible for bandgap reduction. Growth conditions could influence sites occupied by Ni such as Ni^{2+} substituting Zn^{2+}, interstitial sites, impurity bands, and oxygen vacancies and result in different bandgap reduction rates.

In later study, ZnNiO was grown under varying temperature of 450 (Set C) and 550 ^{o}C (Set D) and pressure from 22 to 100 Torr, with constant precursors' flows and other growth conditions. The crystal quality of ZnNiO reduced with an increase in the pressure in both the sets. ZnNiO grown at 450 ^{o}C and lower pressure showed sharper ultra-violet photoluminescence peaks as compared to higher temperature or higher pressure samples. Absorption spectra showed a significant reduction in intensity at high pressure. Sharper band edges at ~3.3 eV were observed in samples grown at or under a pressure of 30 Torr at 450 ^{o}C and 550 ^{o}C. Growth conditions with temperature in mass transport regime and close to the decomposition temperature of metal-organic sources, and a pressure of $\leq$30 Torr were optimum for the MOCVD growth of ZnNiO. A sample from Set C with 30 Torr growth pressure was annealed at 1000 ^{o}C for 30 mins in air. The photoluminescence quality reduced upon annealing due to a reduction in luminescence centers. Absorption spectra showed a reduction in band gap from 3.289 to 3.277 eV upon annealing, due to a possible activation of sites occupied by Ni in ZnNiO that favor a bandgap reduction. Post-growth annealing could help to tune the bandgap of ZnNiO.

Manganese doping in ZnO was studied using a bis(cyclopentadienyl) manganese (Cp_2Mn) source maintained at 150-162 ^{o}C. Crystal orientation in (002) direction was observed along with possible Mn_xO_y related phases. ZnMnO showed a better crystal quality as compared to ZnNiO. Photoluminescence peaks in ultraviolet region and oxygen vacancy or zinc interstitial or defects related luminescence around 2.2 eV were observed. Absorption bandgap reduced from 3.291 eV at 0% and 11% Mn source injection to 3.275 eV at 25% Mn injection. Annealing improved the crystal quality due to an intermix of overlapping ZnO-like and Mn_xO_y-like phases. Luminescence at ~3.3 eV reduced but

defect-related luminescent centers at ~4 eV appeared. Absorption intensity increased and bandgap reduced upon annealing. ZnMnO with 11% Mn source injection and 3.29 eV had a bandgap of 3.27 eV upon annealing, due to activation of possible Mn-related energy states near the valence or conduction band that are conducive for bandgap reduction.

Transition metal doping could help to controllably introduce energy states in ZnO and result in characteristics such as bandgap tunability, for photovoltaic and spintronic applications.

7.1.3. Development and Analysis of Field-effect Schottky Solar Cells. Gallium arsenide (GaAs) / Au based field-effect Schottky solar cells with ZnO/Al_2O_3 passivation layers were developed. An external gate contact isolated from carrier collection layer was used to increase or maintain the band-bending and Schottky barrier height. An optimized development process was followed for the field-effect Schottky solar cells' fabrication. Variations in the current-voltage characteristics were observed with externally applied gate voltages. An increase in the short circuit current density with external gate voltage was a combination of photogenerated current due to the field-effect and forward gate-ohmic related current.

7.1.4. Development of Equivalent Circuit Model for Infrared Frequency Selective Surfaces. An equivalent circuit model (ECM) based on transmission lines was developed for infrared frequency selective surfaces (FSS) considering a hexagonal close packed disk array (HCP) on aluminum ground plane separated by a silicon dielectric. High frequency structure simulator (HFSS) was used to acquire reference frequency responses. A wavelength of 8-14 μm was considered, with HCP disk diameter of 1-2 μm, disk periodicity of 2-4 μm, and dielectric height of 0.05-0.5 μm to acquire a quarter wave mode

peak. The FSS was modeled as a combination of resistance, inductance, and capacitance, the ground plan as resistance and inductance, and the dielectric as a transmission line.

The equivalent circuit elements were functions of the geometry parameters of the HCP FSS structure, and the reflection coefficients were determined considering the circuit parameters and transmission line. Responses from ECM model matched with HFSS simulation results with an R^2 of over 0.95. HCP inductance increased with height and periodicity, and reduced with diameter, due to an increase in mutual-disks coupling and self-inductance. Ground inductance increased with dielectric height due to mutual inductance. Mutual inductance components from disk diameter and periodicity reduced the net ground inductance. Disk capacitance increased with diameters and decreased in periodicity or height, due to an increase in the charge concentration / storage in the FSS. Disk resistance followed a similar trend as disk inductance and could be its parasitic part. Ground resistance stayed consistent but had to be included in the circuit to effectively model the FSS. The trend of disk capacitance and inductance with geometry parameters was complementary, and their product could define the resonant frequency for the FSS.

Conditions for perfect absorber design in 8-14 μm wavelength range were determined using the ECM. The resonant wavelength is inversely proportional to the disk diameter. This implies an off-balance change in disk capacitance and inductance with diameter resulting in a tunable resonant wavelength. The dielectric thickness or height varied proportionally with periodicity to achieve perfect absorber conditions, as both had similar effects on the FSS circuit elements. An increase in the disk inductance and decrease in disk capacitance with a smaller diameter, or larger height or periodicity, increased the quality factor. (Disk resistance would inversely effect the quality factor for responses with

peak absorptivity lesser than 1.) An insight into the functioning of infrared FSS through an equivalent circuit model could help towards their rapid design.

7.2. FUTURE WORK

This section discusses the future directions of the discussed works.

7.2.1. Spin-related Characterization of MOCVD-grown GaGdN. Spin characterization of MOCVD-grown GaGdN could be continued and related understanding could be enhanced using Anomalous Hall Effect measurement, magnetic circular dichroism (MCD), superconducting quantum interference device (SQUID), and photoluminescence.

Anomalous Hall Effect (AHE) in MOCVD-grown GaGdN with varying carrier density and O or C content could be performed. Effects of varying carrier concentration could help towards understanding the correspondence between the ratio of spin and charge carriers. Studying GaGdN with varying O or C content could help understanding if the presence of O or C is necessary or the spin polarization is related with the O or C content. If the spin and O/C- content are related, an optimum configuration of Gd, O, and C could be determined to achieve efficient spin functionality in GaGdN. Varying temperature measurement could result in changes in the Hall resistivity and other electrical characteristics of GaGdN. Variations in the Hall resistivity or the Anomalous Hall resistivity with the samples' conductivity wherein these resistivities change as a function of temperature for a constant sample could be studied. The trend could be compared with the trend achieved when AHE in samples with different resistivity are plotted and resulting mechanism could be understood in more detail.

Photoluminescence measurement could be performed on GaGdN that shows AHE and compared with un-doped GaGdN and as-grown GaGdN from Cp_3Gd that shows OHE. Intensities, FWHM, peak positions of photoluminescence of GaGdN samples could be inter-related to Hall Effect measurement and electrical characterization results. This could help towards identifying defect states that could be responsible for rendering spin functionality in GaGdN. .

Magnetic circular dichroism or Magneto-optical Kerr Effect (MOKE) could be an effective way to characterize the spin functionality in MOCVD-grown GaGdN[435–439]. Waves depending on their polarization would be absorbed or emitted at different rates by materials based on their magnetic or spin properties. External magnetic field in a positive and negative direction with a fixed polarization (right or left) could be swept and incident on the GaGdN sample, and difference between the reflected left-circularly polarized and right-circularly polarized light could be calculated to determine the spin polarization, as shown in Figure 7.1.

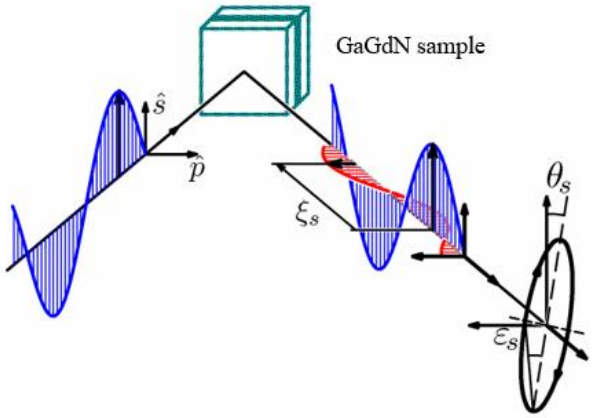

Figure 7.1 Schematic of magnetic circular dichroism measurement process. [from http://alma.karlov.mff.cuni.cz/hamrle/teaching/lectures/hamrle_moke.pdf) (02/19/2020)]

A typical experimental setup for MCD measurement is shown in Figure 7.2[435]. A wave converted to circularly polarized wave through a photo-elastic modulator is incident normal on a sample as shown in the Figure 7.2. Light waves from the sample are acquired by a photodiode and then processed by a computer. Several amplifiers, focusing mirrors, filters, etc. would be used at different paths in the setup.

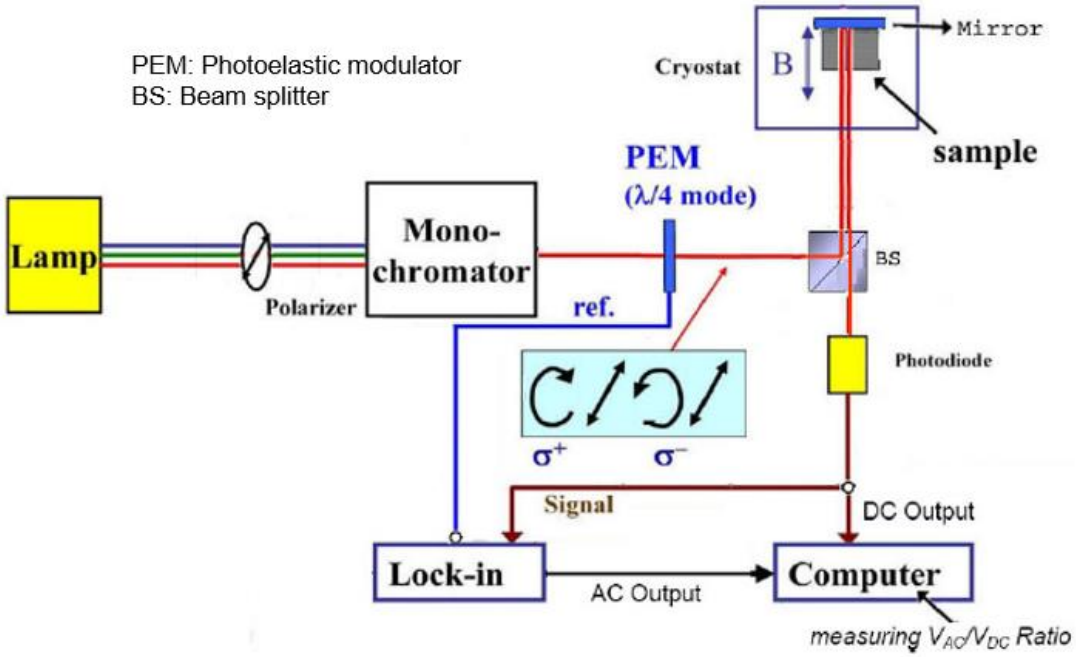

Figure 7.2 Typical experimental setup for magnetic circular dichroism measurement[435].

Magnetic properties of GaGdN containing O or C could be investigated by SQUID characterization. Effects of interfaces or defects or parameters not directly related with the carriers but still influence the magnetic properties could be understood using SQUID. A completely carrier-related mechanism is a preferable case, so defects that result in spin in GaGdN could be identified and potentially reduced.

O- or C-related energy states in GaGdN could be experimentally identified and properties of GaGdN could be characterized by techniques such as electron energy loss spectroscopy (EELS), secondary ion mass spectroscopy (SIMS), and electron paramagnetic resonance (EPR).

7.2.2. MOCVD-GaGdN Based Spin-LEDs. Spin-light emitting diode (Spin-LED) based on MOCVD-grown GaGdN and GaN related quantum wells (QW) could be fabricated as shown in Figure 7.3.

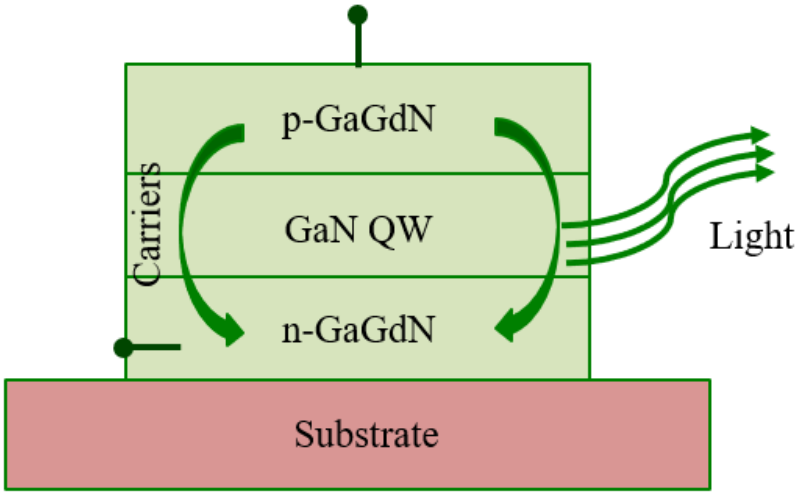

Figure 7.3 Schematic of a MOCVD-grown GaGdN based Spin-LED

Current-voltage characteristics of Spin-LEDs could be measured and related with the spin properties measured using other techniques mentioned in the previous Section 7.2.1. Electroluminescence (EL) spectra could be acquired and response under varying magnetic fields could be evaluated to determine the spin polarization[38,238,440]. Spin relaxation and lifetime could be potentially estimated by comparing the results with un-doped GaN or by tuning the active layer.

Moreover, fabrication of MOCVD-GaGdN Spin-LEDs would show a potential and lead ways towards development of devices such as Spin-diodes, Spin-photodetectors, and Spin-photoemitters.

7.2.3. Additional Characterization of GaN and ZnO Materials. Functionality of GaN and ZnO could be explored by additional characterization. Thermoelectric characterization of MOCVD-grown GaN and ZnO based materials could be performed. Heat dissipation in electronic devices and solar cells could be potentially converted into electricity. Thermo-emf was observed in Ni-doped thin films grown by chemical spray pyrolysis technique, as shown in Figure 7.4[315]. However, the influence of Ni-doping on the thermo-emf and related thermoelectric properties is still not clear.

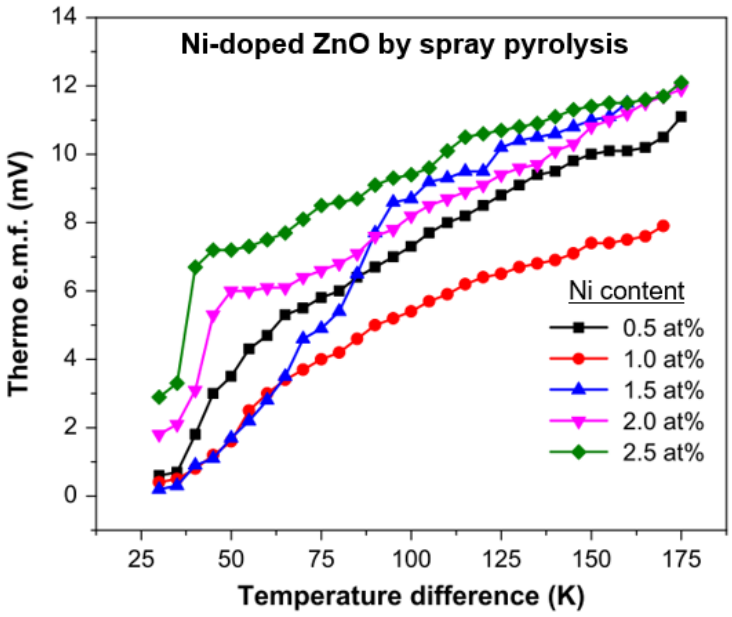

Figure 7.4 Thermo-emf in Ni-doped ZnO by spray deposition[315].

Electrical characterization of ZnO doped with Ni and Mn could be performed. Doping and growth conditions could be tuned to achieve carrier concentration, mobility, and resistivity for device applications such as solar cells and spintronic devices. Energy states introduced in ZnO by Ni or Mn could be studied further by identifying if those add to the intrinsic n-type carrier concentration of ZnO or act as compensating centers. Spin characterization of transition metal doped ZnO could be done to understand the doping effects, phases or clusters, and possible spin interactions in ZnO.

7.2.4. Compound Semiconductor Materials for Bandgap Tunability. In addition to zinc oxide, other compound semiconductors could be explored for bandgap tunability and potential applications in photovoltaics.

Zinc sulfide doped with transition metals has a potential for bandgap tunability and this could also depend on the grown techniques[249–258]. Lowest energy transitions for ZnS doped with transition metals as per first principles calculation are shown in Figure 7.5[441].

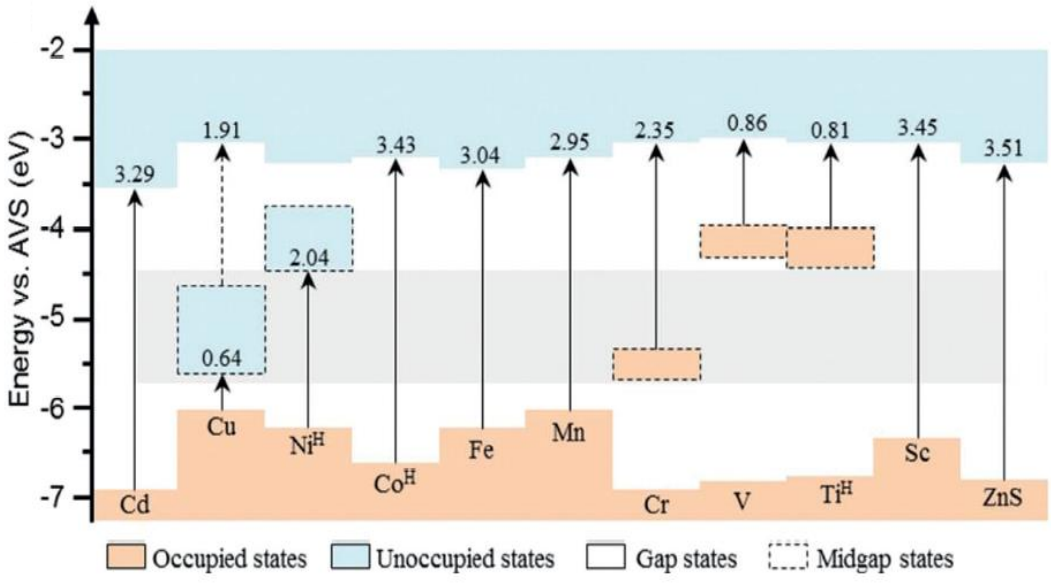

Figure 7.5 Lowest energy electronic transitions of transition metal doped zinc sulfide as per first principles calculations[441].

Zinc sulfide doped with Fe and grown by MOCVD has shown a potential for bandgap reduction, as seen in Figure 7.6[451,452]. The samples were grown at 350 ^{o}C and 760 Torr using dimethyl zinc (DMZn) and H_2S. A ZnFeS (002) was observed and a FeS-like cubic structure (220) became apparent with Fe content over ~25%. A reduction in bandgap was seen with an increase in the Fe content. Similar effect was observed in zinc selenide microspheres grown by a hydrothermal method in (111) orientation and doped with Mn as seen in Figure 7.6.

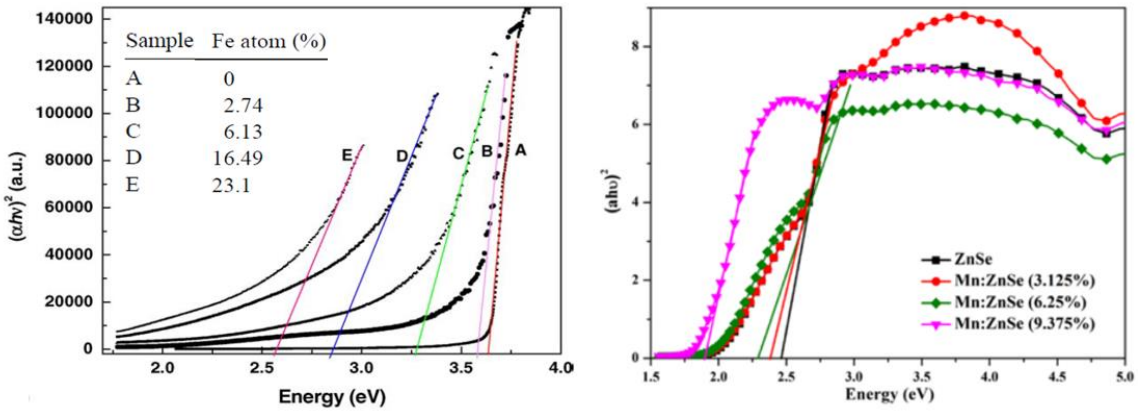

Zinc iron sulfide grown by MOCVD

Zinc manganese selenide grown by hydrothermal method

Figure 7.6 Absorption Tauc plots of MOCVD-grown ZnFeS with varying Fe content[451,452].

7.2.5. Development of ICBS Solar Cells in Multijunction Configuration. Field-effect in Schottky solar cells could be understood in more details. Proof of concept of ICBS has been investigated in other works (from our group). ICBS solar cells with band gap of ~1.8 eV could be developed. Material with a 1.8 eV bandgap could be grown as parts of Section 7.2.4. AlGaAs with 30% Al could also be explored as a 1.8 eV material. A 1.8 eV ICBS solar cell could be combined with a ~1.1 eV silicon solar cell in a dual-junction

configuration. A high power conversion efficiency could be achieved by optimizing the dual-junction configuration.

7.2.6. Investigation of Equivalent Circuit Model for Infrared FSS. The transmission-line equivalent circuit model could be explored to achieve insights in the infrared FSS behavior with varying material properties and at off-axis waves' incidence. Material properties of the dielectric, HCP disks, and ground plan could be tuned and effects on the circuit parameters and the model could be studied. In the case of off-axis incidences, the transmission line would typically accommodate tangent of the incident angle, and equivalent circuit model for normal incidence could be updated accordingly. A broader transmission line model could be developed that could help towards designing infrared FSS with normal as well as off-axis responses. Other models such as capacitance-based model wherein a capacitance is used instead of a transmission line could be compared. Differences in accuracies in the resulting resonant wavelength, absorptivity, and quality factor, using transmission-line model and other models could be studied under normal and off-axis incidences. Such studies could strengthen and possibly help to understand the validity or exception limits of equivalent circuit models, and apply those for rapid design of infrared FSS with a physical insight.

BIBLIOGRAPHY

1. Katayama-Yoshida, H., Sato, K., Fukushima, T., Masago, A. & Seike, M. Computational nanomaterials design for nanospintronics: Room-temperature spintronics applications. in *Rare Earth and Transition Metal Doping of Semiconductor Materials* 3–42 (Elsevier, 2016).

2. Kish, L. B. End of Moore's law: thermal (noise) death of integration in micro and nano electronics. *Phys. Lett. A* **305**, 144–149 (2002).

3. Mann, C. C. The end of Moore's law? *Technol. Rev.* **103**, 42 (2000).

4. Theis, T. N. & Wong, H.-S. P. The end of moore's law: A new beginning for information technology. *Comput. Sci. Eng.* **19**, 41–50 (2017).

5. Khan, H. N., Hounshell, D. A. & Fuchs, E. R. H. Science and research policy at the end of Moore's law. *Nat. Electron.* **1**, 14–21 (2018).

6. Green, M. A. Recent developments in photovoltaics. *Sol. energy* **76**, 3–8 (2004).

7. Costello, D. & Rappaport, P. The technological and economic development of photovoltaics. *Annu. Rev. Energy* **5**, 335–356 (1980).

8. Ravikumar, D., Wender, B., Seager, T. P., Fraser, M. P. & Tao, M. A climate rationale for research and development on photovoltaics manufacture. *Appl. Energy* **189**, 245–256 (2017).

9. Margolis, R. M. Understanding technological innovation in the energy sector: The case of photovoltaics (2002).

10. Lawton, T. C. *Technology and the new diplomacy: The creation and control of EC industrial policy for semiconductors*. (Avebury, 1997).

11. Zhou, X. *et al.* Booming development of group IV–VI semiconductors: fresh blood of 2D family. *Adv. Sci.* **3**, 1600177 (2016).

12. Mowery, D. C. Federal policy and the development of semiconductors, computer hardware, and computer software: a policy model for climate change R&D? in *Accelerating Energy Innovation: Insights from Multiple Sectors* 159–188 (University of Chicago Press, 2011).

13. Mooney, P. M. Deep donor levels (DX centers) in III-V semiconductors. *J. Appl. Phys.* **67**, R1–R26 (1990).

14. Litvinov, V. I. & Dugaev, V. K. Ferromagnetism in magnetically doped III-V semiconductors. *Phys. Rev. Lett.* **86**, 5593 (2001).

15. Ohno, H. Properties of ferromagnetic III–V semiconductors. *J. Magn. Magn. Mater.* **200**, 110–129 (1999).

16. Schubert, E. F. *Doping in III-V semiconductors*. (E. Fred Schubert, 2015).

17. Munekata, H. *et al.* Diluted magnetic III-V semiconductors. *Phys. Rev. Lett.* **63**, 1849 (1989).

18. Tedrow, P. M. & Meservey, R. Spin-dependent tunneling into ferromagnetic nickel. *Phys. Rev. Lett.* **26**, 192 (1971).

19. Žutić, I., Fabian, J. & Sarma, S. Das. Spintronics: Fundamentals and applications. *Rev. Mod. Phys.* **76**, 323 (2004).

20. Wu, J., Shen, Y.-L., Reinhardt, K., Szu, H. & Dong, B. A nanotechnology enhancement to Moore's Law. *Appl. Comput. Intell. Soft Comput.* **2013**, (2013).

21. Hoffmann, A. & Bader, S. D. Opportunities at the frontiers of spintronics. *Phys. Rev. Appl.* **4**, 1–18 (2015).

22. Awschalom, D. D. Rapid #: -14924673.

23. Meier, F., Cerletti, V., Gywat, O., Loss, D. & Awschalom, D. D. Molecular spintronics: Coherent spin transfer in coupled quantum dots. *Phys. Rev. B - Condens. Matter Mater. Phys.* **69**, 1–12 (2004).

24. Odelola, H. A. & Koza, J. Characterization of Nigerian strains of West Nile virus by plaque formation. *Acta Virol.* **19**, 489–492 (1975).

25. Akinaga, H. & Ohno, H. Semiconductor spintronics. *IEEE Trans. Nanotechnol.* **1**, 19–31 (2002).

26. Xi, S. & Scientific, T. Sigma Xi, The Scientific Research Honor Society. **101**, 370–377 (2019).

27. Wolf, S. A. *et al.* Spintronics: a spin-based electronics vision for the future, *Science (80-.).* **294**, 1488–1495 (2001).

28. Johnson, M. & Silsbee, R. H. Interfacial charge-spin coupling: Injection and detection of spin magnetization in metals. *Phys. Rev. Lett.* **55**, 1790 (1985).

29. Baibich, M. N. *et al.* Giant magnetoresistance of (001) Fe/(001) Cr magnetic superlattices. *Phys. Rev. Lett.* **61**, 2472 (1988).

30. Kools, J. C. S. Exchange-biased spin-valves for magnetic storage. *IEEE Trans. Magn.* **32**, 3165–3184 (1996).

31. Turvani, G. *et al.* Design of MRAM-based magnetic logic circuits. *IEEE Trans. Nanotechnol.* **16**, 851–859 (2016).

32. Augustine, C. *et al.* Spin-transfer torque MRAMs for low power memories: Perspective and prospective. *IEEE Sens. J.* **12**, 756–766 (2011).

33. Prejbeanu, I. L. *et al.* Thermally assisted MRAMs: ultimate scalability and logic functionalities. *J. Phys. D. Appl. Phys.* **46**, 74002 (2013).

34. Ikeda, S. *et al.* Tunnel magnetoresistance of 604% at 300 K by suppression of Ta diffusion in Co Fe B⁄ Mg O⁄ Co Fe B pseudo-spin-valves annealed at high temperature. *Appl. Phys. Lett.* **93**, 82508 (2008).

35. Yada, S., Sugahara, S. & Tanaka, M. Magneto-optical and magnetotransport properties of amorphous ferromagnetic semiconductor Ge 1− x Mn x thin films. *Appl. Phys. Lett.* **93**, 193108 (2008).

36. Khaetskii, A. *et al.* Spin injection across magnetic/nonmagnetic interfaces with finite magnetic layers. *Phys. Rev. B* **71**, 235327 (2005).

37. Hall, K. C., Lau, W. H., Gündoğdu, K., Flatté, M. E. & Boggess, T. F. Nonmagnetic semiconductor spin transistor. *Appl. Phys. Lett.* **83**, 2937–2939 (2003).

38. Bhattacharya, A., Baten, Z., Frost, T. & Bhattacharya, P. Room temperature GaN-based edge-emitting spin-polarized light emitting diode. *IEEE Photonics Technol. Lett.* **29**, 338–341 (2017).

39. Farshchi, R. & Ramsteiner, M. Spin injection from Heusler alloys into semiconductors: A materials perspective. *J. Appl. Phys.* **113**, 7_1 (2013).

40. Van Roy, W. *et al.* Spin-injection in semiconductors: materials challenges and device aspects. *Phys. status solidi* **241**, 1470–1476 (2004).

41. Hanbicki, A. T., Jonker, B. T., Itskos, G., Kioseoglou, G. & Petrou, A. Efficient electrical spin injection from a magnetic metal/tunnel barrier contact into a semiconductor. *Appl. Phys. Lett.* **80**, 1240–1242 (2002).

42. Monroe, D. Neuromorphic computing gets ready for the (really) big time. *Commun. ACM* **57**, 13–15 (2014).

43. Sharad, M., Augustine, C., Panagopoulos, G. & Roy, K. Proposal For Neuromorphic Hardware Using Spin Devices. (2012).

44. Fert, A. Challenges and emerging directions in spintronics. 1–2 (2012) doi:10.1109/memsys.2012.6170078.

45. Cerletti, V., Coish, W. A., Gywat, O. & Loss, D. Recipes for spin-based quantum computing. *Nanotechnology* **16**, (2005).

46. Grollier, J., Querlioz, D. & Stiles, M. D. Spintronic nanodevices for bioinspired computing. *Proc. IEEE* **104**, 2024–2039 (2016).

47. Schuman, C. D. *et al.* A survey of neuromorphic computing and neural networks in hardware. *arXiv Prepr. arXiv1705.06963* (2017).

48. Torrejon, J. *et al.* Neuromorphic computing with nanoscale spintronic oscillators. *Nature* **547**, 428–431 (2017).

49. Fukushima, A. *et al.* Spin dice: A scalable truly random number generator based on spintronics. *Appl. Phys. Express* **7**, 0–4 (2014).

50. Ramasubramanian, S. G., Venkatesan, R., Sharad, M., Roy, K. & Raghunathan, A. SPINDLE: SPINtronic Deep Learning Engine for large-scale neuromorphic computing. *Proc. Int. Symp. Low Power Electron. Des.* **2015-October**, 15–20 (2015).

51. Sengupta, A. & Roy, K. A vision for all-spin neural networks: A device to system perspective. *IEEE Trans. Circuits Syst. I Regul. Pap.* **63**, 2267–2277 (2016).

52. Locatelli, N. *et al.* Spintronic devices as key elements for energy-efficient neuroinspired architectures. in *2015 Design, Automation & Test in Europe Conference & Exhibition (DATE)* 994–999 (IEEE, 2015).

53. Kish, L. B. Thermal (Noise) Death of Moore's Law? in *AIP Conference Proceedings* vol. 665 469–476 (American Institute of Physics, 2003).

54. Kish, L. B., Granqvist, C.-G., Khatri, S. P., Niklasson, G. A. & Peper, F. Information, Noise, and Energy Dissipation: Laws, Limits, and Applications. in *Molecular Architectonics* 27–44 (Springer, 2017).

55. Santagati, P. & Beiu, V. Will thermal noise affect nano-communications? in *2013 1st International Conference on Communications, Signal Processing, and their Applications (ICCSPA)* 1–4 (IEEE, 2013).

56. Dierolf, V., Ferguson, I. & Zavada, J. M. *Rare Earth and Transition Metal Doping of Semiconductor Materials: Synthesis, Magnetic Properties and Room Temperature Spintronics*. (Woodhead Publishing, 2016).

57. Dietl, T., Ohno, H., Matsukura, F., Cibert, J. & Ferrand, e D. Zener model description of ferromagnetism in zinc-blende magnetic semiconductors. *Science (80-.).* **287**, 1019–1022 (2000).

58. Patel, S. K. S., Gajbhiye, N. S. & Date, S. K. Ferromagnetism of Mn-doped TiO2 nanorods synthesized by hydrothermal method. *J. Alloys Compd.* **509**, S427–S430 (2011).

59. Patel, S. K. S. & Gajbhiye, N. S. Intrinsic room-temperature ferromagnetism of V-doped TiO2 (B) nanotubes synthesized by the hydrothermal method. *Solid State Commun.* **151**, 1500–1503 (2011).

60. Huang, C., Liu, X., Liu, Y. & Wang, Y. Room temperature ferromagnetism of Co-doped TiO2 nanotube arrays prepared by sol–gel template synthesis. *Chem. Phys. Lett.* **432**, 468–472 (2006).

61. Holub, M. *et al.* Mn-doped InAs self-organized diluted magnetic quantum-dot layers with Curie temperatures above 300 K. *Appl. Phys. Lett.* **85**, 973–975 (2004).

62. Meng, H. J. *et al.* Influence of growth temperature on structural and magnetic characterization of (In, Cr) As quantum dots. *Phys. Lett. A* **373**, 1379–1382 (2009).

63. Paschoal Jr, W. *et al.* Hopping conduction in Mn ion-implanted GaAs nanowires. *Nano Lett.* **12**, 4838–4842 (2012).

64. Wang, S. L. *et al.* Origin of ferromagnetism in self-assembled Ga 1− x Mn x As quantum dots grown on Si. *Appl. Phys. Lett.* **97**, 242505 (2010).

65. Jeon, H. C. *et al.* Magnetic and optical properties of (Ga 1− x Mn x) As diluted magnetic semiconductor quantum wires with above room ferromagnetic transition temperature. *J. Appl. Phys.* **101**, 23508 (2007).

66. Sahoo, Y., Poddar, P., Srikanth, H., Lucey, D. W. & Prasad, P. N. Chemically fabricated magnetic quantum dots of InP: Mn. *J. Phys. Chem. B* **109**, 15221–15225 (2005).

67. Han, D. S. *et al.* Synthesis and magnetic properties of manganese-doped GaP nanowires. *J. Phys. Chem. B* **109**, 9311–9316 (2005).

68. Yang, Y. *et al.* Mn-doped AlN nanowires with room temperature ferromagnetic ordering. *Appl. Phys. Lett.* **90**, 92118 (2007).

69. Wu, H. W., Tsai, C. J. & Chen, L. J. Room temperature ferromagnetism in Mn+-implanted Si nanowires. *Appl. Phys. Lett.* **90**, 43121 (2007).

70. Mandal, S. & Saha, S. K. Ni/graphene/Ni nanostructures for spintronic applications. *Nanoscale* **4**, 986–990 (2012).

71. Silva, A. M. *et al.* Graphene nanoflakes: thermal stability, infrared signatures, and potential applications in the field of spintronics and optical nanodevices. *J. Phys. Chem. C* **114**, 17472–17485 (2010).

72. Güttinger, J. *et al.* Transport through graphene quantum dots. *Reports Prog. Phys.* **75**, 126502 (2012).

73. Bhaumik, A. *et al.* Room-temperature ferromagnetism and extraordinary Hall Effect in nanostructured Q-carbon: implications for potential spintronic devices. *ACS Appl. Nano Mater.* **1**, 807–819 (2018).

74. Rocha, A. R., Martins, T. B., Fazzio, A. & Da Silva, A. J. R. Disorder-based graphene spintronics. *Nanotechnology* **21**, 345202 (2010).

75. Toyli, D. M. *et al.* Measurement and control of single nitrogen-vacancy center spins above 600 K. *Phys. Rev. X* **2**, 31001 (2012).

76. Awschalom, D. D., Epstein, R. & Hanson, R. The diamond age of spintronics. *Sci. Am.* **297**, 84–91 (2007).

77. Ma, Y. *et al.* Electronic and magnetic properties of perfect, vacancy-doped, and nonmetal adsorbed MoSe 2, MoTe 2 and WS 2 monolayers. *Phys. Chem. Chem. Phys.* **13**, 15546–15553 (2011).

78. Srivastava, P., Kumar, P. & Singh, K. Room temperature ferromagnetism in magic-sized Cr-doped CdS diluted magnetic semiconducting quantum dots. *J. Nanoparticle Res.* **13**, 5077 (2011).

79. Li, S.-S., Chang, K., Xia, J.-B. & Hirose, K. Spin-dependent transport through Cd 1− x Mn x Te diluted magnetic semiconductor quantum dots. *Phys. Rev. B* **68**, 245306 (2003).

80. Xiu, F. *et al.* Room-temperature electric-field controlled ferromagnetism in Mn0. 05Ge0. 95 quantum dots. *ACS Nano* **4**, 4948–4954 (2010).

81. Kuryliuk, V., Korotchenkov, O. & Cantarero, A. Carrier confinement in Ge/Si quantum dots grown with an intermediate ultrathin oxide layer. *Phys. Rev. B* **85**, 75406 (2012).

82. He, J., Lyu, P., Sun, L. Z., García, Á. M. & Nachtigall, P. High temperature spin-polarized semiconductivity with zero magnetization in two-dimensional Janus MXenes. *J. Mater. Chem. C* **4**, 6500–6509 (2016).

83. Dong, L., Kumar, H., Anasori, B., Gogotsi, Y. & Shenoy, V. B. Rational design of two-dimensional metallic and semiconducting spintronic materials based on ordered double-transition-metal MXenes. *J. Phys. Chem. Lett.* **8**, 422–428 (2017).

84. Kumar, H. *et al.* Tunable magnetism and transport properties in nitride MXenes. *ACS Nano* **11**, 7648–7655 (2017).

85. Si, C., Zhou, J. & Sun, Z. Half-metallic ferromagnetism and surface functionalization-induced metal–insulator transition in graphene-like two-dimensional Cr2C crystals. *ACS Appl. Mater. Interfaces* **7**, 17510–17515 (2015).

86. Rikken, G. L. J. A. A new twist on spintronics. *Science (80-.).* **331**, 864–865 (2011).

87. Di Ventra, M. & Pershin, Y. V. Spin physics: DNA spintronics sees the light. *Nat. Nanotechnol.* **6**, 198 (2011).

88. Xie, W.-H., Liu, B.-G. & Pettifor, D. G. Half-metallic ferromagnetism in transition metal pnictides and chalcogenides with wurtzite structure. *Phys. Rev. B* **68**, 134407 (2003).

89. Morello, A. Single spins in silicon carbide. *Nat. Mater.* **14**, 135–136 (2015).

90. Behnia, S., Fathizadeh, S. & Akhshani, A. DNA spintronics: Charge and spin dynamics in DNA wires. *J. Phys. Chem. C* **120**, 2973–2983 (2016).

91. Sun, D., Ehrenfreund, E. & Vardeny, Z. V. The first decade of organic spintronics research. *Chem. Commun.* **50**, 1781–1793 (2014).

92. Naber, W. J. M., Faez, S. & van der Wiel, W. G. Organic spintronics. *J. Phys. D. Appl. Phys.* **40**, R205 (2007).

93. Vobornik, I. *et al.* Magnetic proximity effect as a pathway to spintronic applications of topological insulators. *Nano Lett.* **11**, 4079–4082 (2011).

94. Šmejkal, L., Mokrousov, Y., Yan, B. & MacDonald, A. H. Topological antiferromagnetic spintronics. *Nat. Phys.* **14**, 242 (2018).

95. Palmstrøm, C. J. Heusler compounds and spintronics. *Prog. Cryst. Growth Charact. Mater.* **62**, 371–397 (2016).

96. Casper, F., Graf, T., Chadov, S., Balke, B. & Felser, C. Half-Heusler compounds: novel materials for energy and spintronic applications. *Semicond. Sci. Technol.* **27**, 63001 (2012).

97. Xie, W.-H., Xu, Y.-Q., Liu, B.-G. & Pettifor, D. G. Half-metallic ferromagnetism and structural stability of zincblende phases of the transition-metal chalcogenides. *Phys. Rev. Lett.* **91**, 37204 (2003).

98. Hussain, B., Raja, M. Y. A., Lu, N. & Ferguson, I. Applications and synthesis of zinc oxide: an emerging wide bandgap material. in *2013 High Capacity Optical Networks and Emerging/Enabling Technologies* 88–93 (IEEE, 2013).

99. Waldrop, M. M. The chips are down for Moore's law. *Nat. News* **530**, 144 (2016).

100. Zhou, C. *et al.* The current and emerging applications of the III-nitrides. *ECS J. Solid State Sci. Technol.* **6**, Q149–Q156 (2017).

101. Özgür, Ü. *et al.* A comprehensive review of ZnO materials and devices. *J. Appl. Phys.* **98**, 11 (2005).

102. Razykov, T. M. *et al.* Solar photovoltaic electricity: Current status and future prospects. *Sol. energy* **85**, 1580–1608 (2011).

103. Kołodziejczak-Radzimska, A. & Jesionowski, T. Zinc oxide—from synthesis to application: a review. *Materials (Basel).* **7**, 2833–2881 (2014).

104. Jagadish, C. & Pearton, S. J. *Zinc oxide bulk, thin films and nanostructures: processing, properties, and applications*. (Elsevier, 2011).

105. Hussain, B. *et al.* Is ZnO as a universal semiconductor material an oxymoron? in *Oxide-based Materials and Devices V* vol. 8987 898718 (International Society for Optics and Photonics, 2014).

106. Magnusson, E. B. *et al.* Surface acoustic wave devices on bulk ZnO crystals at low temperature. *Appl. Phys. Lett.* **106**, 63509 (2015).

107. Kumar, R., Al-Dossary, O., Kumar, G. & Umar, A. Zinc oxide nanostructures for NO 2 gas–sensor applications: A review. *Nano-Micro Lett.* **7**, 97–120 (2015).

108. Tian, C. *et al.* Performance enhancement of ZnO UV photodetectors by surface plasmons. *ACS Appl. Mater. Interfaces* **6**, 2162–2166 (2014).

109. Saravanan, A., Huang, B., Lin, J., Keiser, G. & Lin, I. Fast photoresponse and long lifetime UV photodetectors and field emitters based on ZnO/ultrananocrystalline diamond films. *Chem. Eur. J.* **21**, 16017–16026 (2015).

110. Janotti, A. & Van de Walle, C. G. Fundamentals of zinc oxide as a semiconductor. *Reports Prog. Phys.* **72**, 126501 (2009).

111. Nause, J. *et al.* ZnO semiconductors for lighting. in *Fifth International Conference on Solid State Lighting* vol. 5941 59410D (International Society for Optics and Photonics, 2005).

112. Ohtaki, M., Araki, K. & Yamamoto, K. High thermoelectric performance of dually doped ZnO ceramics. *J. Electron. Mater.* **38**, 1234–1238 (2009).

113. Ghahari, S., Ghafari, E. & Lu, N. Effect of ZnO nanoparticles on thermoelectric properties of cement composite for waste heat harvesting. *Constr. Build. Mater.* **146**, 755–763 (2017).

114. Li, N. *et al.* Growth of GaN on ZnO for solid state lighting applications. in *Sixth International Conference on Solid State Lighting* vol. 6337 63370Z (International Society for Optics and Photonics, 2006).

115. Alevli, M. *et al.* Characterization of InN layers grown by high-pressure chemical vapor deposition. *Appl. Phys. Lett.* **89**, 112119 (2006).

116. Feng, Y. *et al.* Homogenous $ In_ {x} Ga_ {1-x} N $ alloys on ZnO substrates: A new approach for high performance thermoelectric materials. *arXiv Prepr. arXiv1905.03769* (2019).

117. Burgett, E. A., Hertel, N. E., Nause, J. E. & Ferguson, I. Thin film doped ZnO neutron detectors. (2011).

118. Ghafari, E., Feng, Y., Liu, Y., Ferguson, I. & Lu, N. Investigating process-structure relations of ZnO nanofiber via electrospinning method. *Compos. Part B Eng.* **116**, 40–45 (2017).

119. Hahn, Y.-B. Zinc oxide nanostructures and their applications. *Korean J. Chem. Eng.* **28**, 1797 (2011).

120. Gruber, T. *et al.* Optical and structural analysis of ZnCdO layers grown by metalorganic vapor-phase epitaxy Optical and structural analysis of ZnCdO layers grown by metalorganic vapor-phase epitaxy. **3290**, 1–4 (2006).

121. Nwogu, K. N. The medical research paper: Structure and functions. *English Specif. Purp.* **16**, 119–138 (1997).

122. Zweipfennig, T. & Friedrich, J. Interplay between C-doping , threading dislocations , breakdown , and leakage in GaN on Si HEMT structures Interplay between C-doping , threading dislocations , breakdown , and leakage in GaN on Si HEMT structures. **045028**, (2020).

123. Mishra, P. *et al.* Spatial analysis of ZnO thin films prepared by vertically aligned MOCVD. in *2014 11th Annual High Capacity Optical Networks and Emerging/Enabling Technologies (Photonics for Energy)* 67–70 (IEEE, 2014).

124. Zaidi, T., Melton, A., Fenwick, W. E. & Ferguson, I. n-type, p-type and semi-insulating ZnO: N thin film growth by metal organic chemical vapor deposition with NH 3 doping. *J. Vac. Sci. Technol. B Microelectron. Nanom. Struct. Process. Meas. Phenom.* **27**, 1904–1908 (2009).

125. Saravade, V. *et al.* Nickel doping in zinc oxide by MOCVD: structural and optical properties. in *Quantum Sensing and Nano Electronics and Photonics XVII* vol. 11288 112881X (International Society for Optics and Photonics, 2020).

126. Wang, Y. *et al.* A review of earth abundant ZnO-based materials for thermoelectric and photovoltaic applications. in *Oxide-based Materials and Devices IX* vol. 10533 105331R (International Society for Optics and Photonics, 2018).

127. Pan, M. *et al.* Epitaxial growth and characterization of p-type ZnO. *J. Electron. Mater.* **36**, 457–461 (2007).

128. Pan, M. *et al.* Metal-organic chemical vapor deposition of ZnO. *J. Cryst. Growth* **287**, 688–693 (2006).

129. Feng, Z. C. *et al.* Optical characterization of ZnO materials grown by modified melt growth technique. in *Materials science forum* vol. 527 1567–1570 (Trans Tech Publ, 2006).

130. Avrutin, V. *et al.* Bulk ZnO: Current status, challenges, and prospects. *Proc. IEEE* **98**, 1339–1350 (2010).

131. Kane, M. H. *et al.* Magnetic properties of bulk Zn 1− x Mn x O and Zn 1− x Co x O single crystals. *J. Appl. Phys.* **97**, 23906 (2005).

132. Fenwick, W. E. *et al.* Transition Metal-Doped ZnO: A Comparison of Optical, Magnetic, and Structural Behavior of Bulk and Thin Films. *MRS Online Proc. Libr. Arch.* **957**, (2006).

133. Johnson, M. A. L. *et al.* MBE growth and properties of ZnO on sapphire and SiC substrates. *J. Electron. Mater.* **25**, 855–862 (1996).

134. Iwata, K. *et al.* ZnO growth on Si by radical source MBE. *J. Cryst. Growth* **214**, 50–54 (2000).

135. Kim, K. H., Park, K. C. & Ma, D. Y. Structural, electrical and optical properties of aluminum doped zinc oxide films prepared by radio frequency magnetron sputtering. *J. Appl. Phys.* **81**, 7764–7772 (1997).

136. Alam, M. J. & Cameron, D. C. Preparation and properties of transparent conductive aluminum-doped zinc oxide thin films by sol–gel process. *J. Vac. Sci. Technol. A Vacuum, Surfaces, Film.* **19**, 1642–1646 (2001).

137. Natsume, Y. & Sakata, H. Zinc oxide films prepared by sol-gel spin-coating. *Thin Solid Films* **372**, 30–36 (2000).

138. Sakohara, S., Tickanen, L. D. & Anderson, M. A. Luminescence properties of thin zinc oxide membranes prepared by the sol-gel technique: change in visible luminescence during firing. *J. Phys. Chem.* **96**, 11086–11091 (1992).

139. Fong, C. Y., Ng, S. S., Yam, F. K., Hassan, H. A. & Hassan, Z. Synthesis of two-dimensional gallium nitride via spin coating method: influences of nitridation temperatures. *J. sol-gel Sci. Technol.* **68**, 95–101 (2013).

140. Chaplais, G., Schlichte, K., Stark, O., Fischer, R. A. & Kaskel, S. Template assisted design of microporous gallium nitride materials. *Chem. Commun.* 730–731 (2003).

141. Qiu, H., Cao, C. & Zhu, H. Synthesis of nanocrystalline GaN by the sol–gel method. *Mater. Sci. Eng. B* **136**, 33–36 (2007).

142. Fujimoto, Y., Yanagida, T., Miyamoto, M., Sekiwa, H. & Chani, V. Scintillation and Dosimetric Properties of Cu-Doped Zinc Oxide Thin Films. *e-Journal Surf. Sci. Nanotechnol.* **12**, 275–278 (2014).

143. Myers, M. A., Lee, J. H. & Wang, H. Highly stable non-polar p-type Ag-doped ZnO thin films grown on r-cut sapphire. *Mater. Lett.* **100**, 78–81 (2013).

144. Limpijumnong, S., Zhang, S. B., Wei, S.-H. & Park, C. H. Doping by large-size-mismatched impurities: the microscopic origin of arsenic-or antimony-doped p-type zinc oxide. *Phys. Rev. Lett.* **92**, 155504 (2004).

145. Li, Y. *et al.* Realization of Na-doped p-type non-polar a-plane Zn1− xCdxO films by pulsed laser deposition. *J. Alloys Compd.* **584**, 466–470 (2014).

146. TOMASZ, A. *et al.* Optical and electrical characterization of defects in zinc oxide thin films grown by atomic layer deposition. *Opt. Appl.* **39**, (2009).

147. Ghods, A., Saravade, V., Zhou, C., Kim, C.-S. & Ferguson, I. PEDOT: PSS/n-Si Hybrid Solar Cells with Al 2 O 3 Interfiacial Passivation Layer. in *2019 IEEE 16th International Conference on Smart Cities: Improving Quality of Life Using ICT & IoT and AI (HONET-ICT)* 201–202 (IEEE, 2019).

148. Ghods, A., Saravade, V., Woode, A., Zhou, C. & Ferguson, I. Effect of Gate Voltage on the Photovoltaic Performance of GaAs-based Schottky Junction Solar Cells. in *2019 IEEE 46th Photovoltaic Specialists Conference (PVSC)* 1743–1747 (IEEE, 2019).

149. Illiberi, A., Roozeboom, F. & Poodt, P. Spatial atomic layer deposition of zinc oxide thin films. *ACS Appl. Mater. Interfaces* **4**, 268–272 (2012).

150. Luka, G. *et al.* Aluminum-doped zinc oxide films grown by atomic layer deposition for transparent electrode applications. *J. Mater. Sci. Mater. Electron.* **22**, 1810–1815 (2011).

151. Asghar, M. *et al.* Investigation of VO–Zni native donor complex in MBE grown bulk ZnO. *Semicond. Sci. Technol.* **28**, 105019 (2013).

152. Tang, K. *et al.* Recent progress of the native defects and p-type doping of zinc oxide. *Chinese Phys. B* **26**, 47702 (2017).

153. Vidya, R. *et al.* Energetics of intrinsic defects and their complexes in ZnO investigated by density functional calculations. *Phys. Rev. B* **83**, 45206 (2011).

154. McCluskey, M. D. & Jokela, S. J. Defects in zno. *J. Appl. Phys.* **106**, 10 (2009).

155. Janotti, A. & Van de Walle, C. G. Native point defects in ZnO. *Phys. Rev. B* **76**, 165202 (2007).

156. Kane, M. H. Investigaton of the Suitability of Wide Bandgap Dilute Magnetic Semiconductors for Spintronics. (2007).

157. van Schilfgaarde, M. & Mryasov, O. N. Anomalous exchange interactions in III-V dilute magnetic semiconductors. *Phys. Rev. B* **63**, 233205 (2001).

158. Rao, B. K. & Jena, P. Giant magnetic moments of nitrogen-doped Mn clusters and their relevance to ferromagnetism in Mn-doped GaN. *Phys. Rev. Lett.* **89**, 185504 (2002).

159. Das, G. P., Rao, B. K., Jena, P. & Kawazoe, Y. Dilute magnetic III–V semiconductor spintronics materials: A first-principles approach. *Comput. Mater. Sci.* **36**, 84–90 (2006).

160. Kim, J.-Y. *et al.* Structural and magnetic properties of ultra-thin Fe films on metal-organic chemical vapour deposited GaN (0001). *J. Appl. Phys.* **121**, 43904 (2017).

161. Zhou, Z. *et al.* Investigations on the origin of ferromagnetism in Ga1− xCrxN and Si-doped Ga1− xCrxN films: Experiments and theory. *J. Alloys Compd.* **658**, 800–805 (2016).

162. Lo, F.-Y. *et al.* Structural, optical, and magnetic properties of highly-resistive Sm-implanted GaN thin films. *J. Appl. Phys.* **116**, 43909 (2014).

163. Sekiguchi, H. *et al.* Structural and optical properties of Eu-doped GaN nanocolumns on (111) Si substrates grown by RF-plasma-assisted molecular beam epitaxy. *Jpn. J. Appl. Phys.* **55**, 05FG07 (2016).

164. Dhar, S. *et al.* Gd-doped GaN: A very dilute ferromagnetic semiconductor with a Curie temperature above 300 K. *Phys. Rev. B* **72**, 245203 (2005).

165. Hoang, K. First-principles identification of defect levels in Er-doped GaN. *Phys. status solidi (RRL)–Rapid Res. Lett.* **10**, 915–918 (2016).

166. Gupta, S. *et al.* Electrical and magnetic properties of Ga1− xGdxN grown by metal organic chemical vapor deposition. *J. Appl. Phys.* **110**, 83920 (2011).

167. Kong, Y. *et al.* Optoelectronic properties of Mg doping GaN nanowires. *Opt. quantum Electron.* **48**, 493 (2016).

168. Kaleemullah, N. S. *et al.* Magnetic properties of gadolinium and carbon co-doped gallium nitride. *Solid State Commun.* **249**, 7–11 (2017).

169. Gupta, S., Kang, H., Kane, M. H., Park, E. & Ferguson, I. T. Growth and magnetization study of transition metal doped GaN nanostructures. *Phys. status solidi c* **5**, 1740–1742 (2008).

170. Gupta, S. *et al.* A nucleation study of group III-nitride multifunctional nanostructures. *J. Cryst. Growth* **287**, 596–600 (2006).

171. Ma, Z., Jamer, M. E., Panaitescu, E., Heiman, D. & Menon, L. Structure and magnetism of GaMnN nanowires synthesized with nonmagnetic catalyst. *J. Magn. Magn. Mater.* **394**, 155–159 (2015).

172. Choi, H. *et al.* Single-crystalline diluted magnetic semiconductor GaN: Mn nanowires. *Adv. Mater.* **17**, 1351–1356 (2005).

173. Wang, Z. *et al.* Enhanced ferromagnetism and tunable saturation magnetization of Mn/C-codoped GaN nanostructures synthesized by carbothermal nitridation. *J. Am. Chem. Soc.* **130**, 16366–16373 (2008).

174. Reddeppa, M. *et al.* Ferromagnetic properties of GaN nanorods: Effect of silicon doping and hydrogenation. *Curr. Appl. Phys.* **16**, 886–889 (2016).

175. Gao, X. *et al.* The important role of Ga vacancies in the ferromagnetic GaN thin films. *J. Alloys Compd.* **699**, 596–600 (2017).

176. Roul, B. *et al.* Experimental evidence of Ga-vacancy induced room temperature ferromagnetic behavior in GaN films. *Appl. Phys. Lett.* **99**, 162512 (2011).

177. Bhat, V. J. *et al.* Increased static dielectric constant in ZnMnO and ZnCoO thin films with bound magnetic polarons. *Sci. Reports (Nature Publ. Group)* **10**, (2020).

178. Liu, J. J., Yu, M. H. & Zhou, W. L. Fabrication of Mn-doped ZnO diluted magnetic semiconductor nanostructures by chemical vapor deposition. *J. Appl. Phys.* **99**, 08M119 (2006).

179. Liu, L. Q., Xiang, B., Zhang, X. Z., Zhang, Y. & Yu, D. P. Synthesis and room temperature ferromagnetism of FeCo-codoped ZnO nanowires. *Appl. Phys. Lett.* **88**, 63104 (2006).

180. Shuai, M. *et al.* Room-temperature ferromagnetism in Cu+ implanted ZnO nanowires. *J. Phys. D. Appl. Phys.* **41**, 135010 (2008).

181. Saravanan, R., Santhi, K., Sivakumar, N., Narayanan, V. & Stephen, A. Synthesis and characterization of ZnO and Ni doped ZnO nanorods by thermal decomposition method for spintronics application. *Mater. Charact.* **67**, 10–16 (2012).

182. Wang, D. *et al.* Robust room-temperature ferromagnetism with giant anisotropy in Nd-doped ZnO nanowire arrays. *Nano Lett.* **12**, 3994–4000 (2012).

183. Gou, Z., Yang, H. & Yang, P. Investigation on electronic and magnetic properties of (Fe, In) co-doped ZnO. *J. Alloys Compd.* **695**, 1378–1382 (2017).

184. Xu, H., Rosa, A. L., Frauenheim, T. & Zhang, R. Q. N-doped ZnO nanowires: Surface segregation, the effect of hydrogen passivation and applications in spintronics. *Phys. status solidi* **247**, 2195–2201 (2010).

185. Dai, Z. *et al.* C-doped ZnO nanowires: Electronic structures, magnetic properties, and a possible spintronic device. *J. Chem. Phys.* **134**, 104706 (2011).

186. Barnes, T. M. *et al.* Comparing the fundamental physics and device performance of transparent, conductive nanostructured networks with conventional transparent conducting oxides. *Adv. Energy Mater.* **2**, 353–360 (2012).

187. Berginski, M. *et al.* The effect of front ZnO: Al surface texture and optical transparency on efficient light trapping in silicon thin-film solar cells. *J. Appl. Phys.* **101**, 74903 (2007).

188. Saliba, M. *et al.* Cesium-containing triple cation perovskite solar cells: improved stability, reproducibility and high efficiency. *Energy Environ. Sci.* **9**, 1989–1997 (2016).

189. Wright, M. & Uddin, A. Solar Energy Materials & Solar Cells Organic—inorganic hybrid solar cells: A comparative review. *Sol. Energy Mater. Sol. Cells* **107**, 87–111 (2012).

190. Holman, Z. C. Descoeudres, a, De Wolf, S. and Ballif, C.,"Record Infrared Internal Quantum Efficiency in Silicon Heterojunction Solar Cells With Dielectric/Metal Rear Reflectors,". *IEEE J. Photovoltaics* **3**, 1243–1249 (2013).

191. Ghods, A., Saravade, V. G., Zhou, C. & Ferguson, I. T. Field-effect passivation of metal/n-GaAs Schottky junction solar cells using atomic layer deposited Al2O3/ZnO ultrathin films. *J. Vac. Sci. Technol. A Vacuum, Surfaces, Film.* **38**, 12406 (2020).

192. Gordon, R. G. Criteria for choosing transparent conductors. *MRS Bull.* **25**, 52–57 (2000).

193. Dabirian, A. *et al.* Tuning the Optoelectronic Properties of ZnO: Al by Addition of Silica for Light Trapping in High-Efficiency Crystalline Si Solar Cells. *Adv. Mater. interfaces* **3**, 1500462 (2016).

194. Werner, J. *et al.* Sputtered rear electrode with broadband transparency for perovskite solar cells. *Sol. Energy Mater. Sol. Cells* **141**, 407–413 (2015).

195. Morales-Masis, M., De Nicolas, S. M., Holovsky, J., De Wolf, S. & Ballif, C. Low-temperature high-mobility amorphous IZO for silicon heterojunction solar cells. *IEEE J. Photovoltaics* **5**, 1340–1347 (2015).

196. Faÿ, S. *et al.* Rough ZnO layers by LP-CVD process and their effect in improving performances of amorphous and microcrystalline silicon solar cells. *Sol. Energy Mater. Sol. Cells* **90**, 2960–2967 (2006).

197. Klein, A. *et al.* Transparent conducting oxides for photovoltaics: Manipulation of fermi level, work function and energy band alignment. *Materials (Basel).* **3**, 4892–4914 (2010).

198. Kucukgok, B., Wang, B., Melton, A. G., Lu, N. & Ferguson, I. T. Comparison of thermoelectric properties of GaN and ZnO samples. *Phys. status solidi* **11**, 894–897 (2014).

199. Lany, S. & Zunger, A. Assessment of correction methods for the band-gap problem and for finite-size effects in supercell defect calculations: Case studies for ZnO and GaAs. *Phys. Rev. B* **78**, 235104 (2008).

200. Zhou, C. *et al.* ZnO for solar cell and thermoelectric applications. in *Oxide-based Materials and Devices VIII* vol. 10105 101051K (International Society for Optics and Photonics, 2017).

201. Feng, Y. *et al.* Metal oxides for thermoelectric power generation and beyond. *Adv. Compos. Hybrid Mater.* **1**, 114–126 (2018).

202. Guo, X.-L., Choi, J.-H., Tabata, H. & Kawai, T. Fabrication and optoelectronic properties of a transparent ZnO homostructural light-emitting diode. *Jpn. J. Appl. Phys.* **40**, L177 (2001).

203. Lim, J. *et al.* UV electroluminescence emission from ZnO light-emitting diodes grown by high-temperature radiofrequency sputtering. *Adv. Mater.* **18**, 2720–2724 (2006).

204. Rahman, F. Zinc oxide light-emitting diodes: A review. *Opt. Eng.* **58**, 10901 (2019).

205. Feng, Z. C. *Handbook of zinc oxide and related materials: volume two, devices and nano-engineering*. (CRC press, 2012).

206. Kouzes, R. The 3He Supply Problem, Pacific Northwest National Laboratory, Oakridge, TN, Rep. *PNNL-18388, Apr* (2009).

207. Council, N. R. *The impact of selling the Federal Helium Reserve*. (National Academies Press, 2000).

208. Petti, L. *et al.* Metal oxide semiconductor thin-film transistors for flexible electronics. *Appl. Phys. Rev.* **3**, 21303 (2016).

209. Zhang, Y.-H., Mei, Z.-X., Liang, H.-L. & Du, X.-L. Review of flexible and transparent thin-film transistors based on zinc oxide and related materials. *Chinese Phys. B* **26**, 47307 (2017).

210. Choi, P., Lee, S., Kim, H., Park, J. & Choi, B. Evaluation of Minority Carrier Generation Lifetime for Oxide Semiconductors. *Thin Solid Films* 138023 (2020).

211. Carcia, P. F., McLean, R. S., Reilly, M. H. & Nunes Jr, G. Transparent ZnO thin-film transistor fabricated by rf magnetron sputtering. *Appl. Phys. Lett.* **82**, 1117–1119 (2003).

212. Wang, Y.-L. *et al.* Room temperature deposited indium zinc oxide thin film transistors. *Appl. Phys. Lett.* **90**, 232103 (2007).

213. Tsukazaki, A. *et al.* High Electron Mobility Exceeding 104 cm2 V-1 s-1 in MgxZn1-xO/ZnO Single Heterostructures Grown by Molecular Beam Epitaxy. *Appl. Phys. express* **1**, 55004 (2008).

214. Jin, H., Xu, X., Tao, Y., Feng, B. & Wang, D. Reliability enhancement of zinc oxide varistors using sputtered silver electrodes. *Microelectron. Reliab.* **61**, 91–94 (2016).

215. Levinson, L. M. & Philipp, H. R. Zinc oxide varistors—a review. *Am. Ceram. Soc. Bull.* **65**, 639–646 (1986).

216. Kaufmann, B., Raidl, N. & Supancic, P. Investigation of schottky barriers at Pd-ZnO junctions in varistors. *J. Eur. Ceram. Soc.* (2020).

217. Espitia, P. J. P. *et al.* Zinc oxide nanoparticles: synthesis, antimicrobial activity and food packaging applications. *Food bioprocess Technol.* **5**, 1447–1464 (2012).

218. Roy, S. & Basu, S. Improved zinc oxide film for gas sensor applications. *Bull. Mater. Sci.* **25**, 513–515 (2002).

219. Moezzi, A., McDonagh, A. M. & Cortie, M. B. Zinc oxide particles: Synthesis, properties and applications. *Chem. Eng. J.* **185**, 1–22 (2012).

220. Khan, M. M. *et al.* Antibacterial activities of zinc oxide and Mn-doped zinc oxide synthesized using Melastoma malabathricum (L.) leaf extract. *Bioprocess Biosyst. Eng.* 1–10 (2020).

221. Ghaffari, H. *et al.* Inhibition of H1N1 influenza virus infection by zinc oxide nanoparticles: another emerging application of nanomedicine. *J. Biomed. Sci.* **26**, 70 (2019).

222. Rasmussen, J. W., Martinez, E., Louka, P. & Wingett, D. G. Zinc oxide nanoparticles for selective destruction of tumor cells and potential for drug delivery applications. *Expert Opin. Drug Deliv.* **7**, 1063–1077 (2010).

223. Jiang, J., Pi, J. & Cai, J. The advancing of zinc oxide nanoparticles for biomedical applications. *Bioinorg. Chem. Appl.* **2018**, (2018).

224. Hong, H. *et al.* Red fluorescent zinc oxide nanoparticle: a novel platform for cancer targeting. *ACS Appl. Mater. Interfaces* **7**, 3373–3381 (2015).

225. Hong, H. *et al.* Cancer-targeted optical imaging with fluorescent zinc oxide nanowires. *Nano Lett.* **11**, 3744–3750 (2011).

226. Alkaladi, A., Abdelazim, A. M. & Afifi, M. Antidiabetic activity of zinc oxide and silver nanoparticles on streptozotocin-induced diabetic rats. *Int. J. Mol. Sci.* **15**, 2015–2023 (2014).

227. Davis, K. B., Stringari, S. & Wieman, C. E. Zener Model Description of Ferromagnetism in Zinc-Blende. **287**, 1019–1023 (2000).

228. Saravade, V. G., Ferguson, C. H., Ghods, A., Zhou, C. & Ferguson, I. T. Room Temperature Ferromagnetism in Gadolinium-doped Gallium Nitride. *MRS Adv.* **3**, 159–164 (2018).

229. Liu, C., Yun, F. & Morkoc, H. Ferromagnetism of ZnO and GaN : A Review. **6**, 555–597 (2005).

230. Properties, M., Spintronics, R. T., Dierolf, V., Ferguson, I. T. & Zavada, J. M. Rare Earth and Transition Metal Doping of Semiconductor Materials Synthesis , Magnetic Properties and.

231. Yi, J. B. *et al.* Ferromagnetism in dilute magnetic semiconductors through defect engineering: Li-doped ZnO. *Phys. Rev. Lett.* **104**, 137201 (2010).

232. Sato, K. *et al.* First-principles theory of dilute magnetic semiconductors. *Rev. Mod. Phys.* **82**, 1633 (2010).

233. Dietl, T. A ten-year perspective on dilute magnetic semiconductors and oxides. *Nat. Mater.* **9**, 965–974 (2010).

234. Mittra, R., Chan, C. H. & Cwik, T. Techniques for analyzing frequency selective surfaces-a review. *Proc. IEEE* **76**, 1593–1615 (1988).

235. Luukkonen, O., Costa, F., Simovski, C. R., Monorchio, A. & Tretyakov, S. A. A thin electromagnetic absorber for wide incidence angles and both polarizations. *IEEE Trans. Antennas Propag.* **57**, 3119–3125 (2009).

236. Dederichs, P. H., Sato, K. & Katayama-Yoshida, H. Dilute magnetic semiconductors. *Phase Transitions* **78**, 851–867 (2005).

237. Sato, K., Dederichs, P. H. & Katayama-Yoshida, H. Curie temperatures of dilute magnetic semiconductors from LDA+ U electronic structure calculations. *Phys. B Condens. Matter* **376**, 639–642 (2006).

238. Kane, M. H., Gupta, S. & Ferguson, I. T. Transition metal and rare earth doping in GaN. in *Rare Earth and Transition Metal Doping of Semiconductor Materials* 315–370 (Elsevier, 2016).

239. Pearton, S. J. *et al.* Room temperature ferromagnetism in GaMnN and GaMnP. *Phys. status solidi* **195**, 222–227 (2003).

240. Sonoda, S. *et al.* Coexistence of Mn2+ and Mn3+ in ferromagnetic GaMnN. *J. Phys. Condens. Matter* **18**, 4615 (2006).

241. Kim, K. H. *et al.* Enhanced carrier-mediated ferromagnetism in GaMnN by codoping of Mg. *Appl. Phys. Lett.* **82**, 4755–4757 (2003).

242. Mitra, C. & Lambrecht, W. R. L. Interstitial-nitrogen- and oxygen-induced magnetism in Gd-doped GaN. 1–4 (2009) doi:10.1103/PhysRevB.80.081202.

243. Gan, S. Defect-enhanced ferromagnetism in Gd-. **212502**, (2012).

244. Sapega, V. F., Ramsteiner, M., Dhar, S., Brandt, O. & Ploog, K. H. Large spin splitting of GaN electronic states induced by Gd doping.

245. Kane, M. H. *et al.* Magnetic and optical properties of Ga1− xMnxN grown by metalorganic chemical vapour deposition. *Semicond. Sci. Technol.* **20**, L5 (2005).

246. Centre, C. G. Magnetic properties of gadolinium and carbon co-doped gallium nitride. *Solid State Commun.* **249**, 7–11 (2017).

247. Kane, M. H., Asghar, A., Bonanni, A., Pearton, S. J. & Abernathy, C. R. The Fermi level dependence of the optical and magnetic properties of Ga 1 − x Mn x N grown by metal – organic chemical vapour deposition The Fermi level dependence of the optical and magnetic properties of Ga 1 − x Mn x N grown by metal – organic chemical. (2006) doi:10.1088/0953-8984/18/9/001.

248. Selim, F. A., Weber, M. H., Solodovnikov, D. & Lynn, K. G. Nature of native defects in ZnO. *Phys. Rev. Lett.* **99**, 85502 (2007).

249. Oba, F., Nishitani, S. R., Isotani, S., Adachi, H. & Tanaka, I. Energetics of native defects in ZnO. *J. Appl. Phys.* **90**, 824–828 (2001).

250. Xie, R. *et al.* First-principles calculations of GaN : Gd temperature ferromagnetism. **115003**, (2017).

251. Shvarkov, S. *et al.* Magnetic properties of Gd-doped GaN. *Phys. status solidi* **251**, 1673–1684 (2014).

252. Dhar, S., Brandt, O., Ramsteiner, M., Sapega, V. F. & Ploog, K. H. Colossal magnetic moment of Gd in GaN. *Phys. Rev. Lett.* **94**, 37205 (2005).

253. Hejtmánek, J. *et al.* On the magnetic properties of Gd implanted. **107**, 2006–2009 (2015).

254. Gan, G. *et al.* pss Magnetic properties of. **1684**, 1673–1684 (2014).

255. Khaderbad, M. A. Effect of annealing on the magnetic properties of Gd focused ion beam implanted GaN. 1–3 (2007) doi:10.1063/1.2770762.

256. Thompson, A. G. MOCVD technology for semiconductors. *Mater. Lett.* **30**, 255–263 (1997).

257. Moffat, H. & Jensen, K. F. Complex flow phenomena in MOCVD reactors: I. Horizontal reactors. *J. Cryst. Growth* **77**, 108–119 (1986).

258. Shindo, D. & Oikawa, T. Energy dispersive x-ray spectroscopy. in *Analytical Electron Microscopy for Materials Science* 81–102 (Springer, 2002).

259. Suryanarayana, C. & Norton, M. G. *X-ray diffraction: a practical approach*. (Springer Science & Business Media, 2013).

260. Guinier, A. *X-ray diffraction in crystals, imperfect crystals, and amorphous bodies*. (Courier Corporation, 1994).

261. Warren, B. E. *X-ray Diffraction*. (Courier Corporation, 1990).

262. Zaidi, T. Ferromagnetic and multiferroic thin films aimed towards optoelectronic and spintronic applications. (Dissertation, G. Tech) (2010).

263. Moram, M., Johnston, C., Kappers, M., & Humphreys, C. The effects of film surface roughness on x-ray diffraction of nonpolar gallium nitride films. *J. Phys. D.*: *Appl. Phys.* **42**, 135407 (2009.

264. Jian-Qi, L., Yong-Xin, Q., Jian-Feng, W., Ke, X. & Hui, Y. Analysis of modified Williamson-Hall plots on GaN layers. *Chinese Phys. Lett.* **28**, 16101 (2011).

265. Brandstetter, S., Derlet, P. M., Van Petegem, S. & Van Swygenhoven, H. Williamson–Hall anisotropy in nanocrystalline metals: X-ray diffraction experiments and atomistic simulations. *Acta Mater.* **56**, 165–176 (2008).

266. Chwang, R., Smith, B. J. & Crowell, C. R. Contact size effects on the van der Pauw method for resistivity and Hall coefficient measurement. *Solid. State. Electron.* **17**, 1217–1227 (1974).

267. Hemenger, P. M. Measurement of high resistivity semiconductors using the van der Pauw method. *Rev. Sci. Instrum.* **44**, 698–700 (1973).

268. Phys, A. Ion beam modification of topological insulator bismuth selenide. **242106**, (2017).

269. Jungwirth, T., Niu, Q. & MacDonald, A. H. Anomalous Hall effect in ferromagnetic semiconductors. *Phys. Rev. Lett.* **88**, 207208 (2002).

270. Nagaosa, N., Sinova, J., Onoda, S., MacDonald, A. H. & Ong, N. P. Anomalous hall effect. *Rev. Mod. Phys.* **82**, 1539 (2010).

271. Fernández-Pacheco, A. *et al.* Universal scaling of the anomalous Hall effect in Fe 3 O 4 epitaxial thin films. *Phys. Rev. B* **77**, 100403 (2008).

272. Sangiao, S. *et al.* Anomalous Hall effect in Fe (001) epitaxial thin films over a wide range in conductivity. *Phys. Rev. B* **79**, 14431 (2009).

273. Shim, W. *et al.* Evidence for carrier-induced ferromagnetic ordering in Zn 1− x Mn x O thin films: Anomalous Hall effect. *J. Appl. Phys.* **101**, 123908 (2007).

274. Meng, M., Wu, S. X., Zhou, W. Q. & Li, S. W. Scaling of the anomalous Hall effect in epitaxial antiperovskite Mn3. 5Dy0. 5N involving multiple competing scattering mechanisms. *Appl. Phys. Lett.* **109**, 82405 (2016).

275. Hsu, H. S., Lin, C. P., Chou, H. & Huang, J.-C. A. Room temperature anomalous Hall effect in Co doped ZnO thin films in the semiconductor regime. *Appl. Phys. Lett.* **93**, 142507 (2008).

276. Lee, Y. J., de Jong, M. P., van der Wiel, W. G., Kim, Y. & Brock, J. D. Anomalous Hall effect suppression in anatase Co: TiO 2 by the insertion of an interfacial TiO 2 buffer layer. *Appl. Phys. Lett.* **97**, 212506 (2010).

277. Higgins, J. S., Shinde, S. R., Ogale, S. B., Venkatesan, T. & Greene, R. L. Hall effect in cobalt-doped TiO 2− δ. *Phys. Rev. B* **69**, 73201 (2004).

278. Shon, Y. *et al.* The structural, optical and magnetic properties and anomalous Hall effect of InMnP: Zn epilayers. *New J. Phys.* **10**, 115002 (2008).

279. Scarpulla, M. A., Gallinat, C. S., Mack, S., Speck, J. S. & Gossard, A. C. GdN (1 1 1) heteroepitaxy on GaN (0 0 0 1) by N2 plasma and NH3 molecular beam epitaxy. *J. Cryst. Growth* **311**, 1239–1244 (2009).

280. Phys, A. *et al.* Ferromagnetism and its stability in n-type Gd-doped GaN : First-principles calculation. **232408**, (2016).

281. Ney, A. *et al.* Element specific investigations of the structural and magnetic properties of Gd : GaN Element specific investigations of the structural and magnetic properties of Gd : GaN. **252515**, 1–4 (2007).

282. Mishra, J. K. & Dhar, S. Investigation of defects in Gd doped GaN using thermally stimulated current spectroscopy. *Solid State Commun.* **226**, 25–28 (2016).

283. Li, Y. *et al.* principles calculations Stability and electronic structure of defect complexes in Gd-doped GaN : First-principles calculations. **023901**, (2017).

284. Tripathi, G. S. & Mukherjee, P. K. Effects of strain on the k→·π→ electronic structure and related properties of w-GaN. *J. Phys. Chem. Solids* **141**, (2020).

285. Arifin, P. *et al.* Room-temperature photoluminescence of Mg-doped GaN thin films grown by plasma- assisted MOCVD Room-temperature photoluminescence of Mg-doped GaN thin films grown by plasma-assisted MOCVD. **045123**, (2020).

286. Armstrong, A. *et al.* Impact of deep levels on the electrical conductivity and luminescence of gallium nitride codoped with carbon and silicon. *J. Appl. Phys.* **98**, 53704 (2005).

287. Hashiguchi, M., Sakaguchi, I., Adachi, Y. & Ohashi, N. Quantitative secondary ion mass spectrometric analysis of secondary ion polarity in GaN films implanted with oxygen. *Jpn. J. Appl. Phys.* **55**, 101001 (2016).

288. Xu, J., Li, Q., Liu, J. & Ye, B. A comparative study on ferromagnetic C/O-implanted GaN films by positron annihilation spectroscopy. *Nucl. Instruments Methods Phys. Res. Sect. B Beam Interact. with Mater. Atoms* **375**, 107–111 (2016).

289. Jiang, W., Weber, W. J., Thevuthasan, S., Exarhos, G. J. & Bozlee, B. J. Effect of oxygen ion implantation in gallium nitride. *Mater. Res. Soc. Internet J. Nitride Semicond. Res.* **4**, 622–627 (1999).

290. Thaik, M., Hömmerich, U., Schwartz, R. N., Wilson, R. G. & Zavada, J. M. Photoluminescence spectroscopy of erbium implanted gallium nitride. *Appl. Phys. Lett.* **71**, 2641–2643 (1997).

291. Qiu, C. H. *et al.* Cathodoluminescence study of erbium and oxygen coimplanted gallium nitride thin films on sapphire substrates. *Appl. Phys. Lett.* **66**, 562–564 (1995).

292. Zolper, J. C., Wilson, R. G., Pearton, S. J. & Stall, R. A. Ca and O ion implantation doping of GaN. *Appl. Phys. Lett.* **68**, 1945–1947 (1996).

293. Ziegler, J. F. *Ion implantation science and technology*. (Elsevier, 2012).

294. Running, C. *et al.* Recovery of structural defects in GaN after heavy ion implantation. *MRS Online Proc. Libr. Arch.* **468**, (1997).

295. Alves, E. *et al.* High temperature annealing of Er implanted GaN. *Mater. Sci. Eng. B* **81**, 132–135 (2001).

296. Alves, E. *et al.* RBS lattice site location and damage recovery studies in GaN. *Mater. Res. Soc. Internet J. Nitride Semicond. Res.* **4**, 933–939 (1999).

297. Lorenz, K. *et al.* High-temperature annealing and optical activation of Eu-implanted GaN. *Appl. Phys. Lett.* **85**, 2712–2714 (2004).

298. Ohtomo, A. *et al.* Room-temperature stimulated emission of excitons in ZnO/(Mg, Zn) O superlattices. *Appl. Phys. Lett.* **77**, 2204–2206 (2000).

299. Jin, Y. *et al.* Room temperature UV emission of MgxZn1− xO films. *Solid State Commun.* **119**, 409–413 (2001).

300. Memarian, N. *et al.* Hierarchically assembled ZnO nanocrystallites for high-efficiency dye-sensitized solar cells. *Angew. Chemie Int. Ed.* **50**, 12321–12325 (2011).

301. Li, N. *et al.* Suppression of phase separation in InGaN layers grown on lattice-matched ZnO substrates. *J. Cryst. Growth* **311**, 4628–4631 (2009).

302. Yu, H. *et al.* MOVPE growth of AlGaN/GaN superlattices on ZnO substrates for green emitter applications. *J. Cryst. Growth* **310**, 4904–4907 (2008).

303. Wang, S. *et al.* MOCVD growth of GaN-based materials on ZnO substrates. *Phys. status solidi c* **5**, 1736–1739 (2008).

304. Sheu, J.-K., Lee, M.-L., Lu, Y. S. & Shu, K. W. Ga-doped ZnO transparent conductive oxide films applied to GaN-based light-emitting diodes for improving light extraction efficiency. *IEEE J. Quantum Electron.* **44**, 1211–1218 (2008).

305. Söderström, T. *et al.* ZnO Transparent conductive oxide for thin film silicon solar cells. in *Oxide-based Materials and Devices* vol. 7603 76030B (International Society for Optics and Photonics, 2010).

306. Imanishi, Y., Taguchi, M. & Onisawa, K. Effect of sublayer surface treatments on ZnO transparent conductive oxides using dc magnetron sputtering. *Thin Solid Films* **518**, 2945–2948 (2010).

307. Law, M. *et al.* ZnO− Al2O3 and ZnO− TiO2 core− shell nanowire dye-sensitized solar cells. *J. Phys. Chem. B* **110**, 22652–22663 (2006).

308. Hussain, B., Ebong, A. & Ferguson, I. Zinc oxide as an active n-layer and antireflection coating for silicon based heterojunction solar cell. *Sol. Energy Mater. Sol. Cells* **139**, 95–100 (2015).

309. Ohtomo, A. *et al.* Mg x Zn 1− x O as a II–VI widegap semiconductor alloy. *Appl. Phys. Lett.* **72**, 2466–2468 (1998).

310. Janotti, A. & Van de Walle, C. G. Absolute deformation potentials and band alignment of wurtzite ZnO, MgO, and CdO. *Phys. Rev. B* **75**, 121201 (2007).

311. Gruber, T. *et al.* Optical and structural analysis of ZnCdO layers grown by metalorganic vapor-phase epitaxy. *Appl. Phys. Lett.* **83**, 3290–3292 (2003).

312. Ali, H. *et al.* Influence of nickel doping on the energy band gap, luminescence, and magnetic order of spray deposited nanostructured ZnO thin films. *J. Alloys Compd.* **816**, 1–8 (2020).

313. Chithira, P. R. & John, T. T. Defect and dopant induced room temperature ferromagnetism in Ni doped ZnO nanoparticles. *J. Alloys Compd.* **766**, 572–583 (2018).

314. Jadhav, J. & Biswas, S. Shape-controlled magnetic nanoplatelets of Ni-doped ZnO synthesized via a chemical precursor. *J. Alloys Compd.* **664**, 71–82 (2016).

315. Patil, S. K., Shinde, S. S. & Rajpure, K. Y. Physical properties of spray deposited Ni-doped zinc oxide thin films. *Ceram. Int.* **39**, 3901–3907 (2013).

316. Das, S. C. *et al.* Band gap tuning in ZnO through ni doping via spray pyrolysis. *J. Phys. Chem. C* **117**, 12745–12753 (2013).

317. Mohammadijoo, M., Khorshidi, Z. N., Sadrnezhaad, S. K. & Mazinani, V. Synthesis and characterization of nickel oxide nanoparticle with wide band gap energy prepared via thermochemical processing. *Nanosci. Nanotechnol. Int. J* **4**, 6–9 (2014).

318. Ghotbi, M. Y. Nickel doped zinc oxide nanoparticles produced by hydrothermal decomposition of nickel-doped zinc hydroxide nitrate. *Particuology* **10**, 492–496 (2012).

319. Elilarassi, R. & Chandrasekaran, G. Synthesis and optical properties of Ni-doped zinc oxide nanoparticles for optoelectronic applications. *Optoelectron. Lett.* **6**, 6–10 (2010).

320. Dar, T. A., Agrawal, A. & Sen, P. Pulsed laser deposited nickel doped zinc oxide thin Films: Structural and optical investigations. (2013).

321. Singh, S. D. *et al.* Determination of the optical gap bowing parameter for ternary Ni 1− x Zn x O cubic rocksalt solid solutions. *Dalt. Trans.* **44**, 14793–14798 (2015).

322. Chauhan, R., Kumar, A. & Chaudhary, R. Structure and optical properties of Zn1-xNixO nanoparticles by coprecipitation method. *J. Optoelectron. Biomed. Mater* **3**, 17–23 (2011).

323. Gupta, S. *et al.* MOVPE growth of transition-metal-doped GaN and ZnO for spintronic applications. *J. Cryst. Growth* **310**, 5032–5038 (2008).

324. Tang, K. *et al.* Formation of VZn-NO acceptors with the assistance of tellurium in nitrogen-doped ZnO films. *J. Alloys Compd.* **699**, 484–488 (2017).

325. Ukoba, K. O., Eloka-Eboka, A. C. & Inambao, F. L. Review of nanostructured NiO thin film deposition using the spray pyrolysis technique. *Renew. Sustain. Energy Rev.* **82**, 2900–2915 (2018).

326. Abdel-Wahab, M. S., Jilani, A., Yahia, I. S. & Al-Ghamdi, A. A. Enhanced the photocatalytic activity of Ni-doped ZnO thin films: Morphological, optical and XPS analysis. *Superlattices Microstruct.* **94**, 108–118 (2016).

327. Bouaoud, A. *et al.* Transparent conducting properties of Ni doped zinc oxide thin films prepared by a facile spray pyrolysis technique using perfume atomizer. *Mater. Chem. Phys.* **137**, 843–847 (2013).

328. Ghotbi, M. Y. Nickel doped zinc oxide nanoparticles produced by hydrothermal decomposition of nickel-doped zinc hydroxide nitrate. *Particuology* **10**, 492–496 (2012).

329. Srinet, G., Kumar, R. & Sajal, V. Structural, optical, vibrational, and magnetic properties of sol-gel derived Ni doped ZnO nanoparticles. *J. Appl. Phys.* **114**, (2013).

330. Kayani, Z. N., Anjum, M., Riaz, S., Naseem, S. & Zeeshan, T. Role of Mn in biological, optical, and magnetic properties ZnO nano-particles. *Appl. Phys. A Mater. Sci. Process.* **126**, (2020).

331. Omri, K. *et al.* Magnetic and optical properties of manganese doped ZnO nanoparticles synthesized by sol-gel technique. *Superlattices Microstruct.* **60**, 139–147 (2013).

332. Norouzzadeh, P., Mabhouti, K., Golzan, M. M. & Naderali, R. Consequence of Mn and Ni doping on structural, optical and magnetic characteristics of ZnO nanopowders: the Williamson–Hall method, the Kramers–Kronig approach and magnetic interactions. *Appl. Phys. A Mater. Sci. Process.* **126**, 1–13 (2020).

333. Yin, Q., Qiao, R., Li, Z., Zhang, X. L. & Zhu, L. Hierarchical nanostructures of nickel-doped zinc oxide: Morphology controlled synthesis and enhanced visible-light photocatalytic activity. *J. Alloys Compd.* **618**, 318–325 (2015).

334. El-Hilo, M., Dakhel, A. A. & Ali-Mohamed, A. Y. Room temperature ferromagnetism in nanocrystalline Ni-doped ZnO synthesized by co-precipitation. *J. Magn. Magn. Mater.* **321**, 2279–2283 (2009).

335. Elilarassi, R. & Chandrasekaran, G. Synthesis and optical properties of Ni-doped zinc oxide nanoparticles for optoelectronic applications. *Optoelectron. Lett.* **6**, 6–10 (2010).

336. Elilarassi, R. & Chandrasekaran, G. Synthesis, structural and optical characterization of Ni-doped ZnO nanoparticles. *J. Mater. Sci. Mater. Electron.* **22**, 751–756 (2011).

337. Godlewski, M. *et al.* Optical properties of manganese doped wide band gap ZnS and ZnO. *Opt. Mater. (Amst).* **31**, 1768–1771 (2009).

338. Wójcik, A. *et al.* Magnetic, structural, and optical properties of low temperature ZnMnO grown by atomic layer epitaxy. *ACTA Phys. Pol. Ser. A* **108**, 915 (2006).

339. Avrutin, V. *et al.* Optical and electrical properties of ZnMnO layers grown by peroxide MBE. *Superlattices Microstruct.* **39**, 291–298 (2006).

340. Balamurali, S. *et al.* Optical and magnetic properties of Mn doped ZnO thin films grown by SILAR method. *J. Mater. Sci. Mater. Electron.* **24**, 1782–1787 (2013).

341. Jung, S. W. *et al.* Ferromagnetic properties of Zn 1− x Mn x O epitaxial thin films. *Appl. Phys. Lett.* **80**, 4561–4563 (2002).

342. Ilyas, U. *et al.* Alteration of Mn exchange coupling by oxygen interstitials in ZnO: Mn thin films. *Appl. Surf. Sci.* **258**, 6373–6378 (2012).

343. Muthukumar, S. *et al.* Selective MOCVD growth of ZnO nanotips. *IEEE Trans. Nanotechnol.* **2**, 50–54 (2003).

344. Haga, K. *et al.* High-quality ZnO films prepared on Si wafers by low-pressure MO-CVD. *Thin Solid Films* **433**, 131–134 (2003).

345. Rogelj, J. *et al.* Paris Agreement climate proposals need a boost to keep warming well below 2 C. *Nature* **534**, 631–639 (2016).

346. Nelson, J. *The physics of solar cells*. (World Scientific Publishing Company, 2003).

347. Denholm, P. & Margolis, R. M. Evaluating the limits of solar photovoltaics (PV) in traditional electric power systems. *Energy Policy* **35**, 2852–2861 (2007).

348. Green, M. A. Third generation photovoltaics. (2006).

349. Hovel, H. J. Solar cells. *STIA* **76**, 20650 (1975).

350. Maycock, P. & Bradford, T. Photovoltaics: PV market update. *Renew. Energy World* **7**, 4 (2003).

351. Nemet, G. F. Beyond the learning curve: factors influencing cost reductions in photovoltaics. *Energy Policy* **34**, 3218–3232 (2006).

352. Meinhardt, M. & Cramer, G. Past, present and future of grid connected photovoltaic- and hybrid-power-systems. in *2000 Power Engineering Society Summer Meeting (Cat. No. 00CH37134)* vol. 2 1283–1288 (IEEE, 2000).

353. Drießen, M. *et al.* Solar cells with 20% efficiency and lifetime evaluation of epitaxial wafers. *Energy Procedia* **92**, 785–790 (2016).

354. Shockley, W. & Queisser, H. J. Detailed balance limit of efficiency of p-n junction solar cells. *J. Appl. Phys.* **32**, 510–519 (1961).

355. Wang, A., Zhao, J. & Green, M. A. 24% efficient silicon solar cells. *Appl. Phys. Lett.* **57**, 602–604 (1990).

356. Tiedje, T. O. M., Yablonovitch, E. L. I., Cody, G. D. & Brooks, B. G. Limiting efficiency of silicon solar cells. *IEEE Trans. Electron Devices* **31**, 711–716 (1984).

357. Goetzberger, A., Knobloch, J. & Voss, B. Crystalline silicon solar cells. *New York* 114–118 (1998).

358. Philipps, S. & Warmuth, W. Fraunhofer ISE: Photovoltaics Report 2019. (2019).

359. Beek, W. J. E., Wienk, M. M. & Janssen, R. A. J. Efficient hybrid solar cells from zinc oxide nanoparticles and a conjugated polymer. *Adv. Mater.* **16**, 1009–1013 (2004).

360. Gobat, A. R., Lamorte, M. F. & McIver, G. W. Characteristics of high-conversion-efficiency gallium-arsenide solar cells. *IRE Trans. Mil. Electron.* 20–27 (1962).

361. Zolper, J. C. & Barnett, A. M. The effect of dislocations on the open-circuit voltage of gallium arsenide solar cells. *IEEE Trans. Electron Devices* **37**, 478–484 (1990).

362. Chu, S. S., Chu, T. L. & Yang, H. T. Thin-film gallium arsenide solar cells on tungsten/graphite substrates. *Appl. Phys. Lett.* **32**, 557–559 (1978).

363. Datum, G. C. & Billets, S. A. Gallium arsenide solar arrays-a mature technology. in *The Conference Record of the Twenty-Second IEEE Photovoltaic Specialists Conference-1991* 1422–1428 (IEEE, 1991).

364. Parkinson, B. A., Heller, A. & Miller, B. Enhanced photoelectrochemical solar-energy conversion by gallium arsenide surface modification. *Appl. Phys. Lett.* **33**, 521–523 (1978).

365. Essig, S. *et al.* Raising the one-sun conversion efficiency of III–V/Si solar cells to 32.8% for two junctions and 35.9% for three junctions. *Nat. Energy* **2**, 17144 (2017).

366. Cariou, R. *et al.* Low temperature plasma enhanced CVD epitaxial growth of silicon on GaAs: a new paradigm for III-V/Si integration. *Sci. Rep.* **6**, 25674 (2016).

367. Tanabe, K., Watanabe, K. & Arakawa, Y. III-V/Si hybrid photonic devices by direct fusion bonding. *Sci. Rep.* **2**, 349 (2012).

368. Ali, A., Gouveas, T., Hasan, M.-A., Zaidi, S. H. & Asghar, M. Influence of deep level defects on the performance of crystalline silicon solar cells: experimental and simulation study. *Sol. energy Mater. Sol. cells* **95**, 2805–2810 (2011).

369. Leijtens, T. *et al.* Carrier trapping and recombination: the role of defect physics in enhancing the open circuit voltage of metal halide perovskite solar cells. *Energy Environ. Sci.* **9**, 3472–3481 (2016).

370. Sherkar, T. S. *et al.* Recombination in perovskite solar cells: significance of grain boundaries, interface traps, and defect ions. *ACS energy Lett.* **2**, 1214–1222 (2017).

371. Goto, H. & Hattori, R. High temperature sputtered TiO2 film as an efficient blocking layer for the dye-sensitized solar cells. *Electrochemistry* **74**, 484–486 (2006).

372. Hattori, R. & Goto, H. Carrier leakage blocking effect of high temperature sputtered TiO2 film on dye-sensitized mesoporous photoelectrode. *Thin Solid Films* **515**, 8045–8049 (2007).

373. Godlewski, M. *et al.* ZnO layers grown by Atomic Layer Deposition: a new material for transparent conductive oxide. *Thin Solid Films* **518**, 1145–1148 (2009).

374. Hosono, H., Ohta, H., Orita, M., Ueda, K. & Hirano, M. Frontier of transparent conductive oxide thin films. *Vacuum* **66**, 419–425 (2002).

375. Blakers, A. W., Wang, A., Milne, A. M., Zhao, J. & Green, M. A. 22.8% efficient silicon solar cell. *Appl. Phys. Lett.* **55**, 1363–1365 (1989).

376. Poodt, P. *et al.* High-speed spatial atomic-layer deposition of aluminum oxide layers for solar cell passivation. *Adv. Mater.* **22**, 3564–3567 (2010).

377. Cotal, H. *et al.* III-V multijunction solar cells for concentrating photovoltaics. *Energy Environ. Sci.* **2**, 174–192 (2009).

378. Feifel, M. *et al.* Direct growth of III–V/Silicon triple-junction solar cells with 19.7% efficiency. *IEEE J. Photovoltaics* **8**, 1590–1595 (2018).

379. Yamaguchi, M., Takamoto, T., Araki, K. & Ekins-Daukes, N. Multi-junction III–V solar cells: current status and future potential. *Sol. Energy* **79**, 78–85 (2005).

380. Yamaguchi, M., Takamoto, T. & Araki, K. Super high-efficiency multi-junction and concentrator solar cells. *Sol. energy Mater. Sol. cells* **90**, 3068–3077 (2006).

381. Yamaguchi, M. III–V compound multi-junction solar cells: present and future. *Sol. energy Mater. Sol. cells* **75**, 261–269 (2003).

382. Pulfrey, D. L. MIS solar cells: A review. *IEEE Trans. Electron Devices* **25**, 1308–1317 (1978).

383. Schmidt, J. *et al.* Surface passivation of high-efficiency silicon solar cells by atomic-layer-deposited Al2O3. *Prog. photovoltaics Res. Appl.* **16**, 461–466 (2008).

384. Hoex, B., Bosman, M., Nandakumar, N. & Kessels, W. M. M. Silicon surface passivation by aluminium oxide studied with electron energy loss spectroscopy. *Phys. status solidi (RRL)–Rapid Res. Lett.* **7**, 937–941 (2013).

385. Schmidt, J. *et al.* Advances in the surface passivation of silicon solar cells. *Energy Procedia* **15**, 30–39 (2012).

386. Chen, L., Yu-Ming, Z., Yi-Men, Z. & Hong-Liang, L. Interfacial characteristics of Al/Al2O3/ZnO/n-GaAs MOS capacitor. *Chinese Phys. B* **22**, 76701 (2013).

387. López, J. *et al.* Refractive index and bandgap variation in Al2O3-ZnO ultrathin multilayers prepared by atomic layer deposition. *J. Alloys Compd.* **691**, 308–315 (2017).

388. Jeong, K. S., Kwon, H. M., Lee, H. D. & Lee, G. W. Ultra-thin aluminum oxide as an interface passivation layer for ZnO/p-Si heterojunction solar cells. *Phys. status solidi* **211**, 1850–1856 (2014).

389. Leskelä, M. & Ritala, M. Atomic layer deposition chemistry: recent developments and future challenges. *Angew. Chemie Int. Ed.* **42**, 5548–5554 (2003).

390. Johnson, R. W., Hultqvist, A. & Bent, S. F. A brief review of atomic layer deposition: from fundamentals to applications. *Mater. today* **17**, 236–246 (2014).

391. George, S. M. Atomic layer deposition: an overview. *Chem. Rev.* **110**, 111–131 (2010).

392. Van Delft, J. A., Garcia-Alonso, D. & Kessels, W. M. M. Atomic layer deposition for photovoltaics: applications and prospects for solar cell manufacturing. *Semicond. Sci. Technol.* **27**, 74002 (2012).

393. Niu, W. *et al.* Applications of atomic layer deposition in solar cells. *Nanotechnology* **26**, 64001 (2015).

394. Kinzel, E. Design of a Frequency-Selective Surface strain sensor. in *2014 IEEE Antennas and Propagation Society International Symposium (APSURSI)* 2074–2075 (IEEE, 2014).

395. Landy, N. I., Sajuyigbe, S., Mock, J. J., Smith, D. R. & Padilla, W. J. Perfect metamaterial absorber. *Phys. Rev. Lett.* **100**, 207402 (2008).

396. Bayatpur, F. & Sarabandi, K. A tunable metamaterial frequency-selective surface with variable modes of operation. *IEEE Trans. Microw. Theory Tech.* **57**, 1433–1438 (2009).

397. Asadchy, V. S. *et al.* Broadband reflectionless metasheets: frequency-selective transmission and perfect absorption. *Phys. Rev. X* **5**, 31005 (2015).

398. Oliveri, G., Werner, D. H. & Massa, A. Reconfigurable electromagnetics through metamaterials—A review. *Proc. IEEE* **103**, 1034–1056 (2015).

399. Qu, C. & Kinzel, E. C. Polycrystalline metasurface perfect absorbers fabricated using microsphere photolithography. *Opt. Lett.* **41**, 3399–3402 (2016).

400. Qu, C. & Kinzel, E. C. Infrared metasurfaces created with off-normal incidence microsphere photolithography. *Opt. Express* **25**, 12632–12639 (2017).

401. Qu, C. & Kinzel, E. C. Thermal Radiation From Microsphere Photolithography Patterned Metasurfaces. in *ASME 2017 Heat Transfer Summer Conference* (American Society of Mechanical Engineers Digital Collection, 2017).

402. Liu, T., Qu, C., Almasri, M. & Kinzel, E. Design and analysis of frequency-selective surface enabled microbolometers. in *Infrared Technology and Applications XLII* vol. 9819 98191V (International Society for Optics and Photonics, 2016).

403. Alù, A. & Engheta, N. Optical nanotransmission lines: synthesis of planar left-handed metamaterials in the infrared and visible regimes. *JOSA B* **23**, 571–583 (2006).

404. Yao, Y. *et al.* Electrically tunable metasurface perfect absorbers for ultrathin mid-infrared optical modulators. *Nano Lett.* **14**, 6526–6532 (2014).

405. Chen, S. *et al.* Polarization insensitive and omnidirectional broadband near perfect planar metamaterial absorber in the near infrared regime. *Appl. Phys. Lett.* **99**, 253104 (2011).

406. Fan, Y., Shen, N.-H., Koschny, T. & Soukoulis, C. M. Tunable terahertz meta-surface with graphene cut-wires. *Acs Photonics* **2**, 151–156 (2015).

407. Song, Z., Zhang, L. & Liu, Q. H. High-efficiency broadband cross polarization converter for near-infrared light based on anisotropic plasmonic meta-surfaces. *Plasmonics* **11**, 61–64 (2016).

408. Tao, H. *et al.* A dual band terahertz metamaterial absorber. *J. Phys. D. Appl. Phys.* **43**, 225102 (2010).

409. Engheta, N., Salandrino, A. & Alu, A. Circuit elements at optical frequencies: nanoinductors, nanocapacitors, and nanoresistors. *Phys. Rev. Lett.* **95**, 95504 (2005).

410. Liu, N., Mesch, M., Weiss, T., Hentschel, M. & Giessen, H. Infrared perfect absorber and its application as plasmonic sensor. *Nano Lett.* **10**, 2342–2348 (2010).

411. Pang, Y., Zhou, Y. & Wang, J. Equivalent circuit method analysis of the influence of frequency selective surface resistance on the frequency response of metamaterial absorbers. *J. Appl. Phys.* **110**, 23704 (2011).

412. Pu, M. *et al.* Design principles for infrared wide-angle perfect absorber based on plasmonic structure. *Opt. Express* **19**, 17413–17420 (2011).

413. Raynolds, J. E., Munk, B. A., Pryor, J. B. & Marhefka, R. J. Ohmic loss in frequency-selective surfaces. *J. Appl. Phys.* **93**, 5346–5358 (2003).

414. Kristensen, R. T., Beausang, J. F. & DePoy, D. M. Frequency selective surfaces as near-infrared electromagnetic filters for thermophotovoltaic spectral control. *J. Appl. Phys.* **95**, 4845–4851 (2004).

415. Kou, J., Jurado, Z., Chen, Z., Fan, S. & Minnich, A. J. Daytime radiative cooling using near-black infrared emitters. *Acs Photonics* **4**, 626–630 (2017).

416. Family, R. & Mengüç, M. P. Materials for radiative cooling: a review. *Procedia Environ. Sci.* **38**, 752–759 (2017).

417. Xu, C. *et al.* Metamaterial absorber for frequency selective thermal radiation. *Infrared Phys. Technol.* **88**, 133–138 (2018).

418. Debus, C. & Bolivar, P. H. Frequency selective surfaces for high sensitivity terahertz sensing. *Appl. Phys. Lett.* **91**, 184102 (2007).

419. Monacelli, B., Pryor, J. B., Munk, B. A., Kotter, D. & Boreman, G. D. Infrared frequency selective surface based on circuit-analog square loop design. *IEEE Trans. Antennas Propag.* **53**, 745–752 (2005).

420. Puscasu, I., Schaich, W. L. & Boreman, G. D. Modeling parameters for the spectral behavior of infrared frequency-selective surfaces. *Appl. Opt.* **40**, 118–124 (2001).

421. Govindaswamy, S. *et al.* Frequency-selective surface based bandpass filters in the near-infrared region. *Microw. Opt. Technol. Lett.* **41**, 266–269 (2004).

422. Ginn, J. *et al.* Modeling infrared frequency selective surfaces with frequency dependent materials. *22nd Int. Rev. Prog. Appl. Comput. Electromagn. (ACES 2006)* 307–311 (2006).

423. Costa, F., Monorchio, A. & Manara, G. An equivalent circuit model of frequency selective surfaces embedded within dielectric layers. in *2009 IEEE Antennas and Propagation Society International Symposium* 1–4 (IEEE, 2009).

424. Arik, K., Abdollahramezani, S., Farajollahi, S., Khavasi, A. & Rejaei, B. Design of mid-infrared ultra-wideband metallic absorber based on circuit theory. *Opt. Commun.* **381**, 309–313 (2016).

425. Wen, Q.-Y. *et al.* Transmission line model and fields analysis of metamaterial absorber in the terahertz band. *Opt. Express* **17**, 20256–20265 (2009).

426. Ebrahimi, A. *et al.* Second-order terahertz bandpass frequency selective surface with miniaturized elements. *IEEE Trans. Terahertz Sci. Technol.* **5**, 761–769 (2015).

427. Costa, F., Monorchio, A. & Manara, G. Efficient analysis of frequency-selective surfaces by a simple equivalent-circuit model. *IEEE Antennas Propag. Mag.* **54**, 35–48 (2012).

428. Costa, F., Genovesi, S., Monorchio, A. & Manara, G. A circuit-based model for the interpretation of perfect metamaterial absorbers. *IEEE Trans. Antennas Propag.* **61**, 1201–1209 (2012).

429. Costa, F., Monorchio, A. & Manara, G. Analysis and design of ultra thin electromagnetic absorbers comprising resistively loaded high impedance surfaces. *IEEE Trans. Antennas Propag.* **58**, 1551–1558 (2010).

430. Bossard, J. A. *et al.* The design and fabrication of planar multiband metallodielectric frequency selective surfaces for infrared applications. *IEEE Trans. Antennas Propag.* **54**, 1265–1276 (2006).

431. Staffaroni, M., Conway, J., Vedantam, S., Tang, J. & Yablonovitch, E. Circuit analysis in metal-optics. *Photonics Nanostructures-Fundamentals Appl.* **10**, 166–176 (2012).

432. Palik, E. D. *Handbook of optical constants of solids*. vol. 3 (Academic press, 1998).

433. Campione, S., Warne, L. K., Goldflam, M. D., Peters, D. W. & Sinclair, M. B. Improved quantitative circuit model of realistic patch-based nanoantenna-enabled detectors. *JOSA B* **35**, 2144–2152 (2018).

434. Rosa, E. B. *The self and mutual inductances of linear conductors*. (US Department of Commerce and Labor, Bureau of Standards, 1908).

435. Villarraga Gomes, H. Magneto-optical studies of cobalt-doped nickel oxide thin films. *PHDT* (2010).

436. Zeper, W. B., Greidanus, F., Carcia, P. F. & Fincher, C. R. Perpendicular magnetic anisotropy and magneto-optical Kerr effect of vapor-deposited Co/Pt-layered structures. *J. Appl. Phys.* **65**, 4971–4975 (1989).

437. Florczak, J. M. & Dahlberg, E. D. Detecting two magnetization components by the magneto-optical Kerr effect. *J. Appl. Phys.* **67**, 7520–7525 (1990).

438. Allwood, D. A., Xiong, G., Cooke, M. D. & Cowburn, R. P. Magneto-optical Kerr effect analysis of magnetic nanostructures. *J. Phys. D. Appl. Phys.* **36**, 2175 (2003).

439. De Waard, H., Uggerho/j, E. & Miller, G. L. An experimental investigation of the surface magnetization of iron using the magneto-optical Kerr effect. *J. Appl. Phys.* **46**, 2264–2267 (1975).

440. Chen, L.-C., Tien, C.-H. & Mu, C.-S. Effects of spin-polarized injection and photo-ionization of MnZnO film on GaN-based light-emitting diodes. *Opt. Express* **18**, 2302–2308 (2010).

441. Kurnia, F. & Hart, J. N. Band-Gap Control of Zinc Sulfide: Towards an Efficient Visible-Light-Sensitive Photocatalyst. *ChemPhysChem* **16**, 2397–2402 (2015).

442. Ko, D. H. *et al.* A Novel Chemical Route to Atomic Layer Deposition of ZnS Thin Film from Diethylzinc and 1,5-Pentanedithiol. *Bull. Korean Chem. Soc.* **38**, 696–699 (2017).

443. Kuhs, J., Dobbelaere, T., Hens, Z. & Detavernier, C. Plasma enhanced atomic layer deposition of zinc sulfide thin films. *J. Vac. Sci. Technol. A Vacuum, Surfaces, Film.* **35**, 01B111 (2017).

444. Mohamed, M. B. Effect of doping and changing of the annealing temperature on the structural and optical properties of ZnS. *Int. J. Appl. Ceram. Technol.* **17**, 823–831 (2020).

445. Sharma, R. Structural and optical characterization of ZnS nanoparticles. *Int. Multidiscip. Res. J. 2011*, **1**, 8–11 (2011).

446. Shao, Y., Guo, Z., Li, H., Su, Y. & Wang, X. Atomic Layer Deposition of Iron Sulfide and Its Application as a Catalyst in the Hydrogenation of Azobenzenes. *Angew. Chemie - Int. Ed.* **56**, 3226–3231 (2017).

447. Zhao, W. *et al.* Controlled synthesis of Zn(1-1.5x)FexS nanoparticles via a microwave route and their photocatalytic properties. *RSC Adv.* **5**, 106644–106650 (2015).

448. Akhtar, M. S. *et al.* Chemical bath deposition of Fe-doped ZnS thin films: Investigations of their ferromagnetic and half-metallic properties. *Mater. Sci. Semicond. Process.* **39**, 283–291 (2015).

449. Bakke, J. R., King, J. S., Jung, H. J., Sinclair, R. & Bent, S. F. Atomic layer deposition of ZnS via in situ production of H2S. *Thin Solid Films* **518**, 5400–5408 (2010).

450. Deulkar, S. H., Bhosale, C. H. & Sharon, M. A comparative study of structural, compositional, thermal and optical properties of non stoichiometric (Zn,Fe)S chalcogenide pellets and thin films. *J. Phys. Chem. Solids* **65**, 1879–1885 (2004).

451. Feng, Q. J. *et al.* Influence of Fe content on the structural and optical properties of ZnFeS thin films. *Mater. Chem. Phys.* **96**, 158–162 (2006).

452. Qiao, F. *et al.* Tunability in the optical and electronic properties of ZnSe microspheres via Ag and Mn doping. *ACS omega* **4**, 12271–12277 (2019).

VITA

Vishal Saravade was born in Thane, Maharashtra, India on November 15, 1992. He received a B.Tech. (Bachelor's in Technology) degree in Electronics Engineering from Veermata Jijabai Technological Institute, Mumbai, Maharashtra, India in June 2014. He received a Doctor of Philosophy in Electrical Engineering from Missouri University of Science and Technology, Rolla, MO, in August 2020. His research topic was focused on the investigation of wide bandgap compound semiconductors for room temperature spintronic, and photovoltaic applications. He has been an author or co-author in over 15 research articles.

Vishal was a Teaching Assistant in Fall 2018 and Spring 2019 semesters and taught Discrete-time linear systems lab in Department of Electrical and Computer Engineering at Missouri University of Science and Technology. He was a Department Representative in Electrical and Computer Engineering Department at Missouri S&T during the 2014-2016 academic years. He was a communications engineering trainee/intern at Doordarshan (India's television broadcasting service), Mumbai, Maharashtra, in June 2013.